N° d'ordre : 40534

L'UNIVERSITE DES SCIENCES ET TECHNOLOGIES DE LILLE

THESE

Présentée en vue d'obtenir le grade de

DOCTEUR EN ELECTRONIQUE DE L'UNIVERSITE DE LILLE 1

Spécialité Micro et Nanotechnologies, Acoustiques, et Télécommunications

par

Thi Phuong Nhung Nguyen

Titre de thèse :

Fabrication of Nanostructured Silicon Substrates for the Development of Superomniphobic Surfaces and Surface-Assisted Laser Desorption/Ionization Mass Spectrometry Analysis of Biomolecules

Soutenue le 9-Juin-2011 devant le jury d'examen :

Président	Tuami Lasri	Professeur Université de Lille 1
Rapporteur	Christine Enjalbal	Professeur, Université Montpellier 2
Rapporteur	David Cornu	Professeur, ENSCM, Montpellier 2
Examinateur	Mathilde Reyssat	Maître de Conférences, ESPCI
Examinateur	Wilfrid Boireau	Chargé de Recherche, FEMTO-ST
Examinateur	Jérémy Mallet	Maître de Conférences, Université de Reims Champagne-Ardenne
Directeur de thèse	Rabah Boukherroub	Directeur de Recherche CNRS, IRI
Co-encadrant	Yannick Coffinier	Chargé de Recherche CNRS, IRI
Co-encadrant	Vincent Thomy	Maître de Conférences, Université de Lille 1

Remerciements

*Cette thèse a été menée en collaboration entre l'**IRI** (Institut de Recherche Interdisciplinaire) **et** l'**IEMN** (Institut d'Electronique de Microélectronique et de Nanotechnologie).*

*Je remercie tout d'abord Messieurs **Ralf Blossey et Vincent Villeret**, Directeurs successifs de l'IRI ainsi que Messieurs **Alain Cappy et Lionel Bouchaillot**, Directeur successifs de l'IEMN, pour m'avoir accueillie au sein de leur laboratoire.*

*Je tiens à remercier Monsieur **Vincent Senez**, Responsable du groupe BioMEMS de l'IEMN, pour avoir facilité mon intégration dans son groupe.*

*De plus, j'exprime toute ma gratitude à Madame **Christine Enjabal**, Professeur de l'Université Montpellier 2 et à Monsieur **David Cornu**, Professeur de l'ENSCM à l'Université de Montpellier 2 pour m'avoir fait l'honneur de juger ce travail et d'en être rapporteurs.*

*Je remercie aussi les membres du jury pour avoir accepté d'évaluer mon travail de recherche : Madame **Mathilde Reyssat**, Maître de conférences de l'ESPCI, Monsieur **Tuami Lasri**, Professeur de l'Université Lille 1, Monsieur **Wilfrid Boireau**, Chargé de Recherche à FEMTO-ST, Monsieur **Jéremy Mallet**, Maître de Conférences, de l'Université de Reims, Champagne-Ardenne.*

*Je remercie tout particulièrement Monsieur **Rabah Boukherroub**, Directeur de Recherche de l'IRI, de m'avoir accueillie au sein du Groupe NanoBiointerfaces et je le remercie encore pour avoir dirigé mon travail de thèse, et pour la pertinence de ses conseils.*

*Je remercie sincèrement Monsieur **Vincent Thomy**, Maître de conférences de l'Université Lille 1, pour son soutien, sa gentillesse, et sa disponibilité pendant les trois ans de thèse.*

*J'adresse particulièrement mes remerciements et toute ma reconnaissance à Monsieur **Yannick Coffinier**, Chargé de Rechercher CNRS de l'IRI, pour m'avoir guidée tout au long de ce travail de recherche. Je le remercie vraiment pour sa patience et pour ses précieux renseignements au cours de ces trois ans. Sans lui, cette thèse n'aurait pas pu réussir. Merci Yco ! Oh Yes !*

*Je tiens aussi à remercier Monsieur **Philippe Brunet**, Chargé de recherche dans l'équipe Films (Groupe LEMAC de l'IEMN), pour sa disponibilité et les enseignements qu'il a pu*

m'apporter.

*Je remercie également Monsieur **Oleg Melnyk**, Directeur de Recherche, de m'avoir accueillie au sein du groupe «Chimie des Biomolécules », de l'Institut de Biologie de Lille (IBL), ainsi que Monsieur **Hervé Drobecq**, Assistant ingénieur de l'Université Lille 2, pour sa collaboration et ses conseils.*

Je tiens également à remercier tous les collègues et mes amies de l'IRI et de l'IEMN, en particulier :

*- Du groupe BioMEMS de l'IEMN: **Chang, Florian, Damien, Romuald, Maxime, Antony Timothée, Guillaume, Renaud, François, Farida, Philippe**….*

*- Du groupe Nanointerface de l'IRI : **Mei, Gaëlle, Elisabeth, Manshusha, Maël, Paolo, Alex, Nazek, Nacéra...***

*- De l'équipe Opto : **Christophe, Anisha, Floriane, Djamilla, Thomas, Edy, Arnaud, Antoine, Naïma…***

*- Des autres équipes de l'IEMN : **Eléonore, Marc, Hermance, Yannick, Renaud, Jérémy…***

Tous ceux que je ne saurais oublier qui m'ont encouragé et ont toujours été à mes côtés durant ce séjour à l'étranger, pour tous les bons moments partagés en salle blanche, à la cafétéria, aux soirées…

Mes pensées vont, enfin, à ma famille:

Nam nam xa nha khong phai la ngan, nhung du de con truong thanh, va buoc them mot buoc. Con that su cam on ong ba, bo me, em Quynh chi Diep, anh Hai, chau Hai Minh va chau Hai An, da tin tuong con, dong vien con de con duoc nhu ngay hom nay !

Xuan, Hoa, Thu, Minh, chi Huong va anh Tuan, to khong biet noi gi hon ca, chi biet la cam on cac ban nhieu, cam on da o ben canh to, cam on da chia se voi to nhung ngay thang nam qua! Cam on cac ban nhieu va that nhieu nha !Iu iu iu!

Contents

General Introduction

The major progress made in life sciences takes its origin in the multidisciplinary fields where physics, technological engineering, chemistry and biology converge. Among recent examples, we can cite the human genome description, severe disease diagnosis and treatment such as cancer ... From a physical point, since the view of Feynman about the tremendous possibilities of the nanometer scale, nanotechnology is an example of this convergence for biology, biomedicine or biotechnology.

The field of preparation, characterization and applications of nanostructured silicon substrates is recognized as one of the fast moving and exciting areas. Nanostructured silicon objects possess more attractive properties as compared to bulk silicon, such as better electronic, mechanical, optical and thermal properties, biocompatibility, and high surface-to-volume ratio. Moreover, the surface of silicon nano-objects can be easily chemically modified using a myriad of reactions, as for flat silicon surface, to introduce different chemical terminations, resulting in improved multifunctional interfaces.[1][2][3][4]

The choice of silicon, a low cost material, in this work is based on its dominant position in the semiconductor industry, leading to well known and controlled properties.[1] [5]. Furthermore, different types of silicon nano-objects (nanodots, nanowires, nanorods, nanoribbons, nanoparticles…) can be easily fabricated *via* a large variety of techniques such as lithography, wet and dry etching, electrochemical or electroless etching methods, chemical vapour deposition (CVD), etc. [6][7][8]

Therefore, silicon nano-objects led to a large and various fields of applications such as electronic, optics, biosensing, diagnosis, analytical tools, microfluidic....[9][10][11][12][13] For example, silicon nanowires, prepared *via* the vapour-liquid-solid growth mechanism (VLS), coated with Ag nanoparticles showed a large Raman scattering enhancement for rhodamine 6G (R6G) with a detection limit of 10^{-14} M and an enhancement factor of 2.3×10^8 M. [10] Other examples of applications of nanostructured silicon surfaces, synthesized *via* metal-assisted etching, concern their water repellency and self-cleaning properties. [14] Furthermore, patterned superhydrophobic/superhydrophilic silicon nanostructured substrates permit selective adhesion of *Bacillus cereus* spores in the superhydrophilic areas.[15]

Furthermore, nanostructured silicon surfaces found also applications in the microfluidic field. Indeed, nanostructured silicon surfaces present a high surface roughness than flat silicon and therefore can be applied for the development of superhydrophobic and superominophobic surfaces by mimicking nature (biomimetic surfaces). However, there is no example in nature on existing objects able to repel a large variety of liquids of different surface tensions (from water to oil or organic liquids). Such surfaces are called superomniphobic surfaces. This field became of great interest and brought a large number of applications such as: self-cleaning [14] [16], selective adhesion of cells, spores... [15], environmental and counter-terrorism applications (collect of dangerous or harmful particles from air [14], drag reduction surfaces, digital microfluidic such as electrowetting on dielectric (EWOD) for droplet actuation... [13] [14]

This work has taken profit of a multidisciplinary environment in a relatively small geographical area. The realisation and experimentation depicted in this document have been performed in collaboration with several laboratories: Interdisciplinary Research Institute (**IRI-CNRS 3078**), Institute of Electronics, Microelectronics and Nanotechnology (**IEMN-CNRS 8520**) (BioMEMS and AIMAN groups), and Institute of Biology of Lille (**IBL-CNRS 8161**).

The objectives of this work are multiple. Firstly, we'll focus on the fabrication of nanostructured silicon surfaces of different morphologies using two methods: silicon nanostructures (NanoSi) and silicon nanowires (SiNWs). The obtained interfaces will be used to develop superhydrophobic and superomniphobic surfaces. Finally, the interfaces will be investigated as inorganic matrices for the realization of laser desorption/ionization of small molecules and their mass spectrometry analysis.

This work is organized in four chapters: chapters 1 and 2 are dedicated to NanoSi and SiNWs fabrication techniques and their characterizations, whereas the chapters 3 and 4 deal with the use of these NanoSi and SiNWs substrates for mass spectrometry analysis of small molecules.

In chapter 1, after a brief review of the various types of micro and nanofabrication methods, I will focus on two techniques used in this work to form 1D nano-objects: a wet etching method based on metal-assisted electroless etching and silicon nanowires growth *via* CVD. Both techniques will be also combined with classical optical lithography and dry etching processes to prepare multi-scale structured surfaces.

In chapter 2, the obtained NanoSi surfaces are functionalized with low surface energy molecules such as octadecyltrichlorosilane or perfluorooctyltrichlorosilane and their wetting

properties with liquids presenting various surface tensions ranging from 21.6 to 72.2 mN/m are evaluated using contact angle measurements (Young's, apparent, advancing, receding and hysteresis). Furthermore, the robustness of the functionalized surfaces is assessed using droplet impact experiments.

From these results, I will discuss the balance between the wetting properties (from superhydrophobic to superomniphobic, the well-known Cassie-Baxter and Wenzel models) and surface morphology (linked to the fabrication method).

Part of the work presented **in chapter 3** completes previous studies from the thesis defended by Gaëlle Piret. After a presentation of the general aspects of mass spectrometry, I will discuss in more details the Surface-Assisted Laser Desorption/Ionization Mass Spectrometry technique. Herein, I will demonstrate that the NanoSi and Nanowires interfaces, prepared in chapter 1, can be successfully used as DIOS platforms for MS analysis of small peptides. Furthermore, I will also investigate crucial factors influencing the DIOS-MS efficiency such as: surface morphology, doping type, chemical termination and heat confinement.

In chapter 4, I will report a simple method for the introduction of nitrilotriacetic acid (NTA)-Ni^{2+} complex on the NanoSi surfaces and its use for histidine-tagged peptide enrichment and its subsequent mass spectrometry analysis. The NTA-Ni^{2+} terminal groups are immobilized onto the NanoSi surface *via* Si-C covalent bond. The NTA-Ni^{2+} modified NanoSi interface is characterized using Fourier transform infrared spectroscopy (FT-IR), X-ray photoelectron spectroscopy (XPS) and contact angle (CA) measurements. Finally, I'll demonstrate the ability of the affinity interface to perform peptide enrichment from an artificial mixture using FT-IR, fluorescence measurements and MS analysis.

1. Fabrication of silicon nanostructures via Top-down and Bottom-up

1.1. Introduction

The preparation of silicon nanostructures has been achieved using a wide variety of techniques in the past years. These techniques are basically divided in two main categories: The "Top-down" and "Bottom-up" approaches.[11] [17] [18] [19]

On the one hand, the "Top-down" approach consists in sculpting material to make micro or nano-scale structures using techniques such as lithography, wet and dry etching, electrochemical and electroless etching [18] [20],…. For example, the combination of lithography and deep reactive ion etching (dry etching technique) steps leads to different silicon morphologies such as sharp tips, nanopillars or nanoposts [21] [22]. Porous silicon or silicon nanostructures of various morphologies can be obtained by anodic etching [23] [24] [25] or electroless etching methods [8] [7] [15].

On the other hand, the "Bottom-up" approach consists in the fabrication or synthesis of new objects or structures from the assembly of small entities such as atoms, molecules or nanowires by chemical vapor deposition (CVD), physical vapor deposition (PVD), molecular beam epitaxy (MBE) and sol-gel methods [11] [18] [20] [26].

Sometimes, the nanostructured silicon surfaces can be created by the combination of top-down and bottom-up approaches.

In this chapter, I will review several existing methods for the fabrication of structured silicon substrates. Then, I will focus on the substrates prepared and characterized during this work: Nanostructured silicon (NanoSi) fabrication *via* the metal-assisted etching method using either $HF/AgNO_3$ or $NaBF_4/AgNO_3$ aqueous solutions and on silicon nanowires (SiNWs) synthesis *via* Vapour-Solid-Liquid (VLS) growth mechanism. I will present the different surface morphologies obtained through the control of various fabrication process parameters such as: solution concentration, duration, temperature, and type of wafer used. The surface morphology of the resulting substrates is characterized using Scanning Electron Microscope (SEM).

1.2. Top-down approach

Lithography is the most common technique used for the creation of patterned substrates. The technique serves to write patterns onto a substrate using a mask (optical or electronic), an energy source (photons, electrons…) and a sensitive resist. Depending on the energy source, the resists are either sensitive to electrons (electronic resist) or to photons (optical resist). The main lithography technique used in silicon industry is photolithography (using UV with λ=365 nm) and electron beam lithography (EBL). As shown in Figure 1.1 (a), the resist is first deposited on the substrate by spin-coating, followed by baking steps. Then, an energy beam passes through an optical mask (photolithography) or is used to write directly patterns (from an electronic file containing the patterns). This allows the transfer of patterns from the mask to the resist, leading to a latent image (Figure 1.1(a)). The resist is an organic polymer and is divided into two types: positive or negative. In the case of a positive resist, when the resist is irradiated by the energy beam (electrons or photons), the irradiated zones become more soluble in the developer solution (organic solvent) due to breaking of the chemical bonds inside the resist, and are easily removed by the developer. In contrast to the negative resist, the irradiated zones become insoluble in the developer solution and are not removed by the developer when a negative resist is used. The choice of the resist depends on the desired pattern size and the type of mask [11][18][27][28].

In EBL, the minimum size of pattern which can be reached is about 5 nm depending on the instrumental accuracy. However, EBL is not easy to handle, not suitable for large-scale production, and is time consuming and expensive. Concerning the photolithography, it is more dedicated to mass-production but suffers from resolution limitations (100 nm). This limitation can be overcome by using a smaller wavelength, which is more energetic such as: Deep UV (DUV lithography) and Extreme-UV (EUV) notably by using excimer lasers. However, their illumination sources are expensive [28][29].

In practice, the lithography techniques only serve for the creation of patterns on the substrates. Thus, in order to obtain structured silicon surfaces, this technique must be combined with other techniques such as: dry or wet etching (top-down), film deposition or growth techniques (bottom-up) (which will be presented in the next section). For example, Figure 1.1 (b) illustrates the steps for structured silicon fabrication: After resist patterning by lithography technique, the patterned substrate is either etched (wet or dry etching), or a deposition step is realized. Then, the resist layers are removed in the development solution, leading to the formation of textured surfaces.
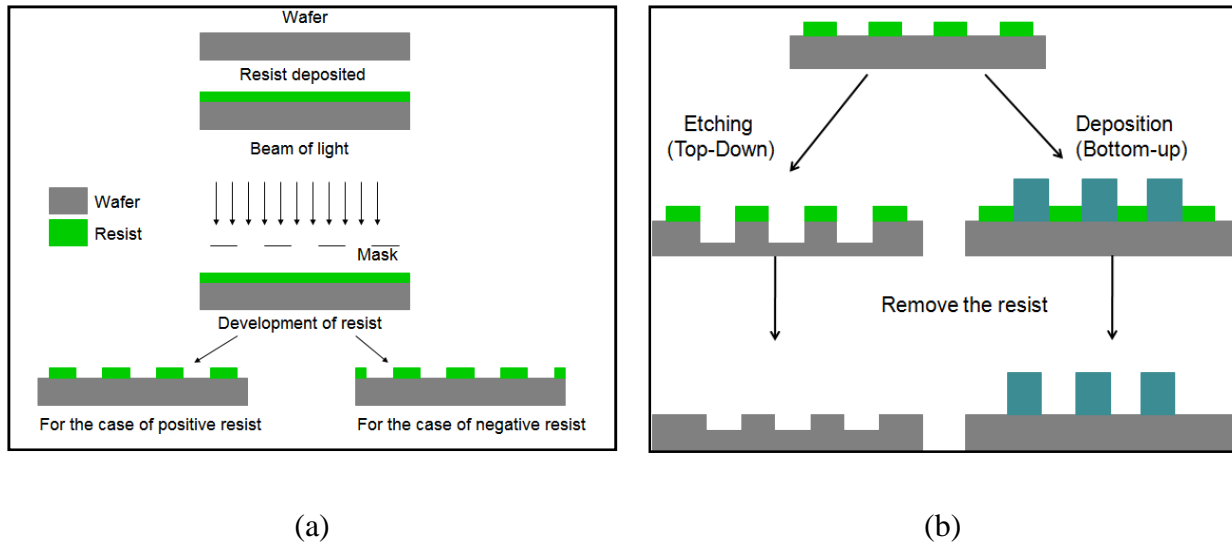
Figure 1.1: (a) Photolithography principle and (b) structured silicon fabrication by the combination of lithography with either etching or film deposition.

1.2.1. Etching Techniques

The etching techniques include **wet and dry etching** [30] [31] [32]. Figure 1.1 (b) illustrates the etching process carried out on the patterned substrate: the area which is not covered by the resist is etched away, whereas the protected area is left intact. Here, the resist serves as a mask to protect the desired layer which should not be etched. The mask can be any other material which is resistant to the etchant. Usually, the etching technique is estimated by various parameters: etch rate, selectivity, bias and the aspect ratio. The etch rate depends on various etching parameters such as: nature of desired material to be etched, etchant concentration, and temperature.

Wet etching

Wet etching uses liquid-phase ("wet") etchants. It is easy to handle and has a high material selectivity. Furthermore, it does not require highly-prized specific equipment (as we will see after concerning the dry etching). However, this method has some disadvantages: difficult to control, very sensitive to temperature, and difficult to achieve well-defined features (aspect ratio).

For crystalline materials like silicon, the wet etching can be isotropic or anisotropic: When the etch rate is the same in all directions, this etching process is called isotropic (Figure

1.2 (a)). On the contrary, when the etch rate is not the same in all the directions, this process is called anisotropic (Figure 1.2 (b)), allowing the formation of specific etching profiles.

(a) Isotropic etching   (b) Anisotropic etching
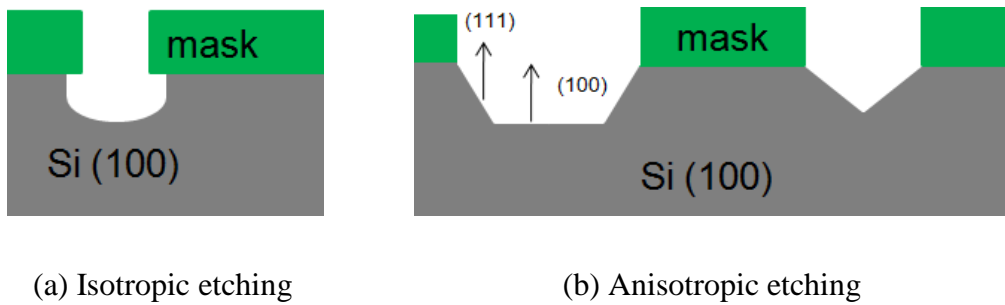
Figure 1.2: (a) Isotropic and (b) anisotropic etching of Si(100).

Silicon anisotropic etching can be performed by common solutions such as potassium hydroxide (KOH), tetramethylammonium hydroxide (TMAH) or an aqueous solution of ethylene diamine and pyrocatechol (EDP). These solutions etch silicon substrate at a preferential rate according to the various crystallographic lattice planes. The silicon is quickly etched in the (100) and (110) directions and slowly in the (111) direction. Thus, for example, an open square patterned Si (100) is etched by KOH, TMAH or EDP aqueous solutions, leading to the formation of "V-grooves" or pyramids (Figure 1.2 (b)). In this etching process, Si_xN_y or SiO_2 are usually used as a protective layer [26] [32] [33] [34] [35] [36]. For example, Figure 1.3 displays SEM images of a silicon grid, which is realized by KOH etching of a Si (100) wafer using Si_xN_y as a mask [37].
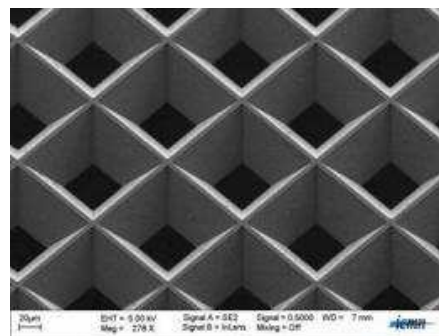
Figure 1.3: SEM image of a silicon grid obtained by KOH etching of Si (100) wafer using Si_xN_y as a protective layer. [37]

Dry Etching

Dry etching techniques are essentially based on plasma etching processes, which occur in specific equipments. Plasmas attack the material using the association of two components: one is a purely physical etching and the second one is a purely chemical etching. It is possible to promote one over the other by playing with parameters such as power, pressure in the chamber and more importantly, the gas used. If the ion energy is higher than 20 eV, the physical effect essentially leads to an anisotropic etching. If the energy ion is lower than 20 eV, the chemical effect will essentially give an isotropic etching. Usually, two techniques are often used in dry etching: RIE (reactive ion etching) and DRIE (deep reactive ion etching) [18] [31] [21].
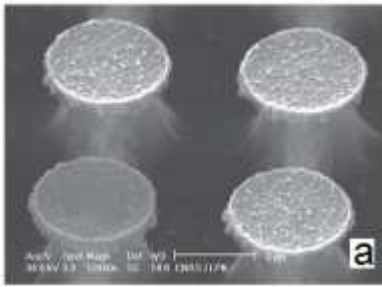
Figure 1.4: SEM image of silicon microstructures prepared by RIE [38]

In the case of RIE, the etching occurs by the reactive plasma, which is generated under low pressure (from 10^{-2} to 10^{-1} Torr) by the application of low frequency RF or DC field. The reactive ions are accelerated and bombard the surface *via* physical and chemical effects. This attack may, or not, be anisotropic, depending on the pressure and the type of the gas used (most of them are fluoride-based gases such as SF_6, CF_4, and CHF_3). In that case, the created ionized species react with the surface (chemical effect). However, the etch rate is slow (about 3μm/h) and a non-controlled attack can lead to an under-etching, as shown in Figure 1.4.

The disadvantages of RIE can be overcome by the DRIE technique (Bosch or cryogenic). The Bosch process is illustrated in Figure 1.5: It utilizes alternative pulses of two fluoride gases, one for passivation (C_4F_8) and the other for etching (SF_6 or others). The passivation layer protects the entire substrate from further chemical attack. During the etching phase of DRIE method, the directional ions (vertical), that bombard the substrate, attack the passivation layer at the top and at the bottom of the trench (but not along the sides). They collide with it and sputter it off, exposing the substrate to the chemical etchant. Thus, the obtained feature shapes depend on parameters such as: time between each pulse (SF_6 and C_4F_8), gas flow, pressure in the chamber, power (RF), and temperature inside the chamber. It is often observed that the sidewall of texture presents rippling or cyclic forms. This effect is called "scalloping" (Figure 1.5 (b) (c) and (d)) and controlled through the etching parameters. The typical etch rate is about 3-10μm/min.
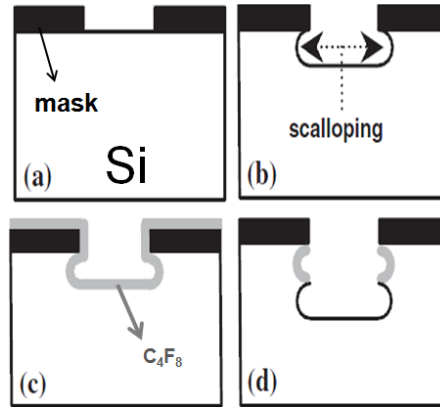
Figure 1.5: Schematic diagram of cyclic Bosh process in DRIE: (a) the patterned silicon surface with a photoresist mask, (b) SF_6 etch with anisotropic bombardment, (c) polymer deposition using C_4F_8, (d) SF_6 etch and polymer deposition is repeated according to the total number of etch cycles [21].

For example, by playing on the etching parameters of DRIE, Choice *et al.* obtained various sidewall profiles of NanoSi as shown in Figure 1.6: (a) a sharp-tip profile, (b) a re-entrant profile, (c) a positively tapered profile, and (d) a nanopost structure. [21]
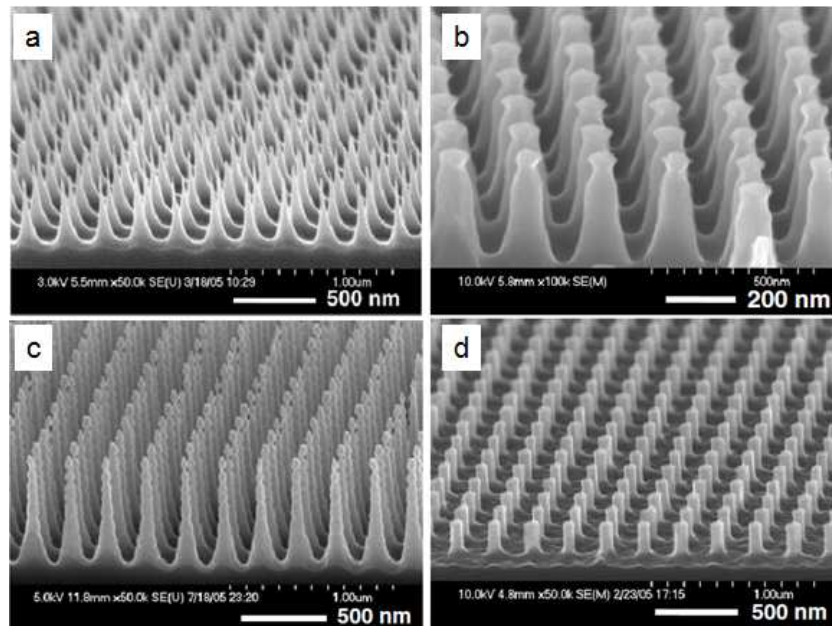
Figure 1.6: SEM images of silicon nanostructures with different shapes: a sharp tip profile (a), re-entrant sidewall profiles (b), positively tapered sidewall profiles (c), and nanopost structure (d). All the surfaces are obtained by the control of the scalloping effect [21]

The fabrication of micro and nanostructured silicon substrates can be obtained by wet or dry etching methods or by a combination of both. Usually, these techniques require the use of a mask in order to define the desired patterns. Nonetheless, it leads to a complex process due to the important number of technological steps: necessity to control the mask transfer on the silicon surface, the etching process … The duration and the cost of fabrication can thus be quite important. As described below, other techniques offer the possibility to prepare nanoscale structures in a more straightforward way and low cost.

1.2.2.   Electrochemical etching

Electrochemical etching is a simple method used in nanofabrication. The substrate does not need to be patterned before the etching process. Meanwhile, it is possible to combine this technique with photolithography for selecting the etched areas. The electrochemical etching routes occur in fluoride-based solutions such as HF, NH_4F…; its mechanism has not been satisfactorily explained yet. However, the most widely accepted model was proposed by Allongue *et al.* as depicted in Figure 1.7. [8] [23] [39] [40] [41] [42]

First, it needs to recognize that the chemical composition of fluoride solutions is complex and not entirely well elucidated. There are different fluoride states such as: HF, HF (aq), HF_2^-, and $H_2F_3^-$, etc... Secondly, it is known that the Si surface is highly reactive, thus it will rapidly oxidize and form a native oxide layer with a thickness of several angstroms. When the native oxide surface is dipped into a fluoride solution, the oxide layer is rapidly etched according to the following equations (1.1) and (1.2) and leaves a hydrogen terminated surface (Si-H) (**Step 1**).

$$SiO_2 + 6HF \rightarrow SiF_6^{2-} + 2H_2O + 2H^+ \qquad \textbf{(1.1)}$$

$$SiO_2 + 3HF_2^- \rightarrow SiF_6^{2-} + H_2O + OH \qquad \textbf{(1.2)}$$
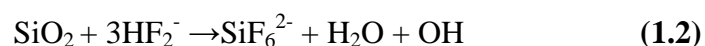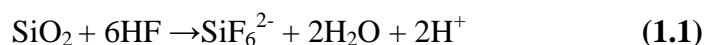
Then, the weak Si-H bond is oxidized to form Si-OH bond by accepting holes from the source such as applied bias or oxidant agent, laser… **(Step 2)**. In the next step, F^- ions replace OH^- groups, forming Si-F bonds **(Step 3)**. These bonds are very polar, leading to the polarization of the adjacent Si-Si bonds. Therefore, Si-Si bond is easily broken by the attack of HF molecules. A Si atom from the bulk is etched away and leaves the remaining Si atoms bound to H atoms. The process then continues from the beginning until it is interrupted.
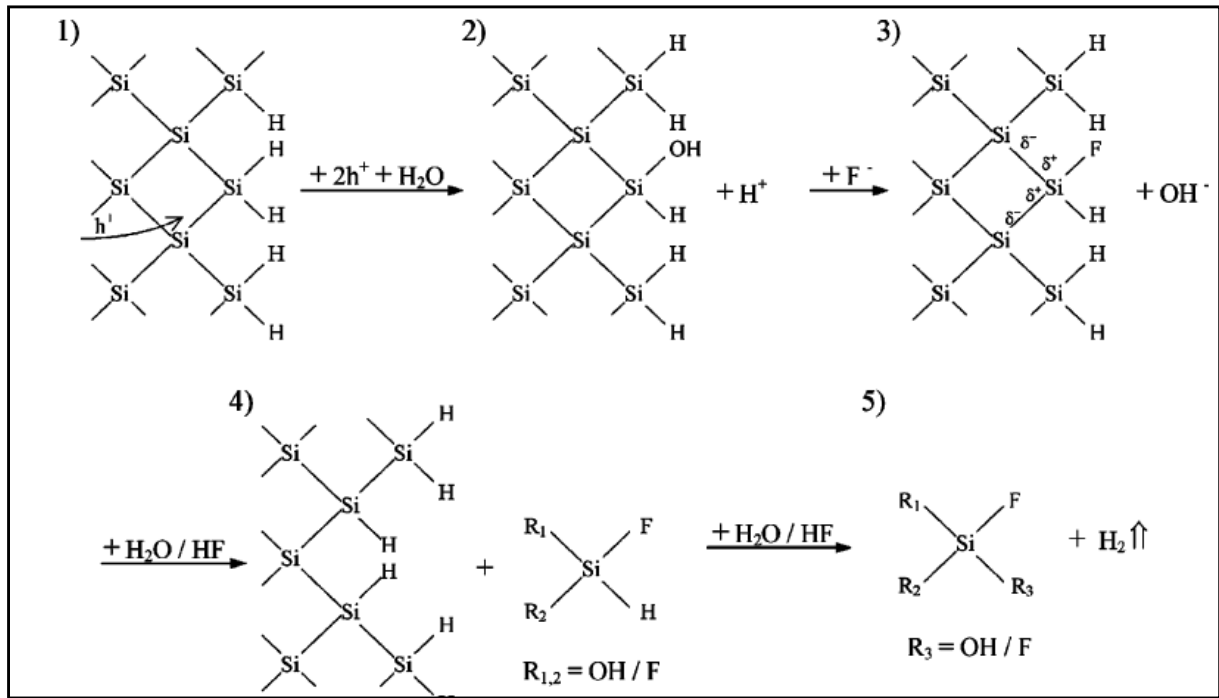
Figure 1.7: Etching of silicon in fluoride solutions (adapted from reference [4])

It is evident that the availability of holes plays a crucial role in the dissolution process of bulk silicon (step 1 in Figure 1.7). Therefore, the applied current density, illumination, and doping level of the substrate have a great influence on the resulting structure, on the properties of nanostructured silicon, and on the etching rate of silicon.

Depending on the sources providing holes in the silicon oxidization step (step 1 in Figure 1.7), the electrochemical etching is termed differently. If holes are generated by an applied bias, the etching process is called anodic etching. If holes injection is done by an oxidant, or by photon absorption, the etching is named electroless or photoelectrochemical etching, respectively. The mechanism of these methods are quiet similar and in practice, it is difficult to distinguish them [25][43]. Among of these techniques, the anodic and electroless etching routes are the most widely used for nanostructured silicon fabrication.

In the anodic etching technique, silicon is etched by tuning the voltage or current between two electrodes (silicon working electrode and inert metal, respectively), resulting in the formation of silicon nanostructures, usually, in a porous form. Their size depends on the applied voltage, time, type of substrate (crystallographic orientation, doping type and level), electrolytic solution (its composition, concentration, etc.), and current density [12] [18] [24] [43] [44] [45]. For example, Figure 1.8 shows three types of porous silicon surface morphologies prepared by

19

anodic etching of different silicon wafers in HF/ethanol aqueous solutions. The porous Si layer consists of well separated straight cylindrical pores of different sizes: mesopores (pore diameter ≈ 50 nm) etched in p-type (0.01 Ohm/cm) silicon wafer, small macropores (pore diameter ≈ 100 nm) etched in n-type (0.01 Ohm/cm), and finally macropores obtained from p-type (10 Ohm/cm) (pore diameter ≈ 100 nm, the distance between two pores is larger than in the previous case). [47]
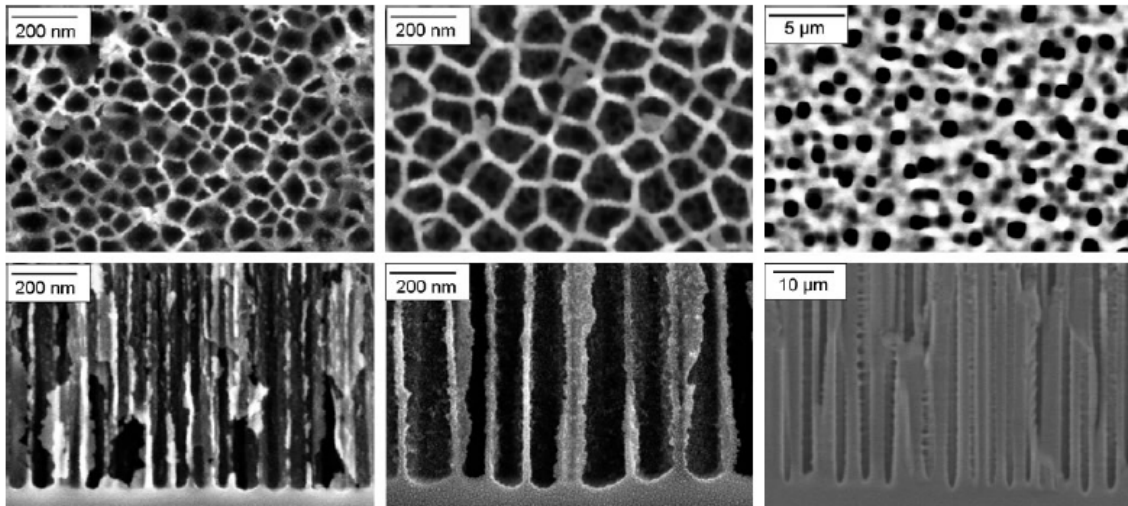
Figure 1.8: SEM images of three types of porous silicon surfaces (Top and cross views). First: mesopores etched from p-type 0.01 Ohm/cm silicon wafer; second: small macropores etched from n-type 0.01 Ohm/cm and finally: macropores obtained from p-type 10 Ohm/cm.[47]

Concerning the electroless etching process, nanostructured silicon substrates are formed without the intervention of a power supply. An electrochemical step implies that there are anode and cathode sites on the surface with local current flowing between them. At the anodic site, the silicon is oxidized, while the oxidant is reduced at the cathode site. The electroless etching techniques are sub-divided into three types: the stain etching, chemical vapor etching and metal-assisted etching. [7] [8] [28] [48] [49]

- In the stain etching technique, the etching solution contains both fluoride ions (HF, HBF_4, $HSbF_6$, NH_4F…) and an oxidizing agent (HNO_3, $NaNO_2$, $KMnO_4$, $KBrO_3$...). The silicon wafer is dipped in this solution.

- In the case of chemical vapor etching, the solution is made up from concentrated HF and concentrated HNO_3. However, the Si wafer is not immersed in the solution, but kept above the solution. The etched Si process occurs in the vapor phase.

- In the metal-assisted etching method, deposited metal particles or films (Au, Ag, Pt, Pd…) are involved; the metal serves as a mask and as catalyst for the chemical etching of silicon. During this work, I focused on the fabrication of silicon nanostructures by metal-assisted etching method. Thus, we will describe in more details this method in the next section.

1.2.3. Metal-assisted etching using fluoride solutions

The metal-assisted etching method requires that metal particles or films to be deposited (Ag, Au, Pt, Ni, Cu…) directly on the silicon substrate. The metallization can be performed by various methods such as sputtering, thermal evaporation or electrochemical deposition. Then, the silicon substrate coated with metal particles or film is etched in a fluoride solution containing an oxidant agent such as: H_2O_2, $K_2Cr_2O_7$, $(NH_4)_2S_2O_8$ or $KMnO_4$ [8] [28] [39] [40] [49] [50] [51] [53]. In our case, we used fluoride (HF or $NaBF_4$) and $AgNO_3$ aqueous solutions for the synthesis of nanostructured silicon substrates. Finally, the metal particles or films are removed using $HNO_3/HCl/H_2O$ (1/1/1) solution or by directly dipping in pure HNO_3 aqueous solution.

The origin of the silicon etching by metal-assisted method is the galvanic displacement reaction, in which two simultaneous processes occur at the silicon/metal interface (Figure 1.9): the cathodic reaction i.e. the reduction of metal ions (Ag^+) and H^+ ions according to equations (1.3) and (1.4), and the anodic reaction (oxidation of silicon) according to equation (1.5): [7] [51] [54]
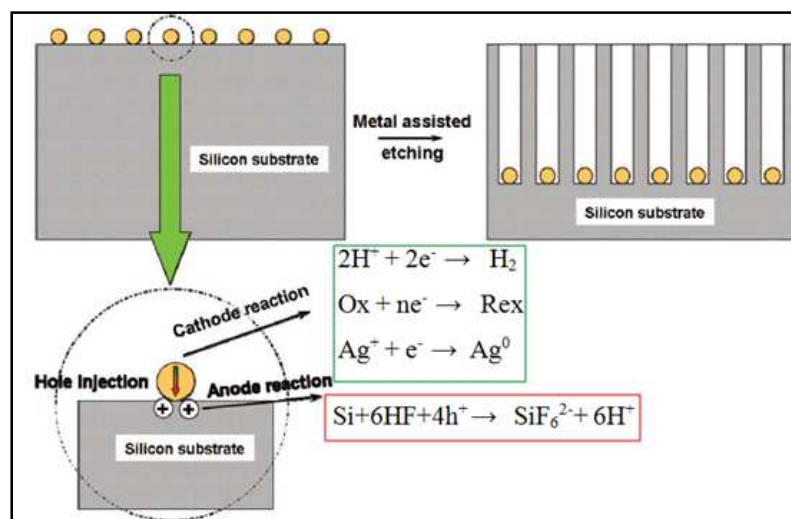
Figure 1.9: Mechanism of metal-assisted etching of silicon using fluoride solutions [51]

21

| **Cathodic:** | $2H^+ + 2e^- \rightarrow H_2$ | $E^0 = 0.00$ (V/SHE) | **(1.3)** |

| | $Ox + ne^- \rightarrow Rex$ | E^0_{redox} (V/SHE) | **(1.4)** |

| | $Ag^+ + e^- \rightarrow Ag^0$ | $E^0_{Ag} = 0.79$ (V/SHE) | |

| **Anodic :** | $Si + 6HF + 4h^+ \rightarrow SiF_6^{2-} + 6H^+$ | E^0_{Si} (V/SHE) | **(1.5)** |
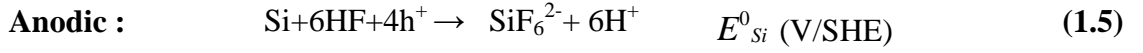
The electrochemical potential of electrons in a redox electrolyte is given by the Nernst expression

Cathodic:

$$E_H = 0.00 + \frac{RT}{F}\ln[H^+]$$ **(1.6)**

$$E_{redox} = E^0_{redox} + \frac{RT}{nF}\ln(\frac{[Ox]}{[Red]})$$ **(1.7)**

$$E_{Ag} = 0.79 + \frac{RT}{F}\ln[Ag^+]$$

Anodic :

$$E_{Si} = E^0_{Si} + \frac{RT}{4F}\ln(\frac{[SiF_6^{2-}] \times [H^+]^6}{[HF]^6})$$ **(1.8)**

In which:

- SHE is the standard hydrogen electrolyte

- E is the equilibrium potential

- R is the ideal-gas constant (8.314 $JK^{-1}mol^{-1}$)

- F is the Faraday constant (96500 $Cmol^{-1}$)

- T is the absolute temperature

The silicon dissolution spontaneously occurs in fluoride solution if the cathodic potential is higher than the anodic one:

$$E_{cathodic} = E_H + E_{redox} > E_{anodic} = E_{Si}$$ **(1.9)**

$$\frac{RT}{F}\ln[H^+] + E^0_{redox} + \frac{RT}{nF}\ln(\frac{[Ox]}{[Red]}) > E^0_{Si} + \frac{RT}{4F}\ln(\frac{[SiF_6^{2-}]\times[H^+]^6}{[HF]^6}) \; \textbf{(1.10)}$$

For the Ag$^+$ case, $\frac{RT}{F}\ln[H^+] + 0.79 + \frac{RT}{F}\ln[Ag^+] > E^0_{Si} + \frac{RT}{4F}\ln(\frac{[SiF_6^{2-}]\times[H^+]^6}{[HF]^6}) \; \textbf{(1.11)}$

From equation (1.10), the silicon dissolution (or the morphology of the nanostructured silicon substrate) is directly connected to the temperature, oxidant agent type and solution concentration. On the other hand, it is known that fluoride ions exist under various forms in the fluoride solution such as HF, HF$_2^-$, etc... Additionally, the value of E$^0_{Si}$ depends on the doping type and level of the silicon substrate. While the redox reaction, for the case of silicon, is hardly determined, it is sure that the real influence of the etching solution composition is not proved [41] [50].

Holes are generated from the oxidant agent and transferred into the silicon valence band through the metal particles or film. This explains why the etching is confined near the metal film or particles. Thus the size of the pits or the silicon nanostructure morphology depends on the form and size of metal particles or film. Finally, the metal particle is always found at the bottom of pits at the end of the etching process as shown in Figure 1.10 [7] [40] [51] [54]. In the metal-assisted etching, the formation of metal dendrites always appears. It is explained by the fact that metal is more conductive than silicon. Thus, the metal ions are attracted by the metal particles for capturing electrons from Si or giving holes to Si (metal ions are formed from the metal film dissolution or initially present in the etching solution). For example, Figure 1.10 displays SEM images (cross-sectional views) of p-type (111) Si wafers etched in 4.6M HF/0.02M AgNO$_3$ aqueous solution for 30 min at 50°C [7]. One clearly sees the formation of silver dendrites on the top of the silicon nanostructures (Figure 1.10 A), but also Ag particles sinking into the pits (Figure 1.10 B).
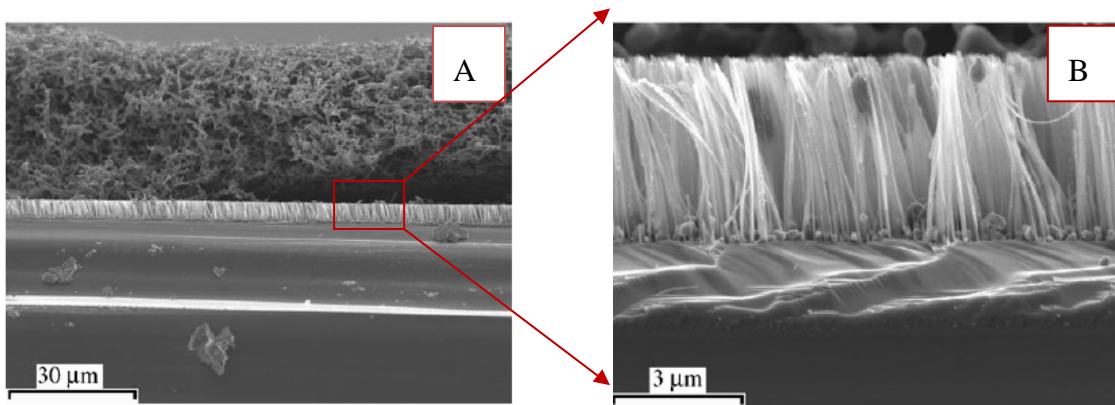
Figure 1.10: SEM images showing cross-sectional views of p-type (111) Si wafer etched in 4.6M HF/0.02 M AgNO₃ solution for 30 min at 50°C [7].

In our study, we have synthesized nanostructured silicon (NanoSi) substrates *via* metal (Ag)-assisted etching using either HF/AgNO₃ or NaBF₄/AgNO₃ aqueous solutions. The resulting NanoSi substrates were further exploited for different applications: fabrication of omniphobic surfaces (chapter 2), matrix-free laser desorption/ionization interfaces for mass spectrometry analysis of small biomolecules (chapter 3), and for biosensing (chapter 4). For controlling NanoSi surface morphology, we have varied the etching parameters (temperature, time, concentration, composition, silicon type). Before the formation of NanoSi by Ag-assisted etching, the silicon wafer is cleaned successively using organic solvents (acetone, alcohol and water) and piranha ($H_2O_2/H_2SO_4 = 1/1$ (v/v)) (Appendix 1). The resulting NanoSi surfaces are characterized by Scanning Electron Microscopy (SEM).

In this work, we used a SEM (Zeiss Ultra 55) equipped with a thermal field emission emitter and a high-efficiency In-lens SE detector. It is maintained at a base pressure of 10^{-5} mbar. The acceleration voltage is 200 eV-30 KeV and the resolution is 1 nm at 15 eV

1.2.4. Fabrication of NanoSi using HF/AgNO₃ aqueous solutions

The NanoSi fabrication using HF/AgNO₃ aqueous solution was first described by Peng *et al.* and was widely detailed in various reports [7] [18] [50] [54]. In our group, we have optimized this NanoSi fabrication process for various applications, including biomolecules' analysis using mass spectrometry [55] [56] [57], selective adhesion of *Bacillus cereus* Spores [15], and lab-on-chip devices [13] [14].

Generally, it is shown that the morphology of NanoSi substrates prepared by chemical etching in HF/AgNO$_3$ varies according to the etching time (Figure 1.11) or to the solution concentration (Figure 1.12), while it is not dependent on the silicon wafer type:

- ✓ Figure 1.11 displays SEM images (top and cross sectional views) of NanoSi surfaces fabricated from two types of wafers (n and p-type, orientation (100)) at 55 °C using 5.25 M HF/0.02 M AgNO$_3$ aqueous solution for various etching times (5, 10, 30, 60 and 120 min).
- ✓ Figure 1.12 shows SEM images of NanoSi surfaces synthesized from p-type Si(100) using different HF concentrations ([HF]) while keeping AgNO$_3$ concentration constant (0.04 M) at 55 °C for 10 min.

	Top view		Cross sectional view	
	n-type	p-type	n-type	p-type
5 min			0.450 µm	0.450 µm
10 min			2.5 µm	2.7 µm
30 min			6 µm	5.9 µm
60 min			7.5 µm	7.3 µm
120 min			12.5 µm	13.6 µm
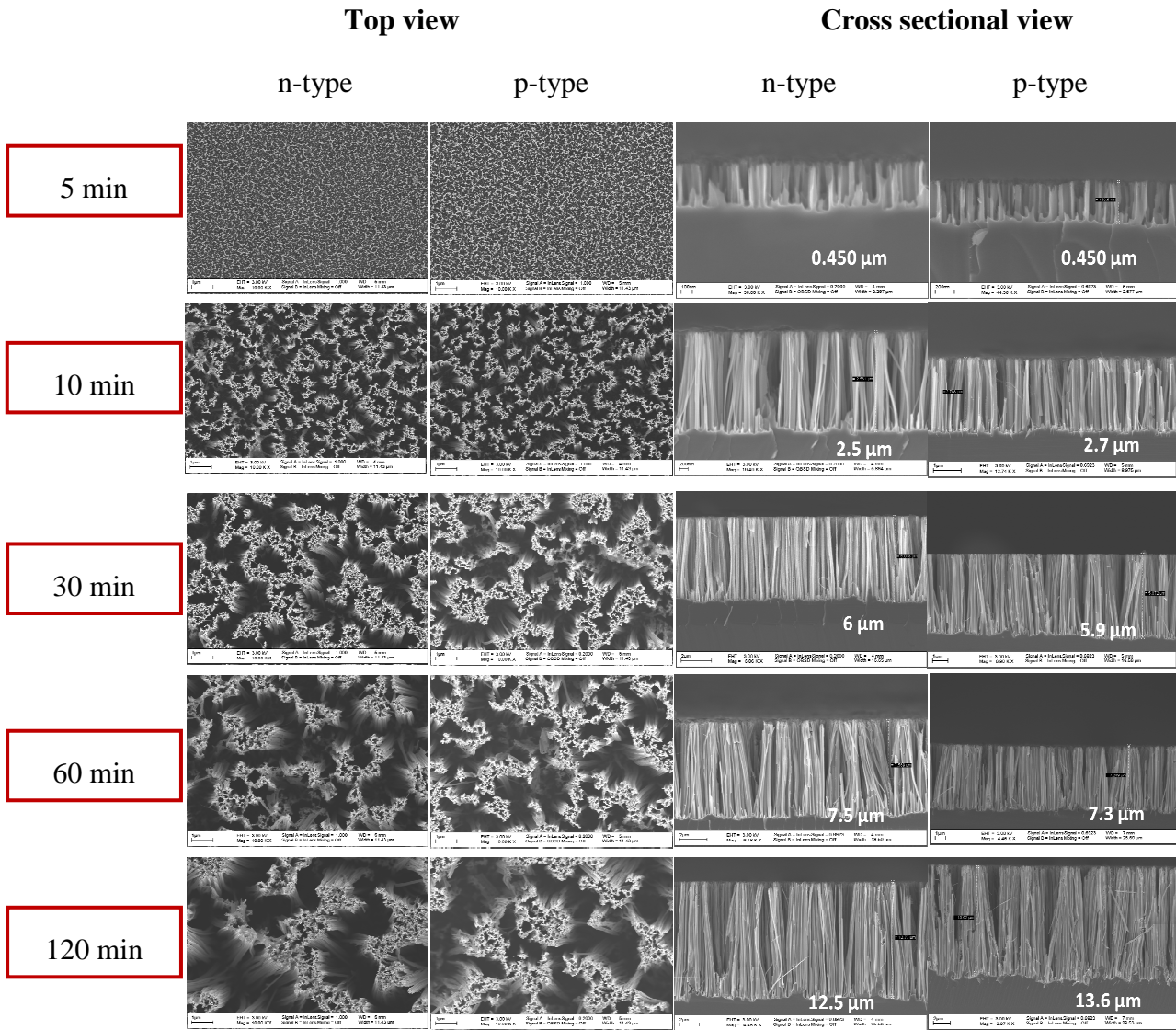
Figure 1.11: SEM images (top and cross sectional views) of NanoSi substrates synthesized using 5.25 M HF/0.02 M AgNO₃ aqueous solution from two types of silicon wafers (n and p-type, orientation (100)) at 55 °C for various etching times (5, 10,30, 60 and 120 min).

26

	Top view		**Cross sectional view**

HF/AgNO₃ 2,62M/0.04M			1.6 µm
HF/AgNO₃ 5,25M/0.04M			2.5 µm
HF/AgNO₃ 13,12M/0.04M			3.9 µm
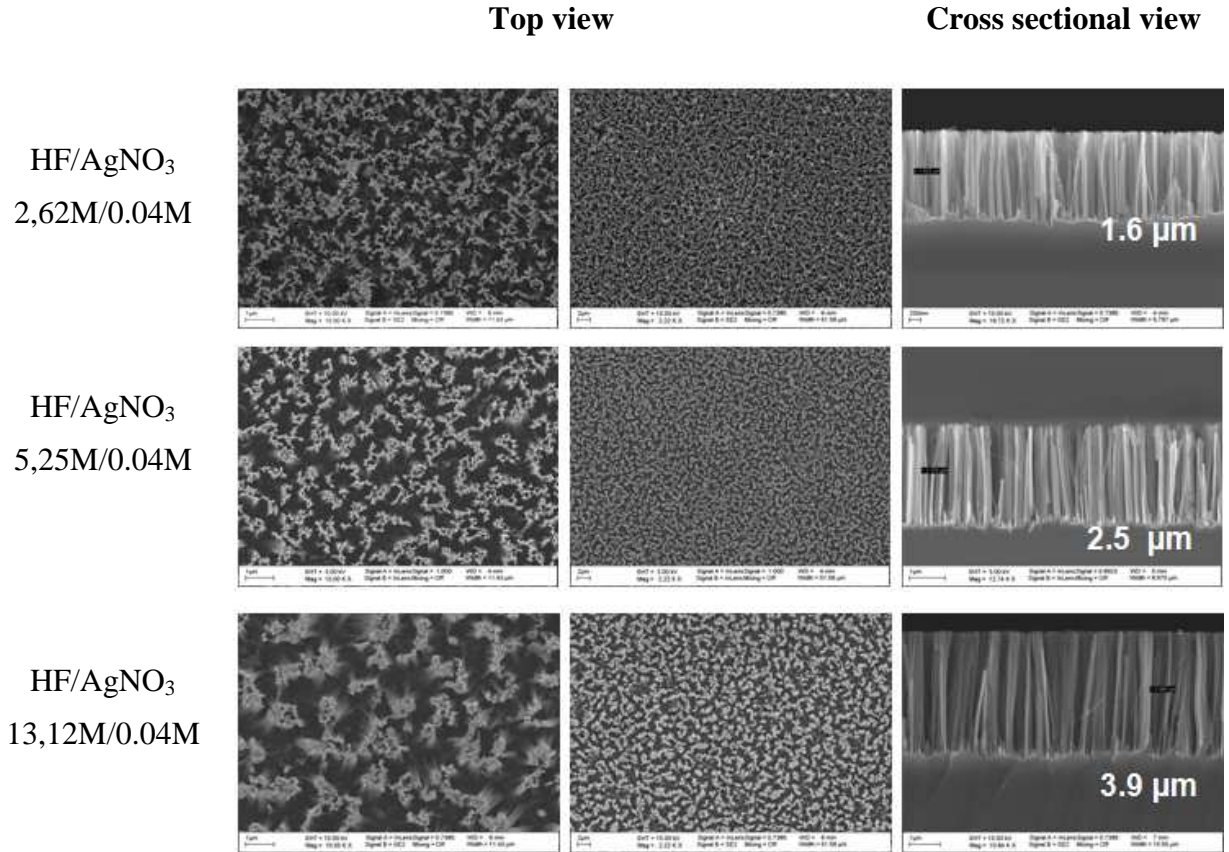
Figure 1.12: SEM images (top and cross sectional views) of NanoSi surfaces synthesized using various [HF]/0.04 M AgNO₃ at 55 °C for 10 min.

From SEM top and cross sectional view images in Figures 1.11 and 1.12, we can notice that the shape of the resulting NanoSi surfaces did not change during the etching process and for different concentrations of etchant:

- The nanostructures consist of vertically-aligned nanofilaments and form bundles upon drying, due most likely to electrostatic interactions. Their morphology is independent on the silicon characteristics (neither on the doping level nor on the orientation of the silicon crystal. [7]

- The height varies from 0.5 to 20 µm as a function of the solution concentration ([HF] and [AgNO₃]) and the etching time (Figure 1.13).

- The diameter of the nanostructures varies from 10 to 100 nm.

- The distance between two bundles of NanoSi is proportional to the etching time and concentration of [HF].

- The nanostructures are homogenous on the substrate and the obtained results are identical for etching either a small surface or an entire wafer.
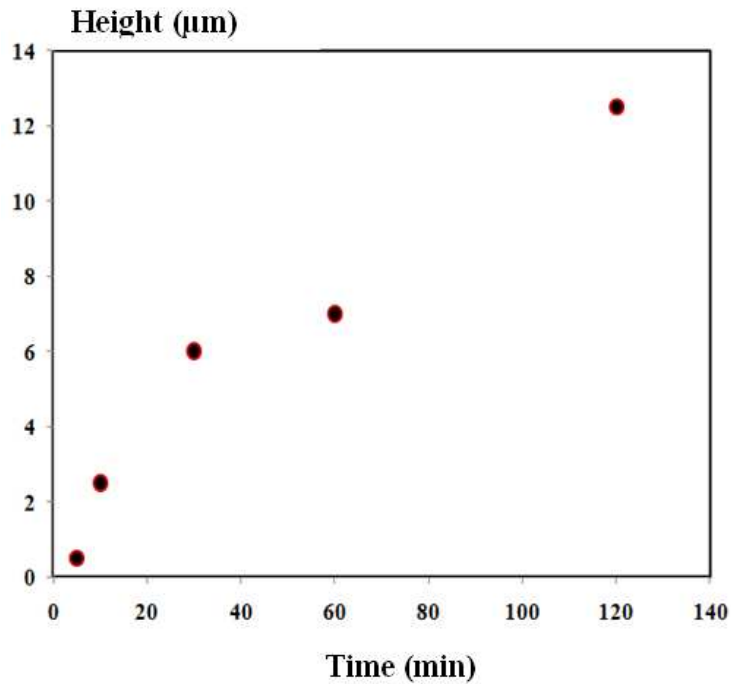
Figure 1.13: Variation of the height (µm) of NanoSi synthesized using 5.25 M HF/0.04 M AgNO$_3$ at 55°C as a function of etching time. This curve is based on SEM measurements in Figure 1.11

1.2.5. Fabrication of NanoSi using NaBF$_4$/AgNO$_3$ aqueous solutions

In this section, we will present the fabrication of NanoSi *via* an original electroless metal-assisted etching method using NaBF$_4$/AgNO$_3$ aqueous solution that we have developed during this work. Here, we used NaBF$_4$ instead of HF because it is less hazardous than HF (Appendix 2). Sodium tetrafluoroborate (NaBF$_4$) is another type of fluoride-based reagent, which can etch silicon oxide. In water, NaBF$_4$ dissolves to give BF$_4^-$ ions which continuously hydrolyze forming species like: BF$_3$OH$^-$, BF$_2$(OH)$_2^-$, BF(OH)$_3^-$, F$^-$, etc. They are metastable and are in equilibrium with BF$_4^-$ [58] [59]:

$$NaBF_4 \longrightarrow Na^+ + BF_4^-$$

$$BF_4^- + OH_2 \rightleftharpoons BF_3OH^- + H^+ + F^\cdot$$

$$BF_3OH^- + OH_2 \rightleftharpoons BF_2OH^- + H^+ + F^\cdot$$
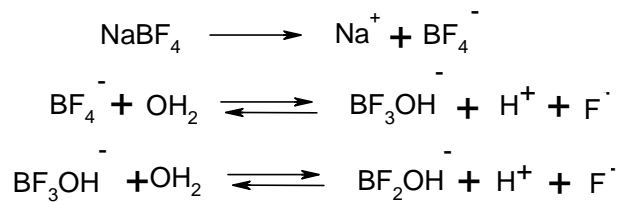
In fact, $NaBF_4$ powder has a limited solubility in water with a saturation around 6 M.

- ✓ The pH of $NaBF_4$ aqueous solution is 2.14 for 1 M < $[NaBF_4]$ < 5M at room temperature

- ✓ At $NaBF_4$ concentrations of 0.5 M and 6 M, the pH is 3.15 and 1.84, respectively.

We have also investigated the etching capacity of silicon oxide by $NaBF_4$ at room temperature during 24 h. Figure 1.14 shows the etch rate of SiO_2 as a function of $[NaBF_4]$. One piece of 1 cm^2 of Si wafer coated with 200 nm thick of SiO_2 layer deposited (Si +200nm SiO_2) by thermal oxidation technique (Appendix 3), was kept in 2 mL $NaBF_4$ aqueous solution for 24 h at room temperature. In order to determine precisely the etching rate of SiO_2, the thickness of SiO_2 is measured before and after etching using an ellipsometer. The ratio of the SiO_2 thickness and the etching time gives the etch rate.
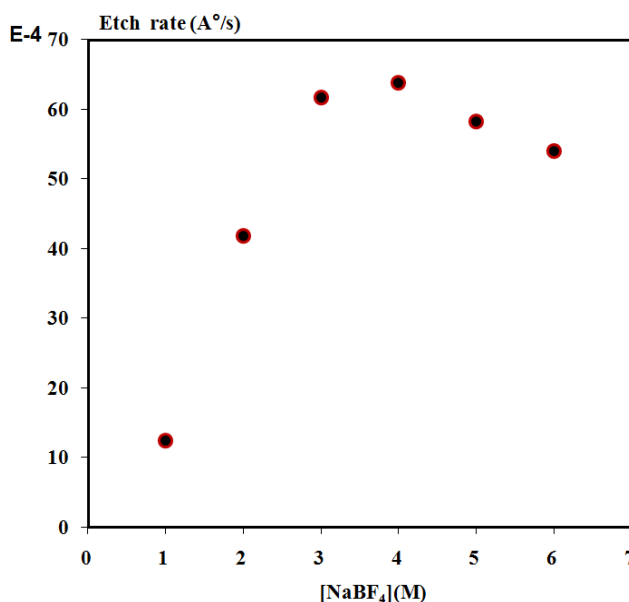
Figure 1.14: Etch rate of SiO_2 as a function of $[NaBF_4]$ (M) at room temperature, t=24 h.

From Figure 1.14, the etch rate of SiO_2 increases rapidly for 1.0 M < [$NaBF_4$] <4.0 M, and decreases slowly for 4.0 M < [$NaBF_4$] < 6.0 M. The maximum etch rate obtained is 6×10^{-3} Å/s or 24 Å/h for 4.0 M $NaBF_4$. It's clear that the etch rate of SiO_2 by $NaBF_4$ solution is very slow in comparison to HF (the etch rate of SiO_2 by 2.5 M HF solution is about 420 Å/h). [31]

As mentioned above, NanoSi etched in HF/$AgNO_3$ aqueous solutions are obtained in form of bundles of vertically-aligned nanofilaments. In the contrary, NanoSi surfaces obtained from $NaBF_4$/$AgNO_3$ solutions:

- The structure has the form of isosceles triangles with a- the apex, b- a base length and h- height: 0.06 µm < a < 0.27 µm, 0.1 µm < b <0.5 µm, 0.5 < h <2.5µm (Figures 1.15 (c) and (d)). In the case of a base value smaller than the height value, the obtained NanoSi has needle shapes (Figure 1.15 (d)). We can also observe the serrated leaves shape on each nanostructure (Figures 1.15 (d) and (e)).

- From Figures (a) and (c), one can see the formation of silver dendrites on the top of the silicon nanostructures but also Ag particles sinking into the pits, as shown in the literature.

- As seen from the top surface of NanoSi (Figure 1.15 (c)), there is an "island" formation, the distance between two islands varies from 0.15 to 0.8 µm.
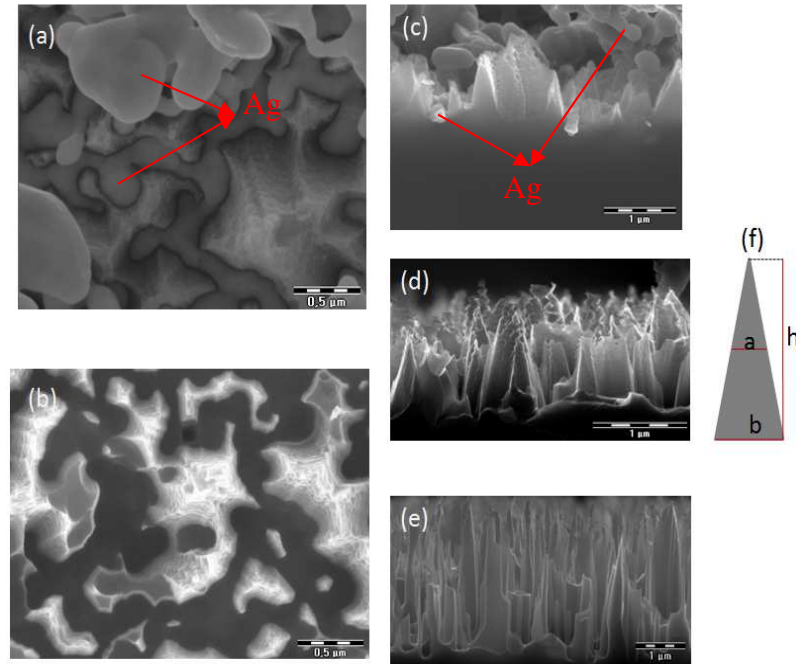
Figure 1.15: SEM images (top (a, b)) and cross sectional *(c, d, e)) views of NanoSi surfaces prepared by chemical etching in 2M NaBF₄ /0.02M AgNO₃ aqueous solution for (a,b,c and d) and 2M NaBF₄ /0.01M AgNO₃ aqueous solution for (e), at 80°C for 2h; (f)is aschematic representation of the isosceles triangle shapes with a: apex, b- base length, and h -height; (a) and (c) SEM images of NanoSi surface before removing the Ag particles.*

1.2.5.1. Influence of reagent concentration

We have developed a new method of NanoSi fabrication using NaBF₄/AgNO₃ aqueous solution. Therefore, we must consider all the etching parameters such as: etching time, concentration of the reagents, temperature and type of wafer to get a better understanding on how these parameters influence the morphology of NanoSi surfaces.

Herein, the etching was performed on a silicon sample of 1 cm² in size. The total volume of solution (NaBF₄ and AgNO₃) used is 4 mL for each experiment.

A. Variation of [AgNO₃]

For this study, NanoSi is prepared from Si wafer, p-type, orientation (100) and resistivity 0.009-0.01 ohm.cm. The concentration of NaBF₄ is maintained constant at 2.0 M while the

[AgNO$_3$] was varied from 0.005 to 0.05 M. SEM images of the resulting surfaces are shown in Figures 1.16 and 1.17, respectively. From these observations one can draw the following conclusions:

- The shape of the nanostructures is always isosceles-like triangles or needles and doesn't depend on [AgNO$_3$].

- The height varies from 0.42 to 2.5 µm: it decreases rapidly for 0< [AgNO$_3$] < 0.03 M and very slowly for [AgNO$_3$] > 0.03 M (Figure 1.17). It seems that a higher [AgNO$_3$] leads to reduced height of NanoSi. It can be explained by the fact that higher [AgNO$_3$] result in more Ag particles and dendrites with bigger sizes. Hence, it is difficult for the etchant solution to diffuse under the Ag particles and dendrites, leading to the diminution of the etching rate.

- It is also observed that the isosceles triangle shape of NanoSi at higher [AgNO$_3$] (>0.01 M) has smaller base length and higher height, thus, presenting a nozzle-like form.

- When [AgNO$_3$] < 0.03 M, the distance between two "islands" increases with decreasing [AgNO$_3$].

- When [AgNO$_3$] > 0.03 M, the distance between two "islands" seems to be identical. However, the appearance of a square pores is observed on each island with higher [AgNO$_3$].

	Cross sectional view	**Top view**
NaBF₄/AgNO₃ **2.0 M/0.01M**		
NaBF₄/AgNO₃ **2.0 M/0.02 M**		
NaBF₄/AgNO₃ **2 M/0.03 M**		
NaBF₄/AgNO₃ **2.0 M/0.04 M**		
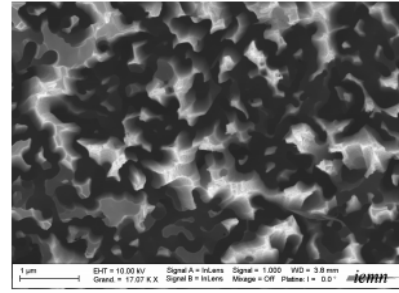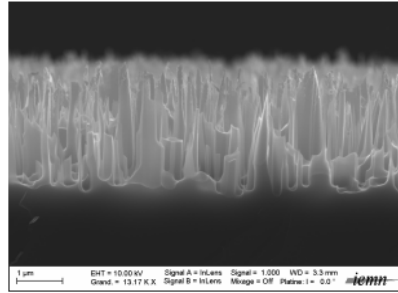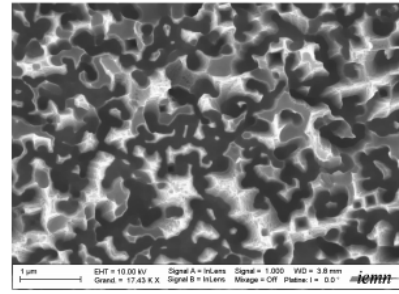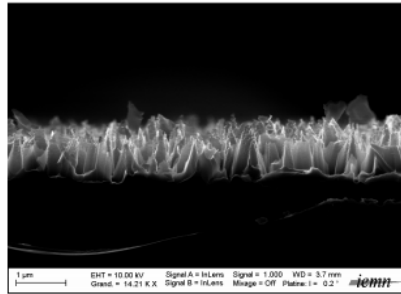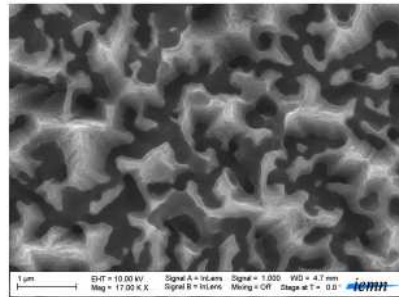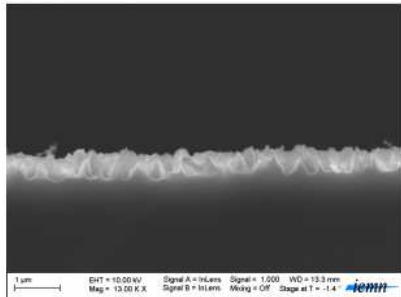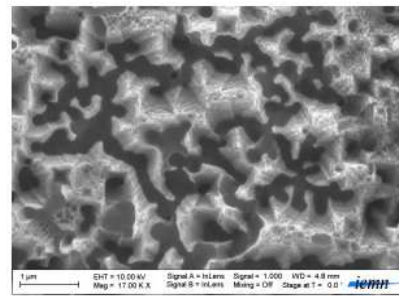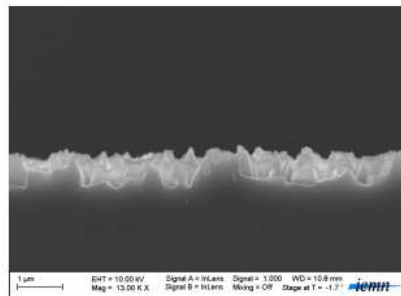
Figure 1.16: SEM images of NanoSi surfaces prepared by chemical etching of Si(100) in AgNO₃/NaBF₄ aqueous solution using various [AgNO₃] and 2.0 M NaBF₄ at 80 °C for 2h.
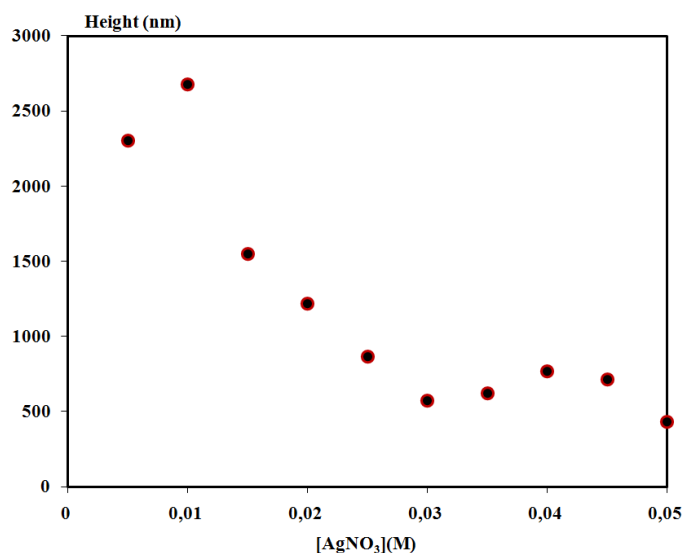
Figure 1.17: Height of the NanoSi as a function of [AgNO$_3$]. This curve is based on SEM measurements in Figure 1.16.

B.   Variation of [NaBF$_4$]

Concerning the variation of [NaBF$_4$], we kept the same experimental conditions as mentioned in the previous paragraph except for [AgNO$_3$] for which we used a concentration of 0.02 M corresponding to NanoSi with average height obtained with various [AgNO$_3$].

The morphologies and height values of the NanoSi substrates are displayed in Figures 1.18 and 1.19, respectively. We observe that:

- The resulting nanostructures are similar to those obtained by varying [AgNO$_3$] i.e. isosceles triangular shape.
- Their heights vary from 0.6 to 1.2 µm as a function of the [NaBF$_4$]: the height of the structures increases quickly when the [NaBF$_4$] was increased from 0 to 1 M and seems to stabilize from 1 to 3 M of [NaBF$_4$] (Figure 1.19).

Consequently, the shape of the NanoSi synthesized using NaBF$_4$/AgNO$_3$ aqueous solutions does not change following the concentration of the solution. The Si dissolution is rapid both with higher [NaBF$_4$] and lower [AgNO$_3$].

	Cross sectional view	**Top view**
NaBF₄/AgNO₃ **0.5 M/0.02 M**		
NaBF₄/AgNO₃ **1.0 M/0.02 M**		
NaBF₄/AgNO₃ **1.5 M/0.02 M**		
NaBF₄/AgNO₃ **2.5 M/0.02 M**		
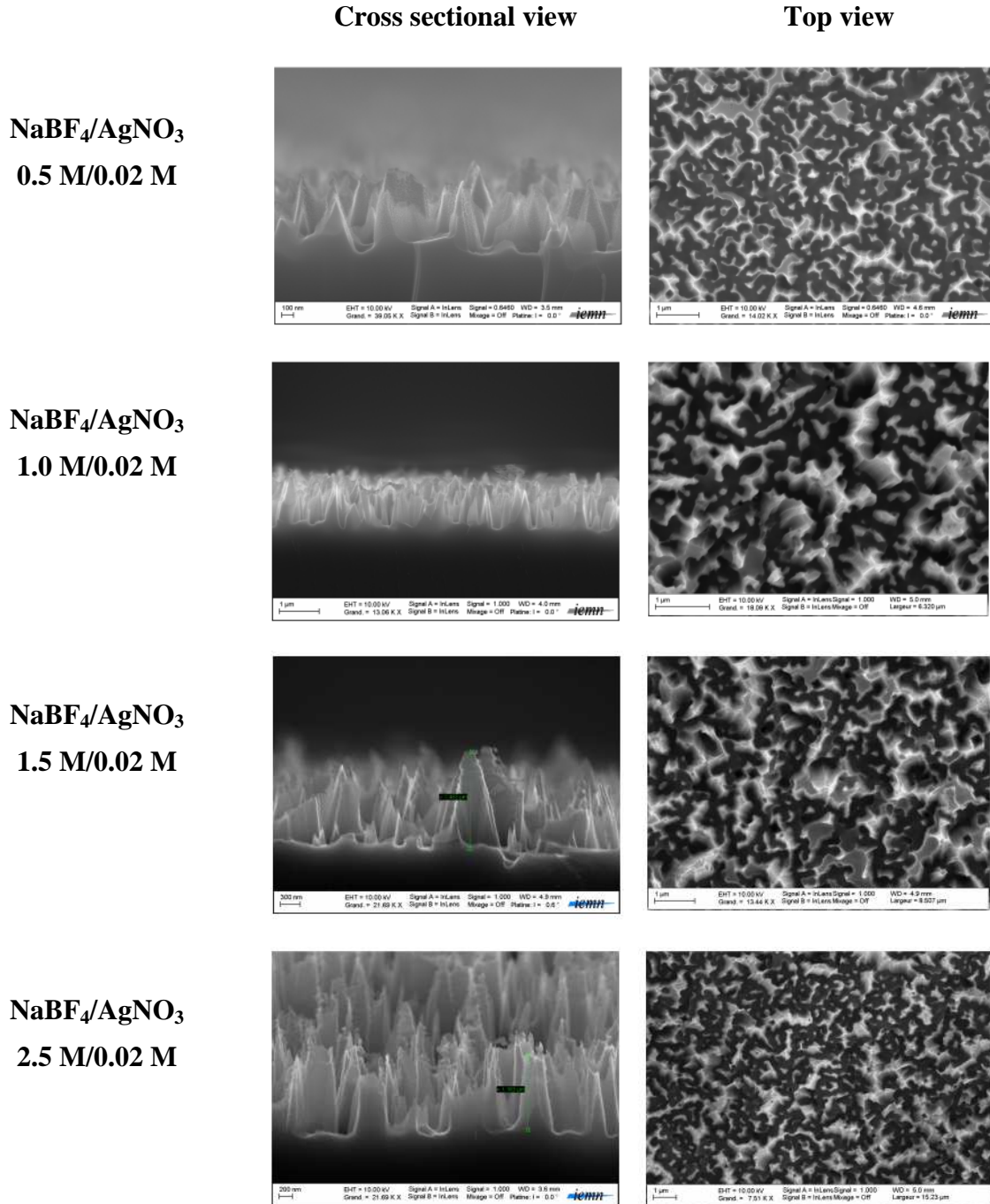
Figure 1.18: SEM images of NanoSi substrates prepared by chemical etching of Si(100) using 0.02M AgNO₃ and various [NaBF₄] at 80 °C for 2h.
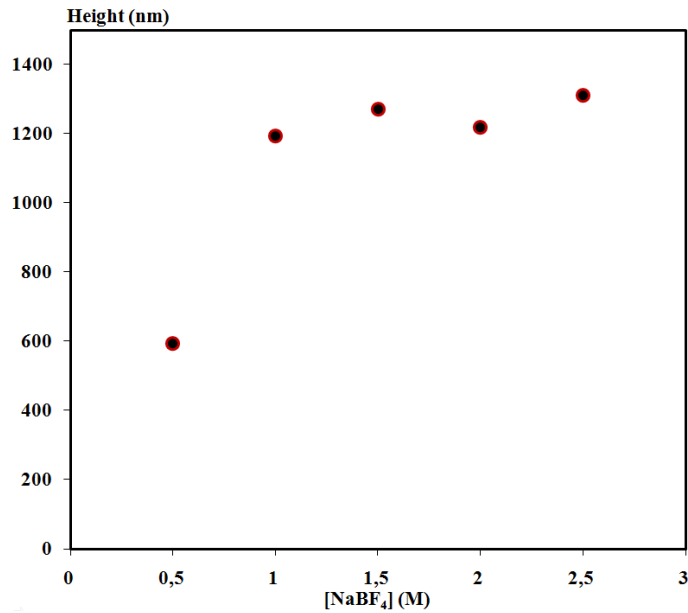
Figure 1.19: Height of NanoSi as a function of [NaBF₄]. This curve is based on measurements from SEM images in Figure 1.18.

1.2.5.2.   Influence of temperature and etching time

We have also investigated the influence of temperature and time on the morphology of NanoSi surfaces. For this study, we used the same type of silicon as mentioned in the previous paragraph (single crystal Si, p-type, orientation (100) and resistivity 0.009–0.01 Ohm/cm) and an etchant solution consists of 2.0 M $NaBF_4$/0.02 M $AgNO_3$.

A.   Variation of etching temperature

For different etching temperatures (50, 60, 70, 80 and 90°C), the morphologies of NanoSi surfaces and the values of their heights are displayed in Figures 1.20 (for 80°C in Figure 1.16) and 1.21, respectively. It shows that:

- The height increases linearly with the etching temperature.
- High temperatures lead to more heterogeneous nanotexturation: the triangle base seems to be larger while the density decreases at high temperatures.

36

Temperatures	Cross sectional view	Top view
50°		
60°		
70°		
90°		
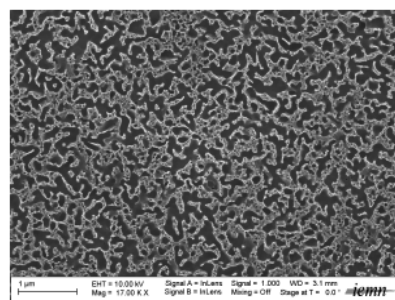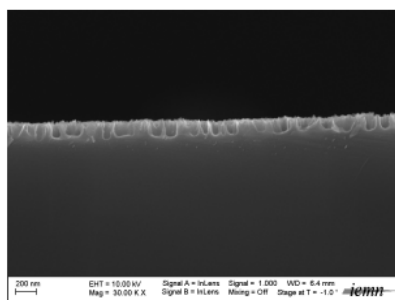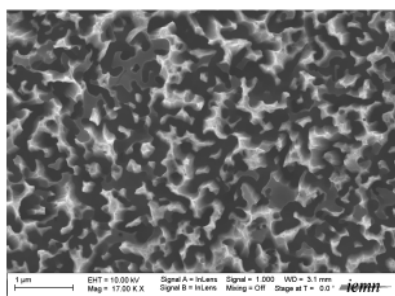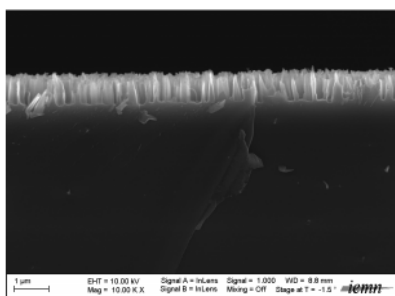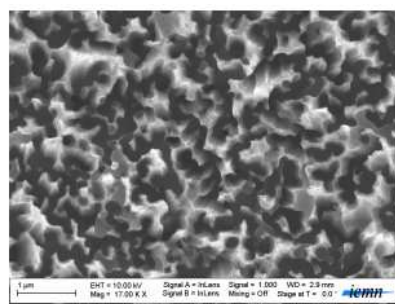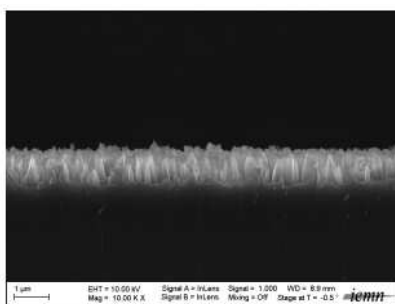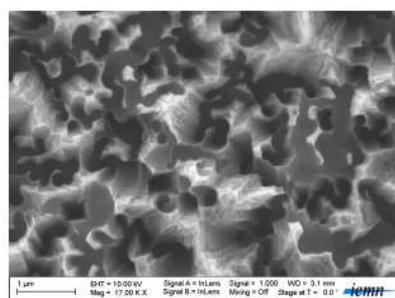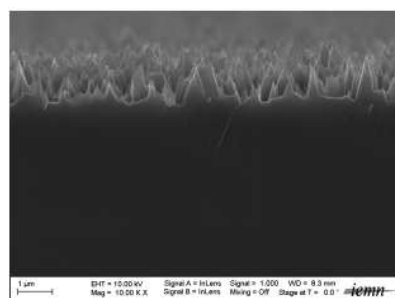
Figure 1.20: SEM images of NanoSi substrates obtained using 0.02 M AgNO$_3$/2.0 M NaBF$_4$ aqueous solution for 2h at different temperatures (50, 60, 70, and 90°C).
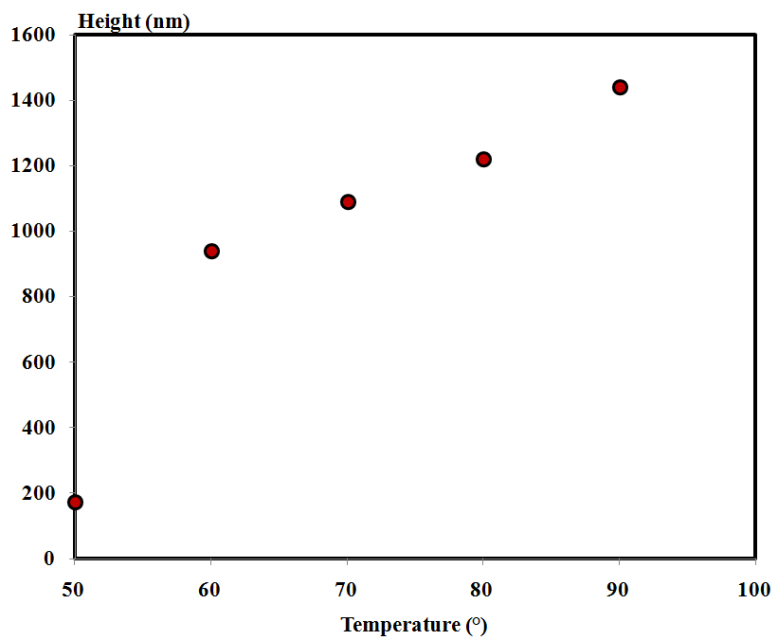
Figure 1.21: Height of NanoSi substrates obtained using 0.02 M AgNO₃/2.0 M NaBF₄ aqueous solution for 2h at different temperatures(50, 60, 70, 80, and 90°C). This curve is based on measurements from SEM images in Figure 1.20.

B. Variation of etching time

SEM images of the silicon nanostructures obtained by chemical etching of Si(100) in 0.02 M AgNO₃/2.0 M NaBF₄ for 2h for different etching times (30, 60, 90, and 120 min) are displayed in Figure 1.22. The results show that:

- No formation of NanoSi is observed during the first 30 min.
- The height of NanoSi increases from 60 to 90 min of etching, and then it seems that there is a saturation of the etching step after this time as observed for 120 min.

38

60min	90min	120min
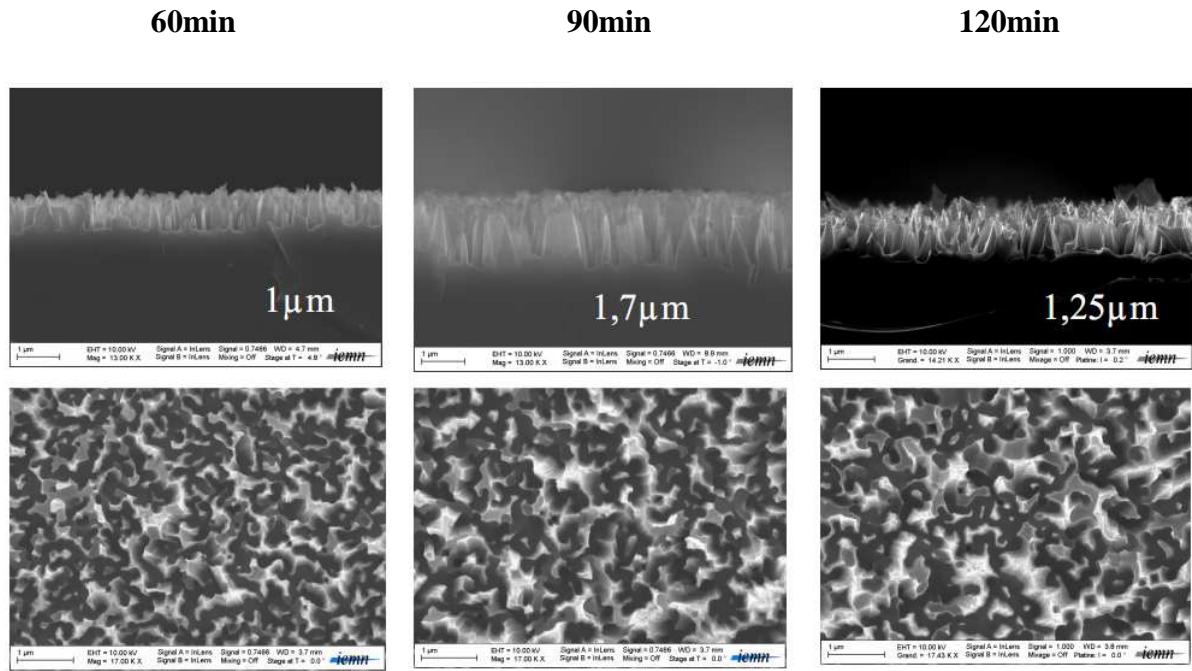
Figure 1.22: SEM images of NanoSi surfaces prepared by chemical etching of Si(100) in 0.02 M AgNO₃/2.0 M NaBF₄ for 2h for different etching times.

1.2.5.3.   Influence of silicon type

In this section, we report the influence of the silicon substrate characteristics (doping type, orientation, doping level) on the morphological structure of NanoSi surfaces. Figure 1.23 displays SEM images of NanoSi surfaces synthesized in 2.0 M NaBF₄/0.02 M AgNO₃ aqueous solution at 80 °C for 2 h using four different types of single crystal silicon wafers:

- S_0: *p-type (100) resistivity 5-10 Ohm/cm*
- S_1: *n-type (100) resistivity 5-10 Ohm/cm*
- S_2: *n-type (111) resistivity 0.03-0.05 Ohm/cm*
- S_3: *p-type (100) resistivity 0.009-0.01 Ohm/cm*

Influence of doping type

S_0 and S_1 surfaces present the same orientation (100) and doping level, but are of different doping types, p- type (S_0 surface) and n-type (S_1). The obtained structures are different as compared to those prepared from highly doped substrates (S_3): for both surfaces (S_0 and S_1) the structures are straight like needle or tips more than isosceles triangle forms. The height of NanoSi on p-type Si substrate (S_0 surface) is 1.3 times larger than those obtained on n-type Si substrate (S_1 substrate) (Figure 1.23 S_0 and S_1 surfaces).

Nowadays, the explanation of the influence of doping type of the Si substrate on the formation of NanoSi is still under debate. Indeed, as previously mentioned, it was shown that the etching process depends on various parameters. Thus, if two parameters are changed at the same time, it is difficult to accurately conclude the influence of the doping type of the Si wafer on the formation of NanoSi. For example, NanoSi formed using $HF/AgNO_3$ solutions under similar experimental conditions display identical height from both p-type and n-type Si substrates [53] [55] [56] [57]. In contrary, Zhang *et al.* showed that NanoSi obtained using $HF/AgNO_3/H_2O_2$ etchant of p-type Si wafers have reduced height than that prepared on n-type Si substrates [49] [60]. However, our results indicate that the n-type Si substrate is etched more slowly than the p-type wafer.

Influence of doping level

S_0 and S_3 wafers present the same orientation (100) and p-doping type, but display different doping levels: 0.009-0.01 ohm.cm^{-1} for S_3 and 5-10 ohm.cm^{-1} for S_0. After the etching step in $NaBF_4/AgNO_3$ solutions, S_0 surface displays NanoSi in a form of tips while S_3 surface shows NanoSi in a form of isosceles triangles. Additionally, the height of NanoSi on S_0 surface (lower doping) is 2.8 times larger than the one obtained on S_3 surface (higher doping). Hence, highly-doped silicon substrates are etched more slowly than low-doped Si in $NaBF_4/AgNO_3$ aqueous solutions (Figure 1.23 S_0 and S_3 surfaces).

On the other hand, no accurate conclusion can be drawn concerning the relationship between etching rate and doping level of the Si wafer. For example, no clear dependence of the doping level was evidenced for Si etching in $HF/AgNO_3$ aqueous solution [7] [53] [55]. In contrast to silicon etching in HF/H_2O_2 aqueous solutions, it was demonstrated that Si substrates of low doping levels are etched more quickly than highly-doped Si substrates [49] [60]. This observation is similar to silicon etching in $NaBF_4/AgNO_3$ aqueous solutions.

Influence of substrate orientation

On (100) Si substrates (S_0, S_1, and S_3), the resulting nanostructures are straight i.e. the etching proceeds along the vertical direction. In contrast to Si (100), the nanostructures prepared on (111) Si substrate (S_2 surface), display a nano-triangle shape with random directions (straight, left and right slopes) (Figure 1.23, S_2 surface).

In the literature [7] [49] [60], the influence of the silicon wafer orientation on the nanostructures' formation was highlighted. It was demonstrated that the formation of NanoSi depends on the type of the etching solution. For example, the Si (111) wafer is etched vertically by $HF/AgNO_3$ solutions but not by $NH_4F/AgNO_3$ or HF/H_2O_2 aqueous solutions.

Consequently, the influence of the doping type, level, or orientation of the Si substrate on the height and morphology of NanoSi surfaces are essentially determined by the type of the etching solution used.

Si wafer type	Cross sectional view	Top view
S_0 **p-type (100) resistivity 5-10 Ohm/cm**		
S_1 **n-type (100) resistivity 5-10 Ohm/cm**		
S_2 **n-type(111) resistivity 0,03-0,05 Ohm/cm**		
S_3 **p-type (100) resistivity 0,009-0,01 Ohm/cm**		
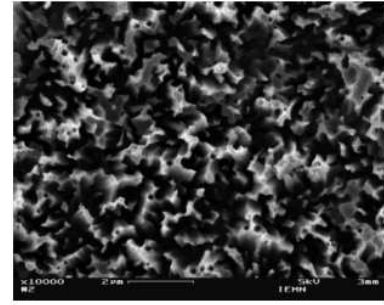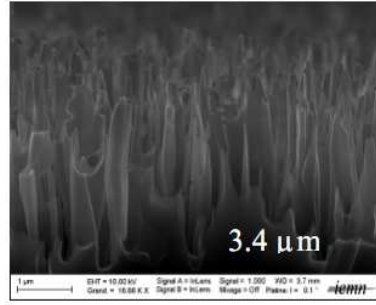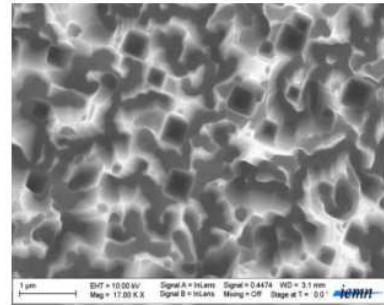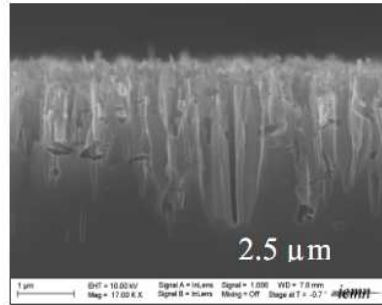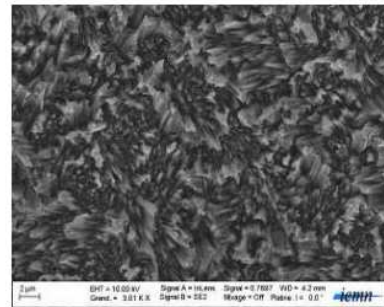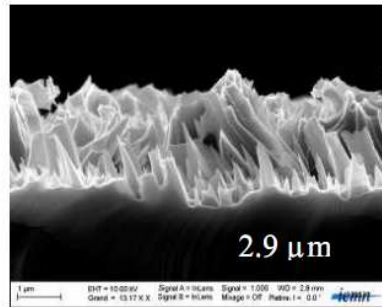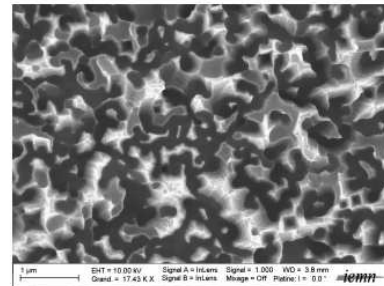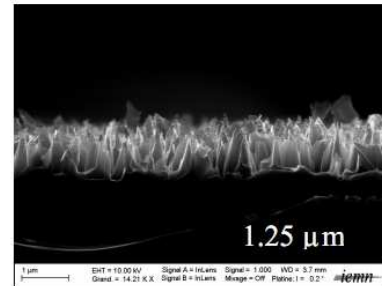
Figure 1.23: SEM images of NanoSi synthesized in 0.02 M AgNO₃/2.0 M NaBF₄ aqueous solution at 80 °C for 2h on different wafer types (doping level, doping type and orientation).

1.2.6. Fabrication of double-scaled micro-nano interfaces

We also performed silicon micro-/nanostructuration through the combination of deep reactive ion etching (DRIE) and metal-assisted etching techniques by etching silicon micropillars (fabricated by DRIE technique) in $NaBF_4/AgNO_3$ aqueous solutions. These surfaces will be used for studying their wetting properties (superhydrophobic/ superomniphobic) that will be detailed in chapter 2.

Silicon micropillars fabrication (µP)

Single side polished silicon (100) oriented p-type wafers (Siltronix) (phosphorus-doped, 0.009-0.01 Ohm/cm resistivity) were used as substrates. The surface was first degreased in acetone and isopropanol, rinsed with Milli-Q water and then cleaned in a piranha solution (3:1 concentrated H_2SO_4/30% H_2O_2) for 15 min at 80°C followed by copious rinsing with Milli-Q water (Appendix 1). A 6 µm thick negative resist AZnLOF 2035 (Clariant, France) is spin-coated at 3000 rpm. A soft bake for 1 min on a hot plate at 110°C is necessary to reduce the solvent content and to prevent resist adhesion to the exposure mask. Then, the exposure, post-exposure bake and development are conducted for transferring the mask patterns to the resist (latent image). Finally, the silicon wafer was etched using Deep Reactive Ion Etching (DRIE), (Silicon Technology System) to produce high aspect ratio micro-pillars (µP) (Appendix 4). Figure 1.24 exhibits a SEM image of a micropillar (10*5*10: diameter*spacing*height (µm)). A re-entrant structure appears due to the ondulating shape occurring during Deep Reactive Ion Etching successive passivation/etching steps.
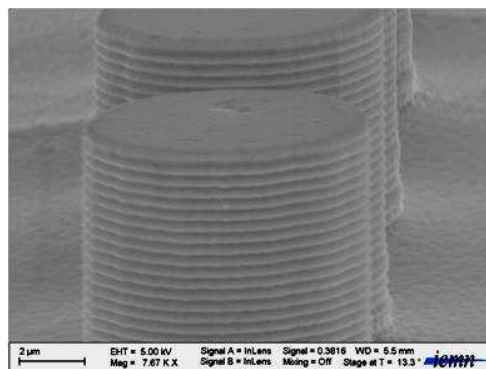
Figure 1.24: SEM image of a micropillar. Re-entrant structure appears due to the ondulating shape occurring during DRIE successive passivation/etching steps.

Then, the µP interface was placed directly in a 2M NaBF₄/0.02M AgNO₃ aqueous solution for 2 hours at 80°C. This treatment allows nano-structuration of the µP, leading to the creation of a double-scaled micro-nano interface (µP/NanoSi) as shown in Figure 1.25. The silicon µP is covered by a dense layer of nanostructures with isosceles triangle shape of ~700 nm in height and a base length ranging from 200 to 400 nm. Moreover, the chemical dissolution of silicon in NaBF₄/AgNO₃ aqueous solutions occurs not only on the micropillars, but also between them.
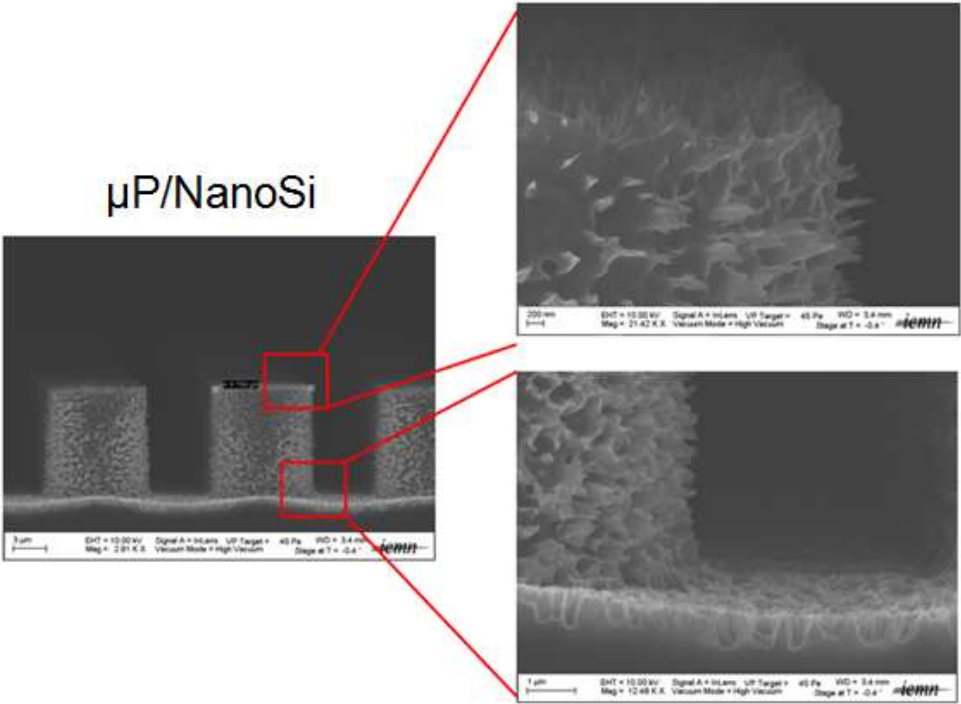
Figure 1.25: SEM images of a µP/NanoSi interface.

1.2.7.   Summary

In this section, we have presented a new metal-assisted etching method for NanoSi fabrication through the use of a fluoride solution containing Ag⁺ ions: NaBF₄/AgNO₃ aqueous solutions. The technique avoids the manipulation of HF acid, which is very dangerous as compared to NaBF₄. We compared our structures with those obtained using HF/AgNO₃ aqueous solutions. Table 1.1 summarizes advantages and disadvantages of the two etching solutions.

	HF/AgNO$_3$	NaBF$_4$/AgNO$_3$
Chemical agent	Hazardous (see Appendix 2)	NaBF$_4$ is less hazardous than HF (see Appendix 2)
Type of Si wafer	For the same etching conditions, the morphology of the NanoSi **is independent on** the silicon wafer characteristics: doping type, doping level, and orientation.	For the same etching conditions, the morphology of the NanoSi surfaces is **greatly dependent** on the silicon wafer characteristics: doping type, doping level, and orientation.
Height of nanostructure	varies from **0.5 to 20 µm**	varies from **0.5 to 3 µm**
Orientation	The nanostructures are bundles of vertically-aligned nanowires for all **type of Si wafers**	The nanostructures **are vertical isosceles triangles or nozzles and form "islands" for Si (100).** For other Si wafer orientations, random orientation of the nanostructures was observed
Size of NanoSi sample	NanoSi can be identically formed on **whatever size** of the silicon wafer from 1 cm^2 to 3 inches wafer.	The investigation was only limited to **small samples** (1cm^2)

Table 1.1: Comparison between the two etching methods: HF/AgNO$_3$ and NaBF$_4$/AgNO$_3$.

1.3. Bottom- up approach

1.3.1. Silicon nanowires

We have used another method to prepare different silicon nanostructures in terms of morphology, diameter and aspect ratio. The "Bottom-up" approach consists in the fabrication or in the synthesis of new objects or structures by spontaneous self-assembly building blocks. It is

based on interactions between atoms or molecules to yield nano-objects or layers with new physical or chemical properties such as: nanoparticles, films, nanowires, nanotubes, etc.…

1.3.1.1.   Silicon nanowires preparation methods

There are different methods for silicon nanowires fabrication among them we can find: Chemical Vapor Deposition (CVD), Annealing in Reactive Atmosphere, evaporation of SiO, Molecular Beam Epitaxy, Laser Ablation, and solution-based techniques, as summarized in Figure 1.26 (list is not exhaustive). The silicon source used can be gas, liquid or solid state [20] [26] [61] [10]. They mainly differ with respect to the catalyst material used and the means by which the silicon is supplied. Among these methods, CVD techniques seem to be the most popular methods used in the nanowires fabrication. In this technique, a gaseous silicon precursor serves as the silicon source. Herein, we will briefly present some of the methods for silicon nanowires synthesis.
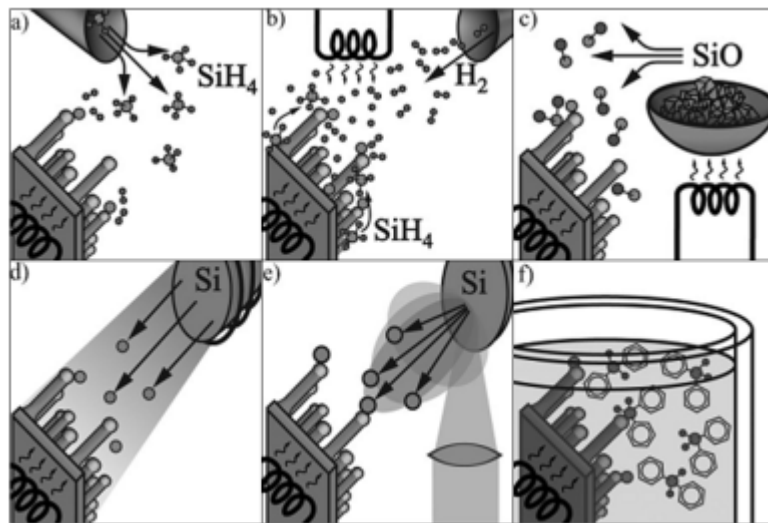
Figre 1.26: Silicon nanowires growth using different techniques: (a) Chemical vapor deposition, (b) Annealing in reactive atmosphere, (c) Evaporation of SiO, (d) Molecular beam epitaxy, (e) Laser ablation, (f) Solution-based techniques. [26]

- **Chemical vapor deposition (CVD)**: Silicon source: SiH_4, $SiCl_4$, SiH_2Cl_2 ... By heating, the gas will be decomposed in the presence of a metal catalyst such as Au, Ni, Cu Al, Zn… [20] on the substrate or in the furnace, resulting in the formation of silicon atoms (Figure 1.26 (a)). CVD permits epitaxial silicon nanowires growth with various growth velocities (from

10^{-2} to 10^{+3} nm/min), depending on the temperature and the silicon source type used. On the other hand, this method offers large silicon nanowire types by controlling the parameters of the growth process such as: gaseous silicon precursor type, time, temperature, pressure, and silicon substrate type. However, by CVD method, nanowires grow following various directions, particularly for the nanowires having a diameter smaller than 5 nm.

- **Annealing in reactive atmosphere**: The silicon nanowires growth occurs due to the presence of metal impurities on silicon substrates and gases like: H_2, I_2 or Br_2 which are injected in the furnace. Then, at high temperature (~ 900°C), the gases will react with the bulk silicon leading to the formation of volatile gaseous halogenous silicon precursors such as: SiH_4, SiI_2, $SiBr_2$. The metal-droplet contamination acts as catalyst and growth proceeds as in conventional CVD. The main advantage of this method is clearly its technical simplicity as compared to other nanowire growth methods, which is presumably the reason why it was used in the early works on silicon nanowire growth. In some sense, this method can be seen as the predecessor of nanowire growth by conventional CVD. As schematically depicted in Figure 1.26 (b), a modification of this method, used nowadays, is the hot-filament CVD.

- **Evaporation of SiO**: The silicon nanowires are generated on a large scale by evaporation of solid silicon monoxide (SiO) (Figure 1.26 (c)). A small of SiO granulate is heated at a temperature ranging from 900 to 1350°C at the hotter end of the furnace. Then, SiO gas flows with the gas stream to the cooler part, where it undergoes a disproportionate reaction into Si and SiO_2, thereby forming silicon nanowires. In principle, two different growth methods are possible: growth with and without metal catalyst. Growth assisted by a metal catalyst is relatively rapid. [26]

- **Molecular beam epitaxy (MBE)**: This technique requires a high purity silicon source, which is placed in front of the substrate (usually (111) Si) as shown in Figure 1.26 (d). In the nanowires growth, both silicon source and silicon substrate are heated in ultrahigh vacuum; the nanowires are generated thanks to metal contamination and growth temperature higher than 500°C [62] and are governed by two fluxes of silicon atoms from the silicon source and substrate. In MBE method, the doping and heterostructure of nanowires can be controlled as well by switching between evaporation sources. However, the diameter of Si nanowires prepared using this method is limited (>40 nm) and the nanowires growth velocity is low, about few nanometers per minute.

- **Laser ablation**: as for MBE technique, the silicon source is placed in front of the substrate. However, the silicon source is the mixed Si-catalyst target which is ablated by a high power

pulsed laser (See Figure 1.26 (e)). Then, the beam of silicon atoms and catalyst target condense to liquid nanodroplets on the substrate by colliding with inert gas molecules in the furnace. The nanowires start growing when the liquid nanodroplets are supersaturated with silicon. In the laser ablation method, the obtained nanowires display a large quantity of ultrathin and high aspect ratios. Their composition can be varied by changing the composition of the mixed Si-catalyst target. Furthermore, the nanowire growth velocity is higher than that obtained using MBE method and is about micrometers per minute. However, the diameter of the nanowires generated depends on both metal catalyst used and the gas injected in the furnace (such as H_2, He or N_2).

- **Solution-based technique**: This method is simple and does not require highly-priced equipment as compared to the methods described above. The silicon source is often a liquid silicon precursor such as diphenylsilane. Silicon nanowires growth occurs in both gaseous and liquid environments in the presence of metal particles catalysts (Figure 1.26 (f)). When the temperature is higher than the metal-silicon eutectic, the nanowires are formed due to the alloy (metal-silicon) supersaturation with silicon. Nanowires with diameters as low as 5 nm and several micrometers in length can be easily synthesized using the solution-based method.

1.3.1.2. Gold as Catalyst

In the silicon nanowires growth, most of the cases, metal catalysts are required for the decomposition or specific adsorption of silicon precursor or silicon atoms. Among the different metal catalysts, we can find Au, Ni, Al, Zn, Cu, Fe, Co…. However, Au is the most commonly metal catalyst used in the synthesis of nanowires thanks to its special properties such as [20] [26] [62]:

✓ A standard metal used for electrical contacts.

✓ A high chemical stability, thus it does not oxidize easily in air. This property is very important for the nanowires pre-growth.

✓ Evaporation systems with Au are available in most semiconductor research institutes. Thus, the deposition of a thin Au layer onto a wafer is not a major obstacle.

✓ The eutectic point with Si occurs at low temperature (363°C) with high Si solubility (19%) as illustrated in Au-Si binary phase diagram (Figure 1.27). As compared to the melting points of pure Au or pure Si, there is a strong reduction of the eutectic point, leading to a significant

decrease of the temperature budget. Indeed, silicon nanowires growth can be achieved at any temperature higher than the eutectic temperature (363°C).
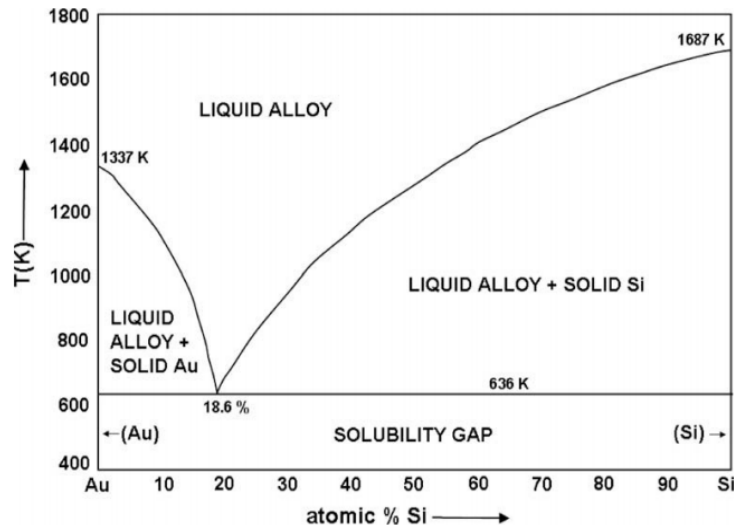
Figure 1.27: Schematic illustration of Au-Si binary phase diagram. [20]

1.3.1.3. Vapor-Liquid-Solid Growth Mechanism

Depending on the phases involved in the reaction, several concepts of growth mechanism appeared such as: Vapor-Liquid-Solid (VLS), Vapor-Solid-Solid (VSS) and Solid-Liquid-Solid (SLS), among which the VLS growth is the most commonly used mechanism. [10] [20] [61] [63] [64] [65]

VLS growth mechanism suggests that silicon from the precursor is dissolved in metal to form a liquid droplet (eutectic liquid, M-Si). The nucleation/growth occurs when the liquid droplet is saturated with silicon. For example, Au nanoparticles are deposited on a silicon wafer (Figure 1.28); when heated at a temperature higher than 363°C in the presence of SiH_4, a Au-Si liquid alloy droplet is formed on the substrate. The silane molecules will be decomposed preferentially on the Au-Si eutectic droplet, allowing the incorporation of Si. When the Si supersaturation of the eutectic droplet (Au-Si) is reached, formation of a crystal occurs (nucleation step) at the solid-liquid interface. Then, additional supply of silicon will allow the elongation of the Si crystal leading to the formation of the Si nanowire with the gold catalyst on top.
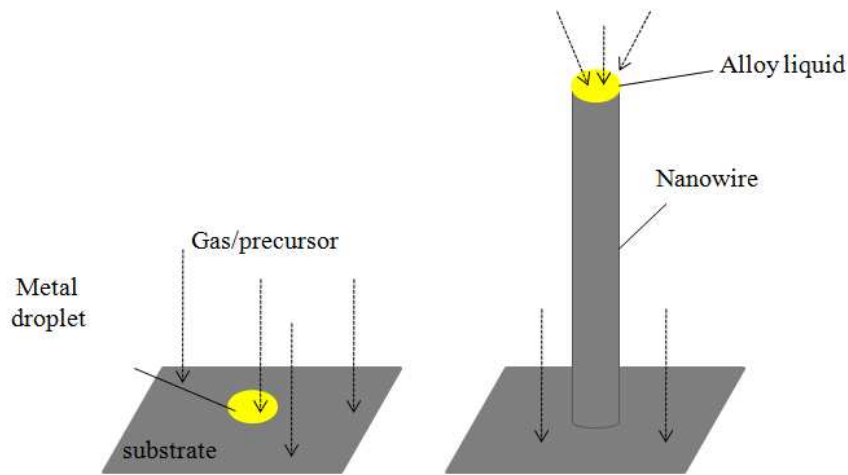
Figure 1.28: Schematic illustration of nanowire growth via VLS growth mechanism. [65]

In practice, the size of the nanowires depends greatly on the size of the metal catalyst. Thus for controlling the size of the nanowires, it is mandatory to control the size of the catalyst particles. Moreover, the length, density and orientation of the wires can be controlled by the pressure, time and orientation of the substrate used for the growth. For example, Figure 1.29 depicts some examples of silicon nanowires prepared in our laboratory *via* the VLS mechanism under different conditions such as: substrate orientation, temperature, time, pressure and density of gold catalysts. In this figure, the silicon nanowires were grown on silicon substrate (111) coated either by 40 (Figure 1.29 (A)) or 20 Å-thick (Figure 1.29 (B)) gold film. The time process was 60 and 15 minutes at a total pressure of 1.1 mbar (P_{SiH4}= 0.08 mbar) at 550°C. The resulting surfaces display straight vertical nanowires (epitaxial growth) with lengths around 3 µm and 1.3 µm and diameters varying between 100 to 180 nm and 100 to 130 nm for 60 and 15 minutes, respectively. By varying the thickness of the gold layer, we have obtained different nanowire densities. Indeed, by the dewetting of gold film of different thicknesses, different densities of gold particles were obtained.
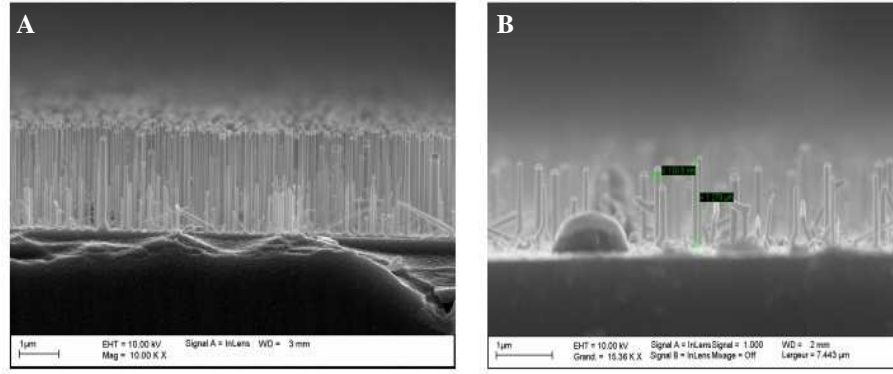
Si (111) with 40 Å-thick Au layer,
T=550°C, 60 min, 1.1 mbar.

Si (111) with 20 Å-thick Au layer,
T=550°C, 15 min, 1.1 mbar.

Figure 1.29: SEM images of silicon nanowires grown by CVD *via* the VLS mechanism.

1.3.2. Preparation of silicon nanowires (SiNWs) interfaces

In our study, the silicon nanowires are synthesized on silicon substrates using the VLS growth mechanism. The process was described in more detail in refs [10] [66] [67]. Briefly, a 300 nm-thick SiO_2 layer is deposited thermally on the silicon substrate (p-type, (100), 0.009-0.01 Ohm/cm), coated with a 40 Å-thick Au layer, and then placed in an oven. The substrate is heated to 500°C, leading to the formation of Au nanoparticles acting as catalyst for silicon nanowires growth. Their size varies from 10 to 100 nm as shown in Figure 1.30. Then, silane gas (SiH_4) is injected; the nanowires growth takes place as explained in the previous section.

Although the orientation of the nanowires is influenced by the pressure prescribed during the VLS process as previously described, herein, we used 300 nm-thick SiO_x layers which ensure relative disorder in the diagonal direction of the nanowires growth. The orientation varies from about 30 to 90° with respect to the horizontal: the larger the pressure, the straighter the nanowires grow (also with a narrower orientation distribution) (Figure 1.31).
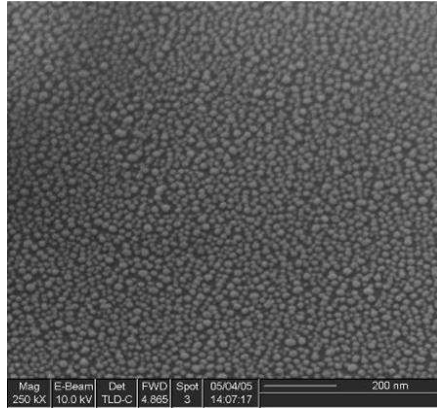
Figure 1.30: SEM image showing Au nanoparticles obtained after dewetting of 40Å-thick gold film on a Si wafer at 500°C.

Surface	Time (min)	Pressure (T)	Length (µm)
VLS1	10	0,4	7
VLS2	60	0,4	45
VLS3	60	0,1	7

Table 1.2: Nanowires growth parameters on silicon substrates at 500°C under a silane flow of 40 sccm.
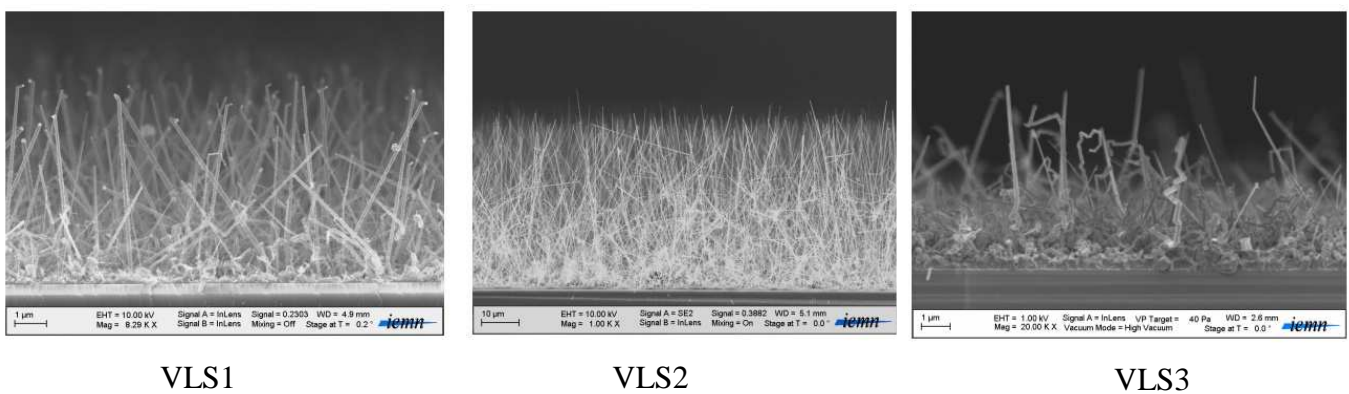
VLS1   VLS2   VLS3

Figure 1.31: SEM images of the silicon nanowires surfaces: VLS1, VLS2, VLS3 corresponding to the growth parameters in Table 1.2.

In our study, three types of silicon nanowires (VLS1, VLS2 and VLS3) are used corresponding to different growth conditions as indicated in Table 1.2; their SEM images are shown in Figure 1.31. The silicon nanowires have diameters ranging from 80 to 150 nm. Compared to the size of the initial Au particles catalyst, it is to be noted that several nanowires have larger size due to a change of the size of the Au particles during the growth process.

- VLS1: The process has growth duration of 10 minutes at a pressure of 0.4 Torr (T). The nanotexture is shown in Figure 1.31- VLS1 (a). It consists of one-layered texture of nanowires of 7 μm in length. Most of the nanowires are straight and have an orientation ranging from 30 to 80° with respect to the horizontal plane. The smaller orientation angle of few nanowires at the forward plan is due to the fact that they have been broken during the cutting of the surface prior to SEM imaging.

- VLS2: The process has growth duration of 60 minutes at a pressure of 0.4 T. The morphology is shown in Figure 1.31- VLS2 (b). It comprises a dense lower layer of tangled nanowires of 25 μm in length and a top layer of straight nanowires of 20 μm in length with the orientation of about 80°.

- VLS3: The process has growth duration of 60 minutes at a pressure of 0.1 T. The nano-texture is shown in Figure 1.31- VLS3 (c). It comprises a dense lower layer made of 2 μm short entangled nanowires with few straight wires of 7 μm in length. In this case, the orientation is more irregular and the average angle with the horizontal is smaller compared to VLS1.

1.3.3. Nanowires growth on silicon micropillars

We also performed silicon micro-/nanostructuration by the combination of Top-down and Bottom-up approaches, by growing silicon nanowires on the top of silicon pillars. All micro-pillar surfaces are covered by a 300 nm-thick SiO_x layer and a 40 Å-thick Au layer. The nanowires growth on the μP surfaces is performed using same conditions as on flat Si wafer as described above. Figure 1.32 displays SEM images (cross-sectional and top views) of VSL1 and VLS2 nanowires grown on different μP surfaces. It has to be noted that the apparent VLS2 and μP+VLS2 surface morphologies are the same because in that case, the silicon nanowires (45μm of total thickness) have completely covered the silicon micropillars, leading to their disappearance under this thick layer of wires. In the opposite, VLS1 nanowires (7 μm) are

shorter than VLS2 nanowires (45µm) and the length of the pillars (10µm). They do not completely cover the pillars and the space between the pillars can be easily observed.

The wetting properties of these surfaces will be investigated in chapter 2.

VLS1 on µP surfaces   **VLS2 on µP surfaces**
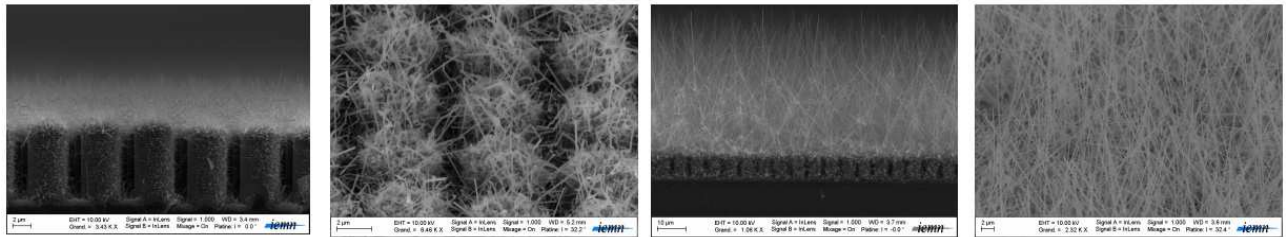
µP (4*2*10)
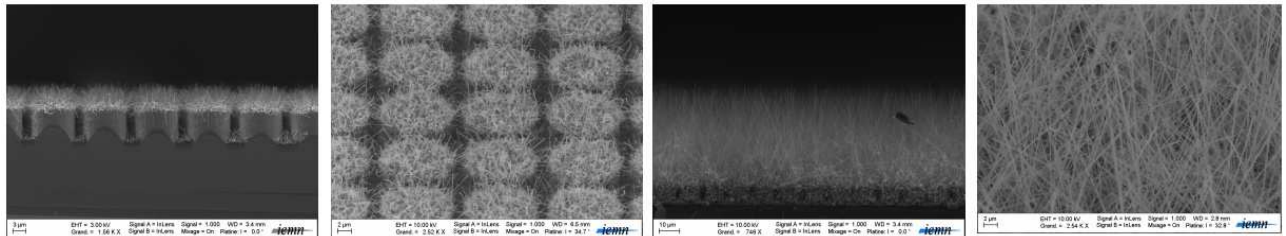
µP (10*2*10
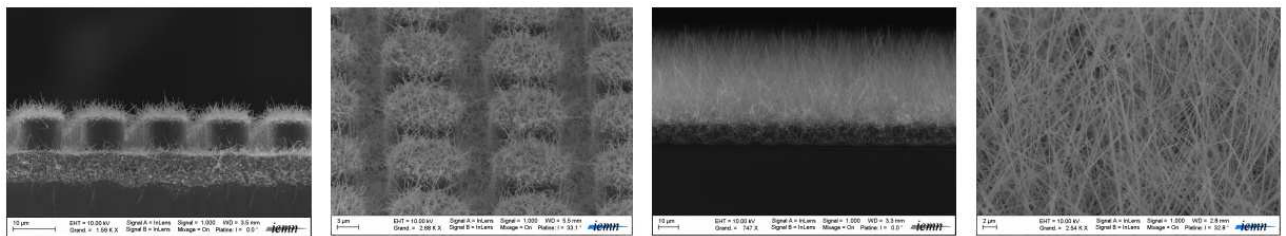
µP (10*5*10)
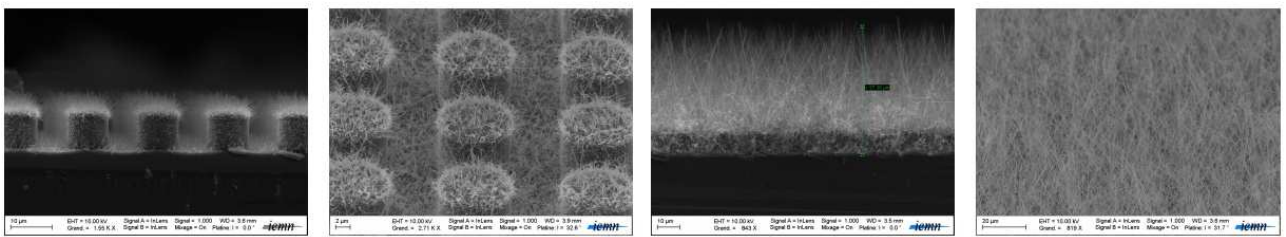
µP (10*7*10)

Figure 1.32: SEM images (cross-sectional and top views) of silicon nanowires grown on µP surfaces.

1.3.4. Summary

In this section, we have disussed the synthesis of silicon nanowires of different morphologies on both flat and micro-pillar surfaces *via* the VLS mechanism by varying the growth parameters. As compared to NanoSi surfaces obtained *via* metal-assisted etching in the previous section, Table 1.3 summarizes advantages and disadvantages of the two fabrication techniques:

	Vapor-Solid-Liquid	*Metal-Assisted Etching*
Chemical agent	*Gaseous silicon precursor (SiH$_4$)*	*Aqueous solutions (HF/AgNO$_3$ or NaBF$_4$/AgNO$_3$)*
Equipment	*Complicated, expensive*	*Simple and cheap*
Budget	*Expensive*	*Low cost*
process	*Complicated*	*Simple*
Form	*Straight cylindrical wires or tangled wires*	*Bundles of vertically aligned nanofilaments, isosceles triangles or needles*
Diameter	*Heterogenous 80-150 nm*	*Difficult to control*
Doping	*Yes, but difficult to control*	*Same as the starting material*
Reproducibility	*Good*	*Good*
Substrates	*Whatever*	*Silicon wafer*
Orientation	*Various*	*Various*
Height	*Not limited*	*Limited (<20μm)*

Table 1.3: Comparison between the silicon nanostructures fabrication techniques: Vapor-Solid-Liquid and Metal-Assisted Etching.

1.4. Conclusion

In this chapter, we have discussed the different techniques used for the preparation of nanostructured silicon substrates. Particularly, we focused on two methods: the metal-assisted etching and the vapor-liquid-solid growth techniques.

By metal-assisted etching, we used two different etching solutions (HF/AgNO$_3$ or NaBF$_4$/AgNO$_3$) for the NanoSi fabrication process. SEM analysis showed that the nanostructures' morphology depends strongly on the etching parameters (duration, temperature, composition, silicon wafer type).

Among the two Ag-assisted etching methods, the synthesis of NanoSi by chemical etching in NaBF$_4$/AgNO$_3$ aqueous solutions is original and investigated for the first time in this work. Furthermore, we have demonstrated that NaBF$_4$ solution can etch SiO$_2$ as HF does, but at lower etching rates. Additionally, this solution is less dangerous than HF solution. Unlike HF/AgNO$_3$ method, the morphology of NanoSi substrates prepared using NaBF$_4$/AgNO$_3$ aqueous solutions depends strongly on the type of the initial Si wafer.

By vapor-liquid-solid growth mechanism, we performed nanowires growth on both flat silicon and silicon micro-pillars surfaces under different growth conditions. We obtained different morphologies of silicon nanowires (simple and double texture, short and long wires) which also are characterized by SEM technique.

We finally discussed the advantage and disadvantage of each technique used in the micro/nanofabrication of our substrates. The SiNWs and NanoSi substrates fabricated in this chapter will be used for some applications such as the development of superhydrophobic and superoleophobic surfaces (chapter 2), as new interfaces for Surface-Assisted Laser Desorption/Ionization (SALDI) and mass spectrometry analysis (chapter3), and biosensor interfaces (chapter 4).

2. Fabrication of Superhydrophobic and Superomniphobic Surfaces

2.1. Introduction

In nature, there are plenty of surfaces such as lotus leaf, duck feather, fish scales, and butterfly wings, etc. that repel effectively water, thanks to their **micro & nano-structured** surfaces. For example, Figure 2.1 illustrates a droplet of water beading up on superhydrophobic butterfly's wings and lotus leaf surfaces. SEM images displayed in the right side of the Figure 2.1 clearly show the multiple scale roughness of the corresponding surfaces. When a water drop is put in contact with these surfaces, it rolls off with almost no friction, collecting at the same time dust particles eventually deposited on their surface, leading to a self-cleaning effect ("rolling ball" effect). These surfaces display a superhydrophobic (SH) character with high contact angle (CA), higher than 150° [68] [69] [70] [71].
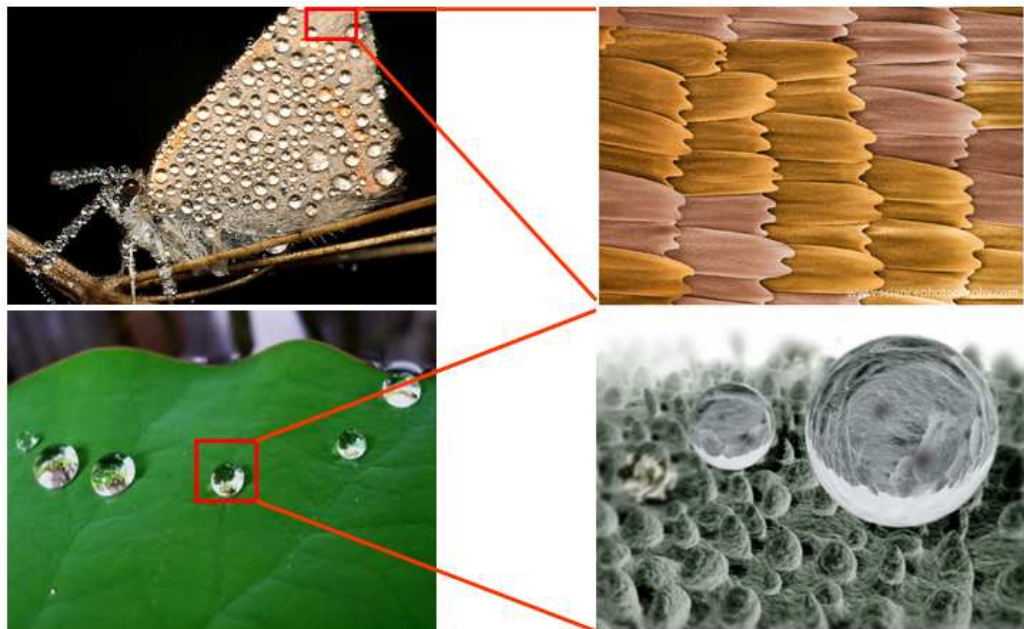
Figure 2.1: A droplet of water beading up on a superhydrophobic butterfly's wings and lotus leaf surfaces (left images). The corresponding multiple scale roughness is displayed in the SEM images on the right side.

Nowadays, artificial SH surfaces fabrication is commonly achieved using different micro/nanofabrication techniques, as depicted in the first chapter. It is admitted that a micro or a nano-structured surface with appropriate low surface energy coating is able to repel water. However, most of the liquid-repellent surfaces are effective only for high-surface tension (γ) liquids such as water ($\gamma = 72.2$ mN/m). The current challenge in their applicability in lab-on-a-chip microfluidics or in high-performance clothes is to design surfaces that repel liquids of low

surface tension. These surfaces are named "superomniphobic" surfaces (SO surfaces). Recent achievements by Tuteja *et al.* [71] [72] employ surfaces with overhanging roughness elements - denoted as "re-entrant", with a regular array of mushroom-shaped posts. These interfaces are able to repel liquids of low surface tension. There are also other kinds of substrates with less regular structures, leading to a high repellence of low-γ liquids [64] [73], for example, alumina nanowire forests [73].

In this chapter, we will first present the general theory of wetting properties of such interfaces. Then, we will discuss the required parameters for the fabrication of superomniphobic (SO) surfaces, and how to characterize their wetting properties. Secondly, we will show that our SO surfaces, fabricated using the methods detailed in the first chapter, display different characteristics: from a simple structure to a double-scaled structure, exhibiting contact angles (CA) ranging from 80° to 160°, depending on the tested liquids. These surfaces are characterized by contact angle measurements (static, advancing, receding, and hysteresis θ_H). The surface presenting the best properties (i.e. largest CA and lowest θ_H for liquids with a wide range of surface tensions) will be dynamically characterized by measuring the impalement pressure threshold P_c with liquids of various γ.

2.2. Theory of wetting and non-wetting solid surface

The wetting properties of a surface are determined by the contact angle (CA) between the liquid and the solid surface. It depends on the surface nature (composition, chemical termination, roughness ...) and the nature of interfacial surface tension (solid-liquid-vapor) [69] [70] [74] [75]. When a liquid droplet is placed on perfectly smooth and chemically homogeneous surface, the CA is described by the Young's relation and is called the Young's contact angle- θ_Y [74] [75]. This CA supports the influence of the interfacial surface tension (liquid-solid, liquid-vapor and vapor-solid).
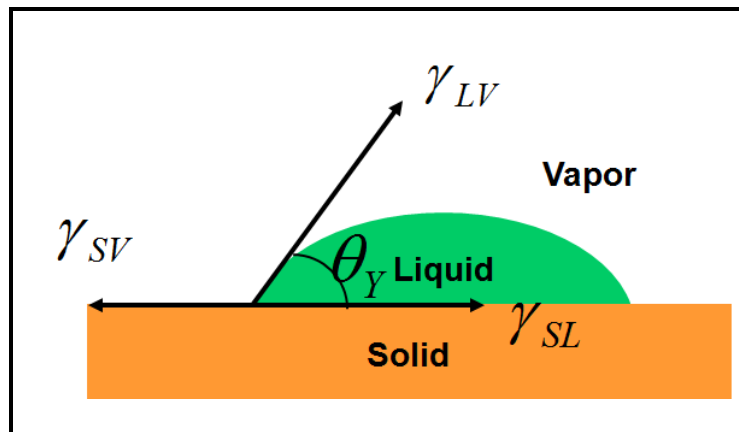
Figure 2.2: A schematic illustration of a liquid droplet on a flat surface.

Figure 2.2 represents an illustration of a droplet on a flat surface with the triple contact line. In the equilibrium state, θ_Y is written as following:

$$Cos\,\theta_Y = \frac{\gamma_{SV} - \gamma_{SL}}{\gamma_{LV}} \quad \textbf{(2.1)}$$

Where:

        γ_{SV} is the solid-vapour surface tension

        γ_{SL} is the solid-liquid surface tension

        γ_{LV} is the liquid-vapour surface tension

In practice, a surface always displays structural defects or roughness as well as chemical heterogeneities. In this case, the CA between the liquid and the surface is described by the apparent contact angle, $\theta*$. While θ_Y is selected by thermodynamics at microscopic scales, $\theta*$

is relevant at macroscopic scales larger than the typical structure length-scale, and can differ from θ_Y [76]. This roughness can be designed on purpose in a controlled fashion, in order to dramatically modify the wettability behaviour. There are a lot of examples of surfaces for which a micro or a sub-microscale structure leads to high surface tension liquid repellency [69] [70] [74] [66] [77]. This property can be relying on two extreme liquid behaviours:

- ✓ Either by achieving a high effective contact area between the liquid and the surface, hence leading to a high surface energy cost, as detailed after, if the solid is treated with a low surface energy coating. This corresponds to a situation where the liquid has been impaled by the structure as shown in Figure 2.3 (a). This approach has historically been proposed by Wenzel and it is denoted as Wenzel state (W), thereafter. [69]

- ✓ Either the entrapment of micro pockets of air between the liquid and the surface, ensuring that the liquid below the drop is mostly in contact with air as shown in Figure 2.3 (b). This is denoted as the Cassie-Baxter (CB) state, thereafter [70]. This situation offers a very low liquid-solid friction, and this feature is particularly interesting for versatile droplet motion, for instance using electrowetting. [66] [70] [78]

In practice, it is possible to obtain intermediate "hybrid" states between the Wenzel and the Cassie-Baxter states (meta-stable Cassie-Baxter state), where the liquid is in partial impalement in the structure, as shown in Figure 2.3 (c). [79]
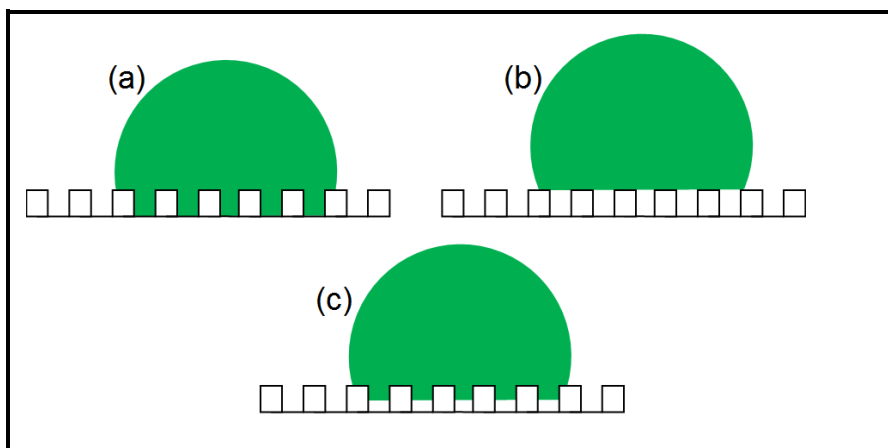
Figure 2.3: A schematic illustration of the formation of composite interfaces. In (a) is represented a liquid droplet in the Wenzel state, (b) in the Cassie-Baxter state and (c) in a meta-stable Cassie-Baxter state. [79]

2.2.1. Wenzel state (1936)

In the Wenzel state, the liquid follows the topography of the solid surface leading to a fully wetted structure. The apparent contact angle θ_W* can thus be determined by surface-energy minimization, in relation with the surface properties.
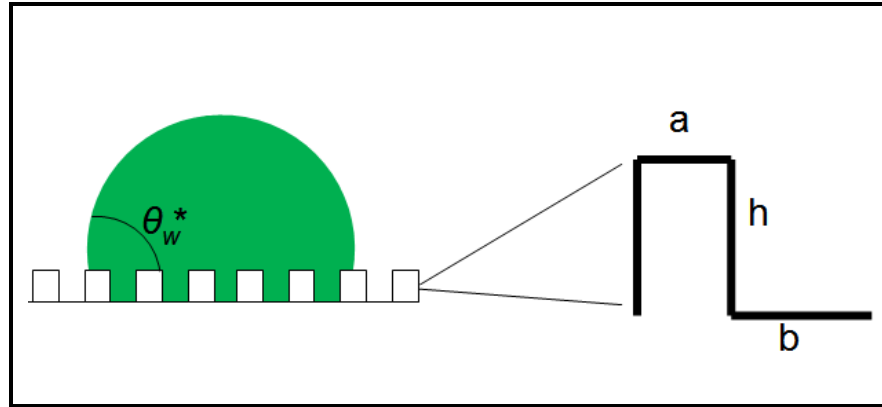
Figure 2.4: A schematic representation of a liquid droplet on a surface structure in the Wenzel state (diameter: a, spacing: b, height: h).

Figure 2.4 shows a liquid droplet on a structured surface in the Wenzel state (diameter: a, spacing: b, height: h) with an apparent contact angle $\theta*_W$. If the droplet is displaced a distance $dA = a + b$ by following the contact line, it leads to an interfacial energy modification of a quantity dE (here, we assume that the feature size of the structured surface is much smaller than the size of the liquid droplet):

$$dE = \gamma_{SL}(a + b + 2h) - \gamma_{SV}(a + b + 2h) + \gamma_{LV}(a + b)Cos\theta*_w \qquad \textbf{(2.2)}$$

Where r corresponds to the surface roughness defined as the actual surface area divided by the projected surface area as shown in equation (2.3):

$$r = \frac{a + b + 2h}{a + b} \geq 1 \qquad \textbf{(2.3)}$$

At the equilibrium: $dE = 0$, the value of $\theta*_W$ is determined by equation (2.4):

$$Cos\theta*_W = r(\frac{\gamma_{SV} - \gamma_{SL}}{\gamma_{LV}}) \qquad \textbf{(2.4)}$$

From equations (2.1) to (2.4), $Cos\,\theta*_W$ can be rewritten as Young contact angle θ_Y (contact angle on a smooth surface possessing identical surface chemistry as the structured surface) as:

$$Cos\theta*_W = rCos\theta_Y \qquad \textbf{(2.5)}$$

Therefore, following the Wenzel model, if we know θ_Y and r, we can determine $\theta*_W$ if the liquid is completely impaled in the structure of a surface.

As *r>1*, thus if $\theta_Y > 90°$ (hydrophobic surface) $\rightarrow \theta*_W > \theta_Y$, while $\theta_Y < 90°$ (hydrophilic surface) $\rightarrow \theta*_W < \theta_Y$

We can note that, even with a high contact angle, in the Wenzel state, the liquid droplet is strongly stuck to the surface. Furthermore in this relation, there is no conditions on *r*, thus it implies that both theoretical states, corresponding to non wetted surface (contact angle equal to 180°) or totally wetted one (contact angle of 0°), can be obtained. In practice, these states can't be obtained, thus there must be a limitation of the value of *r*. For high roughnesses, another model is required.

2.2.2. Cassie-Baxter state (1944)

In the Cassie-Baxter state, the liquid is only in contact with the top of each surface structure whereas air pockets remain trapped inside the structure leading to enhancement of the repellent effect of the liquid. The apparent contact angle $\theta*_{CB}$ in this case can also be determined by the relation to geometrical properties of the substrate when the surface energy is minimal.
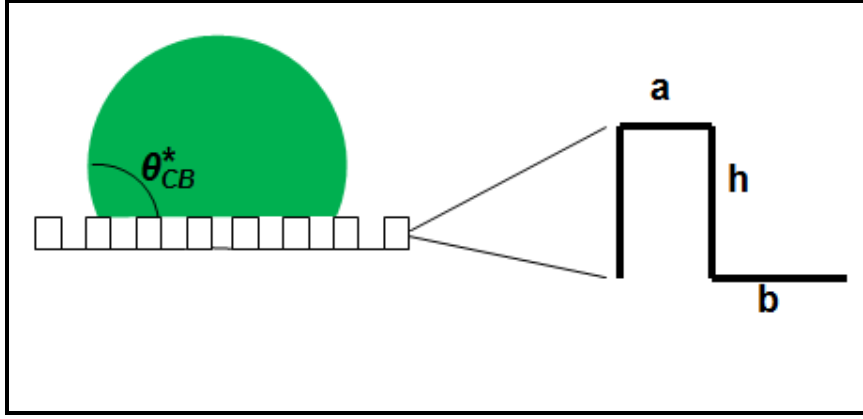
Figure 2.5: A schematic representation of a liquid droplet on a structured surface in the Cassie-Baxter state (diameter: a, spacing: b, height: h) with the contact angle $\theta*_{CB}$

Figure 2.5 shows a schematic illustration of a liquid droplet on a structured surface (diameter: a, spacing: b, height: h, an apparent contact angle- $\theta*_{CB}$) in the Cassie-Baxter state. If the droplet is displaced of a distance $dA = a + b$ (following the contact line), it leads to a modification of the interfacial energy of a quantity dE (here, we assume that the feature size of the structured surface is much smaller than the size of the liquid droplet):

$$dE = \gamma_{SL}a - \gamma_{SV}a + \gamma_{LV}b + \gamma_{LV}(a+b)Cos\theta*_{CB} = (\gamma_{SL} - \gamma_{SV})a + \gamma_{LV}\left[b + (a+b)Cos\theta*_{CB}\right] \text{(2.6)}$$

At the equilibrium $dE = 0$, the value of $\theta*_{CB}$ is determined by equation (2.7):

$$Cos\theta*_{CB} = \frac{(\gamma_{SV} - \gamma_{SL})a - \gamma_{LV}b}{\gamma_{LV}(a+b)} = \frac{\gamma_{SV} - \gamma_{SL}}{\gamma_{LV}} \times \frac{a}{a+b} - \frac{b}{a+b} \quad \textbf{(2.7)}$$

We can simplify it with $f_1 = \dfrac{a}{a+b}$ and $f_2 = \dfrac{b}{a+b}$ leading to $f_1 + f_2 = 1$

Where f_1 is defined by the total area of the solid-liquid interface divided by the projected area and f_2 is the total area of the liquid-vapor interface divided by the projected area. Equation (2.7) can thus be rewritten as:

$$Cos\theta*_{CB} = \frac{\gamma_{SV} - \gamma_{SL}}{\gamma_{LV}} f_1 - f_2 \quad \textbf{(2.8)}$$

$$Cos\theta*_{CB} = f_1 Cos\theta_Y - f_2 \quad \textbf{(2.9)}$$

Independently, Marmur [68] [80] has proposed that if we write $f_1 = r_\Phi \phi_s$ and $f_2 = 1 - \phi_s$ it appears that there is some advantage for the surface presenting more than one structure layer. Here r_Φ is the roughness of the wetted area and ϕ_s is the fraction of the projected area of the solid surface that is wet by the liquid. Whereby it is evident that $r_\Phi \geq 1$ and $\phi_s \leq 1$ and equation (2.9) can be re-written as:

$$Cos\theta*_{CB} = r_\phi \phi_s Cos\theta_Y + \phi_s - 1 \quad \textbf{(2.10)}$$

From equations (2.5) and (2.10), it is clear that the Cassie-Baxter state is reduced to the Wenzel state: if $\phi_s \rightarrow 1$ and $r_\phi \phi_s \rightarrow r$.

In the literature [18] [67] [66] [69] [81], the value of $\theta*_{CB}$ is determined by equation (2.11), which is only valid if $r_\phi = 1$ i.e. the top structure of a surface must be perfectly smooth and chemically homogeneous. However, if the surface presents a double structure as shown in Figure (2.6) where $r_\phi \neq 1$, thus equation (2.11) is not valid.

$$Cos\theta*_{CB} = \phi_s Cos\theta_Y + \phi_s - 1 \quad \textbf{(2.11)}$$
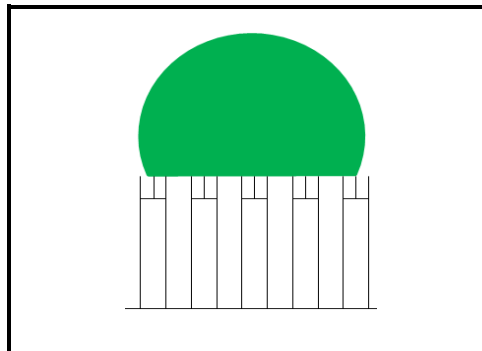
Figure 2.6: A Schematic illustration of a liquid droplet on a double structured surface with

$$r_\phi \neq 1$$
.

Thus, for the Cassie-Baxter model, the apparent contact angle (θ^*_{CB}) is a function of the solid fraction for a given surface with Young's contact angle (θ_Y). The "rolling ball effect" of a liquid droplet on the surface is favoured, because of a low retention force with the surface. To obtain a superhydrophobic surface (θ^*_{CB}>150°), the contribution of the solid part should be as small as possible or a solid material with a very high contact angle [18] [71].

Thermodynamic considerations can be used to determine whether a particular textured surface will exist in the Wenzel or the Cassie-Baxter state [72] [80] [82]. The situation is somewhat complicated by the presence of multiple local free energy minima, leading to so-called "metastable" configuration (Figuren 2.3 (c)). The transition from the Wenzel to the Cassie-Baxter state can be determined by a critical value of the equilibrium contact angle θ_c by equation (2.12).

$$Cos\,\theta_C = \frac{-r(1-\phi_s)}{(r-r_\phi\phi_s)} \textbf{ (2.12)}$$

As we have the following inequalities: $r \geq 1 \geq \phi_s$ leading to $\theta_C \geq 90°$. If $\theta_Y \geq \theta_C$ the Cassie-Baxter state has a lower surface energy: the droplet stays on top of the structure and equation (2.10) is verified. On the contrary, the liquid fills the pores of the structure and equation (2.5) is verified. More recently, it has been shown that the Cassie-Baxter state can be obtained with $\theta^*_{CB} > 90°$ even $\theta_Y < 90°$ [71] [72].

In this section, we have described two extreme states of water droplet on a rough surface. Even if these rough surfaces exhibit a high contact angle, their liquid repellent properties (i.e. the liquid droplet is either stuck on or rolls off the surface) are linked to their roughness.

From an applicative view point, the Cassie-Baxter state has to be promoted in order to reach roll-off properties. We have also seen that the only measurement of contact angle does not permit to define the liquid state on a surface. Therefore, the characterization of the contact angle hysteresis and the transition from one state to another are required. This point will be discussed in more detail in the next section.

2.3. Which parameters define the quality of a liquid-repellent surface?

2.3.1. Low contact angle hysteresis

On a surface, the characterization of a liquid drop can be either static or dynamic, corresponding to the static (θ) or dynamic CA. In the dynamic case, the dynamic CA is a non-equilibrium one and is measured during the growth (advancing contact angle, θ_A) and shrinkage (receding contact angle θ_R) of a liquid drop (Figures 2.7 and 2.8). The difference between θ_A and θ_R is the contact angle hysteresis (θ_H), which is related to the retention force of the drop on the substrate. Thus, a higher θ_H leads to a stronger interaction between the liquid droplet and the surface. In practice, the origin of θ_H is attributed to the presence of chemical heterogeneities and physical defects (non-perfect surfaces) or contaminants from air on the surface [18] [66] [74] [77]. There are two methods for measuring θ_H as illustrated in Figures 2.7 and 2.8:

❖ The "tilted surface" (Figure 2.7) method: a liquid droplet is deposited on the surface and then tilted. θ_A and θ_R are measured just before contact lines depining during tilting.

❖ The "receding/advancing" method (Figure 2.8): θ_A is measured just before the wetting line starts to advance while the volume of the droplet is increasing, and θ_R is determined just before the wetting line is receding.
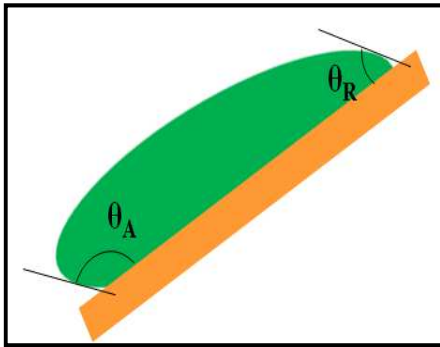
Figure 2.7: A Schematic illustration of the "tilted surface" method.
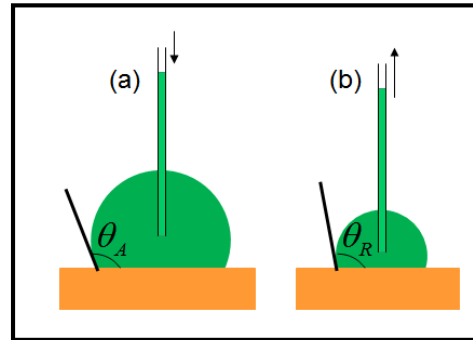
Figure 2.8: A Schematic illustration of the "receding/advancing" method.

From both methods of θ_H measurement, it is to be noted that the value of the contact angle depends strongly on the way the droplet is deposited on the surface. It is important to mention the value of θ_H in the characterization of the surface wetting properties. Moreover, the

liquid droplet in the Wenzel state presents higher θ_H than in the Cassie-Baxter state. If $\theta_H < 10°$, it is sure that a liquid droplet on SH or SO surface is in the Cassie-Baxter state. The droplet can roll off from the surface by simply tilting the substrate by a few degrees. This effect is called "rolling-ball" effect. [64] [67] [84]

In the field of digital microfluidics, to insure displacement of a liquid droplet, various systems require SH or SO surfaces exhibiting low θ_H. Therefore, the surface which displays large static CA and low θ_H enhances the performance of digital microfluidics systems. [13] [14]

What defines a good liquid-repellent surface, is a large apparent contact angle as possible and a low θ_H (typically $\theta_A - \theta_R \leq 10°$), but also its ability to retain a state of low θ_H when large external forces are applied to the liquid - thereafter, we denote "robustness" this property.

2.3.2. High robustness of a surface

As mentioned above (section 2.2.2), if $\theta_Y \geq \theta_C$, the Cassie-Baxter state has a lower surface energy than the Wenzel state: the droplet stays on top of the structure. However, it is possible to keep a liquid-vapour interface in a weakly impaled state even when $\theta_Y \geq \theta_C$. This is related to the meta-stable character of the Cassie-Baxter state as shown in Figure 2.3 (c): in a free-energy landscape, this state can be situated at a *local minimum*, whereas the free-energy is often at a *global minimum* in the Wenzel's state. Therefore, a perturbation of finite strength is required to jump over the energy barrier between Cassie-Baxter and Wenzel states [64] [74] [75] [80] [82] [85] [86] [87]. Thus, high robustness of a surface leads to higher ability to retain a Cassie-Baxter state when large external forces are applied to the liquid.

The robustness of a surface is characterized through the value of liquid pressure threshold P_c before impalement of a liquid into the structure. It can be estimated by different techniques such as: evaporation, EWOD, droplet squeezed between two surfaces, drop impact… [67] [89] [90] [91]. Among which, we chose the drop impact method in our study because this method is easy, fast and does not require specific surfaces compared to EWOD or droplet squeezed between two surfaces methods. It does not require a long time for a measurement (less than 1 min) compared to the evaporation method, which necessitates a long time for one measurement.

The measurement of pressure threshold allows the determination of the ability of a surface to prevent the water droplet to transit from the Cassie-Baxter state to the Wenzel state.

These assertions have been made only with respect to the water as liquid, with a surface tension of 72.2 mN/m. But if we aim to realize biosensors and biochemical interactions on rough surfaces, water is not sufficient and talking of a large variety of liquids in terms of surface tension, and more specifically those of lower ones, appears to be necessary.

2.4.   From superhydrophobic to superomniphobic surfaces

The wetting/non-wetting properties of a solid surface are usually determined by the contact angle (CA) between the liquid and the surface. According to the value of the contact angle, the surface is called hydrophilic, hydrophobic, omniphilic or superomniphobic … The term "**hydro**" is linked to high surface tension such as water, while the term "**omni**" is connected with low surface tension liquids such as oil. Figure 2.9 presents different definitions of the wetted/non-wetted surface:

- When $0 < CA < 90°$: The surface is hydrophilic (for high-γ liquids as water) or omniphilic (for low-γ liquids as oil and hexadecane…)

- When $90° \leq CA < 140°$: The surface is hydrophobic (for high-γ liquids as water) or omniphobic surface (for low-γ liquids as oil and hexadecane…)

- When $CA \geq 140°$: The surface is superhydrophobic (SH) (for high-γ liquids as water) or superomniphobic (for low-γ liquids as oil and hexadecane…) (SO surface).
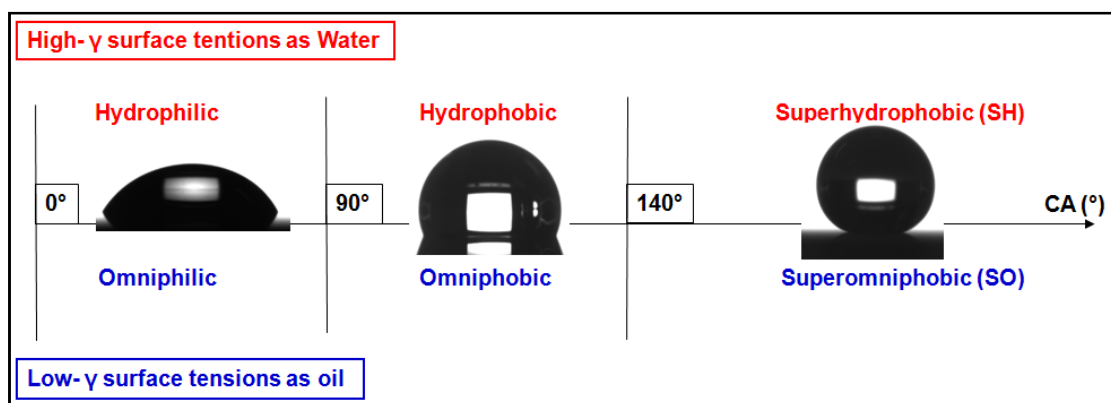
Figure 2.9: Classification of surfaces as a function of their wetting properties for high- γ and low- γ liquid droplets.

In practice, SH biosurfaces can repel water thanks to their micro/nano-structured surface. The most famous examples found in nature is the lotus leaf which presents a contact angle (CA) of

161° for water and 2° CA hysteresis (Figure 2.10 a). In fact, the lotus leaf consists of microscale mounds and nanoscale hair-like structures as shown in the inset of Figure 2.10 (a) [85] [92] [93] [94]. However, the lotus leaf cannot repel liquids of low γ such as hexadecane (γ = 27.4 mN/m); it is completely wetted by this liquid (see Figure 2.10 b, a hexadecane drop spreads on the lotus leaf) [71] [72].
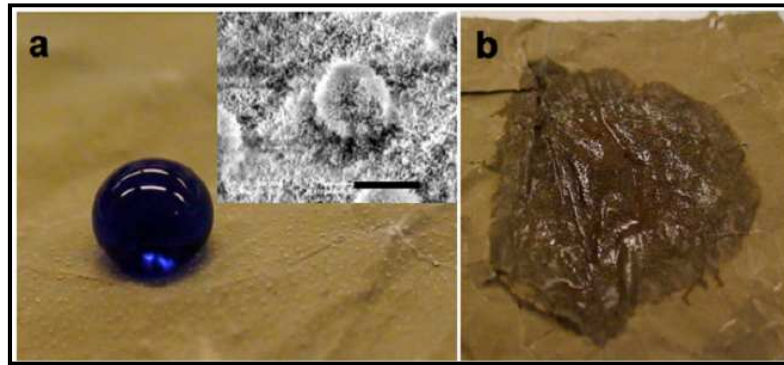
Figure 2.10: Photo of a water droplet (colored with methylene blue) (a) and a droplet of hexadecane spreading on the lotus leaf surface. The inset shows a SEM image of the lotus leaf surface. [71] [72]

However, coating the lotus leaf with electrospun fibers (bead-on-strings morphology) of PMMA (polymethyl methacrylate) + 44wt% fluorodecyl POSS (polyhedral oligomeric silsesquioxane molecules) confers a SO character to the surface [71] [72]. In fact, the electrospun fibers exhibit lower surface tension than epicuticular wax crystalloid of lotus (the natural coating). Figure 2.11 displays a photo of droplets of different liquids on the lotus leaf; it can repel all liquids with γ >21.6 mN/m as water (72.2 mN/m), methylene iodide (50.0 mN/m), methanol (22.7 mN/m) and octane (21.6 mN/m). Thus, the surface chemistry plays a crucial role for creating SO surfaces.

Moreover, it is known that a flat surface without any roughness displays a maximum CA around 125°. For obtaining **CA>125°,** the surface must to be structured [71] [95] [96]. However if the structured surfaces are fabricated from hydro- or omniphilic material, in the absence of a coating layer with low surface energy molecules, they are superhydrophilic or superomniphilic [97] [98] [99] [100]. Therefore, a surface presents SH or SO properties if it satisfies these two conditions:

1. *Being structured, this condition is called a surface geometry factor.*
2. *Being coated with a low surface energy overlayer. This condition is named a chemical surface factor.*

Figure 2.11: Photos of water (colored blue with methylene blue) (72.2 mN/m), methylene iodide (50.0 mN/m), methanol (colored green) (22.7 mN/m) and octane droplets (colored red with oil red O) (21.6 mN/m) on a lotus leaf surface covered with electrospun fibers (beads-on-strings morphology) of PMMA (polymethyl methacrylate) + 44wt% fluorodecyl POSS (polyhedral oligomeric silsesquioxane molecules). [71] [72]

From these two conditions, it is also necessary to quantify the liquid repellency of the surface (SH or SO surfaces) by three parameters:

   i.   Large contact angle

  ii.   Low contact angle hysteresis

 iii.   High robustness

Therefore, what is required for the fabrication of these surfaces? This question will be discussed in the next section.

2.4.1. Chemical surface factor

2.4.1.1. Surface energy

At the contact line (liquid-solid-vapour), there are a lot of intermolecular forces such as: Van der Waals forces, hydrogen bonding, and dipole-dipole interactions…, thus the chemical

composition or termination of a surface is crucial for these interactions and influences the surface wetting properties. [96] [95] [100] [101]

For example, Table 2.1 displays the water and hexadecane contact angles as a function of various chemical terminations that we have realized on a flat silicon surface. The non-wetting capacity of these surfaces is ranked in ascending order: -OH termination < -$(CH_2)_{10}$COOH termination (COOH termination) < -H termination < -$(CH_2)_{16}CH_3$ termination (CH_3 termination) < -$(CH_2)_2(CF_2)_7CF_3$ termination (CF_3 termination). It is clear that the highest quality of liquid repellency is obtained on the CF_3 termination.

Following the Langmuir's theory (intermolecular forces), the surface wetting properties can be explained [96]:

❖ **In the case of aqueous liquids**, for example, the water molecule is polar: highly polar groups of a surface will lead to higher wetting or lower non-wetting properties. This hypothesis is applied for the explanation of the results presented in Table 1:

  ✓ The OH-terminated Si surface has a lower water CA than the H-terminated one, because Si-OH bond is more polar than Si-H.

  ✓ The same phenomenon can be observed for the -COOH group, which is more polar than -CH_3 group. As a result the CH_3-terminated Si surface presents a higher water contact angle than the COOH-terminated one.

  ✓ However, this hypothesis is not verified in the case of -CF_3 termination. Indeed, the C-F bond is more polar than the C-H one because F atom is more electronegative than H atom, while the -CF_3-terminated surface is more hydrophobic than the -CH_3- terminated one.

❖ **In the case of non-aqueous liquids**: The molecules mostly contain -CH_2 groups in their formula. The major mechanism of wetting is the result of the ability of the non-polar group of the liquid to be adsorbed by its hydrocarbon "tail" on the hydrocarbon tail of surfaces. For example, the hydrocarbon "tail" of -$(CH_2)_2(CF_2)_7CF_3$-terminated surface (-CF_3 termination) is very different from the hydrocarbon one of n-hexanedecane [CH_3-$(CH_2)_{14}$-CH_3)] as compared to the -$(CH_2)_{16}CH_3$-terminated surface (-CH_3 termination). Hence, CF_3-terminated surface displays higher omniphobicity than CH_3-terminated surface.

Termination surface	-OH	-H	-(CH$_2$)$_{10}$COOH	-(CH$_2$)$_{16}$CH$_3$	-(CH$_2$)$_2$(CF$_2$)$_7$CF$_3$
Water contact angle (°)	10	84	58	102	120
Hexadecane contact angle (°)	0	0	0	0	69

Table 2.1: Static contact angles of water (γ=72.2 mN/m) and hexadecane (γ=27.4 mN/m) on a flat silicon surface as a function of its chemical termination.

In order to overcome the limitations of the Langmuir theory for aqueous liquids, Zisman *et al.* proposed another explanation about the ability of a surface to be wetted by using the value of the critical surface tension or surface energy [95] [96] [99] [101] [102]. This approach assumes that a surface with a lower surface energy leads to higher non-wetting properties. In Table 2.2 are summarized some values of surface energies γ_E as a function of chemical termination. From this Table 2.2, there are some important observations:

➢ CF$_3$-terminated surface presents the lowest energy ever found. The replacement of a single fluorine atom by a hydrogen atom in the terminal -CF$_3$ group creates a terminal -CHF$_2$ moiety; its γ_E value is two times higher than that of -CF$_3$ termination. Moreover, γ_E regularly increases with progressive replacement of fluorine by hydrogen atoms in the surfaces of bulk polymers.

➢ In the case of a hydrocarbon-terminated surface, the surface of a close-packed -CH$_3$ groups is more hydrophobic than -CH$_2$- groups.

➢ In the case of chlorocarbon-terminated surfaces, the presence of more chloride atoms in the hydrocarbon chain leads to an increase of the value of γ_E.

	Surface termination	γ_E (mN/m)
	$-CF_3$	6.0
	$-CF_2H$	15.0
1/ Fluorocarbon surfaces	$-CF_3$ and $-CF_2-$	17.0
	$-CF_2-$	18.0
	$-CH_2-CF_3$	20.0
	$-CF_2-CFH-$	22.0
	$-CF_2-CH_2-$	25.0
	$-CFH-CH_2-$	28.0
	$-CH_3$ (Crystal)	22.0
	$-CH_3$ (monolayer)	24.0
2/ Hydrocarbon surfaces	$-CH_2-$	31.0
	$-CH_2-$ and $-CH-$	33.0
	$-CH-$(phenyl ring edge)	35.0
	$-CClH-CH_2$	39.0
3/ Chlorocarbon surfaces	$-CCl_2-CH_2$	40.0
	$=CCl_2$	43.0

Table 2.2: Critical surface energies given by Zisman et al. [96]

2.4.1.2. Surface treatment methods

There are two main methods for surface treatment: one is the deposition of hydrophobic materials (*via* physisorption) such as: fluorocarbon polymer, Teflon® or Cytop® by spin-coating, plasma, Langmuir-Blodgett techniques….The second way is the covalent immobilization of low surface energy molecules *via* chemisorption: silanization for oxide surfaces (TiO_2, SiO_x, Al_2O_3…), thioalkylation for noble metal surfaces (Au, Ag, Pt) or hydrosilylation on hydrogenated silicon surfaces.

As mentioned above, the surface with fluorocarbon termination exhibits the highest non-wetting properties. Thus, during this work, we have used two different approaches for the chemical surface treatment with fluorocarbon chains:

- **Deposition of C_4F_8, a gaseous fluoropolymer** *via* plasma: the surfaces were placed onto a holder and then directly transferred in the plasma chamber (Silicon Technology System) to deposit C_4F_8 layers (Si-C_4F_8 surfaces) (Appendix 5).
- **Silanization using *1H, 1H, 2H, 2H*-perfluorodecyltrichlorosilane (PFTS)**: the surfaces were cleaned and activated using UV/O_3 during 30 minutes at room temperature. This treatment removes all organic contaminants and generates silanol groups on the surface. Then the activated surface was modified with PFTS giving CF_3-terminated (Si-CF_3) surfaces (Appendix 6).

Table 2.3 displays water and hexadecane CAs on flat Si surfaces chemically treated with C_4F_8 and PFTS: Si-C_4F_8 and Si-CF_3. We found that both surfaces display similar water contact angles, while Si-CF_3 surface exhibits a higher hexadecane CA than the Si-C_4F_8 surface. Concerning the contact angle hysteresis, both surfaces show similar values of 28° for the two liquids: water and hexadecane.

It is evident that the surface modified with PFTS gives slightly higher CA values for hexadecane. Thus, in our investigation later, we will choose the silanization method with PFTS for the chemical treatment of the surfaces.

Surfaces	Si-C_4F_8	Si-CF_3
Water CA (°)	120	120
Hexadecane CA (°)	53	67

Table 2.3: Static contact angles (CA) for water (γ=72.2 mN/m) and hexadecane (γ=27.4 mN/m) on flat Si surfaces modified with 15 nm-thick C_4F_8 layer and PFTS.

2.4.2. Surface geometry factor

As previously mentioned, surface geometry factor is one of the two main factors determining the SH and/or SO character of a surface. The surface geometry is widely achieved by micro & nanofabrication methods (cf. chapter1), with different materials like: polydimethylsiloxane (PDMS), silicon, silicon oxide, alumina, diamond… [64] [72] [73] [84] [85] [103]

For the preparation of SH surfaces, as depicted before, a rough surface covered by a hydrophobic coating and presenting various forms such as: porous, nanowires, micro-pillars, straight or random nanostructures is sufficient to reach superhydrophobicity with various contact angle hysteresis (θ_H) and robustness. For example, porous or nanostructured silicon interfaces, fabricated by electrochemical etching technique, chemically modified with octadecyltrichlorosilane (CH_3-termination) are superhydrophobic with low θ_H ($\approx 1°$) [13] [14] [55] . Similarly silicon nanowires, grown *via* the VLS mechanism, coated with C_4F_8 polymer are superhydrophobic (CA > 160°) with low θ_H ($\approx 1°$) [66] [67]. Another example of artificial superhydrophobic surface is ZnO nanowire substrate modified with fatty acids. It displays a maximum water contact angle of 167° and low θ_H ($\approx 1°$) [104].

If a surface is hydrophobic such as PDMS or Teflon, the chemical surface treatment may be not required in order to achieve superhydrophobicity. For example, Khorasani *et al.* [105] have demonstrated that superhydrophobic PDMS surfaces (with water CA about 175°) can be prepared using a CO_2 pulsed-laser (Fluency: 0.5-5 J/cm^2, wavelength: 9.1-10.6 µm). However, a careful characterization of the contact angle hysteresis and robustness of these non-wetting surfaces was rarely indicated.

The problem is more complicated for hydrophilic materials. **In that case** the substrates require a more complex geometry compared to 'classical' SH surfaces. In recent years, many

authors have demonstrated that a structure with "re-entrant" angles is required. Indeed, thanks to the overhanged micro or nanostructures even with a hydrophilic material and without any hydrophobic coating, the surfaces are able to repel water droplets [71] [84] [98] [106] [107]. This geometrical criteria can also be theoretically extended to all type of liquids (i.e. whatever their surface tension): to obtain a surface exhibiting a high contact angle (>150°), a re-entrant structure is required whatever the tested liquid. Nosonovsky *et al.* [82] has theoretically investigated several surfaces with nano-scale roughness superimposed over larger micro-scale pillars, and considered the effect of concave and convex nano-roughness upon the stability of a composite interface as shown in Figure 2.12. Their model indicated that:

- The bumps may pin the triple line because an advancing liquid-air interface. It leads to a contact angle decrease ($\theta_A < \theta_Y$) and making the equilibrium stable.

- The grooves provide equilibrium positions corresponding to the Young equation, but the equilibrium is unstable, because an advancing liquid-air interface results in contact angle increase ($\theta_A > \theta_Y$).
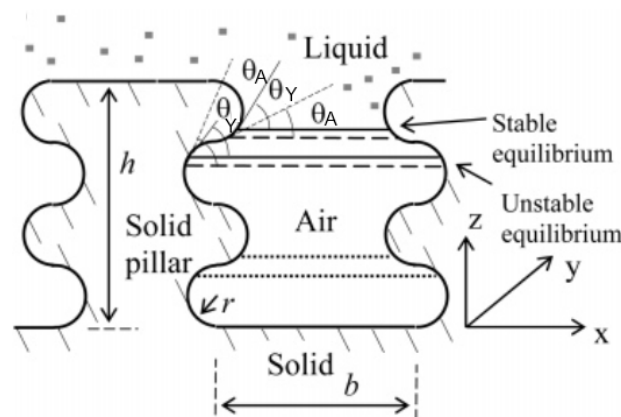
Figure 2.12: Schematic illustration of the expected liquid-air interfaces on two dimensional pillars with semicircular bumps/grooves walls by Nosonovsky. [82]

From an experimental view point, it was suggested that a high contact angle is not the unique goal to reach, but a surface with high robustness. To obtain a low hysteresis and a high robustness, it is preferable to coat the re-entrant structure with an omniphobic layer. Thus, Tuteja's and Ahuja's groups [71] [72] [98] [108] developed Nosonovsky's study for creating alkane-liquid repellent surfaces with a re-entrant curvature profiles such as: a micro-hoodoo surface (Figure 2.13a, Tuteja), and a nano-nail surface (Figure13b, Ahuja). These surfaces were then

coated with a hydrophobic layer using *1H,1H,2H,2H*-perfluorodecyltrichlorosilane for the micro-hoodoo surface and 20 nm-thick fluoropolymer (F/C ratio of 1.55) for the nano-nail surface. The resulting surfaces display a contact angle for organic liquids ($\gamma > 21.8$ mN/m) greater than 150° with low contact angle hysteresis. They also indicated that their surfaces could be SH and SO, even though the Young contact angle was well below 90°.
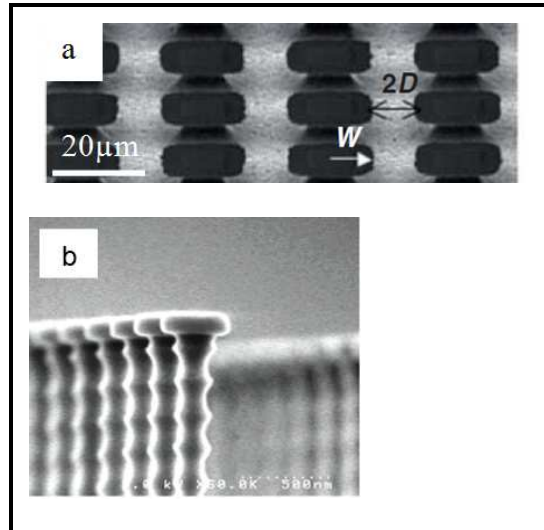
Figure 2.13: SEM images of (a) micro-hoodoo [72], and (b) silicon nanonails surfaces. [108]

To explain why the "re-entrant" surface can improve the non wetting ability Tuteja *et al.* suggested a relation between the local angle of the structure (Ψ) and the Young's CA (θ_Y) (see Figure 2.14):

- If $\theta_Y \leq \Psi$ as shown in Figure 2.14 (a), the net traction on the liquid-vapour interface is downward, thereby facilitating the imbibitions of the liquid into the solid structure, leading to a fully wetted interface.
- If $\theta_Y \geq \Psi$ as shown in Figure 2.14 (b), the net traction is directed upward, thereby supporting the formation of a composite interface.
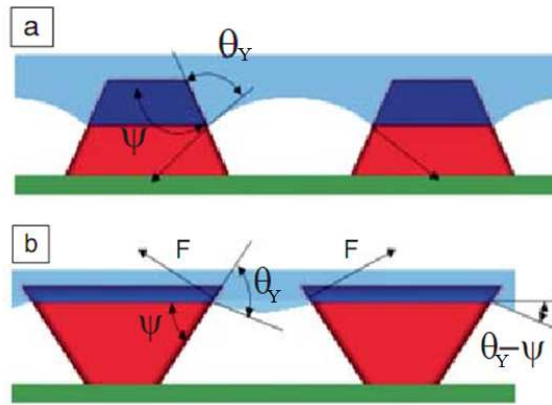
Figure 2.14: Schematic illustration of the expected liquid-air interfaces on two idealized surfaces by Tuteja et al. [71] [72] [98]

In summary, for both SH and SO surface fabrication, the surface must be structured. For the preparation of SH surfaces, a chemical treatment is not mandatory. However to reach a superomniphobic character, coating the rough (structured) surface with extremely low surface energy molecules is necessary. For both SH and SO, the high non-wetting properties with a contact angle larger than 140° can be reached even though the Young's contact angle is well below 90°.

In the next section, we will report on the fabrication of SH and SO surfaces. For this purpose, silicon interfaces with different surface morphologies were prepared using different methods described in chapter 1. These textured surfaces were chemically treated with *1H, 1H, 2H, 2H*-perfluorodecyltrichlorosilane, a low surface energy molecule. The morphology of the resulting surfaces were characterized using scanning electron microscopy (SEM), and their wetting properties were evaluated using contact angle (static, advancing, receding, hysteresis) measurements.

2.5. Fabrication of Superhydrophobic and Superomniphobic surfaces

In this work, we have investigated different strategies for the synthesis of rough surfaces, consisting in simple or double-scale structured using micro & nanofabrication techniques. The high surface roughness combined with chemical modification with *1H, 1H, 2H, 2H-perfluorodecyltrichlorosilane (PFTS)*, a low surface energy molecule, led to the formation of superhydrophobic and/or superomniphobic surfaces.

➕ **Simple structured surfaces:**

- *Nanostructured silicon (NanoSi) obtained via metal-assisted etching method using NaBF$_4$/AgNO$_3$ aqueous solution.*
- *Micropillars (µP) achieved by lithography and reactive ion etching (dry etching).*
- *Silicon nanowires synthesized by chemical vapour deposition (CVD) via the Vapor-Liquid-Solid (VLS) growth mechanism.*

➕ **Double-scale structured surfaces:**

- *Micropillars + nanostructures (µP/NanoSi): etching the µP in NaBF$_4$/AgNO$_3$ aqueous solution.*
- *Micropillars + silicon nanowires (µP/SiNW): nanowires growth on the µP surface.*
- *Deposition of Ag particles on the nanostructured surfaces and subsequent coating with SiO$_x$ overlayers (NanoSi/Ag NPs/SiO$_x$ and µP/NanoSi/Ag NPs/SiO$_x$).*
- *Double layer of silicon nanowires.*

All the processes used to realize these surfaces have been already described in the chapter 1. The double-scale structured surfaces have been prepared through a combination of these processes. They were then chemically modified with *1H, 1H, 2H, 2H-perfluorodecyltrichlorosilane (PFTS)*. The resulting surfaces were characterized using scanning electron microscopy (SEM).

Their wetting properties were evaluated using contact angle measurements (static, advancing, receding and hysteresis) with various liquids ($21.6 \leq \gamma \leq 72.2$ mN/m) as shown in Table 2.4, using a Drop Shape Analysis System (DSA100, Krüss GmbH Germany) (Appendix7). During the sliding experiments of the liquid droplet on the substrate, we assume that we are in a quasi-static state. Static contact angles are measured just after the liquid droplet deposition. While the advancing and receding angles are measured when the liquid droplet starts to move with the changing of wetting line. An error of $\pm 2°$ is assumed on contact angle computation and each measurement is operated 3 times. Furthermore, in some cases, when setting the tilting angle at

60°, no sliding has been observed, the droplet sticks to the surface. In that case the contact angle hysteresis θ_H is noted higher than 60°. Thus the maximum θ_H presented in the next section is voluntary set to 60°. It has to be noted that the rotation axis of the tilting table and the optical axis (corresponding to CDD camera) are the same. Thus on the images and video taken, the surface appears horizontal while the droplet shape is deformed. In this work, single side polished Si (100) P-type wafer (boron-doped, 0.009-0.01 Ohm-cm resistivity, (Siltronix, France) were used as substrates.

Liquids	γ (mN/m)
Water	72.2
Glycerol	63.4
Methylene Iodide	50.0
BMIM BF$_4$*	42.0
BMIM NTf$_2$*	32.0
Hexadecane	27.4
n-decane	23.8
n-octane	21.6

Table 2.4: Different liquids tested.

*BMIM BF$_4$: 1-butyl-3 methylimidazolium tetrafluoroborate, BMIM NTf$_2$: 1 -butyl-3 methylimidazolium Bis (trifluoromethanesulfonyl) imide, which are ionic liquids.

2.5.1. NanoSi, NanoSi/Ag and Nano/Ag/SiO$_x$ interfaces

This section deals with the wetting properties of surfaces based on NanoSi substrates prepared by metal-assisted etching method using NaBF$_4$/AgNO$_3$ aqueous solutions. The surfaces are characterized using CA and θ_H measurements.

2.5.1.1. Preparation and wetting properties of NanoSi interfaces

The fabrication of NanoSi interfaces was already described in chapter [1.3.2]. Briefly, the NanoSi substrates were prepared *via* metal-assisted etching method using NaBF$_4$/AgNO$_3$ (2 M/0.02 M) aqueous solution at 80°C for 120 min. The resulting NanoSi interfaces were

functionalized with PFTS (NanoSi-CF$_3$). The static CA for water and hexadecane was measured on these surfaces (Table 2.5). In comparison to a flat Si surface functionalized with the same molecule (PFTS) (water CA=120°, hexadecane CA=67°), NanoSi-CF$_3$ surface presents a higher non-wetting property with a higher CA for both liquids (water CA=160°, hexadecane CA=110°). The CF$_3$-terminated NanoSi surface is superhydrophobic with low contact angle hysteresis (θ_H ≈1°) and omniphobic with high contact angle hysteresis (θ_H >60°)

Contact angle	Flat Si	NanoSi
Water	120°	160°
Hexadecane	67°	110°

Table 2.5: Static CA for water and hexadecane on flat Si and NanoSi surfaces functionalized with PFTS.

2.5.1.2. Preparation and wetting properties of NanoSi/Ag NPs/SiO$_x$ interfaces

The deposition of silver nanoparticles (Ag NPs) onto the NanoSi substrate will allow the introduction of "re-entrant" angles at the microscopic scale. To do that, a freshly prepared NanoSi surface was dipped in an HF/AgNO$_3$ aqueous solution. Figure 2.15 indicates that the NanoSi substrate is totally covered by Ag NPs after its incubation in a 0.5 M HF/0.01 M AgNO$_3$ aqueous solution for 60 seconds. It is to be noted that the biggest nanoparticles (about 200 nm in diameter) are located at the top of each nanostructure whereas the smallest ones (about 50 nm) are located on the walls.
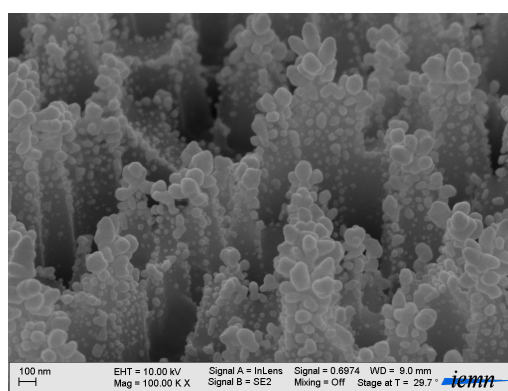
Figure 2.15: SEM image of Ag NPs deposited onto a NanoSi surface using 0.5 M HF/0.01 M AgNO$_3$ aqueous solution for 1 min.

However, it is difficult to perform the direct silanization of the NanoSi/Ag NPs surface compared to the flat silicon or other nanostructured silicon substrates. In fact due to the presence of Ag NPs, there are not enough hydroxyl groups available on the surface, required for the silanization reaction. To overcome this limitation, we deposited SiO_x overlayers on the NanoSi/Ag NPs interface using Plasma-enhanced chemical vapour deposition (PECVD) (Appendix 8). This leads to the formation of NanoSi/Ag NPs/SiO_x interfaces. The SiO_x overlayer totally coats the NanoSi/Ag NPs interface. By increasing the thickness of the SiO_x overlayer, the roughness is "hidden", leading to a "smoother" surface.

To control the size of the "re-entrant" structures, we have performed several Ag NPs depositions by varying [$AgNO_3$] (0.1, 0.05, 0.01 and 0.005 M) for a 60 seconds dip. A 30 nm-thick SiO_x layer was then deposited on the NanoSi/Ag NPs surfaces. The resulting NanoSi/Ag NPs/SiO_x interfaces were subsequently chemically modified with PFTS. Their SEM images are displayed in Figure 2.16. One can clearly sees that Ag dendrites appeared at 0.05 M $AgNO_3$, whereas big balls were observed for 0.1 M $AgNO_3$. For lower [$AgNO_3$] ($\leq$0.01 M), Ag NPs are formed on the top of the NanoSi substrate whereas smaller ones are localized on the walls. Subsequent coating with a SiO_x layer led to the formation of micro-scale mounds of lotus leaf like, as shown in the inset of Figure 2.9 (a)

The wetting properties of these surfaces are characterized by CA measurements for water and hexadecane as indicated in Table 2.6. All the interfaces are superhydrophobic (CA=160°) and present high omniphobic (114°<CA<125°) character. The best interface was obtained for 0.01 M $AgNO_3$ with water and hexadecane CA values of 160 and 125°, respectively.

Concerning the measurement of the contact angle hysteresis, all surfaces present a low θ_H for water ($\theta_H \approx 1$) and high θ_H for hexadecane (>60°).
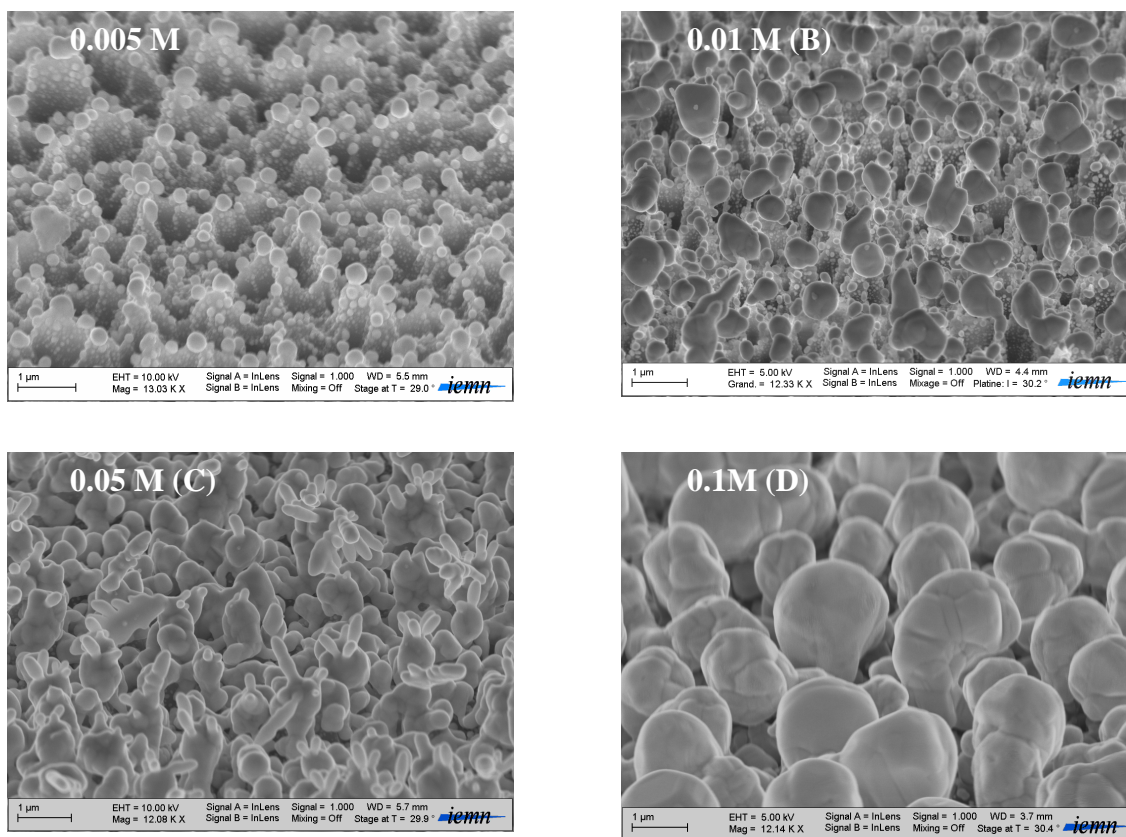
Figure 2.16: SEM images of NanoSi/Ag NPs interfaces coated with 30 nm-thick SiO$_x$ layer. The following conditions were used for Ag NPs formation:(A) 0.005M AgNO$_3$,(B) 0.01 M AgNO$_3$, (C) 0.05 M AgNO$_3$, and (D) 0.1M AgNO$_3$.

[AgNO$_3$] (mol/L)	Water CA (°)	Hexadecane CA (°)
0.005	160	114
0.01	160	125
0.05	160	118
0.1	160	118

Table 2.6: Water and hexadecane CAs on NanoSi/Ag NPs (for various [AgNO$_3$])/30 nm SiO$_x$ surfaces.

Based on this result, the influence of the SiO$_x$ layer thickness has been studied. SiO$_x$ layer of 10, 30, 50, 100 and 200 nm in thickness were deposited on the NanoSi/Ag NPs interfaces

(obtained with 0.01 M AgNO$_3$). Their SEM images are shown in Figure 2.17 and the CA values for water and hexadecane are summarized in Table 2.7
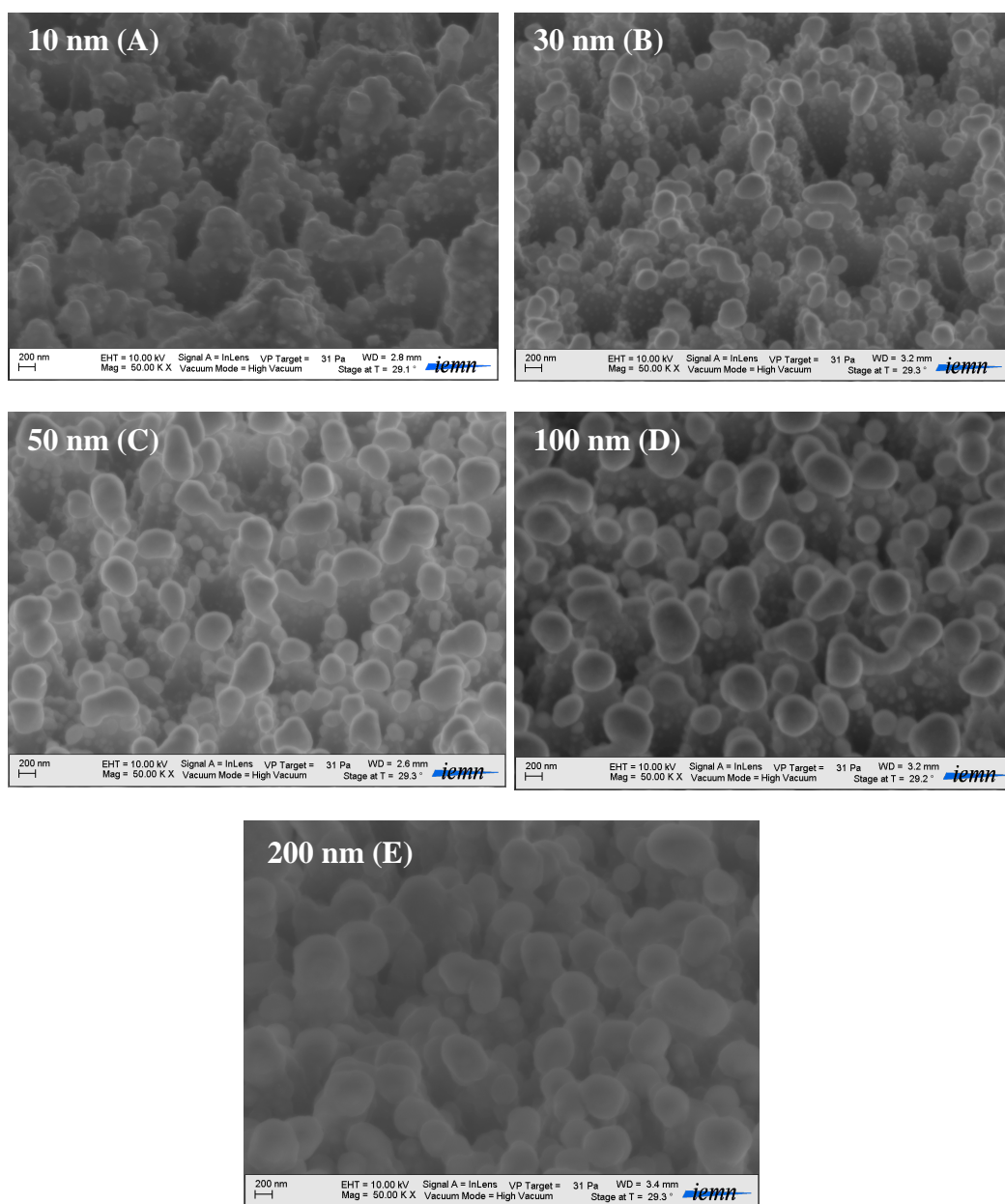
Figure 2.17: SEM images of NanoSi/Ag NPs surfaces coated with SiO$_x$ layers of different thicknesses: (A) 10 nm, (B) 30 nm, (C) 50 nm, (D) 100 nm, and (E) 200 nm.

SiO$_x$ (nm)	Water CA (°)	Hexadecane CA (°)
10	140	104
30	160	125
50	160	118
100	160	118
200	160	113

Table 2.7: Water and hexadecane CA on NanoSi/Ag NPs surfaces coated with SiO$_x$ layers of different thicknesses, from Figure 2.17.

When the NanoSi/Ag NPs interface is coated with 10 nm-thick SiO$_x$ layer, CA values measured for water and hexadecane are 140 and 104° with high θ_H *(>60°)*, respectively. Its liquid repellency ability is lower than that of NanoSi surface (water CA=160° and hexadecane CA=110°). We suggest that the 10 nm-thick SiO$_x$ layer may not be sufficient to cover all the interface of NanoSi/Ag NPs. Thus, the silanization with PFTS was not homogeneous, explaining the lower values of CA obtained on this interface.

For a 200 nm-thick SiO$_x$ overlayer, the ability of non-wettability of the surface decreased. While the interface is still superhydrophobic (water CA=160°), it has to be noted that the CA for hexadecane decreased to 113°. On the SEM image (Figure 2.17 (E)), we can easily observe that the NanoSi morphology has changed. Indeed, the nanostructured silicon surface was totally covered by the SiO$_x$ overlayer. In that case, a "smoothing effect" took place, i. e. the space between the nanostructures have been filled up by SiO$_x$, leading to the smoothing of the interface roughness. The roughness which has been introduced *via* Ag NPs deposition (re-entrant angles on top) is cancelled.

Concerning the NanoSi/Ag NPs coated with 50 and 100 nm-thick SiO$_x$ overlayers, their morphologies are quasi-similar to those coated with 30 nm-thick SiO$_x$ overlayer. Of course, the size of the nanostructures becomes larger when increasing the SiO$_x$ layer thickness (Figure 2.17 (B, C, D)). The interfaces display comparable values of CA for water (160°) and hexadecane (118°), as compared to the 30 nm SiO$_x$ overlayer (water CA=160°, hexadecane CA=125°).

2.5.1.3. Comparison of the wetting properties between flat Si, NanoSi and NanoSi/Ag NPs/SiO$_x$ surfaces

To compare the wettability behaviour of three interfaces: flat Si, NanoSi and NanoSi/Ag NPs/SiO$_x$ surfaces (the latter was prepared using 0.01 M AgNO$_3$ and 30 nm-thick SiO$_x$ overlayer), we have performed CA measurements on all surfaces for various liquids with $21.6 \leq \gamma \leq 72.2$ mN/m. Their static contact angles are displayed in Figure 2.18 and their contact angle hysteresis is summarized in Table 2.8 (the name of the liquids are presented in Table 2.4).
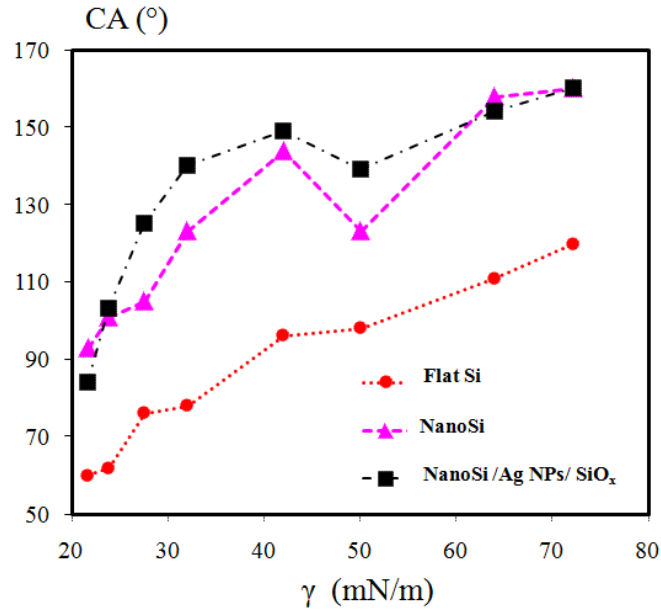
Figure 2.18: CA values as function of the surface tension-γ on three surfaces: flat Si (red points), NanoSi (pink triangles) and NanoSi/Ag NPs/SiO$_x$ (black squares).

γ (mN/m)	Contact angle hysteresis-θ_H (°)		
	Flat Si	NanoSi	NanoSi/Ag NPs/SiO$_x$
72.2	28	1	1
64	27		9
50	35		34
42	22	> 60	44
32	20		>60
27.4	28		
23.8	47		
21.6	45		

Table 2.8: Contact angle hysteresis (θ_H) for different liquids of $21.6 \leq \gamma \leq 72.2$ mN/m on flat Si, NanoSi, and NanoSi/Ag NPs/SiO$_x$ surfaces.

From Figure 2.18, it is clear that both NanoSi and NanoSi/Ag NPs/SiO$_x$ interfaces are superhydrophobic and display higher liquid repellency than the flat Si surface: (i) **NanoSi surface** is superomniphobic for liquids of $\gamma > 42.0$ mN/m with CA $\geq 140°$, except for CH$_2$I$_2$ ($\gamma = 50.0$ mN/m) with CA $= 123°$ (maybe due to high density of CH$_2$I$_2$), **(ii) NanoSi/Ag NPs/SiO$_x$ surface** repel all liquids of $\gamma > 34.0$ mN/m. Among the three tested surfaces, NanoSi/Ag NPs/SiO$_x$ has the highest CA, except with octane for which the CA is 10° lower than on NanoSi surface.

It is to be noticed that the NanoSi and NanoSi/Ag NPs/SiO$_x$ surfaces are non-wetting even though their Young contact angle is smaller than 90°. This phenomenon was also observed in various examples as mentioned above. [71] [72] [84] [85] [98]

On the other hand, we have measured the contact angle hysteresis-θ_H *via* the tilting angle experiment as shown in Table 2.8. The flat Si surface exhibits θ_H ranging from 20 to 50° even for water while the NanoSi surface displays a quasi-null θ_H for water and an important contact angle hysteresis for other liquids ($\theta_H \geq 60°$). Finally for the NanoSi/Ag NPs/SiO$_x$ surface, the value of θ_H is far much lower than those measured on the NanoSi surface. Rolling ball effect occurred for liquids of $\gamma \geq 64.0$ mN/m and θ_H is also higher than 34° for liquids of $\gamma < 64.0$ mN/m.

2.5.1.4. Summary

From the nanostructured surfaces presented in chapter 1, the coating with Ag particles and SiO$_x$ overlayers resulted in the formation of "re-entrant" features and improved the ability of non-wetting properties. Thus both NanoSi and NanoSi/Ag NPs/SiO$_x$ surfaces showed a superhydrophobic character with a quasi-null hysteresis. However, superomniphobicity was only obtained for some liquids: (i) γ ≥42.0 mN/m for NanoSi surface with high θ_H (≥ 60°), and (ii) γ ≥ 34 mN/m for NanoSi/Ag NPs/SiO$_x$ surface (two roughness levels) with high θ_H (≥ 34°) showing the interest to introduce re-entrant features on such NanoSi interfaces.

To further enhance the repellence ability of our surfaces, we will introduce a second level of structuration using micropillar silicon surfaces (µP), leading to double scale structured surfaces with micro- and nano-features.

2.5.2. µP, µP+ NanoSi and µP/NanoSi/Ag NPs/SiO$_x$ interfaces

In previous studies of our group, we have shown that µP surfaces have a low impalement threshold for water droplet, whereas a double structured surface (micro-nano) can achieve a very high resistance to impalement including low contact angle hysteresis [14] [66] [67]. Therefore, we have chosen µP with the same dimensions (10*5*10: diameter*spacing*height (µm)) in this study. Then, we introduced a second nanostructured layer (NanoSi and NanoSi/Ag NPs/SiO$_x$) on the µP surface, resulting in double micro-nano structured interfaces (µP/NanoSi, µP/NanoSi/Ag NPs/SiO$_x$). Their wettability is characterized below.

2.5.2.1. Preparation of µP, µP/NanoSi, and µP/NanoSi/Ag NPs/SiOₓ interfaces

The process for µP and µP/NanoSi surfaces fabrication were described in chapter 1 (1.2.6). Then, the µP+NanoSi surface was coated with Ag NPs by dipping in a 0.5 M HF/0.01 M AgNO₃ aqueous solution for 60 seconds at room temperature and then covered with 30 nm SiOₓ, as described above for the synthesis of NanoSi/Ag NPs/SiOₓ interfaces. This interface is called µP+NanoSi/Ag NPs/SiOₓ and its SEM image is shown in Figure 2.19.
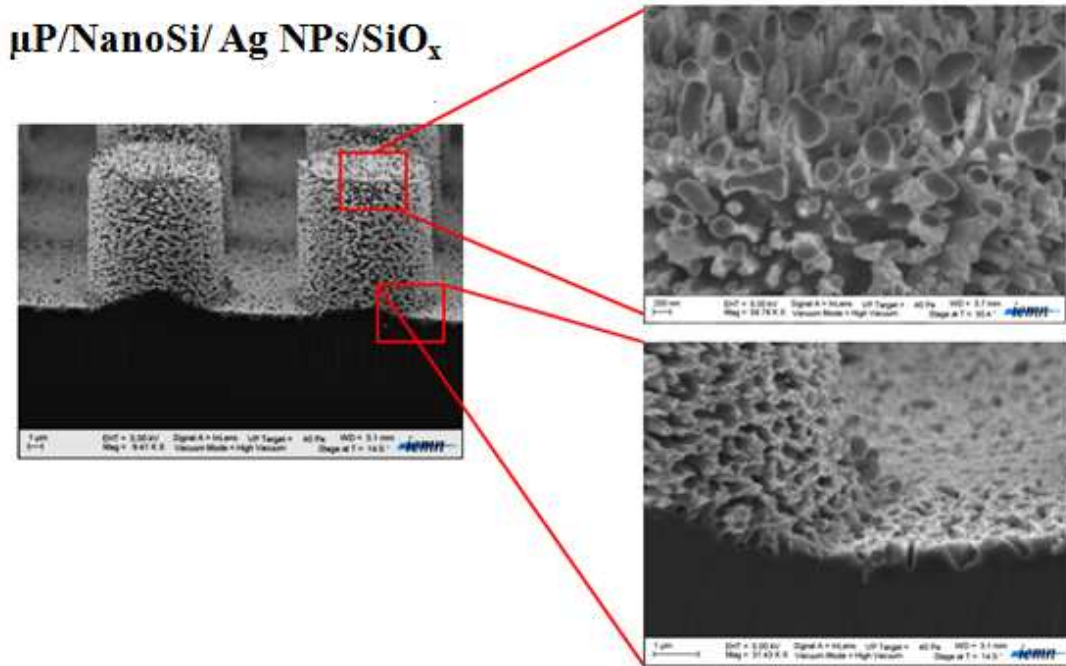
Figure 2.19: SEM images of µP/NanoSi/Ag NPs/SiOₓ interface.
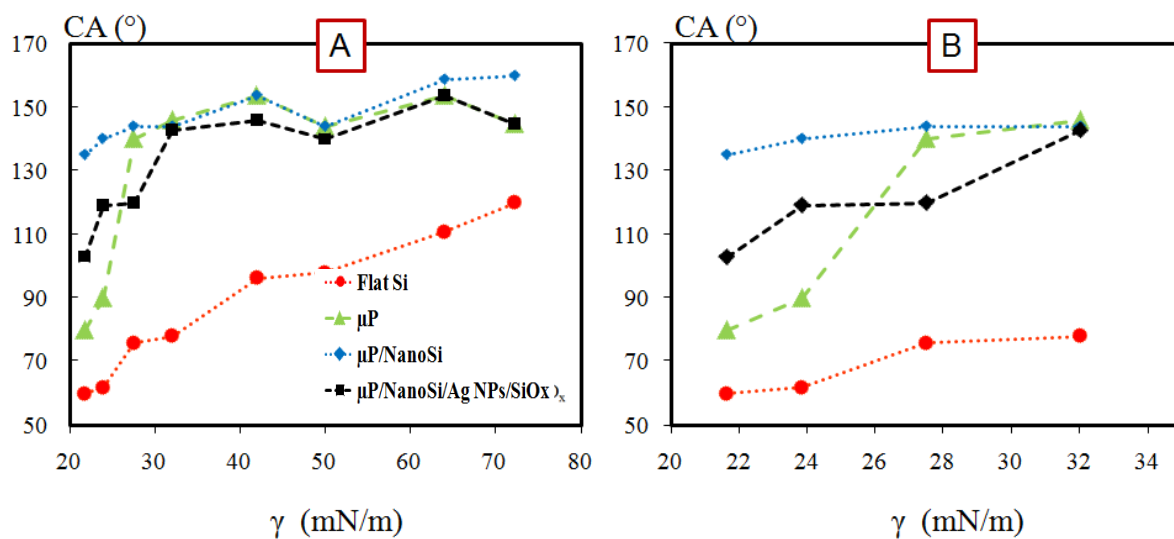
Figure 2.20: (A) Static contact angle (CA) as a function of the surface tension γ (mN/m) on four surfaces: flat Si (red points), μP (green triangles), μP/NanoSi (blue cubes), and μP/NanoSi/Ag NPs/SiO$_x$ (black squares) and (B) the zoom of A in 21.6 ≤ γ ≤32.0 mN/m.

γ (mN/m)	Contact angle hysteresis-θ$_H$ (°)		
	μP	μP/NanoSi/Ag NPs/SiOx	μP/NanoSi
72.2	42	37	1
64.0	42	53	1
50.0	40	> 60	49
42.0	39		45
32.0	>60		51
27.4			53
23.8			> 60
21.6			

Table 2.9: Contact angle hysteresis (θ$_H$) for different liquids of 21.6 ≤ γ ≤72.2 mN/m on surfaces: μP, μP/NanoSi and μP/NanoSi/Ag NPs/SiO$_x$.

2.5.2.2.   Wetting properties of µP, µP/NanoSi, and µP/NanoSi/Ag NPs/SiOₓ interfaces

The wetting properties of the three different surfaces (µP, µP/NanoSi and µP/NanoSi/Ag NPs/SiOₓ) have been evaluated using static CA measurements (Figure 2.20) and θ_H (Table 2.9) for different liquids of ($21.6 \leq \gamma \leq 72.2$ mN/m). The results are compared to the wettability behaviour of a flat Si surface.

Figure 2.20 displays the static CA of the following surfaces: flat Si (red points), µP (green triangles), µP/NanoSi (blue cubes), and µP/NanoSi/Ag NPs/SiOₓ (black squares). Their contact angle hysteresis values (θ_H) are displayed in Table 2.9. It is clear that all the three surfaces are more liquid repellent than a flat Si surface.

- First, µP exhibits surprisingly a superomniphobic character: the apparent CA reaches 140° for Young contact angles below 90°. However, this property is not achieved for liquids of $\gamma < 27.5$ mN/m (hexadecane) (Figure 2.20, green triangles). This phenomenon may not exist starting with a Young contact angle less than 90° if we assume a perfect and smooth pillar surface. Indeed in that case the structure would not enable contact line pining and should result in total wetting. However, a closer look at these structures points out a non perfect edge but rather ondulations evocating a re-entrant structure (Figure 1.24 in chapter 1). This can be explained by the successive passivation/etching steps when using DRIE technique. Large θ_H is observed, which in the case of pillars can be explained by contact line pining and deformation at the microscale. This effect should be theoretically lowered by the addition of a nanotexturation on the pillars. It has to be mentioned that for decane and octane, with γ as low as 23.8 and 21.6 mN/m, respectively, square shape droplet is observed proving the total impalement of the liquid inside the microstructuration with a huge θ_H (Figure 2.21).

- Following electroless etching, the CA increased for all liquids. Compared to µP surface, the µP/NanoSi surface showed a superomniphobic character (CA≈ 140°) for liquids of $\gamma > 21.6$ mN/m (Figure 2.20, blue cubes). Furthermore, µP/NanoSi interface displays a low θ_H (≈1°) for water and glycerol (Table 2.9), which is consistent with theoretical predictions. Indeed, the energy barrier during displacement of the contact line on pillars is lowered by the nanostructrures. However for low γ, the θ_H is high ($40° < \theta_H < 60°$).

- After coating with Ag nanoparticles, the surfaces exhibit both lower CA and higher θ_H than on µP/NanoSi and µPSi surfaces. This is probably due to the introduction of too

much defects that increase the pinning of liquid droplets even for water. We also can ascribe these limitations to a probable role played by the vertical profile of the micropillars. While it is clear that the nanostructuration can be seen both on the top and on the side of the micropillars, the Ag NPs may not be distributed in the same manner on the top and on the side, leading to droplet pinning more easily on the side of the micropillars.

Figure 2.21 shows SEM images of a polydimethylsiloxane (PDMS) droplet deposited on µP, µP/NanoSi, and µP/NanoSi/Ag NPs/SiO$_x$ interfaces. PDMS is an organic polymer with $\gamma \approx 27.0$ mN/m. The SEM images suggest a Wenzel state of the PDMS droplet on µP/NanoSi/Ag NPs/SiO$_x$ and µP interfaces, whereas a Cassie-Baxter state is observed on µP/NanoSi interface. This confirms that µP/NanoSi displays higher non-wettability behaviour than others and a superomniphobic interface in a Cassie-Baxter state can display a high θ_H for low surface tension liquids.
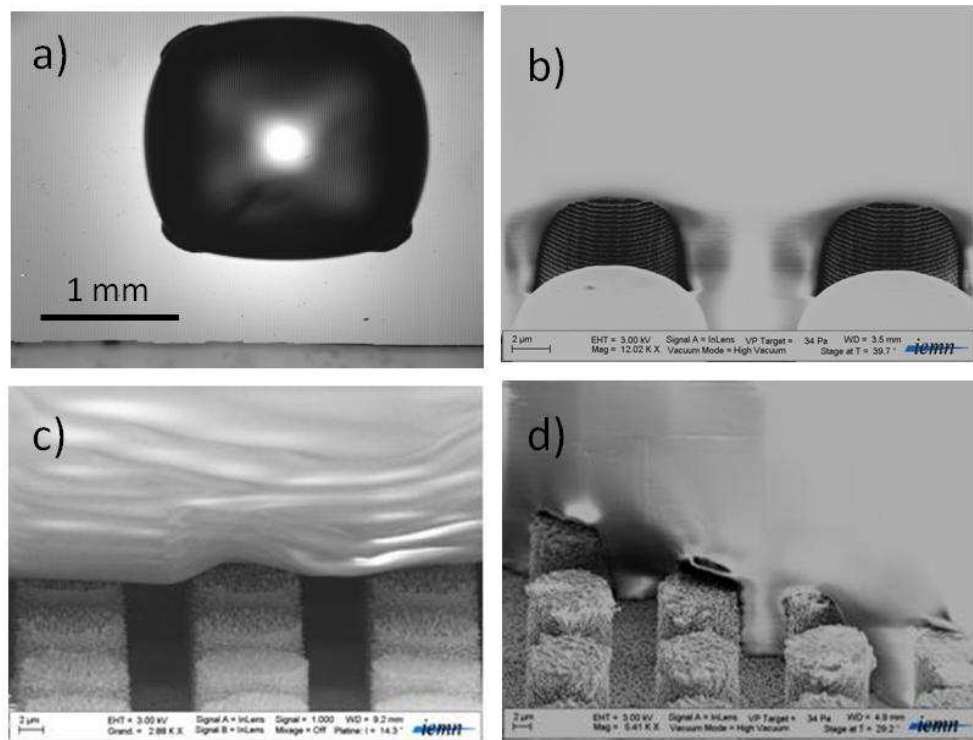
Figure 2.21: Optical and SEM images of a PDMS droplet on different surfaces: a) and b) square shape and total impregnation on µP, illustrating a Wenzel state, c) µP/NanoSi, and d) µP/NanoSi/Ag NPs/SiO$_x$.

2.5.2.3.   Summary

Our previous studies suggest that a micro or a nanotexturated silicon surface always leads to a higher CA whatever the tested liquid, as compared to a flat silicon surface.

The combination of NanoSi and µP (µP/NanoSi) improved the non-wettability behaviour by increasing the CA for all liquids tested particularly, preventing the CA decrease for liquids of low surface tension. Additionally, µP/NanoSi displayed a quasi null hysteresis for liquids of $\gamma \geq$ 64.0 mN/m, but for lower γ, the value of θ_H is still high.

Unfortunately, the combination of NanoSi/Ag NPs/SiO$_x$ and µP surfaces deteriorated the non-wetting properties, as compared to µP/NanoSi and even µP interfaces (lower static CA and higher θ_H). This unexpected result is perhaps due to the presence of too much defects.

Consequently, the integration of a second structure into the structured surface leads to an increase of the roughness that can improve their ability of liquid repellency, if the addition of the structure creates a "re-entrant" geometry. However, the presence of re-entrant curvature is not a sufficient condition to develop a high liquid-repellent surface. If the creation of a double structured surface is accompanied with so many defects, the repellent property of the surface is reduced.

The inherent limitation of the employed technology (wet attack) is the length of the realized nanostructures to about few micrometers. Clearly, even if this rapid, low cost and simple process gives high contact angle and low hysteresis for high surface tension liquids, it is quite limited for low surface tension liquids.

In the next section, we will report in more detail on the fabrication of SH and SO surfaces based on silicon nanowires (SiNWs) grown *via* the VLS growth mechanism. Different surface morphologies were developed by changing the growth parameters such as pressure, temperature and time. Each nanowire has smaller dimensions (diameter ranging from 80 to 150 nm) than the silicon nanostructured (NanoSi) substrate presented above. Their wetting properties were investigated using previous molecules with $21.6 \leq \gamma \leq 72.2$ mN/m through static CA and θ_H measurements. All data were compared to µP/NanoSi interface (the best non-wetting surface obtained in this section).

2.5.3.   Silicon nanowires interfaces

2.5.3.1.   Preparation of Silicon nanowires interfaces

Silicon nanowires-VLS have been synthesized on flat and µP silicon surfaces as already described in chapter 1 (section 2.2). In this section, five types of silicon nanowires (VLS1, µP+VLS1, VLS2, µP+VLS2, and VLS3) are investigated for the preparation of SH and SO surfaces. Their morphologies have been characterized by SEM (Figure 2.22):

- ✓ *VLS1: It consists of one-layered texture of nanowires of 7 µm in length. Most of the nanowires are straight and have an orientation ranging from 30 to 80° with respect to the horizontal plane.*
- ✓ *VLS2: It comprises a dense lower layer of tangled nanowires of 25 µm in length and a top layer of nanowires of straight wires of 20 µm in length with the orientation about of 80° with respect to the horizontal plane.*
- ✓ *VLS3: It comprises a dense lower layer made of 2 µm short entangled nanowires with few straight wires with 7 µm in length. In this case, the orientation is more irregular and the average angle with the horizontal is smaller compared to VLS1.*
- ✓ *µP+VLS1: Silicon micro pillars (µP) (10* 5 * 10) covered by VLS1 nanowires.*
- ✓ *µP+VLS2: Silicon micro pillars (µP) (10* 5 * 10) covered by VLS2 nanowires.*

It has to be noted that the apparent VLS2 and µP+VLS2 surface morphologies are the same because in that case, the silicon nanowires (45µm of total thickness) have completely covered the silicon micropillars, leading to their disappearance under this thick layer of wires.
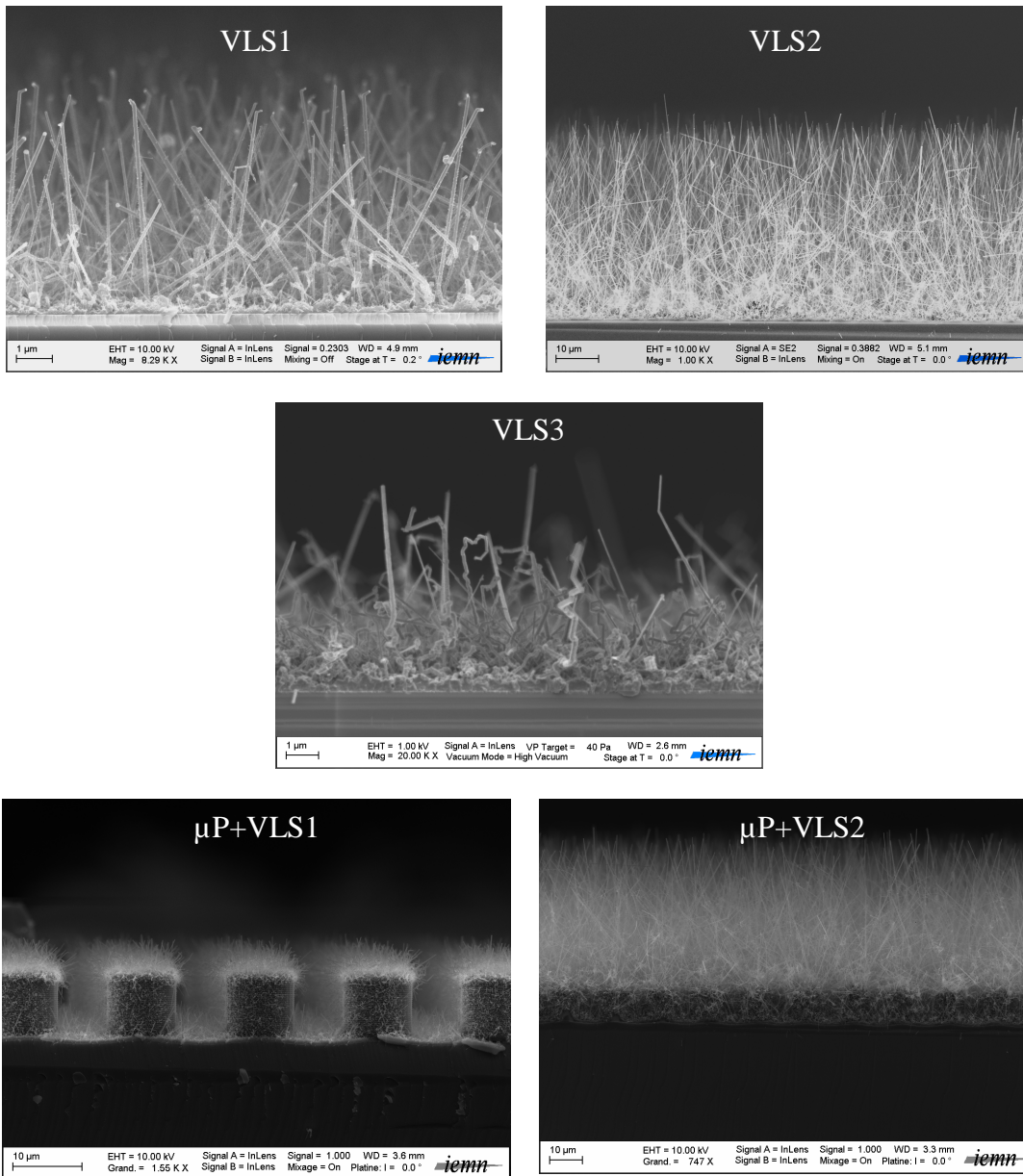
Figure 2.22: SEM images of the silicon nanowires surfaces: VLS1, VLS2, VLS3, µP+VLS1 and µP+VLS2.

2.5.3.1. Wetting properties of the silicon nanowires interfaces

After PFTS modification, the SiNWs surfaces were characterized by static CA (Figure 2.23) and contact angle hysteresis-θ_H (Table 2.10) measurements and compared to µP/NanoSi surface.

Static contact angle (CA)

Figure 2.23 displays the static CA values measured on the flat Si (red points), VLS1 (yellow-white cubes), µP+VLS1 (green points), VLS2 (red-white triangles), µP+VLS2 (blue squares), VLS3 (black triangles), and µP/NanoSi (black-white points). It is clear that:

- All of these surfaces show a CA decrease from 160° to 140° until a surface tension of 27.4 mN/m. However, it has to be noted that µP+VLS1 shows a slightly higher CA than VLS1.

- For lower surface tension liquids, the CA decreases down to 98°, 110°, 125°, 126°, 96° and 135° for VLS1, µP+VLS1, VLS2, µP+VLS2, VLS3 and µP-NanoSi for γ = 21.6 mN/m (octane), respectively.

- To summarize, the best results, in terms of static contact angle, were obtained for the µP-NanoSi interface followed by those corresponding to VLS2 and µP+VLS2, which display similar CA due to their identical surface morphologies, as already mentioned above. Concerning the VLS1 and µP+VLS1, we can see that the presence of micropillars have slightly improved the static contact angle values for all the tested liquids.
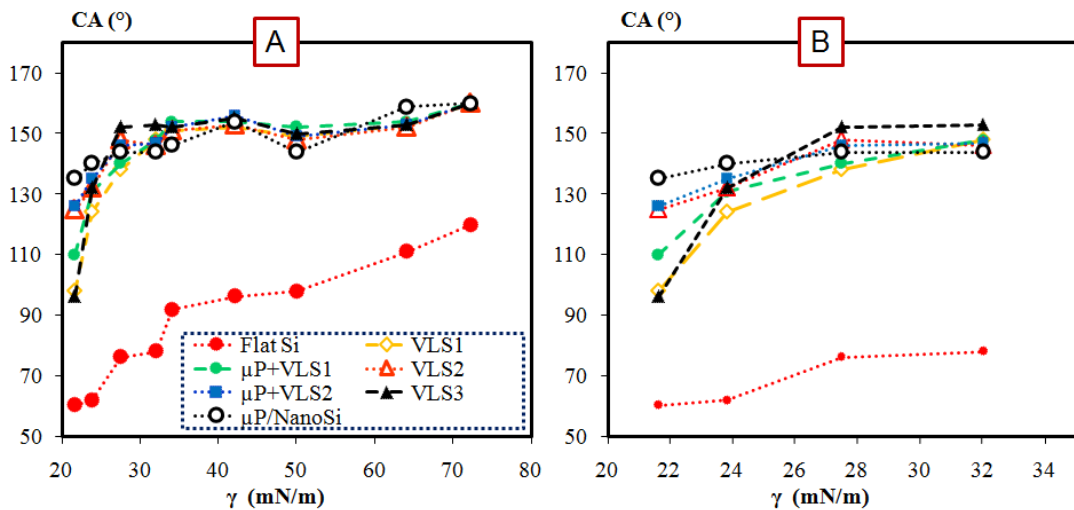
Figure 2.23: (A) Static CA for different liquids (21.6 ≤ γ ≤72.2 mN/m): Flat Si (red points), VLS1 (yellow-white cubes), µP+VLS1 (green points), VLS2 (red-white triangles), µP+VLS2 (blue squares), VLS3 (black triangles), and µP/NanoSi (black-white points), and (B) the zoom of A in 21.6 ≤ γ ≤32 mN/m.

97

γ (mN/m)	Contact angle hysteresis-θ_H (°)					
	VLS1	**µP+VLS1**	**VLS2**	**µP+VLS2**	**VLS3**	**µP/ NanoSi**
72.2	≈1	≈1	≈1	≈1	≈1	≈1
64.0						
50.0						49
42.0						45
32.0	38	29	15	14		51
27.4	>60	49	18	17	8	53
23.8		>60	>60	>60	>60	>60
21.6						

Table 2.10: Contact angle hysteresis (θ_H) for different liquids with $21.6 \leq \gamma \leq 72.2$ mN/m on surfaces: VLS1, µP+VLS1, VLS2, µP+VLS2, VLS3, and µP/NanoSi.

Contact angle hysteresis- θ_H

Interestingly, Table 2.10 displays the θ_H values corresponding to the surfaces shown in Figure 2.23. We observe that:

- All silicon nanowires-based interfaces exhibit lower θ_H than the µP-NanoSi, which has high θ_H ($> 45°$) for most liquids, except for water and glycerol with $\theta_H = 1°$.

- The θ_H of µP+NanoSi increased brutally at $\gamma = 50.0$ mN/m to a value of 49° and then, slowly increases until $\theta_H > 60°$ ($\gamma = 23.8$ mN/m).

- For the silicon nanowires-based interfaces, very low θ_H values are calculated for $\gamma > 42.0$ mN/m.

- However for $\gamma < 42.0$ mN/m, some differences, in terms of θ_H values, have appeared and are related to the difference in surface morphologies. Indeed, the θ_H increases brutally to 38 and 29° for VLS1 and µP+VLS1, respectively for $\gamma = 32.0$ mN/m whereas the θ_H values are still lower with 15 and 14° for VLS2 and µP+VLS2, respectively. For VLS3 surface, the θ_H are still quasi-null ($\theta_H = 1°$).

- Then, the θ_H of VLS1 increases to a value >60° for γ =27.4 mN/m whereas the µP+VLS1 displayed a θ_H value >60° only for γ =23.8 mN/m with a θ_H = 49° for 27.4 mN/m. Here, the micropillars seem to slightly improve the θ_H for liquids of γ < 32.0 mN/m. However, the θ_H values of VLS2 and µP+VLS2 are 18 and 17°, respectively for γ =27.4 mN/m and increased for decane and octane to values >60°. While VLS3 still displays a low θ_H of 8° for γ =27.4 mN/m; this value also increases to values >60° for γ < 23.8 mN/m.

A comparison between the different surfaces suggests some clues towards the optimal strategy to reach both a high CA and a low θ_H for most liquids, including those of low surface tension. Herein, we suggest that the threshold of surface tension- γ_C below which the θ_H sharply increases and higher than 10°, is a relevant indication of the quality of the super-omniphobicity of a surface: it has to be as small as possible for a better omniphobic character:

- *µP/NanoSi surface: 50.0<γ_C<64.0 mN/m.*
- *VLS1, µP+VLS1, VLS2, and µP+VLS2 surfaces: 32.0<γ_C<42.0 mN/m. Because θ_H of VLS2 (or µP+VLS2) is smaller than that of VLS1 and µP+VLS1 for these liquids of 32.0<γ <42.0 mN/m, thus it can be sure that the γ_C value for VLS2 is lower than for VLS1 or µP+VLS1 surfaces.*
- *VLS3 surface: 23.8 <γ_C< 27.4 mN/m.*

2.5.3.2. Summary

We have successfully prepared SH and SO surfaces using different micro or nanostructures or their combination. Their wetting properties (CA and θ_H) depend strongly on the morphology of the micro- and nano-texturation. The ones with the best repellency performance with most of the liquids have a double layered structure: nanoscale-nanoscale - VLS2 and VLS3. We will use these surfaces for performing droplet impact experiment in the next section. Whereby measuring the pressure threshold, it allows evaluating the value of surface tension threshold (γ_C) and quantifying the non-wettability behaviour.

2.5.4. Measurement of pressure threshold

We used a dripping faucet that releases a drop of a liquid (water, hexadecane, mix of water and ethanol…) from a sub-millimetric nozzle. The drop is released from the nozzle under the action of gravity, which overcomes the capillary retention forces. Hence, the diameter of the

drop is determined by the capillary diameter and is well reproducible at d=2.6 mm. The speed of the droplet corresponds to the law of free fall:

$$V = \sqrt{2gh} \ \textbf{(2.13)}$$

Where h is the height of fall and g is the acceleration due to the gravity, then the threshold pressure is determined by this equation: $P_C = \rho V^2$ (ρ is the density of the liquid, and V is the speed of drop in accordance with Equation 2.13).

Using backlighting together with a high-speed camera (at a maximal rate of 4700 frame/s with a resolution of 576x576), the shape of the interface during the spreading and bouncing processes can be determined. The magnification allows a resolution of 15µm per pixel. The height of fall-h was larger by increasing the distance between the nozzle and the surface. This displacement is performed until the drop impalement threshold, i.e. the drop bounced partially with a small impalement. As an example, Figure 2.24 displays successive snapshots showing the impact of drop (water+ethanol (70/30)) on the silicon nanowires surface with the impalement threshold. On images 7 and 8, we can see a partial drop which is stuck after bouncing on the surface.
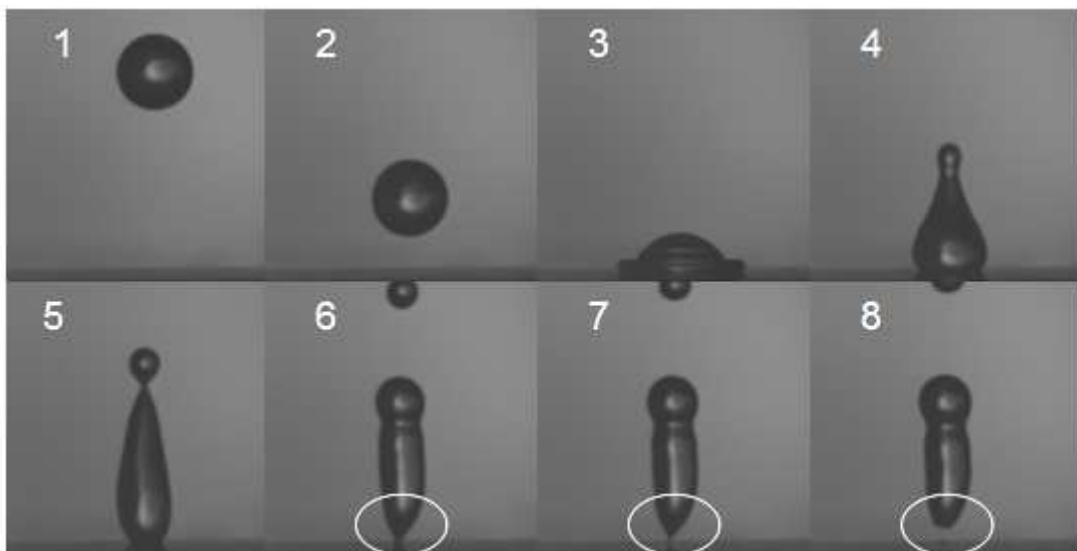
Figure2.24: Successive snapshots showing the impact and the bouncing of a drop (Water+ethanol 70/30) over the silicon nanowire surfaces followed by impalement.

In practice, it is important to notice that the viscosity of the liquid (ν) has a great influence on the dynamics of spreading and bouncing phases, while the use of non-viscous liquids such as water leads in most of the cases, to a droplet atomization, i. e. the main drop is divided into many smaller droplets during the spreading phase (especially at high impact velocity). In the section above, among the liquids used for measuring the CA, some of them are so viscous (glycerol, ionic liquids: BMIM-BF4 and BMIM-NTf2) that their drops haven't bounced on the surface although they haven't been impaled. Thus, it is difficult to observe the threshold impalement for such liquids. It is the reason why we choose moderately viscous liquids of the order of a few mm^2/s, to avoid the undesirable mentioned effects. Table 2.11 shows the list of the investigated liquids with their physical properties (density-ρ, viscosity-ν and surface tension- γ).

Liquids	Density (ρ g/cm^3)	Viscosity (ν mm^2/s)	Surface tension (γ mN/m)
Water	1.00	1.00	72.2
Water+Glycerol (50/50)	1.126	4.93	67.4
Water + Ethanol (95/05)	0.988	1.42	59.6
CH$_2$I$_2$	3.32	2.26	50.0
Water + Ethanol (85/15)	0.973	2.23	45.2
Water + Ethanol (70/30)	0.951	2.47	33.0
Water + Ethanol (50/50)	0.910	2.20	27.9
Water + Ethanol (38/62)	0.882	1.98	26.0
Water + Ethanol (35/65)	0.871	1.89	25.6

Table 2.11: Physical properties of the investigated liquids.
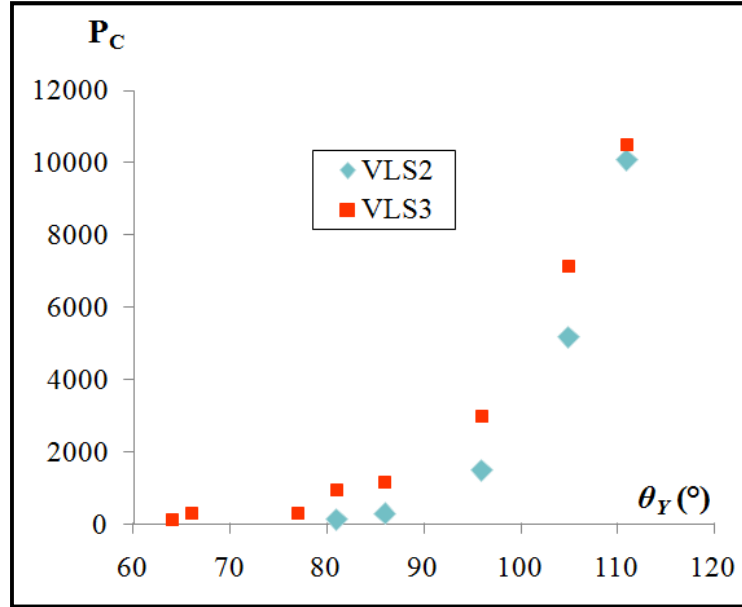
Figure 2.25: Pressure threshold for liquid impalement versus the Young's contact angle (θ_Y) for VLS2 (blue cubes) and VLS3 surfaces (red squares).

Figure 2.25 shows that the critical pressure threshold P_C versus Young's contact angle (θ_Y) for VLS2 (blue cubes) and VLS3 (red squares) surfaces. Whatever the liquid used, the pressure threshold is always higher for the VLS3 surfaces. This plot is the confirmation of the high robustness of SiNWs surface against liquid impalement, even for liquids of low surface tensions with $\theta_Y < 90°$. Although the phenomena are indicated being not possible by the Wenzel and Cassie-Baxter theories. However, this robustness tends to deteriorate for highly wetting liquids. The influence of the nanowires orientation on the robustness can seemingly be counter intuitive. In practice, the nanowires on the top of VLS2 layer are straight vertical while the nanowires of VLS3 grow diagonally, leading to a disordered structure as mentioned above (Figure 2.22). Here, we suggest that straight vertical nanowires do not offer the best robustness. Therefore, VLS3 surface is more robust than VLS2 surface.

On the other ones, each surface has a limit in surface tension (as discussed above), which is called the surface tension threshold - γ_C. In our case, the values of γ_C are about 33 and 25.6 mN/m for VLS2 and VLS3 surfaces, respectively. If the liquid has a surface tension being smaller than γ_C, this liquid drop spontaneously gets impaled into the structures. It means that the capillary pressure itself is large enough to overcome the pressure threshold: $P_c < \dfrac{2\gamma}{R}$ (where γ is the surface tension of liquid and R is the radius of liquid drop) [64]. We suggest if the surface tension threshold - γ_{AC} of the surface A is smaller than γ_{BC} of the surface B: $\gamma_{AC} < \gamma_{BC}$. Their

repellence ability of liquid - depends on the nature of liquid i.e. the surface tension- γ as following:

- If $\gamma_{AC} < \gamma < \gamma_{BC}$ the surface A is more robust than surface B i.e. the quality of liquid-repellency of surface A is better than surface B

- If $\gamma < \gamma_{AC} < \gamma_{BC}$, the liquid is impaled into the structures of both surfaces A and B with a different rate. The liquid goes more quickly into the structures of the surface A than the surface B. It implies that the static CA of the surface B is larger than that of surface A. Hence, it can explain why the VLS3 surface (γ_{AC} =26) is more robust than VLS2 surface (γ_{BC} =33) while VLS3 surface presented lower CA for liquids of γ <26.0 mN/m than VLS2 interface, for example, the case of n-decane (γ =23.8 mN/m) and n-octane (γ =21.6 mN/m) (see Figure 2.23).

2.6. Conclusion

In this chapter, we prepared SH and SO surfaces, consisting of simple or double structured surfaces using different techniques: lithography, electroless-etching, growth of nanowires using the VLS (vapour-liquid-solid) growth mechanism... The wettability of the resulting surfaces is characterized by measuring the static contact angle and contact angle hysteresis. Furthermore, their robustness was investigated by carrying out drop impact experiments. Their wetting properties depend strongly on the morphology of the micro- and nano-texturation. A part of this work was published in Langmuir in 2010 (see ref [64]).

To summarise the CA and θ_H measurements on various surfaces, Table 2.12 displays two values of surface tension thresholds: one applies for CA>140°, the other one applies for θ_H <10°. It is noted that:

- **Concerning the static CA:** The value of surface tension threshold for CA>140° decreases from microscale to nanoscale structure. The double structured surfaces show always better liquid repellency than simple structured surfaces. The best repellent surface consists of a double micro-nanoscale structured substrate.

- **Concerning the θ_H:** The value of surface tension threshold for θ_H <10° is lower for structures of small sizes. The nanowire-based interfaces showed the highest non-wetting properties, particularly the nanowires surface comprising a double layer. Compared to the first reported super-omniphobic surfaces by Tuteja *et al.* [71] [72] we demonstrated that surfaces with a robust

character can be obtained without a re-entrant shape such as VLS1, VLS2, and VLS3 surfaces. The challenge is now to understand the reason of this robustness, given the geometrical complexity of the nanowire carpet.

🔸 **All the tested surfaces with double structures** and based on silicon nanowires can be considered as omiphobic due to their high contact angle and robustness even for very low surface tension liquids. However, it is not yet clear whether it is the average orientation or the relative disorder of the SiNWs that contribute to a better robustness. Future studies will be focused on elucidating these points.

Surfaces	Surface tension threshold for CA>140°	Surface tension threshold for θ_H <10
Microstructure	$32.0 < \gamma \leq 42.0$ mN/m	$64.0 \leq \gamma \leq 72.2$ mN/m
Nanostructure	$27.4 < \gamma \leq 32.0$ mN/m	$50.0 \leq \gamma \leq 64.0$ mN/m
Micro & nanostructure	$21.3 < \gamma \leq 23.8$ mN/m	
Nanowire	$27.4 < \gamma \leq 32$ mN/m	32.0 mN/m $\leq \gamma$
Micro & Nanowire	$23.8 \leq \gamma \leq 27.4$ mN/m	
Nanowire double layer		$23.8 \leq \gamma \leq 27.4$

Table 2.12: The value of surface tension threshold for CA>140° and θ_H <10.

On the other hand, concerning the evaluation of surface tension threshold by droplet impact experiment (γ_C), we presented the first quantitative measurement of robustness of a superomniphobic surface, for various liquids of different surface tension. The most significant result of our study is that the meaningful parameter for the robustness is the cosine of Young's contact angle that a liquid drop adopts on a smooth surface of the same hydrophobic coating layer.

3. New Surface-Assisted Laser Desorption/Ionization Mass Spectrometry interfaces based on silicon nanostructures

3.1. Introduction

Mass spectrometry is a powerful tool used in biological research and organic synthesis owing to its very high sensitivity and resolution. Indeed, it has become a key technology in the area of proteomics. Mass spectrometry allows determining the presence of analytes, the exact mass of unknown analytes, structural information of the analytes, the presence of post-transductional modifications (PTM) such as phosphorylation, methylation, acetylation, detection of explosive and forensic…. [24]

In this analytical method, the analytes should be first ionized prior to their mass spectrometry analysis. To perform such ionization, different mechanisms exist and involve electron ejection, electron capture, cationization, protonation, and deprotonation. Then, these ions are electrostatically directed into a mass analyzer where they are separated as a function of their mass-to-charge ratio (m/z), and finally detected. The obtained results give the molecular mass and structural information [57] [109] [110] [111] [112].

The development of mass spectrometry is strongly related to the evolution of the ionization source. The first ionization source was Electron Ionization (EI) discovered in 1921 by Dempster. In this method, fast-moving electrons remove an electron from the neutral molecule resulting in molecular ion M^+. EI method is suitable for the analysis of small hydrophobic and thermally stable molecules (<400 Da). There is another common ionization method which is the chemical ionization (CI). In this method, a reactive ion such as CH_5^+ or NH_4^+ transfers a proton to the sample molecule (M), leading to the creation of $[M+H]^+$ ion. In both EI and CI methods, the sample molecule is originally in the gas phase [113]. Thus, these methods are restricted to the analysis of non-volatile sample molecules leading to limited applications in the field of biological chemistry. To overcome these restrictions, there are other ionization sources or methods which have been developed such as fast atom bombardment (FAB), secondary ion mass spectrometry (SIMS), laser desorption/ionization (LDI), and electrospray ionization (ESI). Among these methods, the most commonly used methods for biomoleculars mass spectrometry analysis are LDI and ESI, which produce charged intact biomolecules (they are called the softest ionization methods). In comparison to other ionization sources, LDI and ESI allow mass spectrometry analysis of a wide range of compounds with high sensitivity from pico to femtomole levels. [110] [113]

In ESI method, a certain volume of the liquid sample containing the molecule of interest is introduced into the mass spectrometer by a metal nozzle, which is maintained at a potential

between 700 and 5000V. Thus, the sample droplet is charged and heated until evaporation of the solvent. Then, the ions are formed at atmospheric pressure and are electrostatically directed into the mass analyzer. The advantage of ESI method is that it can detect sample molecules having a mass ranging from 10 000 to 70 000 Da. This method is easily adapted to liquid chromatography technique (LC) and numerous laboratories are equipped with LC-MS instruments with ESI as ionization method. However, ESI technique also presents some disadvantages. Firstly, it requires a sample of high purity. Secondly, ESI method is not very sensitive for analysis of complex mixtures. Finally, the sensitivity of ESI method is reduced in the presence of salts and thus requiring a desalting step.

In the LDI method, the sample containing the molecules of interest is introduced into the mass spectrometer by the sample plate. Then, they are desorbed and ionized thanks to the presence of an organic matrix or surface-assisted, playing the role of an absorbing material, and to the irradiation of a laser beam, corresponding to the two mains techniques: matrix-assisted laser desorption/ionization **(MALDI)** and surface-assisted laser desorption/ionization (**SALDI**).

MALDI-MS technique always requires an organic matrix, which is mixed with the analytes and provides energy for desorption/ionization of analytes after laser irradiation. This technique is suitable for the analysis of samples of high molecular weights (<300.000 m/z). However, it is difficult to identify analytes having low molecular weights (<700 m/z) due to the strong background signal from the matrix itself. [6] [115] [116] [117] [118] [119] To overcome this drawback, SALDI-MS method has been developed. Instead of using an organic matrix, this method employs an inorganic material to perform the LDI step. Thus, SALDI-MS technique can be used for analysis of small molecules (<700 m/z). Desorption/Ionisation on Silicon-MS (DIOS-MS) technique is a type of SALDI-MS based on silicon material. In practice, SALDI-MS or DIOS-MS techniques are complementary to MALDI-MS. Thus, prior to the presentation of the principle of SALDI-MS and DIOS-MS methods, it is necessary to describe more precisely the MALDI-MS technique [120] [121] [122] [123]

This chapter will first focus on general aspects of mass spectrometry with a short description of the instrument, followed by a description of the MALDI-MS technique. Issues of interest include a SALDI review method and the desorption/ionization mechanism. Finally, we will detail DIOS method, which is a special case of SALDI using silicon micro/nanostructured surfaces.

In this work, all the DIOS-MS analysis have been performed at IBL (Institute of Biology of Lille, UMR-8161) in the "Groupe Chimie des Biomolécules" led by Oleg Melnyk (DR-CNRS).

3.2. Mass spectrometry

Generally, the basic components of a mass spectrometer include a sample inlet, an ionization source, a mass analyzer and an ion detector as shown in Figure 3.1. [110] [119]
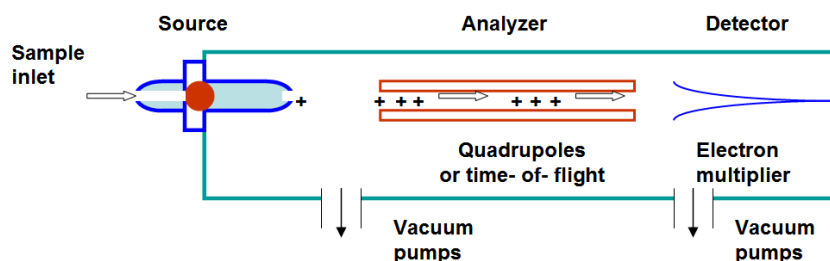
Figure 3.1: Schematic illustration of a mass spectrometer set-up. [110]

3.2.1. Sample inlet and ionization source

Sample inlet is a way for introducing a sample into the mass spectrometer. There are two main techniques: one is a direct insertion by using a probe or plate containing the sample molecule whereas the other one is a direct infusion of the sample molecule using a simple capillary or a capillary column. Normally, the method of sample inlet must be suitable with the ionization sources.

Ionization source: There are different ionization sources which can be classified in two main types: one is a **hard ionization source** generating fragment ions from the initial sample molecules such as: electro ionization-EI, chemical ionization-CI. The other one is a **soft ionization source** generating charged intact sample molecules such as: Fast Atom Ion Bombardment-FAB, Electrospray Ionization-ESI, Atmospheric Pressure Chemical Ionization-APCI, Matrix-assisted Laser Desorption/Ionization-MALDI, Surface-assisted Laser Desorption/Ionization-SALDI. Their advantages and disadvantages are compared in Table 3.1 adapted from Siuzdak *et al*.

Ionization source	Event	Mass (Da)	Matrix interference	Degradation	Complex Mixtures	Sensitivity
ESI	Evaporation of charged droplets	70,000	None	None	Limited	> fmol
Comments: Excellent coupling with liquid chromatography technique (LC/MS tool); low salt tolerance (millimolar); multiple charging usefull, but significant suppression with mixture occurs; low tolerance of mixtures; soft ionization (little fragmentation observed)						
APCI	Corona discharge and proton transfer	1,200	None	Thermal degradation	Somewhat amenable	>fmol
Comments: Excellent LC/MS tool; low salt tolerance (millimolar); uselful for hydrophobic material						
MALDI	Photon absorption/ proton transfer	300,000	Yes	Photo degradation	Good	<fmol
Comments: Possible LC/MS tool; low salt tolerance; excellent sensitivity; soft ionization (little fragmentation observed); photo degradation; suitable for complex mixtures; matrix background can be a problem for low mass ions.						
SALDI	Photon absorption/ proton transfer	3,000	None	Photo degradation	Good	< fmol
Comments:Possible LC/MS tool; low salt tolerance; excellent sensitivity; soft ionization (little fragmentation observed); photo degradation; suitable for complex mixtures and small molecules						
FAB	Ion desorption/ proton transfer	7,000	yes	Thermal degradation	Somewhat amenable	nmol
Comments: Relatively insensitive; little fragmentation; soft ionization; solubility with matrix required						
EI	Electron beam/ electron transfer	500	None	Thermal	Very limited	pmole
Comments: Good sensitivity; unique fragmentation data generated; thermal decomposition a major problem for biomolecules; limited mass range due to thermal desorption requirement						
CI	Proton transfer	500	None	Thermal	Limited	pmole
Comments: Offers a softer ionization approach over EI yet still requires thermal desorption; negative CI particularly sensitive for perflourinated derivatives; a limited but powerful approach for certain derivatized molecule such steroids						

Table 3.1: Different ionization sources (adapted from ref. [110], pp35).

3.2.2. Analyzer and detector

a) Analyzer

The first analyzer which has been developed used a magnetic field for the separation of ions. Then, the evolution of technologies has led to the development of new analyzers increasing the resolution of detection. There are different analyzers such as: quadrupole, ion-trap, time-of-flight, magnetic sector, and Fourier-transform ion cyclotron resonance mass analysis (FTMS), Time-of-Flight reflectron, Quadrupole-ToF. Table 3.2 gives a general comparison of the main mass analyzer types. [110]

Quadrupole

A Quadrupole[*] is a mass analyzer that uses an electric field to separate ions. The Quadrupole consists of 4 parallel rods/poles, where adjacent rods have opposite voltage polarity applied to them. The voltage is applied to each rod. The ion moves in a very complex motion that is directly proportional to the mass of the ion, voltage on the quadrupole, and the radio frequency.

Ion Trap

This analyzer employs similar principles as the quadrupole, it uses an electric field for the separation of the ions by mass to charge ratios[**]. The analyzer is made with a ring electrode of a specific voltage and grounded end cap electrodes. The ions enter the area between the electrodes through one of the end caps. After entry, the electric field in the cavity due to the electrodes causes the ions of certain m/z values to orbit in the space. As the radio frequency voltage increases, heavier mass ion orbits become more stabilized and the light mass ions become less stabilized, causing them to collide with the wall, and eliminating the possibility of traveling to and being detected by the detector.

---

[*]http://chemwiki.ucdavis.edu/Analytical_Chemistry/Instrumental_Analysis/Mass_Spectrometry/Mass_Analyzers_%28Mass_Spectrometry%29

Time-of-flight

The most commonly used analyzer is the time-of-flight (ToF) one, which is often coupled to MALDI-MS technique. Figure 3.2 shows the principle of time of flight analyzer. When ions (M^{+z}) are formed after laser irradiation in electric field, they acquire an energy E= z.e.V and are accelerated. Then, they fly toward the detector through a tube where E=0 at a speed of v= $(2.z.e.V/m)^{1/2}$ (where z is the charge of ion, m is the mass of ion, e is the electric charge ($1.6\ 10^{-16}$ C), and V is the electric potential). Because the electrical field inside the tube is zero, the speed of ions is essentially determined by their m/z allowing their separation. It is clear that the ions having the smallest m/z values will be first detected.

Time-of-Flight reflectron[†]

Similar to time of flight analyzer, however the kinetic energy distribution in the direction of ion flight can be corrected by a reflectron. The reflectron uses a constant electrostatic field to reflect the ion beam toward the detector. The more energetic ions penetrate deeper into the reflectron, and take a slightly longer path to the detector. Less energetic ions of the same charge-to-mass ratio penetrate a shorter distance into the reflectron and, correspondingly, take a shorter path to the detector. The flat surface of the ion detector (typically a microchannel plate, MCP) is placed at the point where ions with different energies reflected by the reflectron hit a surface of the detector at the same time counted with respect to the onset of the extraction pulse in the ion source. A point of simultaneous arrival of ions of the same mass and charge but with different energies is often referred as ToF focus. An additional advantage to the re-ToF arrangement is that twice the flight path is achieved in a given length of instrument.

Magnetic sector

Similar to time of flight analyzer, in magnetic sector analyzers, ions are accelerated through a flight tube, where the ions are separated by charge to mass ratios. The difference between magnetic sector and ToF is that a magnetic field is used to separate the ions. As moving charges enter a magnetic field, the charge is deflected to a circular motion of a unique radius in a direction perpendicular to the applied magnetic field. Ions in the magnetic field experience two equal forces: a force due to the magnetic field and a centripetal force.

[†] *http://en.wikipedia.org/wiki/Time-of-flight_mass_spectrometry*

Fourier-transform ion cyclotron resonance mass analysis[‡]

Ion cyclotron resonance is an ion trap that uses a magnetic field in order to trap ions into an orbit inside of it. In this analyzer, there is no separation that occurs; rather all the ions of a particular range are trapped inside, and an applied external electric field helps to generate a signal. In a Fourier Transform ICR, all of the ions within the cell are excited simultaneously so that the current image is coupled with the image of all of the individual ion frequencies. A Fourier transform is used to differentiate the summed signals to produce the desired results.

Quadrupole-ToF

Quadrupole-ToF is an association between quadrupole and time of flight methods. It offers significantly higher sensitivity and accuracy. Furthermore, quadrupole-ToF mass analyzers are relatively new and have been designed to be coupled to electrospay ionization sources and recently to MALDI. [110]

	Quadrupole	Ion Trap	Time-of-Flight	Time-of-Flight reflectron	Magnetic sector	FTMS	Quadrupole-ToF
Accuracy	*0.01%*	*0.01%*	*0.02 to 0.2%*	*0.001%*	*<0.0005 %*	*<0.0005 %*	*0.001 %*
Resolution	*4,000*	*4,000*	*8,000*	*15,000*	*30,000*	*100,000*	*10,000*
m/z range (Da)	*4,000*	*4,000*	*>300,000*	*10,000*	*10,000*	*10,000*	*10,000*
General comments	*Low cost*	*Low cost*	*Good accuracy and resolution*	*High resolution*	*High resolution*	*High resolution*	*High sensitivity*

Table 3.2: A general comparison of mass analyzer types (ref. [110], pp:58).
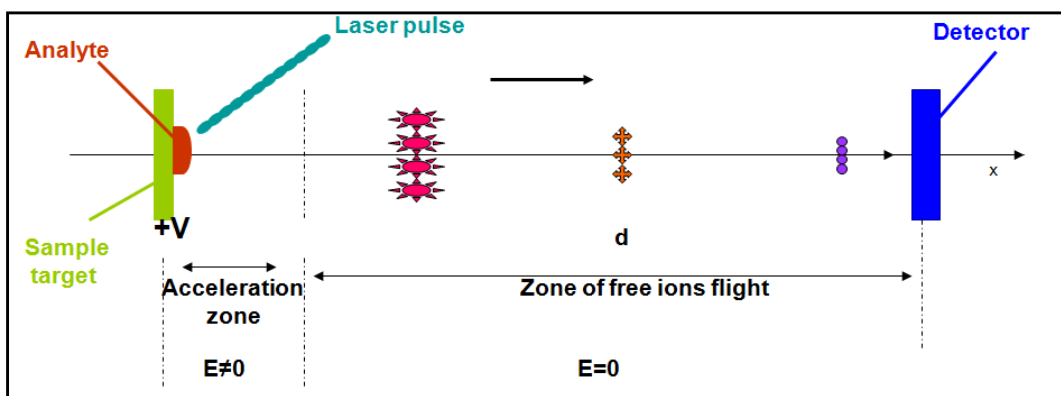
Figure 3.2: Principle of time of flight analyzer.

Normally, each mass spectrometer has one analyzer. However, in the tandem mass spectrometry (MS/MS)§, its mass spectrometer has more than one analyzer; in practice usually two. The two analysers are separated by a collision cell into which an inert gas (e.g. argon, xenon) is admitted to collide with the selected sample ions and causes their fragmentation. The analysers can be of the same or of different types, the most common combinations being: 1) quadrupole-quadrupole, (2) magnetic sector-quadrupole, (3) magnetic sector- magnetic sector, (4) quadrupole-time-of-flight. Tandem mass spectrometry (MS-MS) gives structural information about a compound by fragmenting specific sample ions inside the mass spectrometer and identifying the resulting fragment ions. This information can then be pieced together to generate structural information regarding the intact molecule. Tandem mass spectrometry also enables specific compounds to be detected in complex mixtures on account of their specific and characteristic fragmentation patterns.

b) Ion detector

There are different ion detectors in mass spectrometry such as: Faraday cup, scintillation counting, electron multiplier, high energy dynodes with electron multiplier, array, and charge detection. Table 3.3 displays their advantages and disadvantages. Among them, electron multiplier is commonly used. [110]

---

§ http://www.astbury.leeds.ac.uk/facil/MStut/mstutorial.htm

Detectors	Advantages	Disadvantages
Faraday Cup	Good for checking ion transmission and low sensitivity measurements	Low amplification (around 10)
Scintillation counter (photomultiplier)	Robust Long lifetime (>5 years) Sensitive (gains of around 10^6)	Cannot be exposed to light while in operation
Electron Multiplier	Robust Fast response Sensitive (gains of around 10^6)	Shorter lifetimes than scintillation counter (around 2 years)
High energy dynodes with electron multiplier	Increases high mass sensitivity	May shorten lifetime of electron multiplier
Array	Fast and sensitive	Reduces resolution Expensive
Charge detectors	Detect ions independent of mass and velocity	Limited sensitivity

Table 3.3: A general comparison of ion detectors (ref. [110], pp:64).

3.3. Matrix-assisted laser desorption/ionization mass spectrometry (MALDI-MS)

The matrix-assisted laser desorption/ionization mass spectrometry was introduced and developed in the mid-1980s. It is largely used in the analysis of biomolecules and synthetic macromolecules thanks to its advantages as shown in Table 3.1:

- *It can analyze sample molecules of masses ranging from 700 to 300000 Da.*

- *It has a high sensitivity on the order of fmol.*

- *It is a soft ionization process with almost no fragmentation of the sample molecule.*

- *It can be used in the presence of salt in millimolar concentrations.*

- *It is suitable for the analysis of complex mixtures.*

- *Multiple samples can be prepared at the same time on the sample plate containing one hundred positions, as shown in Figure 3.3.*

Figure 3.3 illustrates a component of MALDI mass spectrometer: one droplet of matrix and one droplet of sample are deposited on the sample plate (often stainless steel). Then, they are mixed together by drawing the combined droplet in and out of the pipette. Once the mixture is dried, the plate is inserted into the mass spectrometer. Then, the laser irradiates this mixture leading to the desorption and ionization of the analytes. The formed ions are then separated according to their mass-to-charge ratio (m/z) thanks to the analyzer. Finally, they directly hit the detector, resulting is a mass spectrum with signal intensities as a function of m/z ratio of the ions. The efficiency of MALDI-MS method depends essentially on the laser type and on the organic matrix used. [110] [115] [116] [119] [124] [125] [126] [127]

(A) **(B)**
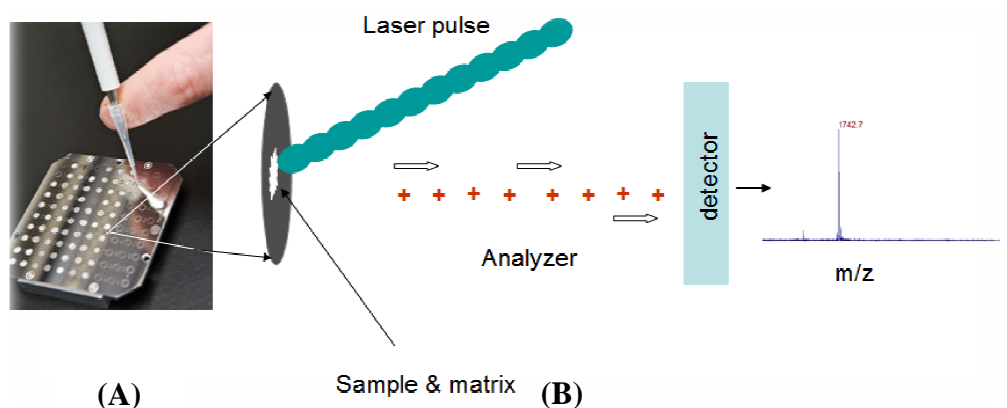
Figure 3.3: Schematic illustration of a MALDI-plate with spots of the co-crystallized organic matrix-analytes (A) and MALDI-MS principle (B).

3.3.1. Laser type

The choice of the laser is important in MALDI-MS technique to reach a high sensitivity and high resolution. The wavelength of the laser dictates the choice of the matrix molecule and nature of analytes. In most cases, lasers having wavelengths in the near-ultraviolet (UV) are widely used in MALDI-MS technique (UV-MALDI-MS technique), particularly, N_2 laser (λ=337 nm) and frequency-tripled Nd:YAG laser (λ=355nm) with a pulse duration ranging from 0.5 to 10 ns. The use of these kinds of laser displays some advantages. [9][119] [120] [113] [128]

➢ It prevents the direct photoexcitation of analytes.
➢ There is a low degree of photochemical products. [127]

Beside near-UV lasers, pulsed infrared (IR) lasers are also used in MALDI-MS technique (IR-MALDI-MS technique), for example, erbium solid-state lasers Er:YAG (λ=2.94 µm) or Er:

YSGG (λ=2.79 µm). The advantages of IR MALDI-MS technique are multiple: 1) softer (less fragmentation); it can be used for ionization of easily fragmented molecules, 2) greater material removal that can be useful for direct gel or cell and tissue ionization, 3) high efficiency for the analysis of large proteins and nucleotides, 4) high mass resolution, 5) compatibility with solvent matrix or surface-assisted laser desorption mass spectrometry. However, the reproducibility from shot to shot in the IR-MALDI-MS is inferior to that in the UV-MALDI-MS technique. [9] [109] [119] [127] [129]

3.3.2.   Matrix molecules

In MALDI-MS technique, the organic matrix molecule has important functions:

1) *It allows formation of a co-crystal with the sample molecule for reducing molecular interactions between the sample molecules.*
2) *It absorbs photons from the laser and transfers it to sample-matrix mixture in LDI process.*
3) *It can protect (in certain cases) the sample molecules from direct UV laser excitation if the sample molecules are sensitive to the laser light.*
4) *It acts as a proton H^+ source for enhancing the ionization of the sample. Indeed, most of the organic matrices used bear an acid group (-COOH).*

Typically, the best MALDI performance is obtained when the absorption maxima of the matrix is near the wavelength of the used laser. On the other hand, the ratio of the matrix to the sample is also an important parameter for successful MALDI analysis; it is often in the range between 1000/1 and 5000/1 (matrix/analytes).

The choice of the matrix depends on the nature of the sample molecule to be analyzed and the laser type. Normally, matrices are low-mass organic molecules having an aromatic ring and acid moieties, as shown in Figure 3.4.
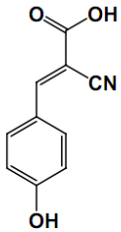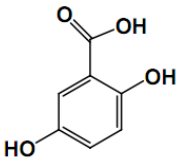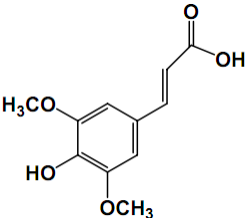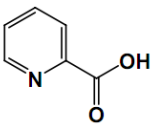
Name of organic matrices	Wavelength absorption maxima (nm)	Application
α-cyano-4-hydroxycinnamic acid	337, 335	Peptides
2,5-dihydroxy benzoic acid	337, 355, 266	Peptides, nucleotides, oligosaccharides, polar polymers
3,5-dimethoxy-4-hydroxycinnamic acid	337, 355, 266	Proteins
2-Picolinic acid	266	Oligonucleotides

Figure 3.4: The common organic matrices used in MALDI-MS technique: structure, chemical name, wavelength of absorption maxima, and their applications.

However, the use of organic matrices introduces some problems for MALDI-MS analysis:

➢ *The analytes should be miscible with the organic matrix and should be well co-crystallized avoiding the creation of "hot spots". These "hot spots" lead to non uniform localisation of analytes and thus to bad signals in the mass spectra. This leads to a difficult selection of the appropriate matrix.*

> *MALDI-MS is not very suitable for MS analysis of small compounds below < 700 Da, because of a strong background due to the presence of parasitic ions from the matrix.*

> *Matrix molecules can also be degraded into small fragments increasing the background signal and thus the sensitivity.*

To overcome these hurdles of MALDI-MS due to the organic matrix, surface-assisted laser desorption/ionisation mass spectrometry (SALDI-MS) method has been developed; it will be discussed in more details in the following section.

3.4. Surface-assisted laser desorption/ionization mass spectrometry (SALDI-MS)

Surface-assisted laser desorption/ionization mass spectrometry (SALDI-MS) technique, also called matrix-free laser desorption/ionization mass spectrometry method, uses an inorganic surface (smooth or rough) instead of an organic matrix. Hence, SALDI-MS overcomes the limitation of MALDI-MS [9] [115] [116] [130] [131] [132]. Actually, to perform SALDI-MS analysis, the same mass spectrometer is used as for MALDI-MS. The only adjustment to perform is the change of the sample plate to accommodate the SALDI interface in the mass spectrometer. For example, Figure 3.5 shows an example of a SALDI interface glued on modified stainless steel plate *via* a "conductive adhesive". Then, a droplet of the sample is simply deposited and let it dry prior to its insertion into the mass spectrometer. Subsequently, the analytes are desorbed and ionized, separated by the ToF analyser and then detected, as already described for MALDI-MS.
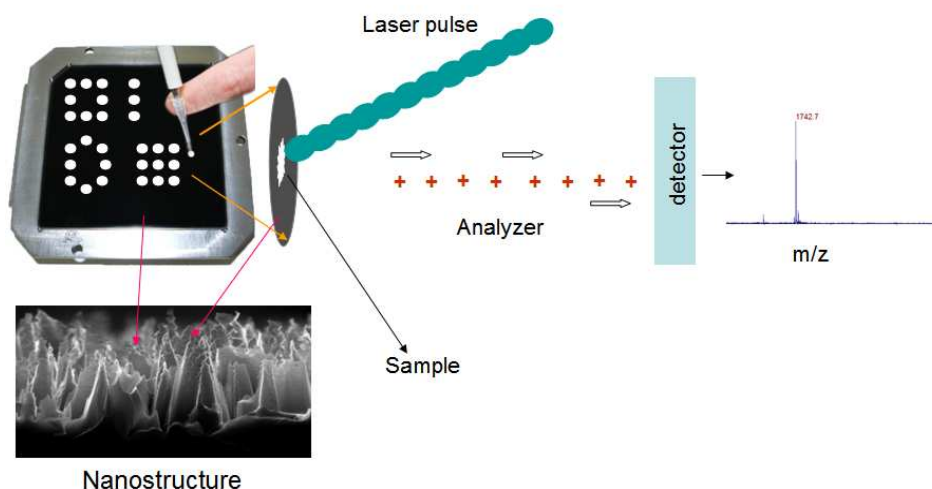
Figure 3.5: SALDI surface (silicon nanostructures) glued on stainless modified sample plate.

As in MALDI-MS technique, the exact desorption/ionization mechanism in SALDI-MS method is still under debate. The most reported work in this area suggests that the inorganic surface is able to absorb photons from the laser pulse. Then, the absorbed energy is transferred through a thermal mechanism (non-radiative dissipation *via* phonons) to the adsorbed analytes for their subsequent desorption/ionization [133]. As compared to MALDI-MS method, SALDI-MS process represents a technique of particular interest with various advantages such as [45] [122] [131] [133] [134] [135]

1) *The use of same mass spectrometer instrument as for MALDI-MS analysis, no additional investment is needed.*

2) *No organic matrix is needed:*

   ➢ *Simple sample deposition/preparation. The sample is just deposited onto the interface and let it dry. The only required step is dissolving the sample molecules in a proper solvent.*

   ➢ *Can detect small molecules (<700 m/z) due to low background signal.*

   ➢ *High sensitivity of detection (ymol).*

   ➢ *High salt tolerance than MALDI.*

3) *High yield of analyte detection thanks to analyte specific interaction in the case of SALDI functionalized substrates.*

4) *Existence of large variety of SALDI surfaces (various morphologies and materials).*

Beside the advantages discussed above, SALDI-MS method also presents some drawbacks such as a limited mass range of detection (>3000 m/z). However, some examples have shown the detection of proteins of high molecular weights (around m/z=17000). Also, despite that there is no matrix used, background ions of unidentified sources can be detected mainly caused by hydrocarbon adsorbed from air or some contaminants leached from storage. [45] [133] [136]

In practice, SALDI surfaces may be flat, micro- or nano-structured inorganic materials presenting different forms and shapes (micropillars, nanotubes, nanocolumns, nanorods, nanowires, nanoparticles, nanoflowers,...) of different chemical nature (Si, ZnO, SiO_x, TiO_2, carbon with different alloy-types such as DLC, fullerene, nanotubes,….). Among them, we can find crystalline silicon [127] [128], porous silicon [122] [136] [137], silicon nanowires prepared by metal-assisted chemical etching [57], carbon nanotubes [111], silicon nanowires prepared *via* VLS growth mechanism [124], ZnO nanowires [138] [138], titania nanotubes [139], gold nanoparticles [140], platinum

nanoflowers [141], etc. These SALDI surfaces showed high sensitivity for the detection of small molecules by MS analysis, as indicated in Table 3.4.

Surface	SALDI surface	Analyte or application	Sensitivity
ZnO nanowires [138] [138]	*Diameter: 25 to 1600 nm* *Length: 250 nm*	*Clonidine (230.1 m/z)* *Azithromycin (749.0 m/z)* *Tamowifen (371.5 m/z)* *Ketoconazole (513.4 m/z)*	*5 pmol*
Titania nanotubes arrays [139]	*Diameter: 70 to 120 nm* *Length: 250 nm*	*Hexadecyltrimethylammonium bromide (CTAB) (284 m/z)*	$\approx$ *50 fmol*
Graphite particles [142]	*Size: 2-150 µm*	*Bradykinin (1061 m/z)*	*1 pmol*
Platinum nanoflowers [141]		*Angiotensin (1298 m/z)* *Neurotensin (1349 m/z)* *Human insulin (5807 m/z)* *Cytochrome (12360 m/z)*	*0.7 -20 fmol*
Porous silicon [122]	*Mesoporous (2-50 nm pore size)*	*Des-arg-bradykinin (904.5m/z)*	*700 amol*

Table 3.4: Some examples of SALDI surfaces with different morphologies from various materials and their LDI-MS sensitivity for analytes detection.

SALDI surfaces based on porous silicon (PSi) were used for the first time for mass spectrometry analysis of peptides and other small molecules such as caffeine, adrenocorticotropic hormone, antiviral drugs,...The SALDI-MS method, based on PSi, is commonly called: DIOS for Desorption/Ionization on Silicon [122].

In the literature, SALDI surfaces based on silicon (micropillars, nanowires, porous silicon...) have been classified under the generic name of DIOS surfaces. These DIOS surfaces have become of a great attention because they can be easily integrated with existing silicon-based technology, allowing for example, their application in miniaturized biosensors, microfluidic chemical reactors [13]. In the following section, we will present first the DIOS-MS method and then the application of our silicon nanostructures and nanowires, fabricated in chapter 1, as efficient DIOS interfaces for MS analysis of peptides.

3.5. Desorption/Ionization on silicon mass spectrometry (DIOS-MS)

As already discussed above, the DIOS-MS method was initially associated with porous silicon [116] [122] [125] [127] [131] [133] [143] [144]. However, DIOS-MS has also been extensively investigated with other structured materials such as: surface scratched, nanostructures, nanowires, nanoparticles, microcolumns, submicrometer structures, nanofilaments, nanowell arrays, nanocavity arrays, and even smooth silicon surfaces. These surfaces showed a high sensitivity for the detection of small biomolecules by DIOS-MS analysis as indicated in Table 3.5. Among them, the rough surfaces are commonly used in DIOS-MS analysis. These surfaces present a high surface area, high photon absorption, and low thermal conductivity (this point will be discussed in more detail in the next section).

These investigations also demonstrated that the fabrication of DIOS surfaces have been achieved by micro/nanofabrication method such as: lithography and dry etching, electrochemical etching, metal-assisted etching, CVD growth… (already mentioned in chapter 1).

DIOS surfaces	Method of fabrication	Dimensions	Analytes	Sensitivity
Groove arrays on silicon surface	Lithography and RIE [145]	Width: 150 nm Spacing: 150 nm Depth: 300 nm	Angiotensin I (1296 m/z)	5 pmol
Silicon microcolumns	Laser irradiation in the presence of water [115]	Radius of tip curvature: 120 nm Height: 800 nm	Bradykinin (756.39 m/z) Angiotensin (1045.53 m/z)	1 pmol
Scratched silicon surface	Sandpaper N°.400 [145]		Angiotension I (1296 m/z)	25 pmol
Porous silicon	Electrochemical etching [125]	Diameter: 70-120 nm Depth: 200 nm	Des-arg-bradykinin (904.5 m/z)	15 fmol
Silicon nanofilaments	Metal-assisted etching [125]	Diameter: 7-12 nm Depth: 2.8 nm	Des-arg-bradykinin (904.5 m/z)	15 amol
Silicon nanocavity arrays	Electron-beam lithography and RIE etching [123]	Diameter:118-558 nm Depth:200-459 nm	Angiotensin III (931.5 m/z)	0.1 mM
Silicon nanowires	CVD growth [124]	Diameter : 10-40 nm Length : 0.5 -10 μm	Verapamil (455 m/z) Midazolam (325.8 m/z)	50 fmol
Silicon nanoparticles	Commercially available (WEN-07, ARA-10)	Diameter: 5, 30 and 50 nm	Propafenone (342 m/z) Verapamil (455 m/z)	33 fmol
Smooth silicon surface (IR-DIOS-MD)	Commercially available [146]	Flat	Bradykinin (1061 m/z) Bovine insulin ($\approx$6000 m/z) Vitamin B$_{12}$ (1356 m/z)	300 fmol
Silicon Nanowell arrays	Lithography and RIE [144]	Diameter:$\approx$ 93 nm Depth: 10-50 nm	Adenosine (268.19 m/z) Pro-Leu-Gly tripeptide (285.19 m/z) Des-arg-bradykinin (904.5 m/z)	1pmol

Table 3.5: Some examples of DIOS surfaces and their sensitivities of detection by MS analysis.

3.5.1. Factors influencing the efficiency of DIOS-MS analysis

Although the SALDI mechanism, including DIOS, has not been clarified entirely, preliminary investigations indicate the signal enhancement factors for molecular ions in the SALDI mass spectra such as: (1) irradiation parameters (laser wavelength, pulse duration, laser fluence, etc), (2) surface morphology, (3) chemical termination, (4) solvent types, (5) presence of surfactants or cations, (6) sample deposition method, (7) positive or negative mode, seem to be crucial to prepare optimized SALDI and DIOS interfaces. [56] [115][116] [122] [125] [127] [131] [133] [143] [144] [145] [147] [148]

3.5.1.1. The role of the laser irradiation

Among these factors, thermal desorption of analyte molecules without thermal decomposition has been widely attributed to the laser-induced rapid temperature increase in the LDI substrate [120] [128]. In such a case, the temperature peak is a function of the optical absorption coefficient, reflectivity, heat capacity, and heat conductivity of the substrates. In particular, the high optical absorption coefficient of substrates enhances the rapid temperature increase during the LDI process, and this helps to effectively transfer energy from the surface to analytes. Therefore, a structured silicon semiconductor surface with high absorption coefficient in the UV region is expected to be an efficient material for DIOS-MS. [128] [131]

It is known that the best LDI-MS performance is obtained when the absorption maxima of surface-assisted is near the wavelength of the laser used. The increased performance is due to efficient energy absorption by the substrate and transfer to the analyte in the desorption/ionization process. Typically, there is a threshold laser fluence above which an analyte signal is obtained. Above this level, the ion signal is roughly linear with increasing the laser fluence. The duration of the laser pulse is also important in generating the signal; it must be short to rapidly desorb the analyte although longer laser pulses have the effect of degrading the analyte before its desorption. [9]

As in MALDI-MS technique, in DIOS-MS technique, two main laser types are used. The ultraviolet laser (UV-DIOS): either the nitrogen laser (λ=337 nm) or Nd:YAG laser (λ=355 nm), and the infrared laser (IR-DIOS) with Er:YAG IR laser (λ=2.94 µm) (see Table 3.6).

Laser	Wavelength	Photon energy (Kcal/mol)	Photon energy (eV)	Pulse width
Nitrogen	337 nm	85	3.68	<1 ns-Few ns
Nd:YAG x 3	335 nm	80	3.49	typs. 5ns
Nd:YAG x 4	266 nm	107	4.66	typs. 5ns
Excimer (XeCl)	308 nm	93	4.02	typs. 25ns
Excimer (KrF)	248 nm	115	5.00	typs. 25ns
Excimer (ArF)	193 nm	148	6.42	typs. 15ns
Er:YAG	2.94 µm	9.7	0.42	85 ns
CO_2	10.6 µm	2.7	0.42	100 ns + 1 µs tail

Table 3.6: Laser wavelength, pulse width and corresponding photon energy. [109]

The IR-DIOS-MS technique has some advantages: (i) it does not require surface structuration and LDI can be realized on crystalline silicon surface, (ii) it allows the analysis of biomolecules having high molecular masses (limitation of biomolecules detection ≈17 kDa), for example: cytochrome c (≈12,500 Da). [9] [127] [128] [146]

In IR-DIOS-MS method, the presence of water or solvent in the sample deposit is always required. It is suggested that the solvent or water serves as "pseudo-matrix" to isolate the analyte and facilitate its desertion. Furthermore, the energy from the IR laser radiation is most likely absorbed directly by the analyte, the residual solvent and water due to their absorption in the OH stretching region near 2.94 µm [127] [146]. Thus, IR-DIOS-MS can be used to analyze bigger biomolecules than UV-DIOS-MS. However, the IR fluence required for the desorption/ionization of analyte is higher than that for the UV laser (> 15 times, see Table 3.6).

In practice, UV laser is the most applied in DIOS-MS analysis because it uses a same mass spectrometer as for MALDI-MS which most of the time uses a UV pulsed laser. [55] [115] [118] [122] [144] The structured silicon surfaces must present a low reflectivity and high absorption in the UV region to maximize photon absorption. It is known that bulk silicon has an indirect band-gap energy of 1.1 eV, which is lower than the energy of a UV laser (For example, photons energy at 266, 337, 355 and 532 nm are 4.71, 3.68, 3.53 and 2.32 eV, respectively). Thus, by UV laser radiation, silicon substrate absorbs photons. The electron of valence band of silicon has enough energy to jump to the conduction band, leading to the generation of free carriers (holes and electrons) as shown in Figure 3.6 (a). Whereas the

125

energy of IR radiation is lower than the silicon band gap energy, so silicon is transparent to it, but the long wavelength radiation is absorbed by the free carriers as shown in Figure 3.6 (b).

After photon absorption, the energy can be dissipated (desexcitation) following 4 mechanisms: 1) *via* radiative recombination leading to photoluminescence, 2) *via* non-radiative recombination; the energy is dissipated through heat *via* phonons, 3) *via* a photoelectric effect (measurement of a photocurrent) and 4) *via* photochemical reaction. In practice, in DIOS technique, the energy is dissipated through heat thanks to phonons. That explains why the LDI process in SALDI and DIOS-MS analysis occurs essentially *via* a thermal mechanism. So, a photoluminescent structured silicon surface won't lead to an efficient DIOS-MS interface.

(a)   (b)
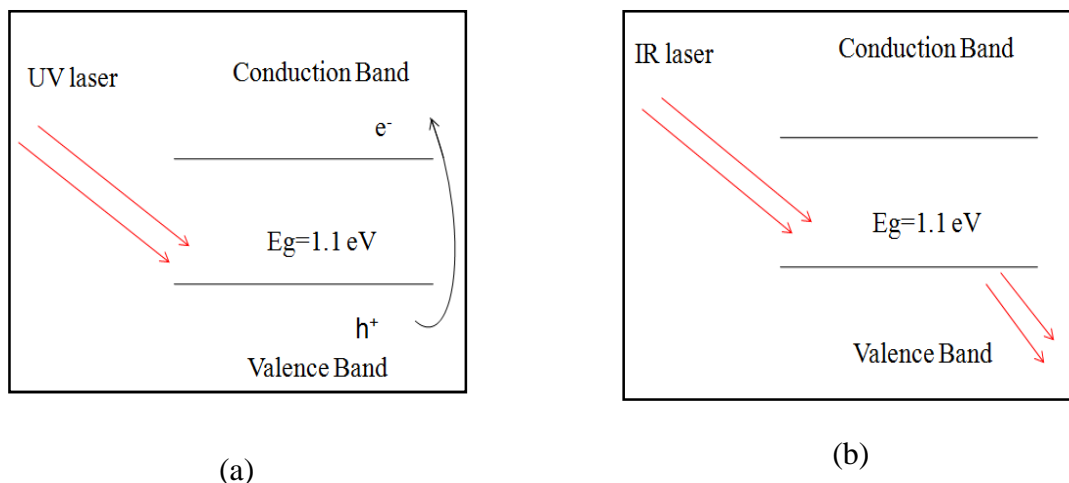
Figure 3.6: Excitation of electron in the valence band of silicon by UV laser radiation (a) and IR laser radiation (b).

The influence of the laser pulse width has also been investigated, but was found to have little or no influence on MALDI mass spectra, at least up to pulse lengths of tens of nanoseconds from commonly available laser sources. This factor indicates that the desorption/ionization process is determined by the energy density supplied to the sample by the laser pulse (fluence, J/cm^2) rather than by the rate of energy flow (irradiance, W/cm^2).

3.5.1.2.   The role of DIOS surface morphology

It has been demonstrated that both smooth and rough silicon surfaces (from micro to nanoscale) can be successfully used in DIOS-MS analysis, but the structured silicon surfaces were the most investigated.

It has also to be noted that there was no enhancement of mass signal in case of rough surfaces, as compared to smooth surfaces in IR-DIOS-MS analysis.

In contrary, rough silicon surfaces could improve the efficiency of UV-DIOS-MS technique, because of their high surface area, strong UV absorption and low thermal conductivity [55] [115] [118] [122] [144]. For example, Wei *et al.* studied LDI-MS analysis of small molecules using porous silicon substrate fabricated by electrochemical etching method. They demonstrated that the surface with small pore size gave a more intense ion signal with a sensitivity of 700 attmol for Des-arg-bradykinin (904.5 m/z) analysis. [122] In addition, the low thermal conductivity of porous silicon confines the heat near the surface, thus increasing locally the temperature. For example, the high porosity of porous silicon is known to reduce its thermal conductivity (~1.2 W/(m·K)), as compared to that of a single-crystalline flat silicon wafer (~130 W/(m·K)) [149]. In the case of silicon nanowires, the surface temperature increases sharply because of the 1D quantum-confined thermal energy and the decrease in thermal conductivity of the nanowires. As a result, the use of a silicon nanowires substrate results in a remarkable decrease in the minimum laser irradiation energy required for analyte desorption/ionization [124]. It was shown that SiNWs substrates require a lower laser fluence (0.3µJ/pulse) than PSi substrates to reach sufficient surface temperature required for desorption/ionization of molecules. The use of such surfaces further reduces the risk of fragmentation of the molecules to analyze and at the same time the background noise.

On the other hand, different surface morphologies yield various wetting behaviours. This leads to various amounts of solvent or water containing the analytes located either on top or inside of the structure of the DIOS interface, influencing the efficiency of DIOS-MS analysis. Thus, it is difficult to indicate a precise role of the substrate morphology on DIOS-MS analysis. [123]

In addition to the thermal desorption/ionization process, experimental results strongly support other contributions of non-thermal processes in the desorption/ionization mechanism in ion desorption enhancement in DIOS-MS. Northen *et al.* found a correlation between the signal of the DIOS mass spectrum and the changes in the surface morphology (surface restructuring and surface melting). They suggested that the desorption process in DIOS-MS is driven by surface restructuring and is not strictly a thermal process. [45]

3.5.1.3. The role of surface termination

In DIOS-MS analysis, chemical modification of the surface allows to control the precise location of analytes and to increase its stability over time, leading to a higher efficiency as compared to the surface without chemical modification. [118] [122] [137] In addition, the surface terminal group can also serve as a source of protons for ionization such as hydrogen- or hydroxyl-terminated silicon substrates. [120] [116] It is also known that, for the same DIOS surface morphology, the chemical modification can change its wettability behaviour and thus alters the interaction between the surface and the adsorbed molecules (see chapter 2).

Therefore, different surface chemical terminations result in various efficiencies of DIOS-MS analysis. For example, Trauger *et al.* [137] prepared porous silicon (PSi) surfaces modified with various chemical terminations: $-NH_2$, $-CH_3$, $-CF_3$, $-C_6F_5$. They showed that the PSi surfaces terminated with $-NH_2$, $-CH_3$, and $-CF_3$ groups displayed similar S/N ratios as for hydrogen-terminated PSi surface. While PSi surfaces with C_6F_5 termination exhibited the highest sensitivity (800 yoctomoles for Des-arg-bradykinin). Moreover, they also demonstrated that hydrophobic derivatized surfaces ($-CH_3$, $-CF_3$, $-C_6F_5$ terminated PSi) could detect both hydrophilic and hydrophobic molecules, while NH_2-terminated PSi substrates showed selectivity only towards hydrophilic or polar analytes.

In some cases, the derivatization of the surface can permit the isolation and separation of biomolecules and their subsequent detection by mass spectrometry analysis [118] [124] [150]. This point will be discussed in more details in chapter 4. For example, Go *et al.* showed that perfluorophenyl-derivatized silicon nanowires (diameter: 10-40 nm, length: 0.5-10 µm) grown *via* the VLS technique could be used as a Thin Layer Chromatography (TLC)-like for the separation and identification of molecules in the area of chromatography, followed by DIOS-MS analysis. The capability of SiNWs to separate a simple sample mixture lies in its high surface-to-volume ratio and in the difference in analyte-surface interactions. When combined with its ability to support laser desorption/ionization mass spectrometry, chromatographic separation followed by MS analysis with SiNWs provides a simple, inexpensive, rapid, and qualitative means to separate and analyze sample mixtures such as tenoxicam: 338 m/z and piroxicam: 332 m/z at 1 mg/mL.

3.5.1.4. Role of solvent, acid, surfactant and salt in the sample preparation

The presence of solvent, water, acid, surfactants or cations in the sample preparation also plays a significant role in DIOS-MS efficiency [45] [116][122] [131]:

- ✓ Water or alcohol is used as a "pseudo-matrix", which absorbs IR irradiation for desorption/ionization of analytes in IR-DIOS-MS analysis (as discussed in the previous section [3.4.1.1]).

- ✓ Water and acid (for example: HCl, TFA) can provide protons for increasing the protonation process. It leads to an improvement in the DIOS-MS efficiency [116].

- ✓ Addition of a solvent (for example: alcohol) in the initial sample preparation facilitates a part of solvent and analyte molecules to be trapped into the structures [122] [125]. The residual solvent in the structure is vaporized by a temperature increase at the surface, resulting in a rapid heating of the substrate and improvement of the desorption/ionization efficiency of analytes. [45] [136]

- ✓ Addition of perfluorinated surfactants in the sample preparation increases the efficiency of DIOS-MS technique. For example, Nordström *et al.* [45] showed that the use of perfluorinated surfactants enhances the mass signal of LDI-MS analysis of both small biomolecules and peptides on the C_8F_{17}-terminated porous silicon substrate. The surfactant interacting with the perfluoro-terminated surface allows the analyte and solvent molecules to be tapped on the rough substrate. Thus, it enhances the explosive vaporization, resulting in the improvement of DIOS-MS efficiency. Among the tested surfactants such as: heptadecaflurooctan-sulfonic acid (PFOS), perfluoroundecanoic acid (PFUnA), 3-(perfluorodecyl) paropane-1-ol (PFDOH), and sodium dodecyl sulfate (SDS), PFOS and PFUnA present the highest quality of mass signal in DIOS-MS analysis of 100 fmol Bovine serum albumin (with a higher value of S/N at least 3-fold compared to other surfactants).

- ✓ Using metal cations in the sample preparation facilitates the analysis of hydrocarbons and lipids by DIOS-MS technique. For example, Muck *et al.* suggested that doping SiNW arrays with lithium hydroxide yielded high S/N values with low limits of detection (750 pg tripalmitin on target with S/N=5) and efficient ionization for a range of fatty acids (FA), mono-, di- and triglycerides and hydrocarbons (HC). The lipids interacting with lithium ions form doped lipidic species, leading to enhancement of DIOS-MS efficiency. [147]

From the same DIOS surface (morphology and chemical termination) and prior to DIOS-MS analysis, the sample needs to be deposited. This step plays a pivotal role and can be divided into three steps:

➤ Choice of buffer or solvent depending on the molecule to analyze.

➤ Addition of surfactants or cations in the sample or on the DIOS surface prior to sample deposition. [45][147]

➤ Sample deposition on the DIOS surface: (1) using a pipette (most used method) followed by a drying step, (2) by dipping the DIOS surface into the sample solution followed by a drying step [123], (3) electrospray deposition [135], (4) electrowetting to enhance the penetration of the sample into the structure of the interface [125], (5) short contact [122] [137], (6) precise distribution of sample nanodroplet in specific locations using digital microfluidic displacement. [13]

In the next section, we'll discuss the sample deposition methods in more details.

3.5.2.   The method of peptide deposition on DIOS surface

Once the analyte droplet is deposited on the surface and allowed to dry, evaporation of the solvent forms either a uniform spot (homogenous analyte deposition) or a ring (non-homogenous analyte deposition). The observed ring is called "coffee-staining" or "coffee-ring" effect. In DIOS-MS analysis, it is evident that the formation of a uniform spot is preferred to a "coffee-ring" spot. Indeed, in the uniform spot, the analyte concentration is higher and homogeneously distributed within the spot. A single laser pulse irradiation is sufficient to realize desorption/ionization of a higher amount of adsorbed analyte on the surface in a uniform spot as compared to the "coffee-ring" case. This spot therefore results in a higher efficiency. For this reason, the concentration of molecules inside a uniform spot is crucial. In this section, we will report different methods for creating a uniform sample molecules spot on DIOS surface.

3.5.2.1.   What happens during the drying of analytes droplet?

The "coffee-ring" effect originates from the phenomenon when a coffee drop dries on a surface, as shown in Figure 3.7. A darker ring is formed after water evaporation with most of the solid particles deposited at the edge of the spot whereas very little amount is observed in the

centre of the ring. This phenomenon is explained by the advection phenomenon arising during evaporation [151] [152].

Figure 3.7: Observation of coffee-ring effect on a surface. [152]

Figure 3.8 depicts the mechanism of evaporation of a droplet on two types of surfaces (hydrophilic (a) and hydrophobic surface (b)). For each surface, different results have been obtained: a ring is formed on the hydrophilic surface whereas a uniform spot is observed on the hydrophobic one.

In the case of a hydrophilic surface i.e. when the CA<90°, the analytes are pulled to the edge of the spot by the advection phenomenon during the drop evaporation (Figure 3.8 (a)). Thus the coffee-ring effect occurs, leading to non-homogenous analytes deposition on the surface i.e. most of the analyte are concentrated at the edge and only a small amount is localized in the centre of the "coffee-ring" [152] [153]. This phenomenon reduces the efficiency of DIOS-MS analysis by lowering the signal intensity and increasing the background due to a non-uniform deposition of analytes. This phenomenon can be compared to the one observed in MALDI with the creation of "hot spots" when the co-crystallization of analytes and organic matrix is not uniform. Hence, the hydrophilic surface has a limitation in DIOS-MS analysis. However some strategies have been proposed to overcome this problem (see below).

In the case of a hydrophobic surface i. e. when the CA>90°, the advection inside the drop develops some turbulences thereby mixing well the analytes during evaporation, as illustrated in Figure 3.8 (b). Additionally, the surface contact area with the liquid is reduced and the evaporation rate from the perimeter (solid-liquid-vapour interface) is very slow due to vapour saturation (CA>90°). This results in the formation of a uniform spot of analytes on the hydrophobic surface. It is evident that the coffee-staining ring is greatly reduced in the case of a hydrophobic surface and most of the analytes are concentrated inside the spot [152][153]. Thus, we

assume that this effect is favourable for LDI-MS analysis of molecules. Therefore, higher contact angles will lead to a higher concentration of analytes within a restricted zone.

Hydrophilic surface   **Hydrophobic surface**

(a)   **(b)**

After the evaporation of solvent
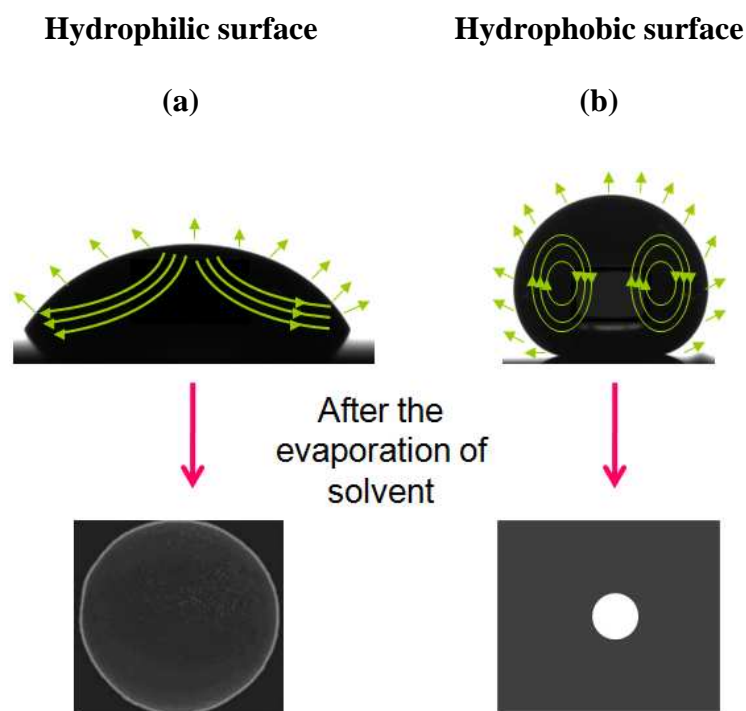
Figure 3.8: Scheme showing droplet evaporation with internal advection (a) on a hydrophilic surface and (b) on a hydrophobic surface. [152][153]

However, as discussed in chapter 2, in the case of superhydrophobic or superomniphobic surfaces (SH or SO surfaces), the liquid droplet can be either in a Cassie Baxter state (no impalement) or in the Wenzel state (total impalement), or in a semi-Cassie Baxter state (partial impalement).

Figure 3.9 displays the distribution of analytes during the evaporation process on SH or SO surfaces (rough or structured surfaces). If the initial state of the liquid analytes droplet is in the Cassie-Baxter state (Figure 3.9 (a), the contact angle decreases until the complete evaporation of the liquid occurs. The radius of the analyte droplet (R_c) is thus reduced. This causes an increase of the Laplace pressure P_c ($P_c=2\gamma/R_c$, where γ is the surface tension of the liquid and Rc is the radius of the droplet).
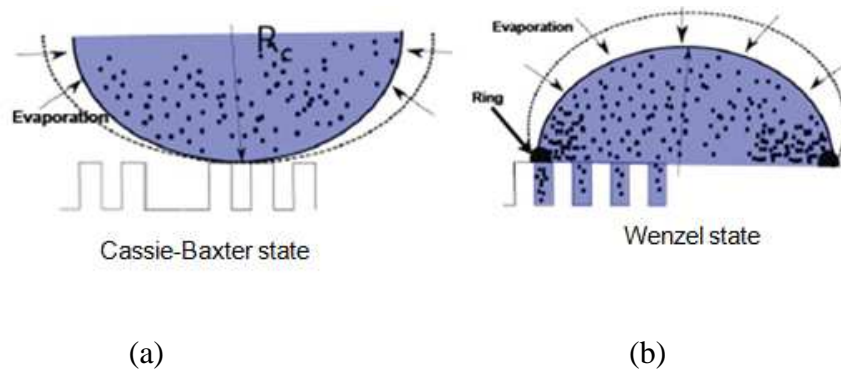
Figure 3.9: Schematic illustration of liquid droplet evaporation with a transition from Cassie-Baxter state to Wenzel state. [154]

➢ If this pressure is higher than the threshold pressure of the surface, a fraction of the droplet penetrates into the structures, and the contact line starts to be pinned onto the surface. We can speculate that the gradual transition from the initial Cassie-Baxter state to the Wenzel state, during the drying process, takes place when $R_c = R$ (where R is the radius of the spot) (Figure 3.9 (b)). Then, the liquid continues to evaporate under the Wenzel state with a receding contact angle always lower than 90°. Then, the evaporation occurs as on a hydrophilic surface and leads to the formation of "coffee ring" like spot almost as on the hydrophilic surface. Furthermore, the analytes can penetrate into the structure, as shown in Figure 3.10 (2). Compared to a hydrophilic surface, during droplet evaporation on superhydrophobic and superomniphobic surfaces with the transition from Cassie-Baxter state to Wenzel state, the diameter of the "coffee ring" is smaller i.e. the analytes are more concentrated.

➢ If the Laplace pressure is smaller than the threshold pressure of the surface, meaning that the resistance to the transition from the Cassie-Baxter to the Wenzel state is stronger i.e. high robustness (see chapter 2), the droplet will not penetrate into the structure. So, during droplet evaporation, a uniform spot is formed with high analytes concentration on the top of the structures, as shown in Figure 3.10 (1).
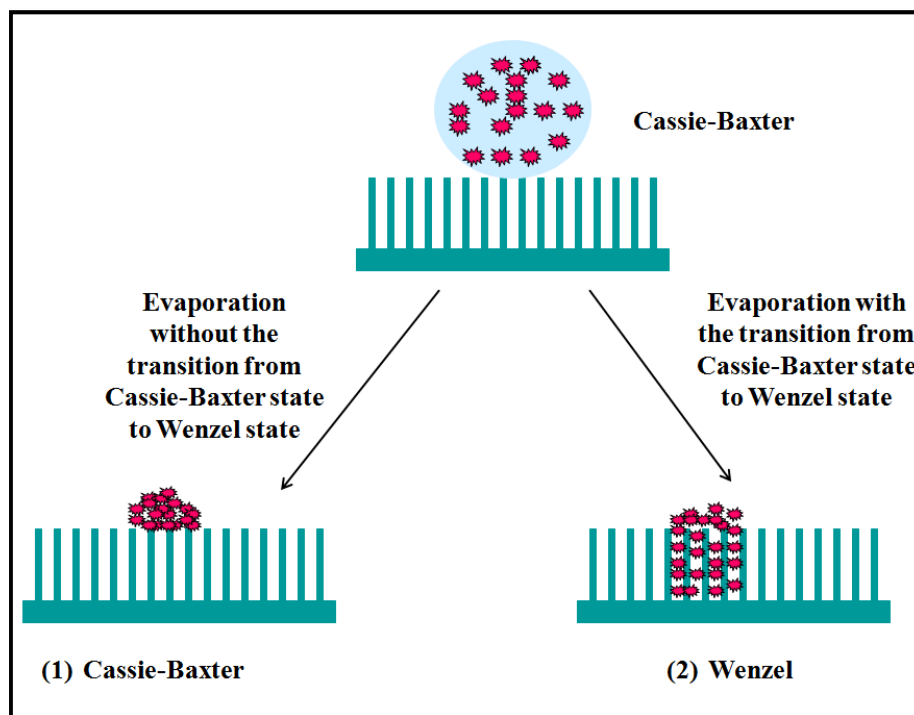
Figure 3.10: Schematic illustration of the distribution of sample molecules after droplet evaporation: (1) with and (2) without transition from Cassie-Baxter state to Wenzel state.

Consequently, different morphologies of the DIOS substrates impact their wetting properties, leading to different analyte distribution within the structure during droplet evaporation. Therefore, liquid repellent DIOS surfaces lead to a very uniform spot formation increasing the DIOS-MS analysis efficiency. It has to be noted that in most cases, the DIOS surfaces reported in the literature are chemically modified with low surface tension molecules such as perfluoroalkyl or alkyl chains, leading to superhydrophobic surfaces. [45][125] [135] [137]

3.5.2.2. Strategies for the creation of uniform spots of analytes on the DIOS surface

To control analyte deposition at a precise location, the DIOS surface is chemically modified by either silanization or hydrosilylation. The chemical functionalization with low surface energy molecules often leads to a superhydrophobic DIOS surface having a low contact angle hysteresis, on which it is difficult to deposit a liquid droplet because of the rolling-ball effect. To overcome this problem and to form a uniform spot of analytes after droplet deposition on a SH surface, different methods are proposed:

➢ **Keeping the liquid droplet in contact with the surface**: Siuzdak's group have first elaborated a technique consisting of keeping a liquid droplet of analytes in contact with the superhydrophobic porous silicon surface for few seconds, and then the droplet is withdrawn into the pipette. This procedure can be repeated up to five times to maximize analyte loading [45] [137]. It results in the location of analytes on the top of the structure, as shown in Figure 3.11. This method is very simple and allows retrieving the solvent and eventually contaminants such as salts, leaving only analytes of interest on the surface.
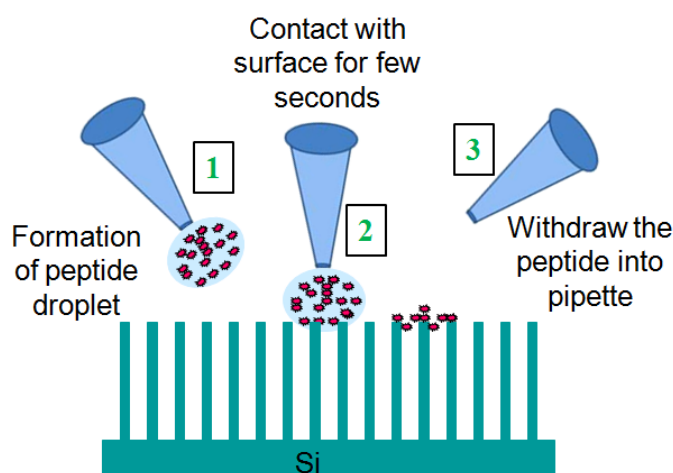
Figure 3.11: Schematic illustration of the manipulation of a peptide droplet by bringing it in contact with a superhydrophobic porous silicon surface for 30 seconds.

➢ **Creating a superhydrophobic hole** that allows analytes droplet to be maintained on the superhydrophobic surface without slipping off. For example, A. Ressine *et al.* fabricated superhydrophobic porous silicon nanoarrays chip with holes of 350 µm in diameter using an electrochemical etching combined with lithography, as shown in Figure 3.12. Depending on the robustness of the surface, the analytes can be distributed either on the top or inside the structure.
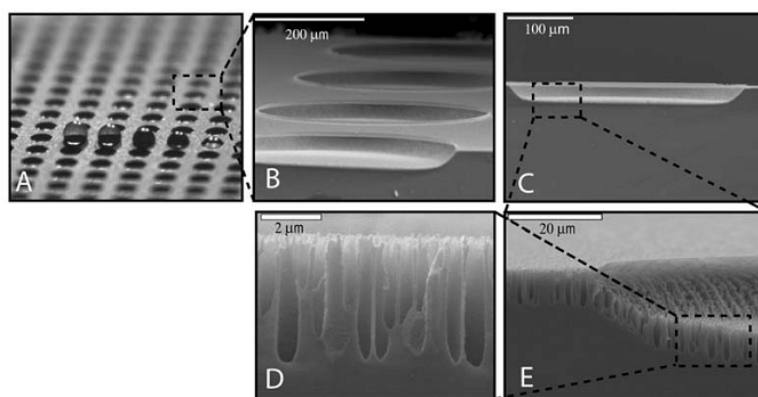
Figure 3.12: (A) Superhydrophobic porous silicon nanovial chip for analyte droplets deposition providing a convenient way of liquid handling, (B-E) SEM images of the porous nanovial array along with several close-up views. [151]

➢ **Superhydrophilic regions on a superhydrophobic surface**: in this case, the size of the droplet should be bigger than the size of the superhydrophilic area to avoid analyte solution to penetrate deep inside the structure. For example, Figure 3.13 displays a superhydrophobic NanoSi surface with superhydrophilic apertures. Firstly, NanoSi surface was fabricated by electroless etching and coated by OTS, leading to a superhydrophobic surface. Secondly, superhydrophilic apertures were created by removing the organic layer (OTS layer) by oxygen plasma after an optical lithography step. By this method, the analytes are distributed both on the top and inside the structure after droplet evaporation. [13]
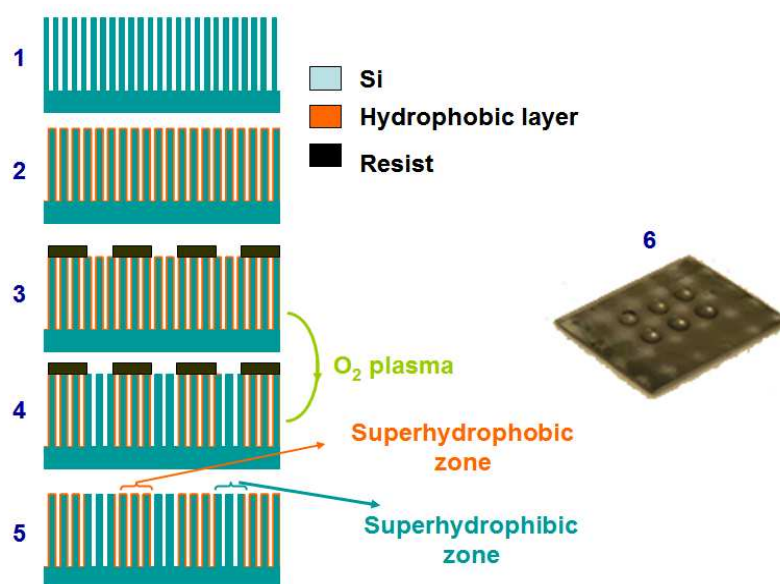
Figure 3.13: Schematic illustration of the different steps for the creation of superhydrophilic zones on a superhydrophobic surface. NanoSi substrate (1) is coated with a hydrophobic layer (orange colour) (2), covered by a photoresist layer (black colour) for the lithography step (3), then the hydrophobic layer is removed by O₂ plasma (4). Finally, the resist layer is removed yielding superhydrophilic zones surrounded by the superhydrophobic surface (5). A photo of the patterned surface with peptide droplets (6).

> **Penetration of the analytes inside the structure by applying a voltage provoking an electrowetting** during the sample deposition on porous silicon (PSi) and silicon nanofilament (nSi) surfaces [125]. This technique allows homogenous deposition of analytes on top and inside the structures. In that case, various applied voltages will cause different levels of penetration of analytes into the structure. Tsao *et al.* showed that high applied voltages allow more analyte to penetrate deep into the structure, resulting in a better mass spectrometry signal quality. They also reported a detection limit of 15 fmol for Angiotensin I (898.9 m/z) with S/N = 300 at 75 V. Furthermore when they applied a voltage of 125 V, the quality of the mass signal was improved by a factor of 2 with a S/N = 600. This technique was used for aqueous solutions of analytes. It has to be noted that electrowetting is not required when the analytes are dissolved in an organic solvent such as acetonitrile. Because the organic solvent causes the reduction of surface tension, leading to a decrease of the contact angle on the substrate and thus a penetration of analytes inside the structures.

137

- **Electrospray deposition** [135]**:** This technique is similar to the electrowetting method described above. Here, a potential is applied between the DIOS surface and the sample, leading to the formation of a uniform thin layer of analytes deposited on the DIOS surface. This method allows a quantitative analysis and corresponds to a combination between liquid chromatography and DIOS-MS analysis**.**

- **Changing the surface energy of the DIOS surface** to reach final water contact angles ranging between 110 and 140°, and thus facilitating the droplet deposition. The change of the surface energy of a DIOS surface can be realized by chemical modification notably by the introduction of different alkyl chain lengths such as octyl, decyl…instead of octadecyl chains. Alternatively, the surface energy can be also changed by partial degradation of the organic layer *via* UV/Ozone treatment. In that case an octadecyl chain is partially degraded (see next section).

- **Changing the surface tension of the analyte solution** by addition of a solvent such as: ethanol, methanol or acetonitrile. The quantity of the solvent depends on the surface wetting properties. For example, NanoSi-CF$_3$ has lower surface energy than NanoSi-CH$_3$ (see chapter 2 [3.2]) thus for obtaining the same final contact angle, the amount of solvent added in the analyte solution for -CF$_3$ is higher than for the -CH$_3$ termination (see next section). These methods are simple and do not require any lithography step or electrowetting manipulation of the droplet. Thus, we will choose this method for our DIOS-MS analysis.

3.5.2.3.   Summary

The studies of DIOS-MS analysis are very broad, but its mechanism is still unclear and complex. The high quality of DIOS-MS analysis results from an interplay of various parameters such as: laser pulses, morphology of the surface, chemical composition of the surface, composition of the sample solution, wetting properties of the surface, and also the method of analyte deposition.

In our group, we have developed silicon nanostructured (NanoSi) substrates for DIOS-MS analysis of small molecules and for lab-on-chip applications [13]. In the continuation of the work of Gaëlle Piret (thesis 2010), we optimized in this thesis the performance of various interfaces such as silicon nanostructures prepared by metal-assisted etching either using HF/AgNO$_3$ or NaBF$_4$/AgNO$_3$ aqueous solutions, or synthesized *via* CVD growth (silicon nanowires) for DIOS-MS analysis. In the following section, we will first present the sample

preparation for DIOS-MS analysis. Secondly, we will report the results obtained by mass spectrometry analysis using different surface morphologies, and evaluate their sensitivities. Finally, we will consider the influence of doping type, SiO_x deposition and effect of the chemical composition of the NanoSi surface on DIOS-MS efficiency.

3.6. DIOS-MS analysis of peptides on nanostructured silicon surfaces

3.6.1. Surface preparation

The nanostructured silicon substrates investigated here were prepared *via* metal-assisted etching using $NaBF_4/AgNO_3$ or $HF/AgNO_3$ aqueous solution (as described in chapter 1). In DIOS experiments, the NanoSi surfaces were first silanized with octadecyltrichlorosilane (OTS) conferring a superhydrophobic character to the surface with a water contact angle (CA) of 160°. For an easy deposition of the droplet, the CA was decreased to 120° by UV/O_3 treatment (4 mW/cm^2 at 220 nm) for 4 minutes, as shown in Figure 3.14. The interfaces were attached to a MALDI target plate using conductive double-side carbon tape.
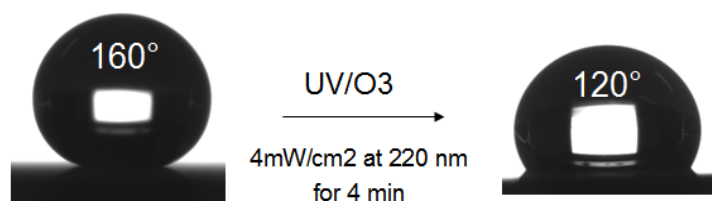
Figure 3.14: Water contact angles of OTS-terminated NanoSi surfaces before (CA=160°-left) and after UV/O₃ treatment (CA=120°-right).

3.6.2. Sample preparation

The performance of the NanoSi surfaces for DIOS analysis was evaluated using a standard peptide mixture composed of Des-arg1-Bradykinin (M= 904.5 m/z, isoelectric point pI = 10.0), Angiotensin I (M=1296 m/z, pI= 7.4), Glu1-Fibrinopeptide I (M=1570 m/z, pI= 4.0) and Neurotensin (M=1673 m/z, pI= 8.7) (Table 3.7). The peptides Mix1 were obtained from a sequazyme peptide mass standard kit of Applied Bisosystems (AB) (Part number P2-3143-00). They were diluted in 1 mM ammonium citrate buffer (pH=5.5) to 50 fmol/µL, except for Neurotensin (10 fmol/µL). A 1 µL of the analytes solution was directly deposited on the NanoSi

surface and allowed to dry in air before insertion into the mass spectrometer, as shown in Figure 3.15. As the CA is 120°, the droplet of peptides does not spread out, remaining in a localized area of ~ 250 µm in diameter.

Figure 3.15: Schematic illustration of the peptides mixture deposition on DIOS surface.

Peptides	Molecular weight (Da)	pI	Charge in 1 mM ammonium citrate buffer (pH=5.5)
Des-arg1-Bradykinin	904.5	10	+
Angiotensin I	1296	7.4	+
Glu1-Fibrinopeptide I	1570	4.0	-
Neurotensin	1673	8.7	+

Table 3.7: Physico-chemical properties of the tested peptides.

3.6.3. DIOS-MS analysis

For performing the Laser Desorption/Ionization and mass spectrometry analysis, we used a Voyager-DE-STR time-of-flight (ToF) mass spectrometer (Applied Biosystem) with delayed extraction, operating with a pulsed N_2 laser at 337 nm (3 ns pulse). Positive ion mass spectra were acquired in a reflector mode of operation, an accelerating potential of 20 KV, and a grid voltage at 73%. No guide wire voltage was used, and the extraction delay time was 200 ns. Each spectrum is the result of about 50 averaged laser pulses.

As the DIOS process is performed in positive ion mode; we choose ammonium citrate as a buffer to limit sodium and potassium adducts formation. Additionally, the pH of the buffer solution also allows formation of positive ions from most of the peptides, increasing the MS signal intensity [116] [136]. When the pI > pH, the peptide carries a net positive charge in

ammonium citrate buffer solution. Here, all peptides are positively charged (Des-arg1-Bradykinin, Angiotensine I, Neurotensin), except Glu1-Fibrinopeptide I which is negatively charged (See Table 3.7).

The following are the different steps of the DIOS-MS analysis protocol:

1. Three droplets (1 µL each) were deposited at three different locations on four NanoSi surfaces.
2. Let them dry in air.
3. Perform DIOS-MS analysis on one spot with various laser fluences until obtaining the best mass spectrum as possible at certain laser intensity (I_L).
4. Then, DIOS-MS analysis is performed on the three other spots using the laser intensity I_L. However, for each spot, we tried to obtain the best MS signal so the I_L need to be tuned meaning that the applied laser intensity for each spot on the same surface may be slightly different.
5. The standard deviation for each peptide was determined from the results obtained from three different spots.

To estimate the quality of the MS signal, values of signal to noise (S/N) ratio were considered. The S/N ratios were calculated from the ion counts obtained using Data Explorer (Applied Biosystems) for each peptide. The peptide signal value was then divided by the average ion count for the m/z interval 1900-2000, resulting in "summed" S/N values.

3.6.4. NanoSi surfaces fabricated by NaBF$_4$/AgNO$_3$ aqueous solutions

For the optimization of DIOS-MS analysis, we first used nanostructured silicon (NanoSi) surfaces prepared by chemical etching in **HF/AgNO$_3$ aqueous solution.** This substrate was previously optimized in our group [13] [14] [55] [56] [57]. The best quality of LDI-MS signal was obtained with NanoSi surfaces having a high density and a medium height of about 2.5 µm. Based on this result, we investigated NanoSi surfaces prepared by chemical etching of crystalline silicon in **NaBF$_4$/AgNO$_3$ solutions** (see chapter 1 [1.2.3.2]) as new substrates for LDI-MS. Herein, we studied three NanoSi surfaces of different morphologies. They have been synthesized from various types of silicon under the same experimental conditions i. e. 2 M NaBF$_4$/0.02 M AgNO$_3$ aqueous solution at 80°C for 2 h (Figure 3.16 S$_1$, S$_2$ and S$_3$). Their ability for LDI-MS analysis are compared to NanoSi surface fabricated using **0.02 M HF/2.5 M AgNO$_3$**

aqueous solution at 53°C for 10 minutes and called S_4 (Figure 3.16 S_4). This surface-S_4 will serve as a reference in terms of DIOS-MS performance. Figure 3.16 exhibits top and cross view SEM images of these interfaces.

- **S_1 surface** was prepared from n-type (100) silicon wafer, resistivity 5-10 Ohm-cm. The surface displays a porous-type structure with silicon needles *(diameter of the tips: 50-300 nm, diameter of the pores: 250-450 nm and height ≈ 2.5 µm).*

- **S_2 surface** was obtained from n-type (111) silicon wafer, resistivity 0.03-0.05 Ohm-cm. The resulting nanostructures are randomly oriented and consist of nano-triangles *(diameter of the tips: 30-400 nm and height ≈ 2.9 µm).*

- **S_3 surface** was synthesized from p-type (100) silicon wafer, resistivity 0.009-0.01 Ohm-cm. Their structures consist of isosceles triangles *(diameter of the tips: 90-600 nm and height: 1.25 µm).*

- **S_4 surface** was fabricated from the same silicon wafer as in S_3 surface: p-type (100), resistivity 0.009-0.01 Ohm-cm. This surface comprises vertically-aligned silicon nanofilaments *(diameter of the filaments: 20-100 nm and height: 2.5 µm).* Top-view SEM characterization showed a porous silicon-like structure.

On the other hand, these surfaces present a low reflectance values (<1.5%) over a wavelength range of 200-1300 nm, as shown in Figure 3.17, suggesting that these surfaces absorb efficiently the energy of the UV laser pulse radiation at 337 nm.

To assess the DIOS-MS performance of the interfaces for a standard peptide mixture at a concentration of 50 fmol/µL, three droplets (1 µL each) were deposited at three different locations on the four NanoSi surfaces. Figure 3.18 displays mass spectra recorded on each surface. Table 3.8 reports their average S/N values and standard deviation for each peptide on each surface.

S_1

n-type (100) resistivity 5-10 Ohm-/cm

S_2

n-type (111) resistivity 0.03-0.05 Ohm/cm

S_3
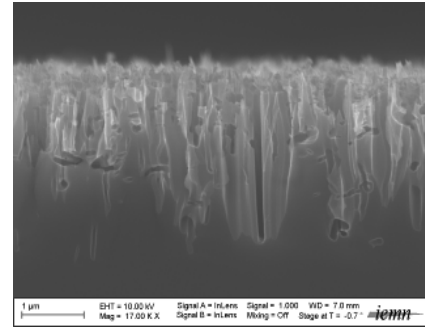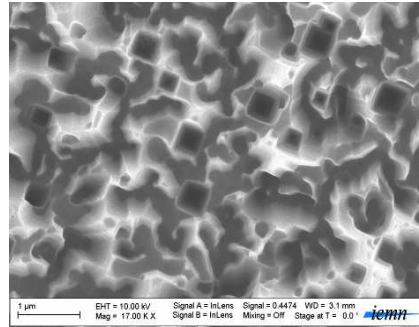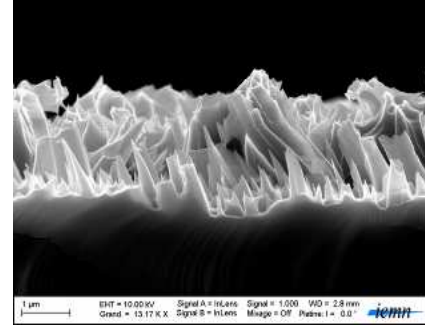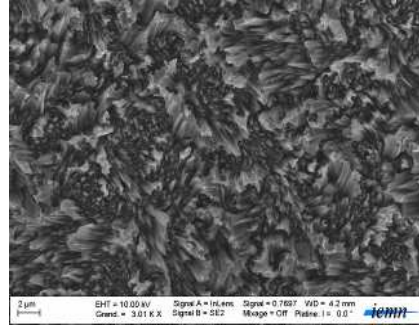
p-type (100) resistivity 0.009-0.01 Ohm/cm

S_4
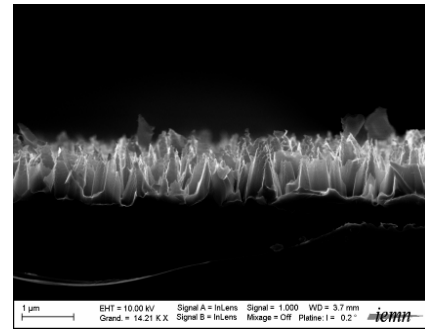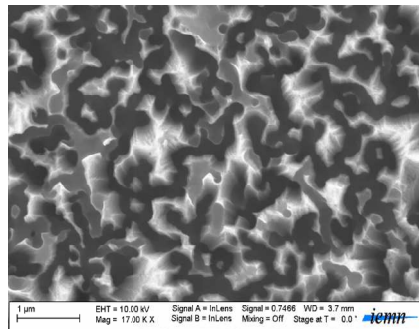
p-type (100) resistivity 0.009-0.01 Ohm/cm
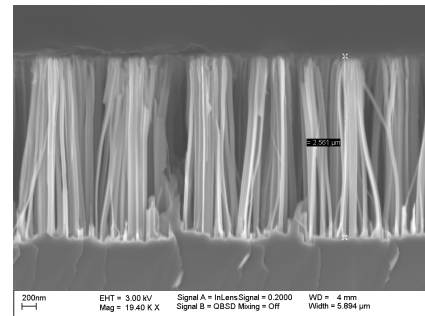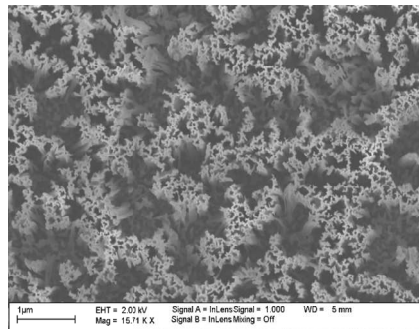
*Figure 3.16: SEM images (top-views and cross-views) of NanoSi surfaces prepared using **2 M NaBF₄/0.02 M AgNO₃** aqueous solution at 80°C for 2 h from S_1: n-type (100), resistivity 5-10 Ohm-cm, S_2: n-type(111) resistivity 0.03-0.05 Ohm-cm, S_3 **and** S_4**:** p-type (100), resistivity 0.009-0.01 Ohm-cm. S_4 was synthesized using **2.5 M HF/0.02 M AgNO₃** aqueous solution at 53°C for 10 minutes.*
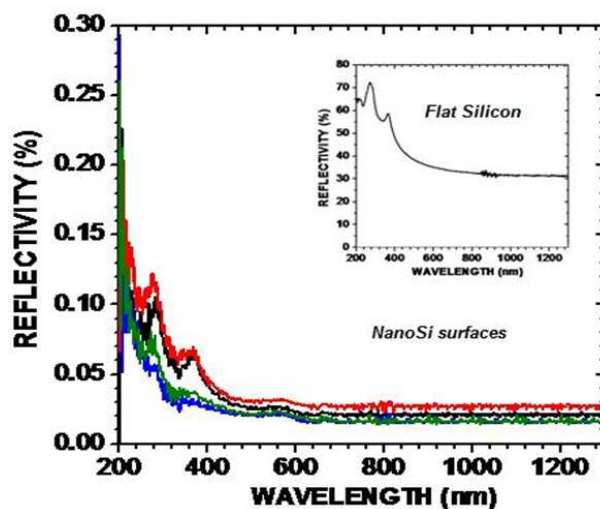
Figure 3.17: Total reflectance of the substrates and a flat silicon surface (inset) over a wavelength range of 200-1300 nm.
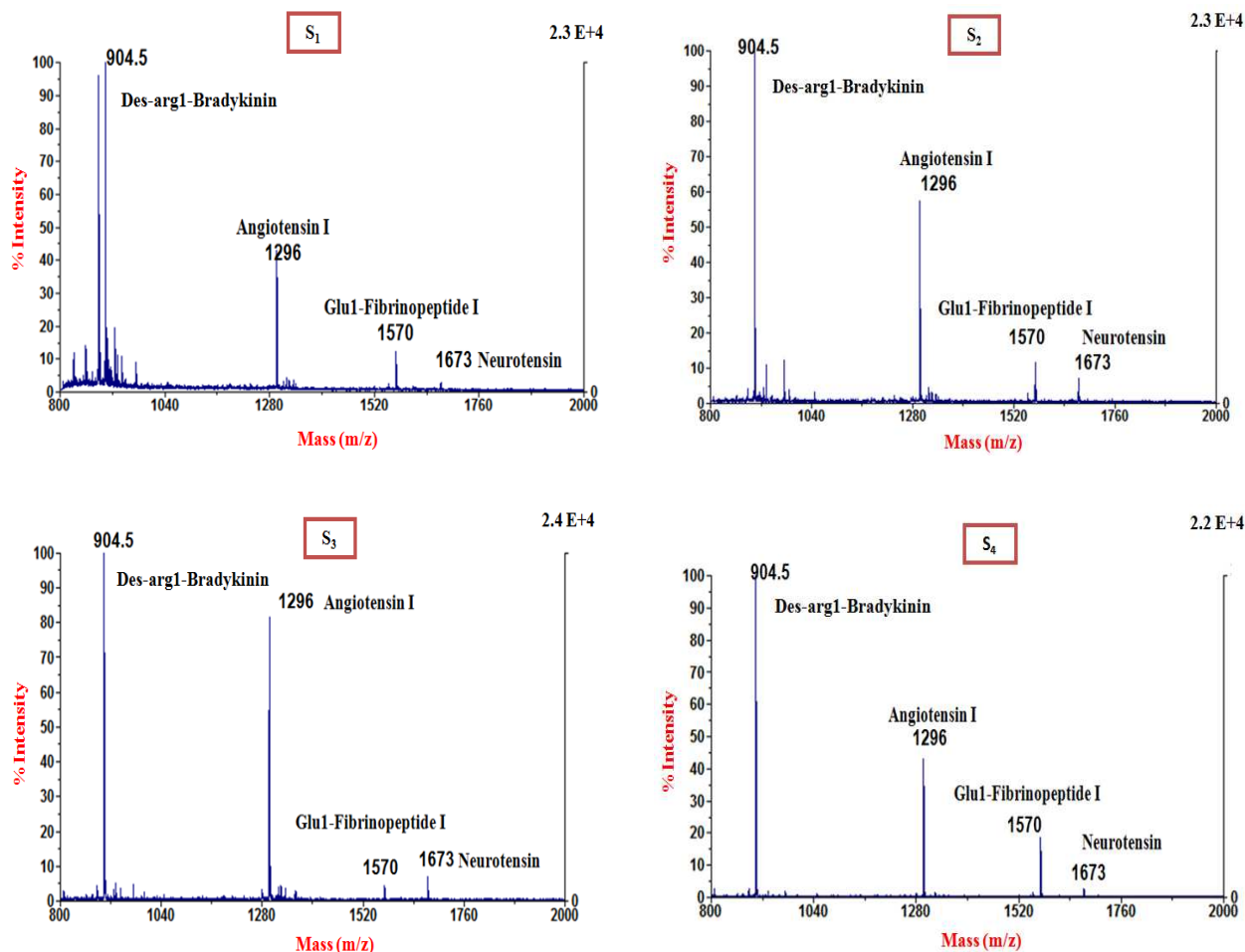
Figure 3.18: Mass spectra of the peptide mixture at 50 fmol/µL (10 fmol/µL for neurotensin) on NanoSi surfaces S_1, S_2, S_3, and S_4.

144

Surfaces	S/N and (Standard deviation (SD) (%)			
	Des-arg1-Bradykinin	Angiotensine I	Glu1-Fibrinopeptide I	Neurotensin
S_1	871 (22%)	429 (32%)	129 (56%)	32 (40%)
S_2	799 (8%)	388 (37%)	82 (14%)	43 (37%)
S_3	1002 (25%)	769 (26%)	153 (19%)	69 (26%)
S_4	1160 (17%)	731 (35%)	530 (55%)	80 (76%)

Table 3.8: Average S/N ratio values and standard deviations for each tested peptide on different NanoSi surfaces (S_1, S_2, S_3 and S_4).

From these results we can see that:

1) All the tested surfaces, fabricated using $NaBF_4/AgNO_3$ aqueous solution, are able to detect the four peptides as in the case of the S_4 reference interface.

2) The S/N ratio for each peptide is not identical for the same surface. This may be due to the fact that each peptide could be adsorbed at various levels on the surface, due to their different physico-chemical properties or the different interactions with the surface functional groups. Thus, it leads to different D/I efficiencies under the same laser irradiation. It should be noticed that Neurotensin and Glu1-Fibrinopeptide I present the smallest S/N values than the other peptides. Glu1-Fibrinopeptide I carries a negative charge in ammonium citrate buffer solution. It should be more difficult to produce a positive ion from this peptide, thus the efficiency of detection of this peptide is lower. However, we did not realize a test in the negative mode. For Neurotensin, the small S/N values recorded for all surfaces are related to its concentration. Indeed, this peptide is 5 times less concentrated (10 fmol/µL) in the peptide mixture, as compared to the other peptides.

3) The detection of each peptide is not identical on each surface:

Des-arg1-Bradykinin: All surfaces allow the detection of this peptide with high sensitivities with S/N values of 871, 799, 1002 and 1160 for surfaces S_1, S_2, S_3 and S_4,

respectively. The Des-arg1-Bradykinin is considered as the base peak for the MS spectra for each surface. The surface S_4 presents the best quality of peak in terms of S/N. For this peptide, the SD is similar for each surface (around 20%), except for S_2 which displayed a SD of 8%.

Angiotensin I: The S_1 and S_2 surfaces show a quasi identical detection for Angiotensin I, (S/N values of 429 and 388, respectively) with an efficiency 1.5 times lower than S_3 and S_4 surfaces (S/N values of 769 and 731, respectively).

Glu1-Fibrinopeptide I is negatively charged under our experimental conditions and normally the positive mode is not favourable for the detection of such a peptide. Nevertheless, all surfaces are able to detect it and S_4 seems to be very efficient as compared to S_1, S_2 and S_3. However, S_4 present a SD of 55% as compared to S_1, S_2 and S_3 with 57, 15 and 19%, respectively, suggesting that S_4 is very sensitive towards this peptide but the interspot MS analysis showed highly different values. The surfaces S_1 and S_2 exhibited lower S/N values than S_3 with a higher SD for the S_1 surface 57% (15% for S_2).

Neurotensin: The four different surfaces are able to detect Neurotensin with an interspot SD of 26, 37, 40 and 76% for surfaces S_1, S_2, S_3 and S_4, respectively. Here again, the S_4 surface seems to be the most sensitive but shows highly variable values of S/N between each spot.

<u>Summary</u>

The efficiency of LDI-MS of each surface is different for each peptide. Nevertheless, two groups of DIOS surfaces seem to appear by comparing the S/N values for each peptide. First group includes S_1 and S_2 surfaces and a second group composed by S_3 and S_4 surfaces. It is found that S_3 and S_4 surfaces display similar results in terms of S/N values and higher LDI-MS efficiency, as compared to the first group (S_1 and S_2). Except for Glu1-Fibrinopeptide, the results for S_3 and S_4 are similar.

The S_3 and S_4 surfaces were fabricated from the same silicon type, i. e. from boron-doped silicon (p-type), but from different solutions (S_3 and S_4 using $NaBF_4/AgNO_3$ and $HF/AgNO_3$ aqueous solutions, respectively). They showed quasi identical efficiencies for LDI-MS analysis for the tested peptide mixture, except for the detection of Glu1-Fibrinonpeptide I. Indeed, S_4 surface presents a S/N value for Glu1-Fibrino peptide I of 530 whereas S_3 shows a S/N value of 153 i. e. 3.5 times lower. Concerning the surfaces S_1 and S_2, they were fabricated from phosphorous-doped silicon wafer (n-type). A possible influence of the silicon doping could be the origin of the difference in the LDI-MS performance for all the surfaces tested in this work.

However, the most sensitive surface is the S_4 for the peptides we have analyzed, but with the highest SD values. A good compromise should be the surface S_3 combining good sensitivity and low SD.

We suggest that SD may be caused by: (i) surface inhomogeneity, (ii) problem of reproducibility of the peptide deposition, leading to different amounts of peptide, (iii) a slight difference in the laser intensity.

We can explain the difference in terms of LDI-MS performance of all the DIOS surfaces by the various morphologies obtained as a function of the silicon wafer type (n or p-type or dopant concentration) and from the etching solution (HF or $NaBF_4$) used. We suggest that:

- The different morphologies can lead to a variation in the amount of analytes deposited on top or inside the structure due to different levels of penetration of the liquid droplet into the structures, even for the same initial contact angle.

- It is known that a deeper penetration of the analytes in the structures leads to a better LDI-MS performance [125]. At the same time, the residual amount of water or solvent inside the structure of a DIOS interface can greatly influence the LDI-MS efficiency [45] [127] [128]. In that case, the solvent acts as a "pseudo matrix".

- Finally, the different surface morphologies obtained can cause a variation in the thermal conductivity of the surfaces, resulting in various DIOS-MS analysis efficiencies.

3.6.5. Influence of doping type on DIOS-MS efficiencies

To gain a better understanding and based on the previous results, we investigated the influence of the doping level on the LDI-MS performance. Gaëlle Piret, during her thesis, has shown that using different silicon wafers in terms of type and doping level, silicon nanostructured surfaces of similar morphologies can be obtained. These substrates did not show any significant difference in the LDI-MS performance.

However, in our case, it is difficult to conclude on the real influence of the substrate morphology and silicon type (n or p-type and concentration of dopant) on the performance of DIOS-MS analysis. Firstly, because we have observed that electroless etching assisted by metal gave different NanoSi surface morphologies using $NaBF_4/AgNO_3$ solution (see chapter 1 [1.2.3.2]). We don't know if the type and level of silicon doping has a direct or an indirect influence on LDI-MS analysis performance, i. e. if the dopants play a crucial role on the etching process by forming different morphologies, influencing the LDI-MS performance or if the

dopants affect directly the performance of the LDI-MS analysis by influencing photons absorption, reflectivity....

To investigate a real influence of such dopants, we have performed DIOS-MS analysis using silicon nanowires prepared by CVD. For that we used the same peptide mixture as before. The advantage of such substrates is that they have similar morphologies whatever the presence or not of dopants and whatever the type and level of dopants (Figure 3.19). They are straight with a length of 6-7 µm and diameters ranging from 50 to 100 nm. These NWs were grown at 500°C, at a total pressure of 10 mbar during 20 minutes, partial pressure of silane (P_{SiH4}) of 0.65 mbar, and B:Si (B_2H_6) and P:Si (PH_3) ratios of 10^{-4}.

Table 3.9 displays the average S/N values and their interspot standard deviation in percentage for each peptide on different SiNWs surfaces tested: undoped, p-doped and n-doped silicon nanowires. We can see that the number of active dopants incorporated in the silicon nanowires is 25 times higher for boron as compared for phosphorus. This is explained by the fact that the kinetics of incorporation during the growth process is the not the same for both atoms and so in practice, it is very difficult to precisely control the dopants incorporation in SiNWs. However, they are still highly doped with around 10^{19} atoms of dopants/cm^3. The results of mass spectrometry analysis showed that undoped SiNWs present the best performance than doped SiNWs notably with better S/N ratios for each tested peptide. So, the important point here is that the presence of dopants leads to a decrease of the SiNWs performance for LDI-MS analysis of peptides. However, when S/N ratios and SD are compared for n-doped and p-doped SiNWs substrates, we can clearly see that p-doped NWs gave better results than the n-type NWs, as already observed for the NanoSi interfaces in section [3.6.4].
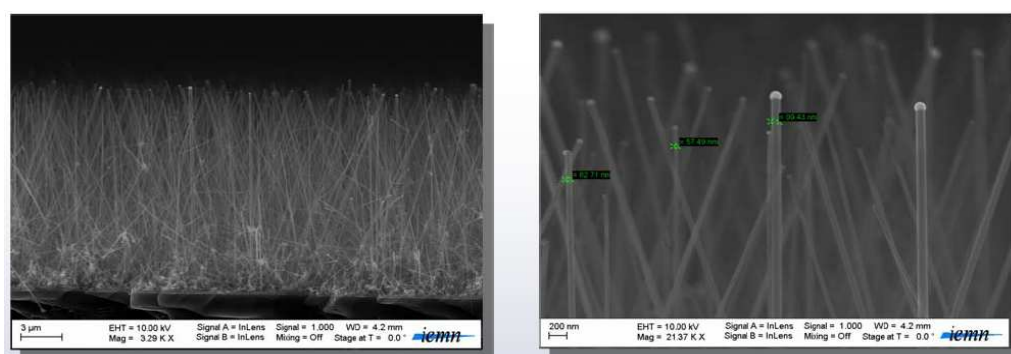
Figure 3.19: CVD silicon nanowires prepared via the VLS mechanism.

Silicon nanowires (SiNWs)		S/N and Standard deviation (SD) (%)			
Type of dopants	Dopant level (dopants/cm^3) *	Des-arg1-Bradykinin	Angiotensine I	Glu1-Fibrinopeptide I	Neurotensin
Undoped	None	1074 (17%)	299 (7%)	45 (29%)	37,(24%)
p-doped (boron)	100 x10^{19}	704 (7%)	266 (28%)	79 (SD 13%)	22 (32%)
n-doped (phosphorous)	4x10^{19}	462 (25%)	192 (34%)	28 (20%)	15 (33%)

*Table 3.9: Average S/N ratio values and their SD for each peptide tested on different CVD-grown silicon nanowires (SiNWs): undoped, p-doped and n-doped. *measured by electrical characterization (active dopants).*

3.6.6. Sensitivity of DIOS-MS analysis using our DIOS interfaces

We have tested the sensitivity of detection of two of our NanoSi surfaces: S_3 (NaBF$_4$) and S_4 (HF). For that, we have prepared different concentrations of the peptide mixture (50, 5 and 1 fmol/µL). On each surface, we have deposited three spots. In Table 3.10 are summarized the S/N ratio values after DIOS-MS analysis. Both surfaces are able to detect 1 fmol/µL of Des-arg1-Bradykinin, Angiotensine I, Glu1-Fibrinopeptide I and 0.2 fmol of Neurotensin. Between the two tested surfaces, S_4 is the most sensitive.

S/N ratios and SD (%) for S_4 surface fabricated using HF/AgNO$_3$ aqueous solution			
Peptide	**50 fmol/µL**	**5 fmol/µL**	**1 fmol/µL**
Des-arg1-Bradykinin	1160 (17%)	1120 (19%)	337 (13%)
Angiotensine I	731 (35%)	28 (35%)	30 (26%)
Glu1-Fibrinopeptide I	530 (55%)	216 (28%)	56 (14%)
Neurotensin	80 (76%)	7 (28%)	6 (16%)
S/N ratios and SD (%) for S_3 surface prepared using NaBF$_4$/AgNO$_3$ aqueous solution			
Peptide	**50 fmol/µL**	**5 fmol/µL**	**1 fmol/µL**
Des-arg1-Bradykinin	1002 (25%)	919 (18%)	25 (56%)
Angiotensine I	769 (26%)	30 (26%)	10 (40%)
Glu1-Fibrinopeptide I	153 (19%)	158 (22%)	8 (50%)
Neurotensin	69 (26%)	4 (25%)	4 (25%)

Table 3.10: Average S/N ratio values and their SD for each peptide in DIOS-MS analysis on NanoSi surfaces, prepared using HF/AgNO$_3$ (S_4 surface) and NaBF$_4$/AgNO$_3$ (S_3 surfaces) aqueous solutions, for different concentrations of the peptide mixture (the concentration of Neurotensin is 5 times lower than the other ones).

3.6.7. Influence of SiO$_x$ deposition over NanoSi surfaces on DIOS-MS analysis

As discussed above, the main mechanism in DIOS process for the formation of ions seems to occur *via* a thermal mechanism (see section [3.5.1]. After photons absorption, the energy is dissipated *via* non-radiative recombination through phonons. Thus, the thermal conductivity of the surface greatly influences the efficiency of DIOS-MS analysis. Here, we have tried to decrease the thermal conductivity of some of our interfaces by depositing silicon dioxide (thermal insulator) layers of different thicknesses. We have investigated the influence of SiO$_x$ layer thickness (10, 30 and 50 nm) on the DIOS-MS efficiency for the peptide mixture analysis. Herein, the deposition of SiO$_x$ layers was realized on two surfaces, S$_1$ and S$_3$ (see Figure 3.16), by plasma-enhanced chemical vapour deposition (PECVD) using an OXFORD instrument (annex 2).

Herein, we choose the surfaces S$_1$ and S$_3$ because they have structures with triangular shapes with vertical and sharp tips on which a homogenous SiO$_x$ deposition can be achieved. The S$_2$ surface has a random structure while S$_4$ surface nanostructures are well-packed and vertically aligned (Figure 3.16), thus it is difficult to obtain homogeneous depositions of SiO$_x$ on such surfaces.

The DIOS-MS performance was assessed using the standard peptide mixture at 50 fmol/µL, and 1 µL of solution was spotted three times on each surface. Figure 3.20 displays representative mass spectra obtained from each surface. Table 3.11 reports their average S/N values and SD.
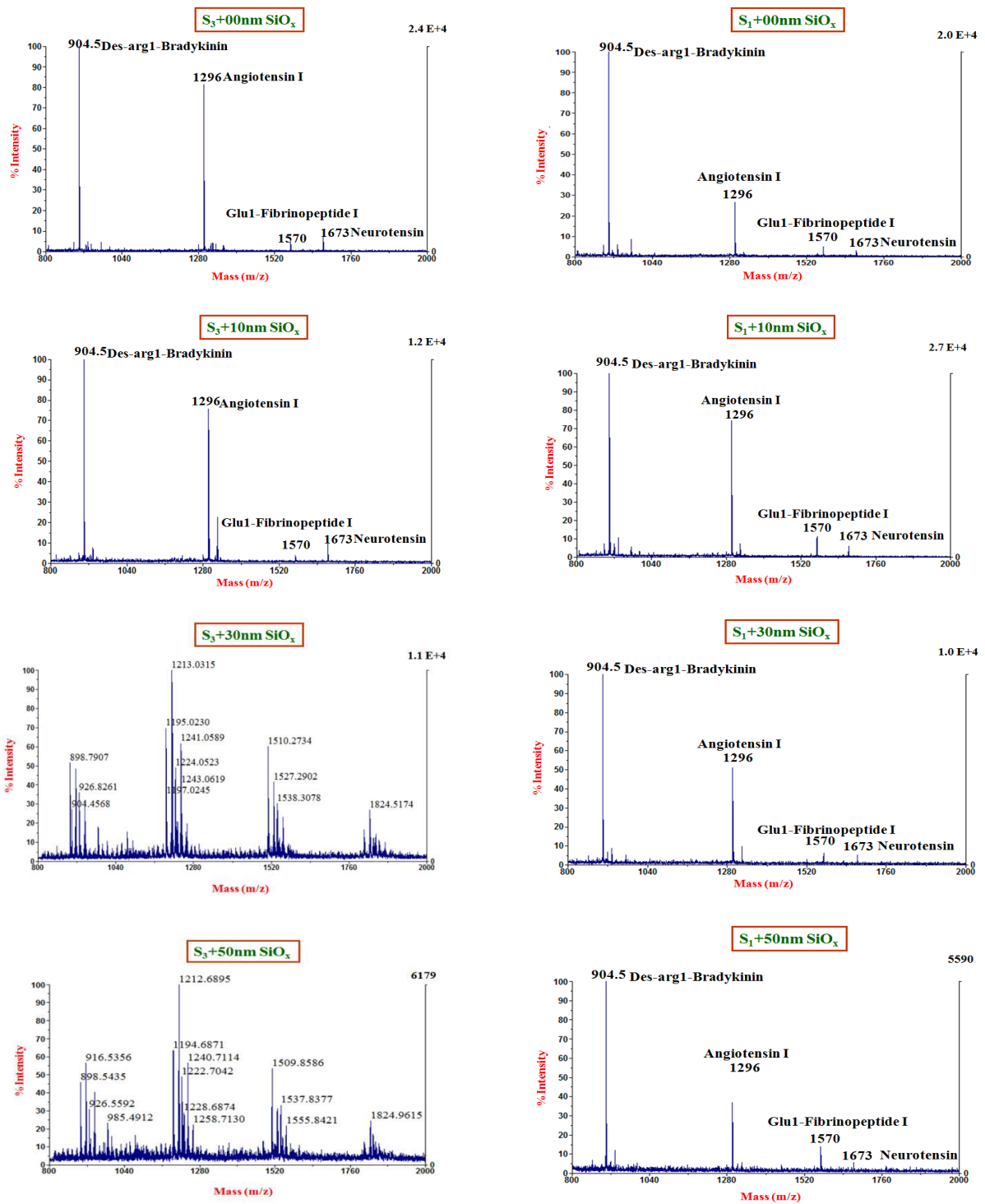
Figure 3.20: Mass spectra recorded on different NanoSi surfaces: (right) S₃ without SiOₓ layer (S₃+0nm SiOx) and S₃ + n-thick SiOₓ layer (n=10, 30 and 50 nm), (left) S₁ without SiOₓ (layer (S₁+0nm SiOx) and S₁ + n-thick SiOₓ layer (n=10, 30 and 50 nm).

Surface	Des-arg1-Bradykinin	Angiotensine I	Glu1-Fibrinopeptide I	Neurotensin
S_3	1002 (25%)	769 (26%)	153 (19%)	69 (26%)
S_3+10 nm	408 (26%)	285 (42%)	22 (36%)	32 (34%)
S_3+30 nm	high background			
S_3+ 50 nm				
S_1	871 (22%)	429 (32%)	129 (56%)	32 (40%)
S_1+10nm	853 (21%)	513 (36%)	94 (31%)	45 (27%)
S_1 + 30 nm	394 (25%)	166 (58%)	20 (45%)	16 (56%)
S1+ 50 nm	193 (37%)	72 (43%)	30 (67%)	9 (33%)

Table 3.11: Average S/N ratio values and their SD for each peptide on different surfaces: S_1 and S_3 without SiO_x layer and with various thicknesses of SiO_x (10, 30 and 50 nm).

From Figure 3.20 and Table 3.11, we observe that:

- When the S_3 surface is covered by 10 nm-thick SiO_x layer, all peptides were detected. However, in comparison to S_3 surface without SiO_x layer, the S/N values are reduced significantly (**2 times** lower for Des-arg1-Bradykinin, Angiotensine I, Neurotensin and **6 times** lower for Glu1-Fibrinopeptide I). Moreover, when the S_3 surface is coated with 30 or 50 nm-thick SiO_x layer, the spectra become very noisy, so it is difficult to identify the peptide peaks.

- When S_1 is coated with 10 nm-thick SiO_x layer, the S/N values are quasi-similar for all peptides compared to the S_1 surface without SiO_x layer and no influence of such oxide layer is observed. However when the SiO_x layer thickness was increased to 30 and 50 nm, even though the four peptides were detected, their S/N values decreased: 3 and 5 times lower for S_1+30 and S_1+50 nm thick SiO_x, respectively compared to S_1 without SiO_x layer.

From these results, it is clear that the introduction of SiO_x layer over the surface influences the DIOS-MS efficiency. Indeed, SiO_x layer is a thermal insulator causing the reduction of thermal conductivity of the surface. Thus, LDI-MS efficiency is decreased. To detect the peptides, an

increase of the laser fluence is required, leading to a significant increase of the background signal (due to peptides' fragmentation or silicon clusters). However, the S_3 surface seems to be more affected by the increase of the oxide layer than S_1. Indeed, the DIOS-MS efficiency of S_3+10 nm of SiO_x is comparable to that of S_1+30nm of SiO_x.

3.6.8. Chemical derivatization of DIOS surfaces

As mentioned above, the chemical derivatization of DIOS surfaces is an important factor in DIOS-MS analysis. It permits to stabilize and enhance the efficiency of DIOS-MS process. In our work, we have also investigated the efficiency of DIOS-MS analysis of our NanoSi substrates with various chemical terminations. The surface S_3 with different surface terminations: $-CH_3$, $-CF_3$, $-C_6F_5$ and $-COOH$ groups was chosen for the following reasons:

1) NanoSi-CH_3: -CH_3 termination (OTS) was used in previous studies in our group and has shown the highest performance in DIOS-MS analysis. [13] [14][55] [67]

2) NanoSi-CF_3: -CF_3 termination (PFTS) was used in the fabrication of omniphobic surfaces, as shown in chapter 2 (2.5).

3) NanoSi-C_6F_5: -C_6F_5 termination was developed in DIOS-MS analysis by many groups; it showed the highest sensitivity (see section [3.4.1.3]).

4) NanoSi-$COOH$: -$COOH$ termination can act as a proton donor for improving the protonation of the molecules of interest.

The -CH_3, -CF_3, -C_6F_5 and -$COOH$ terminations were introduced to the NanoSi surface either by silanization or through hydrosilylation reactions:

NanoSi-CH_3, NanoSi-CF_3 and NanoSi-C_6F_5 were prepared by silanization reaction. For that, we used octadecyltricholorosilane for the CH_3 termination (NanoSi-CH_3), *1H, 1H, 2H, 2H-*perfluorodecyltrichlorosilane for the CF_3 termination (NanoSi-CF_3), and pentafluorophenylpropyl trichlorosilane for the C_6F_5 termination (NanoSi-C_6F_5). The silanization process is described in annexe 5. NanoSi-CH_3, NanoSi-CF_3 and NanoSi-C_6F_5 surfaces are superhydrophobic with a water CA of 160°. As already discussed above, a droplet of peptide is very difficult to deposit on all these surfaces because of the "rolling-ball" effect. To overcome this problem, the hydrophobic layer was degraded by UV/O_3 treatment (4mW/cm^2, 220 nm) to reduce the contact angle from 160 to 120°. It should be noticed that a CA for water of 120° was

obtained after 4 minutes of UV/O$_3$ treatment for NanoSi-CH$_3$ surface. This leads probably to the formation of oxidized species (called here, NanoSi-CH$_{3\text{-(UV/O3)}}$).

However, NanoSi-CF$_3$ and NanoSi-C$_6$F$_5$ surfaces were resistant to the UV/O$_3$ treatment, making it impossible for the partial destruction of the hydrophobic coating, because fluorine forms the strongest bond with carbon in organic chemistry[**]. In that case, we choose to change the surface tension of the peptide droplet to reduce the water contact angle by adding 50 and 5% ethanol in the peptide solution, leading to a water CA of 120° on both NanoSi-CF$_3$ and NanoSi-C$_6$F$_5$ surfaces. We also tested NanoSi-CH$_3$ without UV/O$_3$ treatment (called NanoSi-CH$_3$). For that, 5% of ethanol was added to the peptide solution.

The NanoSi-COOH surface was prepared by hydrosilylation reaction of undecylenic acid with hydrogen-terminated NanoSi substrate (COOH termination) for 6 hours at 150°C (this reaction will be described in detail in chapter 4 [4.3.1]). NanoSi-COOH presents a strong hydrophobic behaviour with a water CA = 120° mainly due to the long alkyl chain composing the molecule. Thus, a droplet of analyte can be directly deposited on this surface without additional treatment or reagent.

The DIOS-MS performance was assessed using the standard peptide mixture at 50 fmol/µL. 1 µL of solution was spotted three times on each surface. In the case of NanoSi-COOH and NanoSi-CH$_{3\text{-(UV/O3)}}$, a peptide droplet is directly deposited on these surfaces, in the contrary to NanoSi-CH$_3$, NanoSi-C$_6$F$_5$ and NanoSi-CF$_3$ surfaces where ethanol at 5, and 50 % (v/v) have been added to the peptide solution, leading to surface tensions ≈ 60.0 mN/m (5%) and ≈ 28.0 mN/m (50%) (see Table 2.14 in chapter 2). DIOS-MS analysis was realized on the three spots. Figure 3.21 displays representative mass spectra obtained from each surface. Table 3.12 summarizes their average S/N values and SD.


[**] http://en.wikipedia.org/wiki/Carbon%E2%80%93fluorine_bond
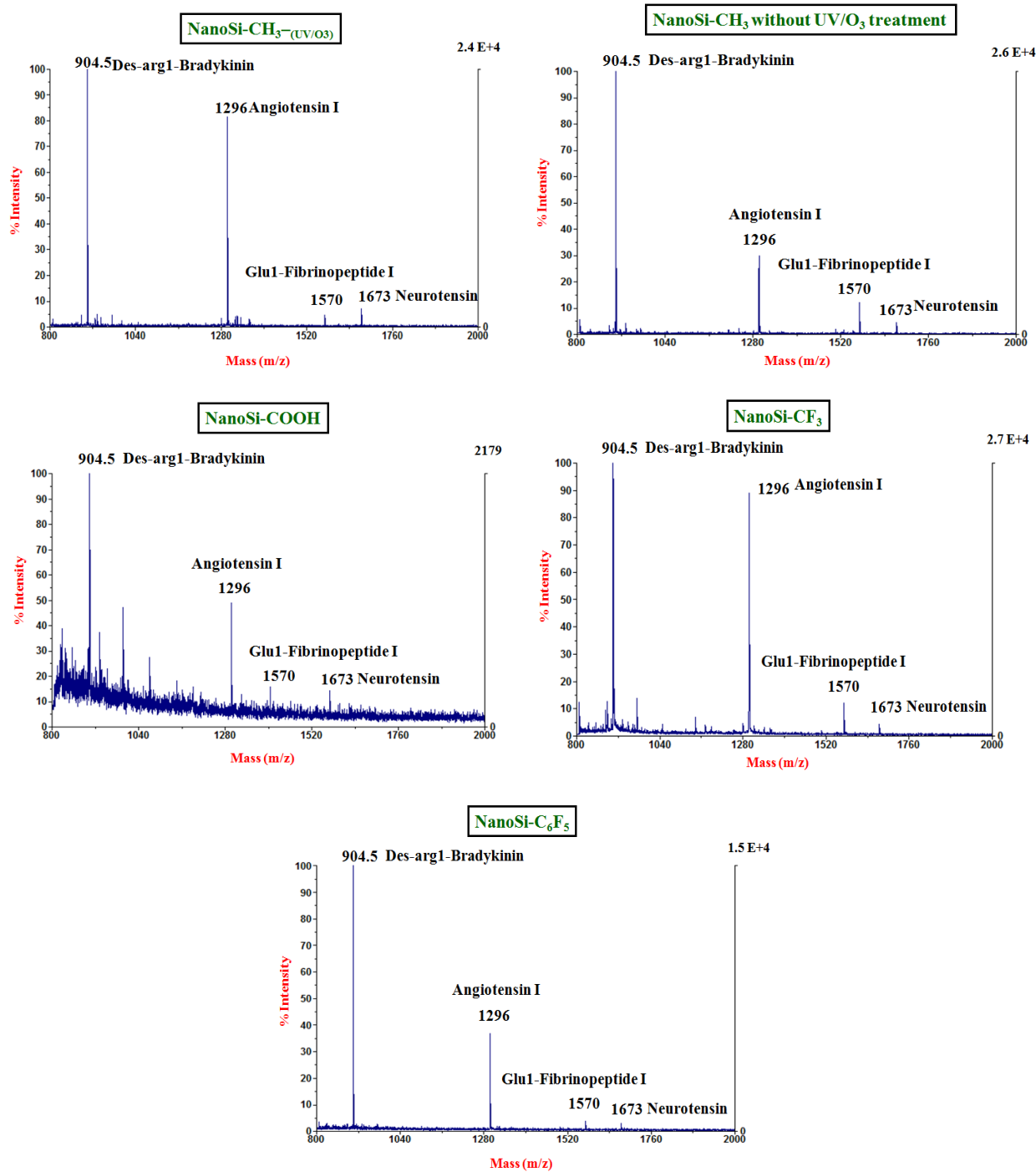
Figure 3.21: Mass spectra of 1µL (50 fmol/µL) of a peptide mixture deposited on NanoSi surfaces of different chemical terminations: NanoSi-CH₃, NanoSi-CH₃₋(UV/O₃), *NanoSi-COOH, NanoSi-CF₃, and NanoSi-C₆F₅.*

Surface termination	S/N forstandard mixture (50 fmol/µL*) and SD (%) *10 fmol/µL (Neurotensin)			
	Des-arg1-Bradykinin	*Angiotensine I*	*Glu1-Fibrinopeptide I*	*Neurotensin*
NanoSi-CH$_3$-(UV/O$_3$)	1002 (25%)	769 (26%)	153 (19%)	69 (26%)
NanoSi-CH$_3$	*1104 (31%)*	*352 (46%)*	*96 (84%)*	*37 (52%)*
NanoSi-CF$_3$	*632 (35%)*	*505 (34%)*	*43 (56%)*	*17 (41%)*
NanoSi-C$_6$F$_5$	*600 (12%)*	*195 (26%)*	*22 (13%)*	*12 (58%)*
NanoSi-COOH	*134 (*)*	*48 (56%)*	*4 (*)*	*5 (*)*

Table 3.12: S/N ratios for each tested peptide using various surfaces: NanoSi-CH$_3$, NanoSi-CH$_{3-(UV/O3)}$, NanoSi-COOH, NanoSi-CF$_3$ and NanoSi-C$_6$F$_5$ surfaces. (*): no reproductible

The results showed that all surfaces are able to detect the four peptides with high S/N values, except for the NanoSi-COOH interface which led to the lowest S/N values and lack of reproducibility. Thus, it is clear that the -COOH function, as a possible proton donor, did not improve the LDI-MS efficiency for the detection of such peptides. Moreover, the undecylenic acid has a pKa around 5 and the pH of the ammonium citrate solution is around 5.5. Thus, the carboxylic groups are mostly under their un-protonated forms. By adding a strong acid, such as trifluoroacetic acid (TFA), in the solution, the LDI process on such carboxylic surface should be improved. Also, the acid layer was grafted on the NanoSi *via* Si-C bond i. e. without intervening oxide layer, in contrast to the other surface terminations achieved *via* silanization reaction on a native oxide layer. Additional experiments are needed to clarify this point.

By comparing the efficiencies of DIOS-MS analysis of the NanoSi-CF$_3$, NanoSi-C$_6$F$_5$, and NanoSi-CH$_3$ (without UV/O$_3$ treatment) surfaces, it turns that the NanoSi-CH$_3$ is more performant than NanoSi-CF$_3$ and NanoSi-C$_6$F$_5$, except for Angiotensine I for which NanoSi-CF$_3$ presents a higher S/N value. When NanoSi-CH$_{3-(UV/O3)}$ and NanoSi-CH$_3$ surfaces are compared, the NanoSi-CH$_{3-(UV/O3)}$ gave the best results in terms of S/N values. Therefore, NanoSi-CH$_3$

degradation seems to yield the highest performance of analysis, as previously observed on NanoSi prepared using HF/AgNO$_3$ solution (surface S$_4$). [55] [56]

It seems that the -CH$_3$, -CF$_3$, -C$_6$F$_5$ and -COOH terminations introduced on the NanoSi surface S$_3$ either *via* silanization or hydrosilylation didn't lead to an enhancement of the efficiency of the DIOS-MS analysis, as compared to the NanoSi-CH$_{3-(UV/O3)}$ surface. Surprisingly, the fluoro-terminated surfaces are less efficient than the -CH$_3$ after UV/O$_3$ treatment, in contrast to the literature studies. [137]

Moreover, the wetting properties also play a crucial role even for surfaces presenting the same contact angle, notably on the spot formation and analytes distribution.

These results clearly indicate the importance of omniphobic surfaces in DIOS-MS analysis of hydrophobic molecules. Indeed, to analyze hydrophobic or non polar biomolecules, which are insoluble or partially soluble in water or buffer solutions, an organic solvent (such as DMF, acetonitrile, ethanol, DMSO...) is added in the buffer solution. That leads to a lower surface tension of the peptide solution. However, analytes droplet with such a low surface tension is difficult to deposit on surfaces with either -CH$_3$, -C$_6$F$_5$ or hydrogen termination. The droplet will spread all over the DIOS surface, leading to a non uniform spot formation ("coffee stain"). The omniphobic surfaces with –CF$_3$ termination can be very useful in this case. Indeed, as shown above, the NanoSi-CF$_3$ surface displayed a contact angle of 120° for a peptide solution dissolved in ethanol/water (50/50 v/v). This surface is superhydrophobic and omniphobic. These properties lead to the formation of uniform spots and to the possibility to detect highly insoluble molecules such as lipids by DIOS-MS analysis on such a surface.

3.7. Conclusion

In the first part of this chapter, I presented a general review on the DIOS-MS method, which corresponds to one type of SALDI-MS techniques based on silicon. The SALDI or DIOS surfaces are able to absorb photons from a pulsed laser irradiation (UV) and then thanks to non-radiative recombinations and heat confinement allow the desorption/ionization of adsorbed analytes. For SALDI- and DIOS-MS processes, the substrate morphology, chemical termination, even the presence of water and solvent seem to have an important role. A big advantage of SALDI-MS and DIOS-MS methods is that they do not require organic matrices and thus can be

used for the detection of small biomolecules (<700 m/z) with high quality of MS due to the absence of matrix ions.

In the second part, I discussed our results on DIOS-MS performance of NanoSi substrates synthesized by chemical etching of crystalline silicon in $NaBF_4/AgNO_3$ or $HF/AgNO_3$ aqueous solutions and SiNWs prepared *via* CVD growth. All the substrates were successfully used as DIOS platforms in LDI-MS analysis of peptides with a high performance (high sensitivity: 0.2 fmol). Among the tested surfaces, NanoSi fabricated by chemical etching of crystalline silicon in $HF/AgNO_3$ aqueous solution showed the best performance in DIOS-MS analysis. There was no apparent influence of the doping type and level of the silicon substrate on the LDI-MS efficiency. However, in the case of NanoSi, synthesized by chemical etching of crystalline silicon in $NaBF_4/AgNO_3$ aqueous solutions, it was hard to establish a clear influence of the doping type or level of the silicon substrate on DIOS-MS efficiency. Indeed, the different silicon types led to various NanoSi surface morphologies using $NaBF_4/AgNO_3$ aqueous solutions. On the other hand, DIOS-MS analysis performed on SiNWs surfaces, prepared using the VLS growth technique, indicates that undoped SiNWs are more performant in LDI-MS analysis of peptides than the doped SiNWs.

Finally, I investigated the influence of SiO_x coating and chemical modification of the NanoSi surfaces to improve their efficiency of DIOS-MS analysis. It was found that:

1. SiO_x deposition on NanoSi surfaces led to a decrease of LDI-MS efficiency.
2. Acid-terminated NanoSi surfaces permit LDI-MS detection of all tested peptides, but with a high background signal. The other chemical terminations ($-CH_{3-(UV/O3)}$, $-CH_3$, $-CF_3$ and $-C_6F_5$) showed higher performances with the best result found for $-CH_{3-(UV/O3)}$, termination. The good results obtained for the $-CF_3$ termination suggests that such a surface can be applied for LDI-MS analysis of insoluble molecules for which an organic solvent is required.

4. Affinity-Laser Desorption/Ionization Mass Spectrometry Analysis on Silicon Nanostructures

4.1. Introduction

For the analyses of complex biological mixtures, the sample preparation plays a critical role and can lead to improve the sensitivity and to get a better peak shape. Indeed, mass spectrometry analysis of compounds at low concentration levels from complex mixtures, such as body fluids or tissue homogenates, is greatly facilitated by selective capture and enrichment approaches. The need for selectivity is particularly acute in the area of small molecule analysis for forensic purposes, food quality control, metabolomic, and pharmacology, where examples of complex and heterogeneous mixtures abound. [155]

In laser desorption/ionization mass spectrometry (LDI-MS), including surface-assisted laser desorption/ionization (SALDI) and matrix-assisted laser desorption/ionization (MALDI), signal suppression from multiple components in biological samples is a significant disadvantage. An isolation step is often performed prior to the separation from downstream analysis to achieve selective analysis. [156] This step avoids any direct mass spectrometry evaluation of analytes selectively captured and enriched on a support surface and hinders rapid and sensitive analysis. Many efforts to achieve analytes enrichment and subsequent mass spectrometry analysis have been made [111]. Weinberger *et al.* [121] developed surface-enhanced laser desorption/ionization (SELDI) technique combining chromatography and MS analysis on a same chip. In that case, the affinity ligand is covalently bounded to the surface and allows specific capture of the target protein. Then organic matrix is deposited for MALDI-MS analysis. Dunn *et al.* [157] have shown that a gold interface modified with nitrilotriacetic acid (NTA)-Fe(III) complex can be used for specific capture of phosphopeptides and their subsequent MALDI-MS analysis. Shen *et al.* [134] reported a simple method for the preparation of a self-assembled nitrilotriacetic acid (NTA) monolayer on gold surface, which can be used as a matrix-assisted laser desorption/ionization time of flight mass spectrometry (MALDI-ToF-MS) sample target specifically for recombinant oligohistidine-tagged proteins/peptides and phosphorylated peptides. The NTA functional groups are immobilized onto the gold surface *via* the linkage of 1,8-octanedithiol, which forms a self-assembled monolayer on gold. The chemically modified surface shows strong affinity toward the analytes of interest and allows effective removal of the common salts and detergents, and therefore leads to improved signal/noise (S/N) ratio and detection limit [134]. Another report described the functionalization of carbon nanotubes (CNT) with iminodiacetic acid (IDA) for the human body fluids exploration using MALDI-ToF-MS that can be related to biomarkers detection for the diagnosis of a disease. The CNT-IDA substrates were investigated as material-

enhanced laser desorption/ionization (MELDI). The IDA-CNT substrates were found to be an excellent material for the selective binding of biomolecules from a complex sample and their subsequent analysis with MALDI/ToF-MS. The most eye-catching features of the derivatized nanotubes are their characteristics like sensitivity, reproducibility and efficiency in the higher mass range, which is not much evident with other existing support materials [158]. Another example described in the literature is the use of spots, consisting of a thin film of anatase titanium dioxide (TiO_2) sintered onto a conductive glass surface. This on-target phosphopeptide enrichment method showed specific enrichment and direct analysis by MALDI-MS of phosphorylated peptides. The protocol leads to an enrichment efficiency that is superior to what has been reported before for similar methods. But these interfaces still require organic matrices to realize the LDI of the captured analytes. [159].

A broad range of surface chemistries and specific biomolecular capture agents including antibodies, enzymes, receptors, DNA fragments, and aptamers have been reported. However, the need of a matrix in SELDI means that scope for small molecule analysis remains limited. We know that SALDI interfaces such as porous silicon, silicon nanowires, metal oxide wires, carbon-based interfaces, metal nanoparticles and many others are efficient interfaces for LDI of small compounds giving high MS sensitivity of detection (see chapter 3). However, only few attempts concerning affinity SALDI-MS interfaces have been described in the literature. Lowe *et al.* [117] have exploited the presence of certain functional groups and, in particular, fluorinated species, such as pentafluorophenyl groups on the porous silicon (pSi) surface, for the detection of small hydrophobic molecules from complex biological samples by means of selective capture of hydrophobic species from aqueous solution and removal of abundant hydrophilic species such as salts. While this development clearly sets the stage for selective analysis in matrix-free LDI-MS, further advances will depend particularly on surface modifications yielding specific molecular affinity. Inroads have certainly been made to incorporate affinity capture in pSi LDI-MS using immobilization of protein receptors [160] [161] [162] or surface functionalization with fluorosilanes in combination with perfluoroalkyl affinity tagged analytes [150]. However, these studies have not yet demonstrated sensitive and selective capture of target analytes from a mixture of structurally similar molecules in aqueous solution. Recently, Lowe *et al.* [118] performed the immobilization of antibodies antibenzodiazepine (illicit drugs) on porous silicon *via* isocyanate chemistry, producing an immunoaffinity surface. They have demonstrated that the functionalized interfaces are able to selectively capture benzodiazepine, from a mixture of 2 benzodiazepines and cocaine, and subsequently detected by matrix-free LDI mass-spectrometry.

However, the immunoaffinity SALDI interfaces are costly and less sensitive than usual hydrophobic porous silicon LDI-MS interfaces. Another example, combining specific capture and mass spectrometry analysis was the use of TiO_2 nanoparticles spots on aluminum foil for phosphopeptides enrichment. The TiO_2 was used as a specific affinity for *in situ* enrichment of phosphopeptides and as SALDI-MS analysis with lower sensitivity (few pmoles) [163]. However, to date, no highly efficient affinity SALDI interface has been demonstrated.

In this chapter, we report a simple method for the preparation of NTA self-assembled monolayer on silicon nanostructures (NanoSi) surface, which is a derivative of the well-known immobilized metal ion affinity chromatography (IMAC) technique. The method is widely used because of its purification performance and its simplicity to handle. We have demonstrated in previous studies that NanoSi substrates display very good mass spectrometry sensitivity for small molecules' analysis [55], and they are able to detect different levels of peptide methylation [56]. We have also shown that NanoSi substrates can be easily coupled to a digital microfluidic system [13] for a precise distribution of nanodroplets of peptides on specific locations, followed by DIOS-MS analysis of the deposited peptides. The NTA-NanoSi-LDI chip, developed in this work, allows a specific capture of the target of interest and its subsequent MS analysis without any re-deposition, addition of matrix or any other post-treatment of the captured analytes, both performed on the same interface. This provides an easy approach for on-probe enrichment, purification or separation of 6*histidine-tagged peptide.

We will first present the technique for the immobilization of NTA on NanoSi surface and its characterization. Secondly, we will perform specific interaction between histidine-tagged peptide and NTA-Ni^{2+}-terminated NanoSi surface. The different steps leading to peptide immobilization were characterized using FT-IR, contact angle (CA) and fluorescence measurement, and DIOS-MS analysis.

4.2. Histidine amino acid and NTA-Ni^{2+} coordination complex

4.2.1. Properties of histidine amino acid residue

Histidine amino acid (Aa) residue is one of the 22 proteinogenic amino acids. This peptide is a weak base containing an imidazole ring on its side chain and three dissociable groups (alpha-carboxyl group COOH, alpha-amino group NH_2 and NH for imidazole ring) and the pK_a for those groups ($pK_{a1}=1.8$, $pK_{a2}=9.2$ and $pK_{aR}=6$, respectively)[††]. Histidine residue can be present under different tautomeric forms as shown in Figure 4.1, depending on pH:

✓ **pH < pKa$_1$=1.8**, histidine Aa residue is in the tautomeric **form 1** and the net charge is about +2 on the alpha-amino group (NH_3^+) and the NH^+ of the imidazole ring.

✓ **pK$_{a1}$=1.8 < pH < pK$_{aR}$=6**, histidine Aa residue is in the tautomeric **form 2** and the net charge is about +1 on three dissociable groups (COO^-, NH^+ and NH_3^+).

✓ **pK$_{a\ R}$=6< pH < pK$_{a2}$=9.2**, histidine Aa residue is in the tautomeric **form 3** and the net charge is 0 on two groups (COO^- and NH_3^+).

✓ **pH > pK$_{a2}$=9.2**, histidine Aa residue is in the tautomeric **form 4** and the net charge is -1 on alpha-carboxyl group (COO^-).
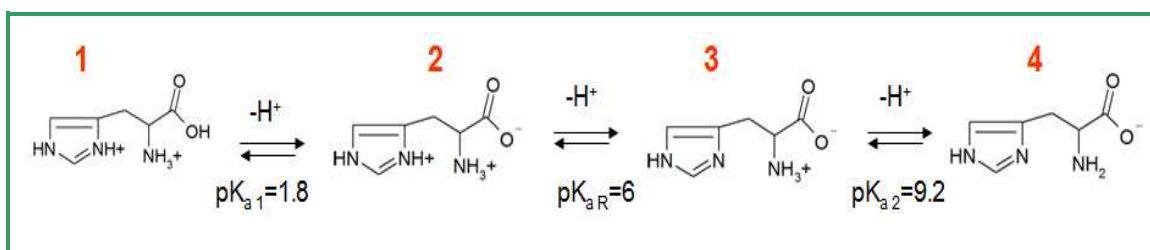
Figure 4.1: Different tautomeric forms of histidine Aa residues as a function of pH.[1]

To achieve an efficient interaction between His-tagged fusion peptides or proteins with NTA-Ni^{2+} interface as shown in Figure 4.2, histidine Aa must be in the tautomeric form 3, i.e. the net charge equals to zero. Thus, for realizing this coordination link we must work near neutral pH allowing one of the nitrogen from imidazole ring to be un-protonated in order to act as an electron donor.

[††] http://en.wikipedia.org/wiki/Histidine

4.2.2.   NTA-Ni^{2+}-Histidine-Tag interaction

Nitrilotriacetic acid (NTA) is a tetradentate complexing agent. Indeed NTA group can give four electron pairs to Ni^{2+} ions (three pairs from the COOH groups and one pair from the nitrogen atom), leading to the formation of NTA-Ni^{2+} complex. Furthermore, Ni^{2+} ion has six empty orbitals, and used only four empty orbitals to accept four electron pairs from NTA group. Thus, two empty orbitals of Ni^{+2} are free after the complexation with NTA. Thus, the free orbitals left will accept two other electron pairs from two water molecules, as illustrated in Figure 4.2 (a). Then, when histidine Aa residues are present in the protein or peptide, a coordination link between NTA-Ni^{2+} and nitrogen of imidazole ring (from the histidine) will take place as shown in Figure 4.2 (b). [164] [165] [166] [166]
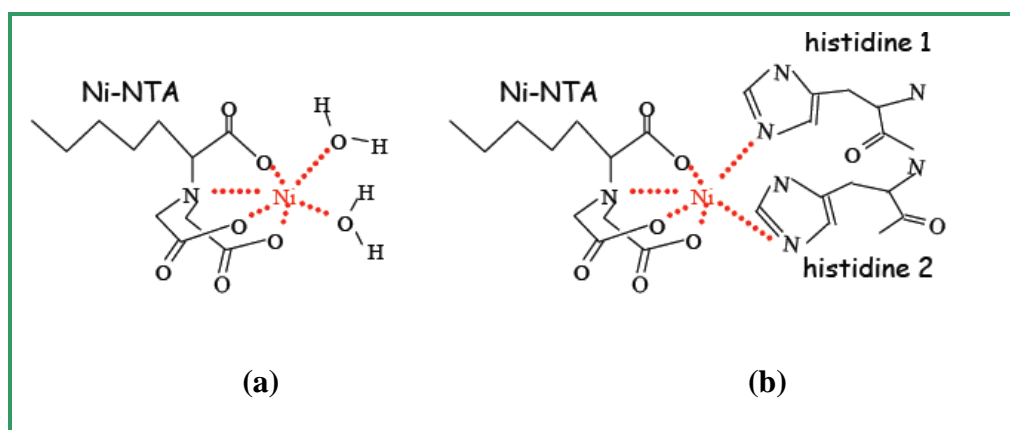
Figure 4.2: NTA-Ni^{2+} interaction with (a) two water molecules and (b) two histidine Aa residues.

To break this coordination link between NTA-Ni^{2+} complex and the His-tagged peptide (or protein), i.e. their release from the NTA-Ni^{2+} complex, there are several methods. [164][165] [167] [168][169] [170]

1. *Adding an excess of a competitor such as imidazole, which will interact with NTA-Ni^{2+} and substitute the His-tagged biomolecules.*

2. *Decreasing the pH. Indeed, the nitrogen of the imidazole group of histidine will be protonated and couldn't form anymore the coordination link with the NTA-Ni^{2+} complex, leading to the release of the captured biomolecules.*

3. *Removal of the complexed Ni^{2+} ions by addition of ethylenediamine tetraacetate (EDTA). In that case, all captured biomolecules and bivalent ions are released in the solution.*

Therefore, the sensor surface with NTA-Ni^{2+} termination can be quickly regenerated and reused. It has to be noted that decreasing the pH is the most used method for releasing the captured biomolecules.

4.3. Strategy for linking NTA groups on NanoSi surface

To couple IMAC with DIOS-MS techniques, we have performed the immobilization of NTA-Ni^{2+} groups onto NanoSi surface in several steps *via* a hydrosilylation reaction, as illustrated in Figure 4.3:

(1) Coupling of a terminal carboxylic acid monolayer onto NanoSi-H by thermal hydrosilylation reaction with undecylenic acid via a Si-C bond.
(2) Conversion of COOH-termination to amino-reactive linker, NHS-ester.
(3) Introduction of NTA-termination by covalent attachment via an amide link.
(4) Formation of NTA-Ni^{2+} complex.

Each step of the chemical surface modification has been characterized by Fourier transform infrared spectroscopy (FT-IR), contact angle (CA) measurements and X-ray photoelectron spectroscopy (XPS).
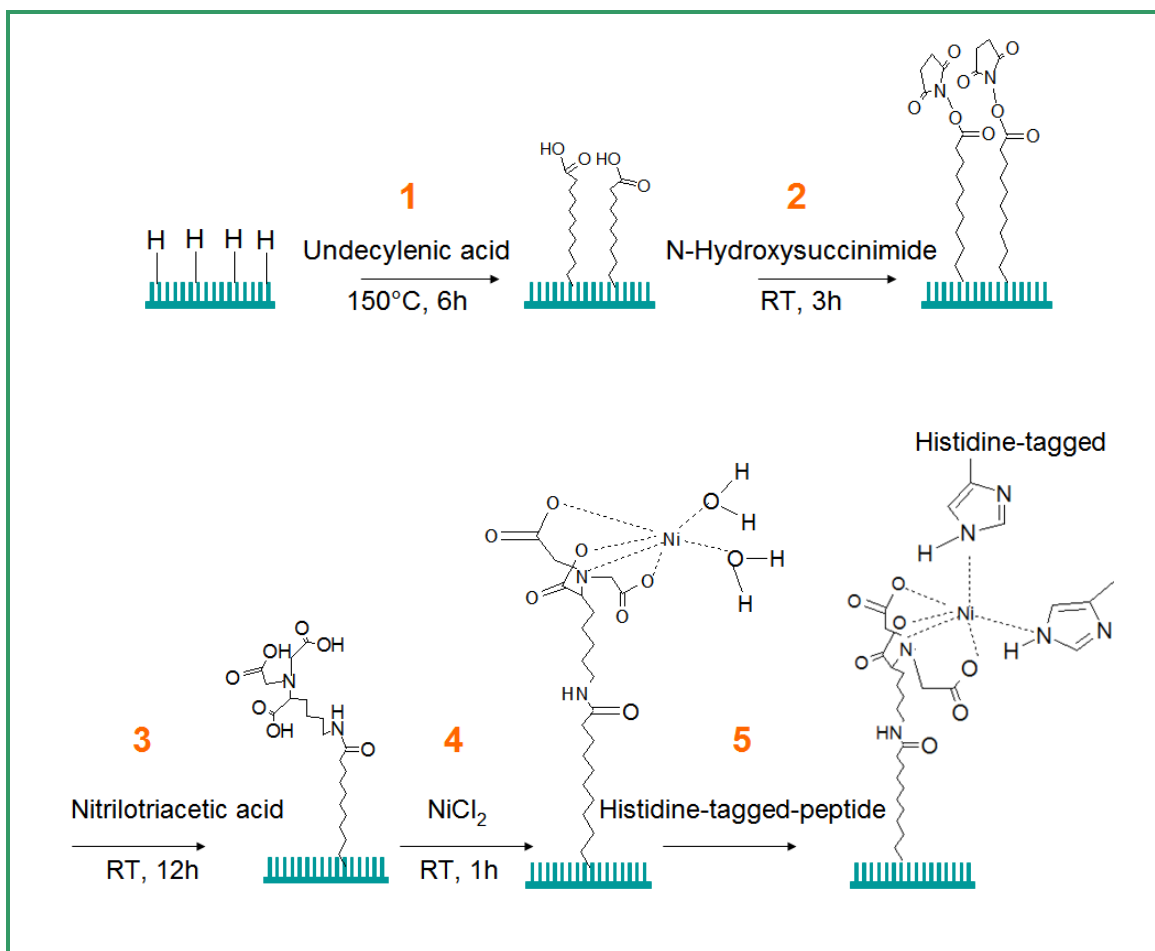
Figure 4.3: Different steps for NTA incorporation onto NanoSi surface.

The fabrication of our DIOS interfaces was achieved using two methods: (1) metal-assisted chemical etching using $NaBF_4/AgNO_3$ or $HF/AgNO_3$ aqueous solution, resulting in NanoSi surfaces, (2) growth of silicon nanowires *via* the Vapour-Solid-Liquid, resulting in SiNWs (see chapter 1). All the prepared substrates showed good LDI-MS performance (see chapter 3). However, in this chapter, we used NanoSi interface, fabricated using 0.02 M $AgNO_3$/2.5 M HF aqueous solution at 53°C for 10 minutes, as affinity DIOS interface. We have chosen it due to the fact that this interface was already optimized for mass spectrometry analysis in previous studies [13] [55].

4.3.1. Carboxylic acid termination

The carboxylic acid-terminated NanoSi surface (NanoSi-COOH) was obtained by thermal hydrosilylation reaction between the hydrogen-terminated NanoSi and undecylenic acid (Figure

4.3 and step 1). This reaction was widely described in the literature on flat and porous silicon surfaces. [170][171][172][173] [174] Herein, the same protocol was applied for our surfaces:

- NanoSi interfaces were first immersed in 50% hydrofluoric acid for 1 min, resulting in hydrogen-terminated silicon surface (NanoSi-H). This step must be done just before the thermal hydrosilylation reaction. Because, the Si-H bond reacts quickly in ambient air to form an oxide sub-monolayer.

- Then, the NanoSi-H surface was placed in a Schlenk tube containing previously deoxygenated neat undecylenic acid. The thermal reaction was performed at 150°C for 6h under nitrogen gas bubbling to inhibit oxidation of the hydrogen-terminated surface. The resulting surface was washed thoroughly in dichloromethane (2x5 minutes) and twice in ethanol (5 minutes each) under orbital agitation.

- However, the formation of undecylenic acid mutlilayers is not excluded and can occur because of the weak interactions between the molecules such as the Van der Waals forces and hydrogen bonding. Thus, the surfaces were immersed in hot acetic acid for 10 min in order to obtain an acid monolayer on the surface. Finally, the surfaces were again washed twice with deionized water under agitation for removing acetic acid traces and then dried under a gentle stream of nitrogen.

4.3.2.   Activation of carboxylic acid with *N*- hydroxysuccinimide

To couple the NTA molecule through amide bond formation, NanoSi-COOH surface should be activated with *N*-Hydroxysuccinimide to yield reactive NHS ester-terminated NanoSi interface (NanoSi-NHS) (Figure 4.3, step 2). A freshly prepared carboxylic interface was dipped in a solution of 0.2 M NHS and 0.4 M dicyclocarbodiimide (DCCI) in *N,N*-dimethylformamide (DMF) for 3h at room temperature. To remove the excess of unreacted reagents, the surface was washed three times in DMF and then two times in ethanol under agitation and dried under a stream of nitrogen.

4.3.3.   NTA termination

The NTA group was introduced onto the surface by immersing the NanoSi-NHS surface in 0.01 M N-(5-Amino-1-carboxylpentyl) iminodiacetic acid (NH$_2$-NTA) in dimethylsulfoxide (DMSO) solution and 0.07 M triethylamine (TEA) for 20h at room temperature under agitation.

Then, the surface was washed three times with DMSO and two times with ethanol under agitation to remove the excess of unreacted reagents. Finally, the surface was dried under a stream of nitrogen, resulting in NanoSi-NTA surface.

4.3.4. NTA-Ni^{2+} complex formation

Prior to the interaction with His-tagged biomolecules, the NTA group must be complexed to Ni^{2+} ions leading to a NTA-Ni^{2+}-terminated NanoSi interface. The carboxylic moieties (-COOH) of the NTA group were first deprotonated by dipping the interface in 50 mM NaOH solution for 5 minutes at room temperature. Then, the surface is quickly rinsed in deionised water and then immersed in a 200 mM NiCl$_2$ aqueous solution for 1h at room temperature. Finally, the complexed interface is rinsed with deionised water before specific binding with His-tagged biomolecules. This reaction is performed just before peptide incubation.

4.4. Surface Characterizations

4.4.1. Fourier transform infrared spectroscopy (FT-IR)

Fourier transform infrared spectroscopy (FT-IR) is a vibrational spectroscopic technique based on the absorption of infrared beam by the interface or material to be analyzed, giving information about chemical bonds and groups present on the tested surfaces (Appendix 9). FT-IR analysis can be performed in routine very quickly (a spectrum can be obtained within 10 minutes). It's a very accurate surface analysis tool, which is largely applied. However, this technique cannot be used for the analysis of NanoSi surfaces, because of diffraction phenomenon leading to a very weak transmission signal through the sample. To overcome this problem, we used porous silicon (PSi) instead of NanoSi. For that, we performed the chemical modifications for the two surfaces: PSi and NanoSi at the same time in the same chemical bath. By using FT-IR, we were able to control the efficiency of each chemical modification step. Figure 4.4 displays the FT-IR spectra of the following surfaces: PSi-H (a), PSi-COOH (b), PSi-NHS (c), and PSi-NTA (d).
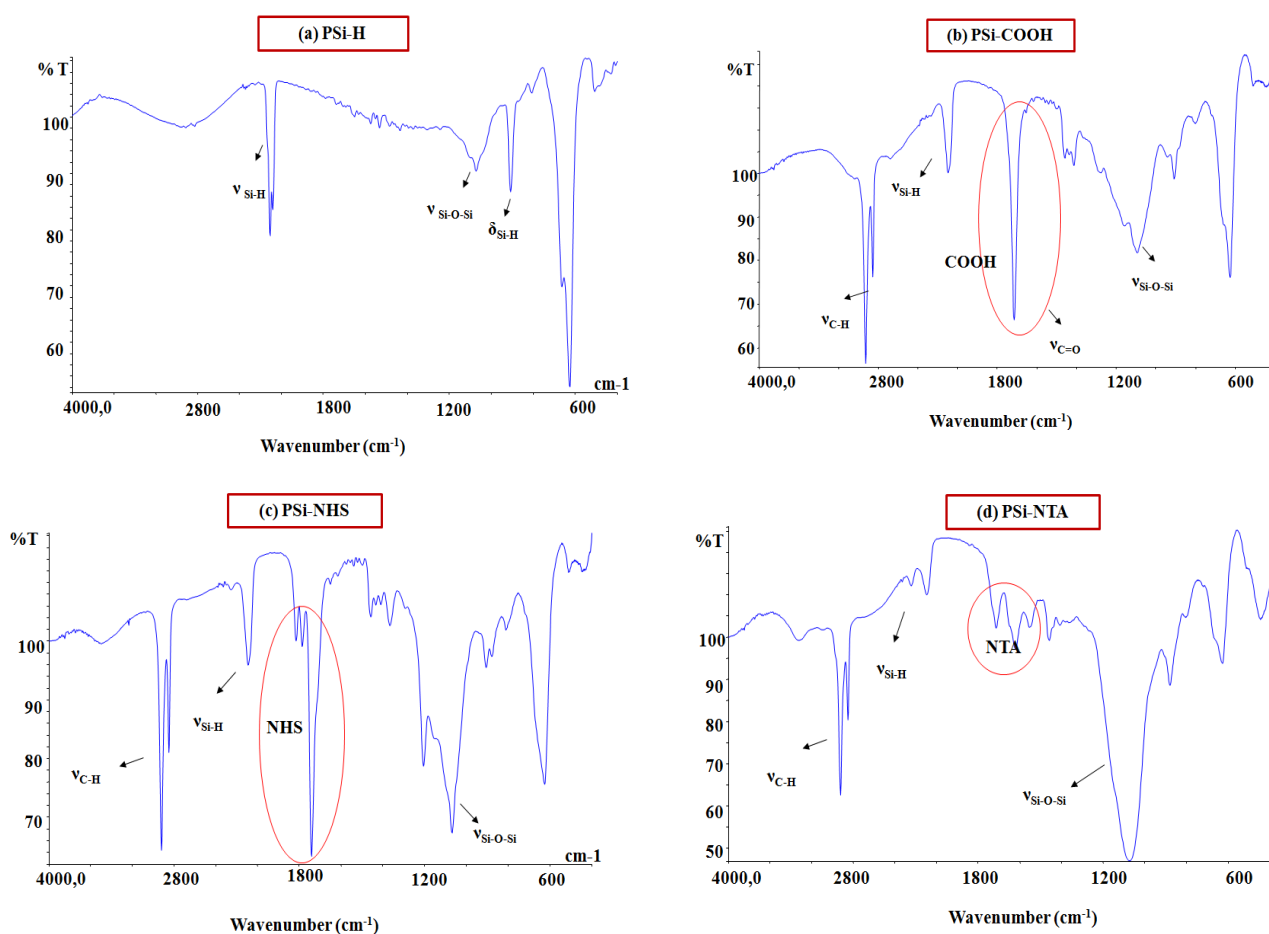
Figure 4.4: FT-IR spectra in transmission mode of (a) PSi-H, (b) PSi-COOH, (c) PSi-NHS, and (d) PSi-NTA.

Figure 4.4(a) exhibits the FT-IR spectrum of the **PSi-H**. It displays a typical band for Si-H stretching modes v_{Si-H} at 2087 and 2113 cm^{-1}, Si-H scissor mode δ_{Si-H2} at 912 cm^{-1}. A small peak at 1037 cm^{-1} due to Si-O-Si stretching mode resulting most likely from a small oxidation of the reactive surface upon exposure to ambient air. These results are in accordance with those reported in the literature. [171] [172][175]

After thermal hydrosilylation reaction between PSi-H and undecylenic acid, new peaks at 2852, 2923, 1460 and 1715 cm^{-1}, due to C-H stretching, C-H deformation and C=O stretching, respectively appeared in the FT-IR spectrum (**Figure 4.4 (b)**). A large decrease of v_{Si-H} (2115 cm^{-1}) and δ_{Si-H2} (912 cm^{-1}) intensity was observed, indicating that the reaction took place with silicon-hydride consumption. However, a small increase of $v_{Si-O-Si}$ suggests that a partial oxidation of the surface occurred during the thermal process. The FT-IR results clearly indicate that the thermal reaction between the PSi-H surface and undecylenic acid has successively led to

170

the formation of COOH-terminated PSi surface. The results are similar to those reported in the literature. [171] [172][175][176] **Figure 4.4 (c)** displays the FT-IR spectrum of **PSi-NHS.** It shows a complete disappearance of the peak at 1715 cm^{-1} ($\nu_{C=O}$ from the COOH group) as compared to Figure 4.4 (b) and the appearance of new peaks at 1818, 1787 and 1741 cm^{-1} assigned to the succinimidyl ester (stretching modes of the carbonyl at 1818 and 1787 cm^{-1} are characteristic of succinimidyl moiety). [171] [172] [175] [176] From these results, we can confirm that the acid-terminated surface is transformed to NHS termination.

The transmission FT-IR spectrum of **PSi-NTA** is shown in **Figure 4.4 (d).** It exhibits a complete disappearance of peaks corresponding to NHS (1818, 1878 and 1741 cm^{-1}) and the appearance of new peaks at 1712 cm^{-1} ($\nu_{C=O}$ of COOH group), 1620 cm^{-1} ($\nu_{C=O}$ of HN-C=O group), 1552 cm^{-1} (ν_{N-H} of amide II) and 1460 cm^{-1} (ν_{C-O} of COOH group). From these results we can conclude that the NTA group is grafted onto the PSi surface *via* amide bond formation. [168] [170] [177] [178]
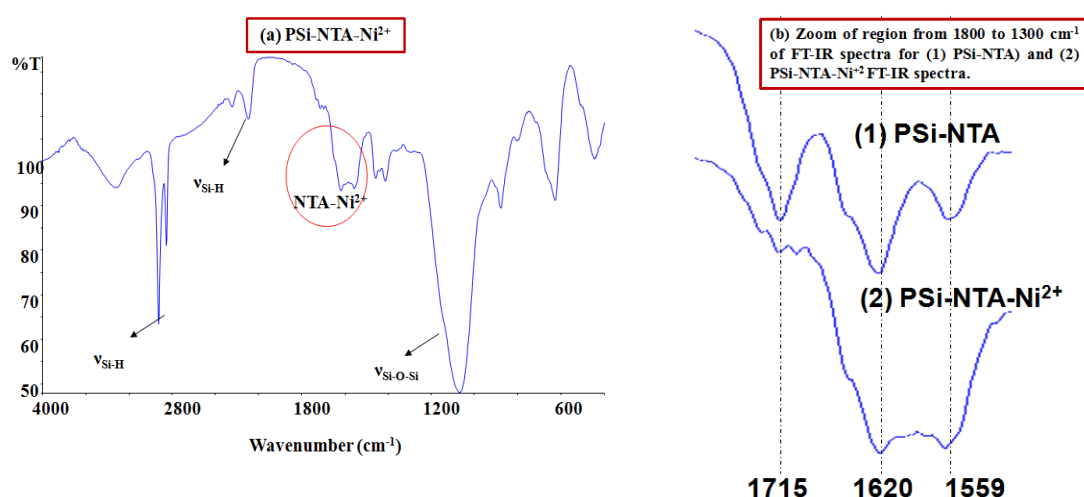
Figure 4.5: Transmission FT-IR spectra of a) PSi-NTA-Ni^{2+} and (b) Zoom of the region from 1800 to 1300 cm^{-1} of (a) PSi-NTA and (b) PSi-NTA-Ni^{2+}.

Figure 4.5 shows the FT-IR spectrum of **PSi-NTA-Ni^{2+}** complex (a) and a zoom of the region (1800-1300 cm^{-1}) of the spectra of **PSi-NTA and PSi-NTA-Ni^{2+}** surfaces (b). After deprotonation of the carboxylic acid group and the complexation of Ni^{2+} ions to the NTA group, it is observed that:

- The peak at 1715 cm^{-1} associated with C=O of the COOH group disappeared (Figure 4.5 (a)), as compared with Figure 4.4 (d). It confirms that the COOH group is readily deprotonated.

- In Figure 4.5 (b), two peaks at 1620 and 1552 cm^{-1} of PSi-NTA are observed (see above Figure 4.5(b) -(1)). However, once the NTA is complexed to Ni^{2+}, a new wide band ranging from 1620 to 1559 cm^{-1} appeared (Figure 4.5 (b)-(2)). Herein, we suggest that this result were obtained by the association of four bands corresponding to: (1) C=O of the COO$^-$ group (1615-1650 cm^{-1}) [178] (2) C=O of the HN-C=O group (1620 cm^{-1}) , (3) coordination link between NTA group and Ni^{2+} (at 1594 cm^{-1}) [168][177] , and (4) N-H of the amide II (1552 cm^{-1}). Therefore, the complexation between Ni^{2+} ions and NTA occurred.

In Figures 4.4 and 4.5, it is also observed that the intensity of Si-O-Si band increases progressively during the successive chemical steps leading to NTA termination. Surface oxidation accounts for the reaction of the remaining Si-H bonds on the PSi surface. Indeed, the thermal process consumes the maximum of 50% of the Si-H bonds. The remaining Si-H bonds are prone to hydrolysis in aqueous media, but also in ambient.

Table 4.1 summarizes the vibration modes of the chemical bonds and their associated values of frequencies represented in Figures 4.4 and 4.5.

Frequency (cm^{-1})	Mode description
2923	-CH$_2$- Asymmetrical stretching
2852	-CH$_2$- Symmetric stretching
2113	Si-H$_2$, Symmetrical stretching
2083	Si-H$_1$ Asymmetrical stretching
1700-1725	C=O (COOH)
1615-1650	C=O Asymmetrical stretching (NH-C=O or COO$^-$ group)
552	N-H (Amide II)
1460	C-O (COOH and COO$^-$
1410	C=O symmetric stretch vibration (COO$^-$)
1037	Si-O-Si
912	Si-H$_2$ scissor

Table 4.1: Frequencies of vibration modes for each chemical bond.

Consequently, the characterization of NTA-Ni^{2+} immobilisation on structured silicon is proved, although the FT-IR analysis was performed on PSi instead of NanoSi surface. To confirm this result, we characterized the functionalized NanoSi surface by contact angle (CA) measurements and XPS analysis. The results obtained will be presented in the next parts.

4.4.2. Contact angle (CA) measurements

After each chemical modification step, CA measurement was performed. This very simple and macroscopic characterization can be achieved routinely and quickly giving a good indication of the wetting properties of a surface, which are linked to their chemical termination and homogeneity. Table 4.2 displays the values of water CA after each chemical functionalization step of PSi and NanoSi surfaces. We note that:

A CA decrease from COOH to NTA-Ni^{2+} termination for both PSi and NanoSi surfaces.

173

- **PSi surfaces** with whatever termination (COOH, NHS, NTA and NTA-Ni^{2+}) are **hydrophilic**: CA of PSi-COOH=60°, PSi-NHS=53°, PSi-NTA=43° and PSi-NTA-Ni^{2+}=38°. While **NanoSi surfaces** are **hydrophobic** for COOH, NHS and NTA terminations (the CA of NanoSi-COOH=129°, NanoSi-NHS=123° and NanoSi-NTA=104°), and hydrophilic for the NTA-Ni^{2+} termination with a CA=10°. This is due essentially to the difference in terms of morphology between NanoSi and PSi surfaces and to the presence of silicon oxide formed during the chemical modification (see FT-IR characterization) on PSi. Indeed, NanoSi surface is rougher than the PSi one (Appendix 11). It has to be noted that NanoSi substrates are also oxidized (see section below, XPS characterization). Thus, NTA-Ni^{2+} terminated-NanoSi surface is more hydrophilic than NTA-Ni^{2+}-terminated PSi substrate.

- CAs of the COOH- and NHS-terminated NanoSi or PSi surfaces are close (CA of NanoSi-COOH =129° and NanoSi-NHS=123°, PSi-COOH=60° and PSi-NHS=53°).

- NanoSi-NTA surface is less hydrophobic than NanoSi-NHS and NanoSi-COOH surfaces. Because the NTA group contains three COOH groups, the interface is less hydrophobic.

- For the NTA-Ni^{2+} termination on NanoSi, the surface is superhydrophilic, probably due to the interaction of Ni^{2+} with 2 molecules of water, leading to a highly wetted surface.

CA (°)	-COOH	-NHS	-NTA	-NTA- Ni^{2+}
PSi	60°	53°	43°	38°
NanoSi	129°	123°	104°	10°

Table 4.2: Values of water CA measured on PSi and NanoSi surfaces after each chemical modification step.

4.4.3. X-ray photoelectron spectroscopy (XPS)

To further confirm the NTA grafting on NanoSi interfaces, we carried out XPS measurements (Appendix 10). Survey and high resolution spectra were recorded for the following elements: C, N, O, Si, and Ni for each chemical modification step. The XPS survey spectra are displayed in Figure 4.6. All elemental atomic concentrations increased except for Si, whose atomic concentration decreased due to the shortening of the measurement depth. From Figure 4.6, the first thing we can notice is that nitrogen peak was observed on NHS-NanoSi

interface due to the tertiary amine group from NHS-ester. After NTA grafting, the N1s signal increases significantly. Indeed, the amino-NTA molecule carries one primary amine involved in amide bond formation allowing its anchoring onto the NanoSi interface, and a tertiary amine group carrying three carboxyl branches (see Figure 4.3).

The high resolution spectra of C1s region are represented in Figure 4.7. Here, the C1s spectra for each chemical step are shown. For the first step, i. e. the introduction of carboxyl group, HO-C*=O and C-C* carbon species are detected at 289 and 285 eV, respectively with 10% of the C1s area corresponding to the carboxyl group. Grafting NTA moiety *via* an amide bond on NanoSi interface led to an increase of the peak intensity at 288.7 eV corresponding to carbonyl of the COOH group O-C*=O and to amide group HN-C*=O. As shown in Figure 4.6, the Ni^{2+} complexation didn't change the C1s spectrum.

Table 4.3 indicates that Ni^{2+} was successfully complexed on NTA-NanoSi interface with a Ni2p atomic concentration of 2.5% and peaks position at 857.6 and 875.2 eV for $Ni2p_{3/2}$ and $Ni2p_{1/2}$, respectively (Figure 4.8). It has to be noted that the SiO_x contribution increased with the successive chemical steps to reach 12% of the total area of Si2p for NTA-interface. However, no more silicon dioxide increase was observed after Ni^{2+} complexation. XPS measurements confirmed our finding from FT-IR and CA measurements proving that the NTA molecules were immobilized on our NanoSi interfaces.
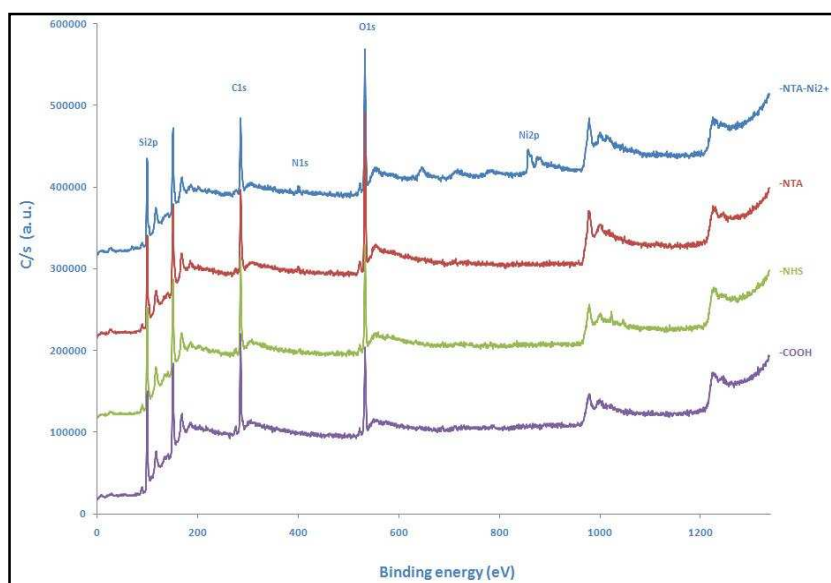
Figure 4.6 : XPS survey spectras for the different chemical modification steps of NanoSi.

175
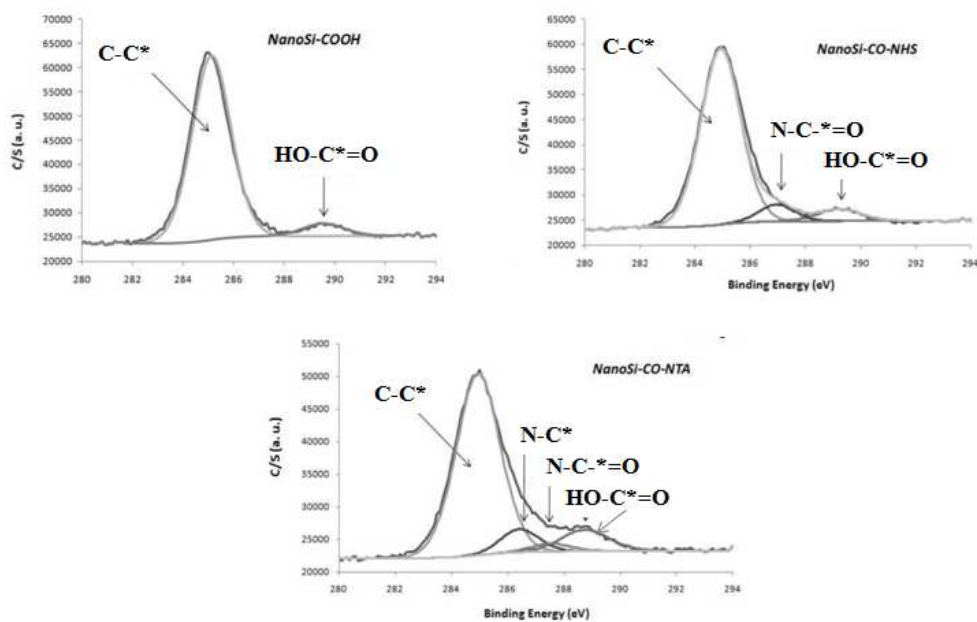
Figure 4.7: XPS high resolution spectra of C1s for the different chemical modification steps of NanoSi.

NanoSi	% of the total area				
	Si2p	O1s	C1s	N1s	Ni2p
-NTA	39.684	24.039	34.658	1.618	nd
-NTA-Ni^{2+}	39.242	23.346	33.443	1.482	2.488

Table 4.3: Atomic concentrations of the following elements: C, N, O, Si, and Ni after each chemical modification step. nd = not detected
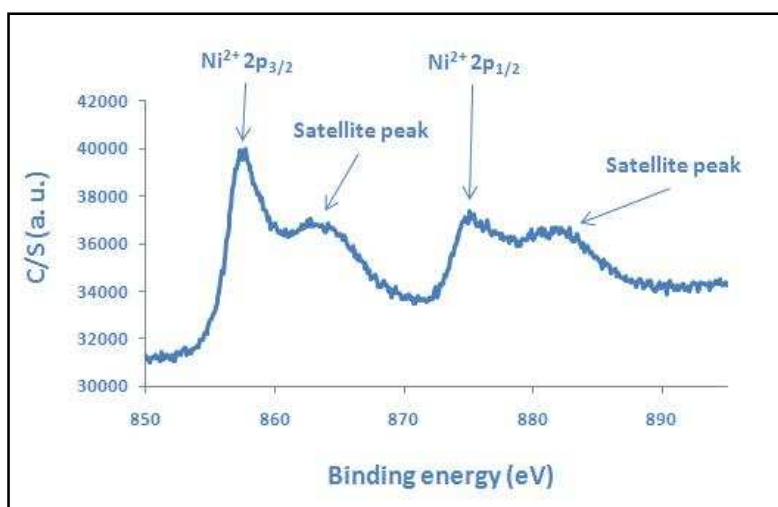
Figure 4.8: XPS high resolution spectrum of Ni2p.

4.4.4. Summary

In this section, we have successfully introduced NTA moieties onto NanoSi and PSi surfaces and performed their complexation with Ni^{2+} ions. The different steps leading to Ni^{2+} complexation were characterized using different methods (FT-IR, CA measurements and XPS). Therefore, the immobilization of His-tagged peptide can be performed on such interfaces.

4.5. Specific capture of fluorescent His-tagged peptide by NTA-Ni^{2+}-NanoSi interfaces.

4.5.1. Incubation of NTA-Ni^{2+} NanoSi interfaces with peptide solution

First of all, we decided to follow the efficiency of the capture of His-tagged peptide by our interface using fluorescence measurements, FT-IR spectroscopy and MS analysis. For that, we used two peptides:

1. Rho-His-tagged peptide (Rho-His): Rho-SYYYGG**HHHHHH**GSGG-COOH (Mass=2202 Da)

2. *Rho-HA: Rho-GGYPYDVPDYAGG-COOH (Mass=1742 Da). This peptide has no histidine residues. **(Rho= Tetramethylrhodamine)***

⬥ The protocol of peptide interaction

1. The peptides were dissolved in a PBS buffer solution (pH=7) at a concentration of 10^{-4} M.

2. 25 µL of the peptide solution were deposited onto the NTA-Ni^{2+} interfaces: NanoSi-NTA-Ni^{2+} and PSi-NTA-Ni^{2+}.

3. To avoid any evaporation problem, a small glass slide was placed above the droplet, thus creating a liquid film over the NTA-Ni^{2+} interface. This film was left in contact with the NTA-Ni^{2+} interfaces during 1h at room temperature.

⬥ The rinsing protocol

After incubation of NTA- Ni^{2+} interfaces in the peptide solution, the surfaces were washed as following:

1. *PBS buffer (5 min).*
2. *Water (5 min).*
3. *Ethanol (1 min).*
4. *Dry under a stream of nitrogen.*

Finally, the surfaces were characterized by FT-IR (Figure 4.9), fluorescence measurements (Figure 4.10) and DIOS-MS analysis (Figure 4.11).

4.5.2. Characterizations of the peptide immobilization on NTA-Ni^{2+} surfaces

1) Fourier transform infrared spectroscopy (FT-IR)

Figure 4.9 shows FT-IR spectra of (a) PSi-NTA-Ni^{2+}-Rho-His and (b) PSi-NTA-Ni^{2+}-Rho-HA surfaces. We can notice:

- The appearance of a new peak at 1715 cm^{-1} (C=O bond of COOH group) in the FT-IR spectra of the surfaces incubated in the peptide solution, as compared to the spectrum before incubation (NTA-Ni^{2+}) (Table 4.1).

- There are additional two peaks at 1620 cm^{-1} (C=O of NH-C=O and COO^- group) and at 1548 cm^{-1} (N-H of NH-C=O group) due to the interaction of NTA-Ni^{2+} with the two tested peptides Rho-His and Rho-HA.

From the FT-IR characterization, it is clear that both peptides are present on the surface after incubation. However, it is difficult to distinguish any specific capture using this technique.

It has to be noted that in the literature, most of the reports using infrared spectroscopy for studying His-Tag-peptide immobilization through NTA-Ni^{+2} complex did not mention any experiment with a peptide control i. e. a peptide without histidine residues. [168] [170] [177] From these published studies, we cannot exclude that the obtained results are essentially due to specific interaction or to non-specific adsorption or both.
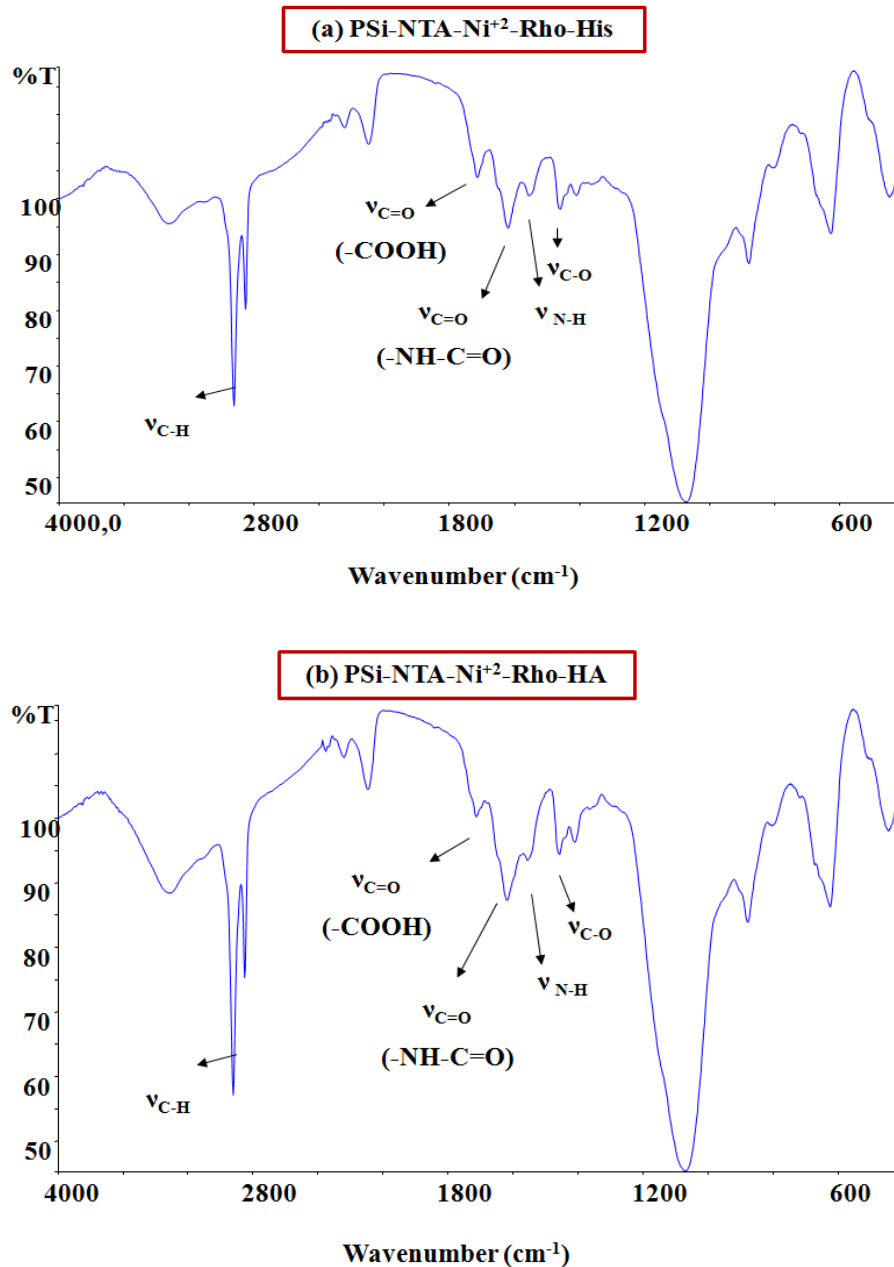
Figure 4.9: FT-IR spectra of (a) PSi-NTA- Ni^{2+}-Rho-His, (b) PSi-NTA- Ni^{2+}-Rho-HA surfaces.

2) Fluorescence and mass spectrometry characterization

Furthermore, we have performed fluorescence measurements on (a) NanoSi-NTA-Ni^{2+}-Rho-HA, (b) NanoSi-NTA-Ni^{2+}-Rho-His, (c) PSi-NTA-Ni^{2+}-Rho-HA, and (d) PSi-NTA-Ni^{2+}-Rho-His surfaces and estimated the values of intensity (I): 27839, 61255, 3170 and 3755, respectively. From these values, it is evident that non-specific adsorption occurred. The fluorescence intensity ratio for Rho-His/Rho-HA peptides is 2.3, suggesting that our NanoSi-NTA-Ni^{2+} interfaces seem to be able to capture specifically His-tagged peptides. However, non-

specific interaction is still occurring even after intensive rinsing. Subsequently, NanoSi-NTA-Rho-HA and NanoSi-NTA-Rho-His surfaces were also analyzed by DIOS-MS (Figure 4.11). From the spectra, only a peak at m/z=2202 due to Rho-His was detected. This confirms the specific interaction between Rho-His and the NTA-Ni^{2+} complex on NanoSi surface, but with a high background (S/N=11) and a low signal intensity.

(a) NanoSi -NTA-Ni^{2+} -Rho-HA
I=27,839

(b) NanoSi -NTA-Ni^{2+} -Rho-His
I=61,255

(c) PSi-NTA-Ni^{2+} -Rho-HA
I=3170

(d) PSi-NTA-Ni^{2+} -Rho-His
I=3755
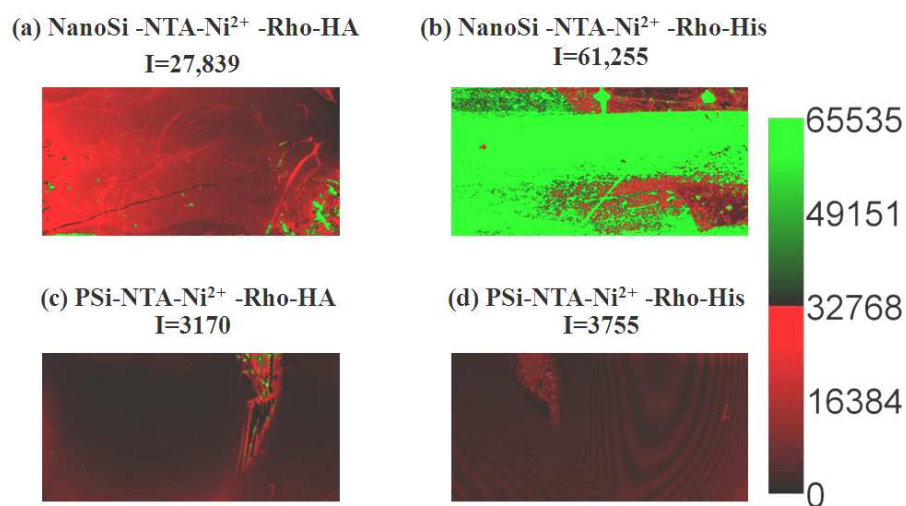
Figure 4.10: Fluorescence images and intensity values (I) of the NTA-Ni^{2+} interfaces incubated in Rho-Histidine-tagged and Rho-HA peptides.

(a) NanoSi-NTA-Ni^{2+}-Rho-HA   *(c) PSi-NTA-Ni^{2+}-Rho-HA*

(b) NanoSi-NTA-Ni^{2+}-Rho- His   *(d) PSi-NTA-Ni^{2+}-Rho- His*
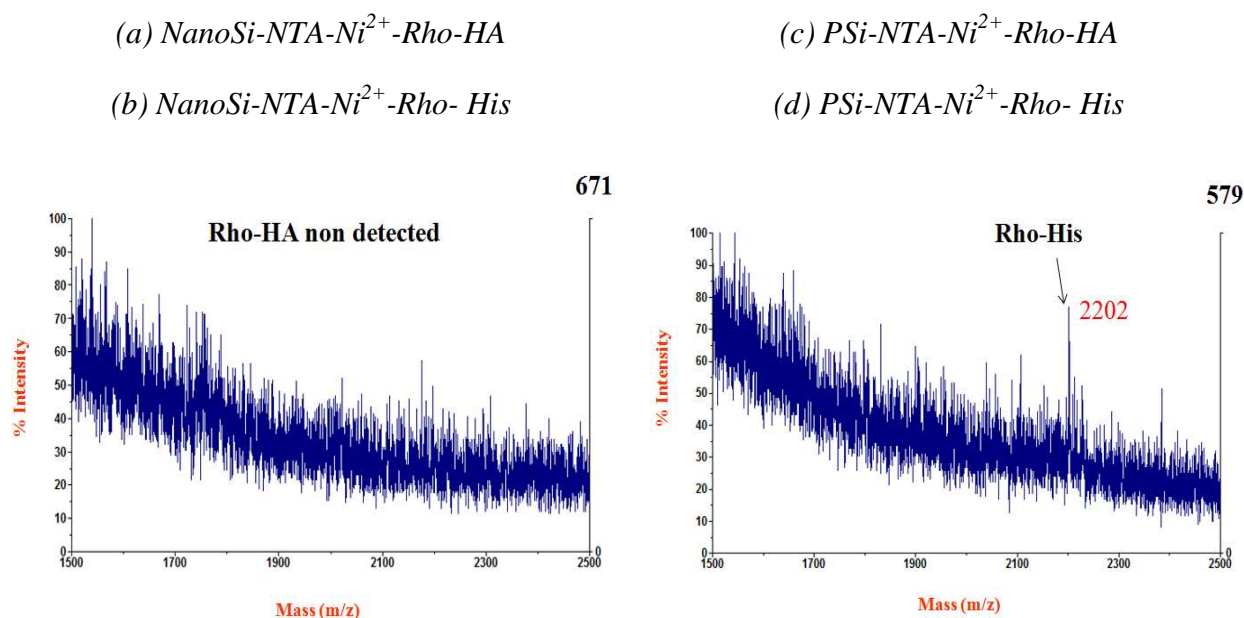
Figure 4.11: Mass spectra obtained from DIOS-MS analysis of Rho-His and Rho-HA on NTA-Ni^{2+}-terminated NanoSi surfaces.

As a control experiment, we measured the fluorescence intensity of PSi and NanoSi surfaces without chemical modifications. Their fluorescence intensities were very low (**I=103 for PSi, and I=173 for NanoSi**), as shown in Figure 4.12 compared to the fluorescence intensities obtained in Figure 4.10 for the modified NanoSi and PSi interfaces, i. e. NTA- Ni^{2+}on NanoSi and PSi incubated with Rho-HA or Rho-His peptides (**I=27839 for NanoSi-NTA-Ni^{2+}-Rho-HA, I=61255 for NanoSi-NTA-Ni^{2+}-Rho- His).**
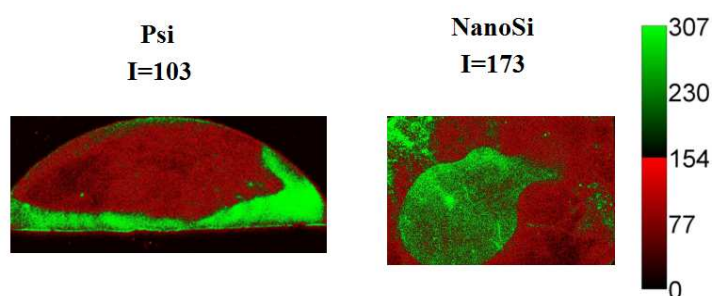
Figure 4.12: Fluorescence images and intensities (I) of PSi (left) and NanoSi (right) without chemical modification.

3) Summary

We have successfully prepared NTA-Ni^{2+}-terminated PSi and NanoSi surfaces and studied their ability for specific capture of His-Tag-peptide using FT-IR, fluorescence measurements and mass spectrometry analysis. We also performed control experiments with Rho-HA peptide (without His-Tag). Fluorescence measurements and MS analysis suggest that our NanoSi-NTA-Ni^{2+} interfaces are able to capture specifically the target peptide although a strong non-specific adsorption was observed. We tried to correlate the fluorescence measurements and MS analysis on the same substrate. Although we have clearly shown that specific interaction occurred between Rho-His and NTA-Ni^{2+} complex by fluorescence measurements on both NanoSi and PSi interfaces, only traces of the Rho-His peptide was detected by MS.

We further used other peptides, the Des-arg1-Bradykinin modified or not with a His (6*)-Tag to check the influence of the buffer solution. These peptides don't carry a Rhodamine moiety so the characterization of the interaction between the NTA-Ni^{2+} complex and peptides will be only assessed by mass spectrometry.

4.5.3. Influence of the buffer solution on DIOS-MS analysis

Usually, in the IMAC experiments, physiological buffers such as PBS are used for performing the capture of His-proteins or peptides (see section 1.1). However, the last experiments showed that although a specific interaction occurred between Rho-His and NTA-Ni^{2+} complex (fluorescence measurements) on both NanoSi and PSi interfaces, only traces of the Rho-His peptide were detected by MS. Thus, one has to be sure that the PBS buffer used in our experiments, containing different concentrations of salts, is suitable firstly for the specific capture and secondly for DIOS-MS analysis.

For this purpose, we investigated two new peptides (without Rho-tag)

- ✓ Des-arg 1-Bradykinin-6*His-Tag (DAB-His): (Ac)-**HHHHHH**RPPGFSPF-OH (MW=1768 Da, pI=9.84, 1 positive charge @ pH 7.4, polar).
- ✓ Des-Arg^1-Bradykinin (DAB): NH_2-RPPGFSPF-OH (MW=904 Da, pI=10, (1 positive charge @ pH 7.4, relatively non polar).

DAB-His and DAB peptides were dissolved in three different buffer solutions with a molar ratio DAB-His/DAB = 1 in deionized water (pH = 6.8), PBS (pH 7.2) and ammonium citrate 1 mM (adjusted to pH 7.5). Then, 1 µL droplet of the peptide mixture solution (100 fmol/µL) was deposited on a NanoSi-OTS, UV/O$_3$ treated to reach a final CA of 120°, and dried in air (see chapter 3). The obtained mass spectra are displayed in Figure 4.13 with PBS (a), water (b) and ammonium citrate buffer (c). Their average S/N and error values are summarized in Table 4.4 (average of three measurements).

In Figure 4.13(a), no peaks were detected in the mass spectrum of the peptide mixture dissolved in PBS. In contrast, both peptides (DAB-His and DAB) were detected in the mass spectra of the peptide mixture dissolved in water and ammonium citrate buffer (Figures 4.15 (b) and (c)). The best signal intensity and S/N ratios values were obtained for ammonium citrate buffer for both peptides. It was found that the S/N value of DAB peptide was always higher than that of DAB-His peptide in both water and ammonium citrate buffer solution. Indeed, in water, the S/N value of DAB-His is very small and sometimes not detected, while a value of 286 was calculated for DAB. In ammonium citrate buffer, the S/N value of the DAB peptide (S/N=1582) is 2 times higher than that of DAB-His (S/N=793).

In fact, the PBS buffer solution contains Na^+ or K^+ counter ions, which provide new ion species or adducts leading to the hindering of the quality of mass spectra as already mentioned in

chapter 3. In contrary, ammonium citrate buffer solution is rich in NH_4^+ ions known to enhance LDI process in DIOS analysis .

From this, we decided to use ammonium citrate buffer solution for further experiments of IMAC-DIOS-MS analysis.
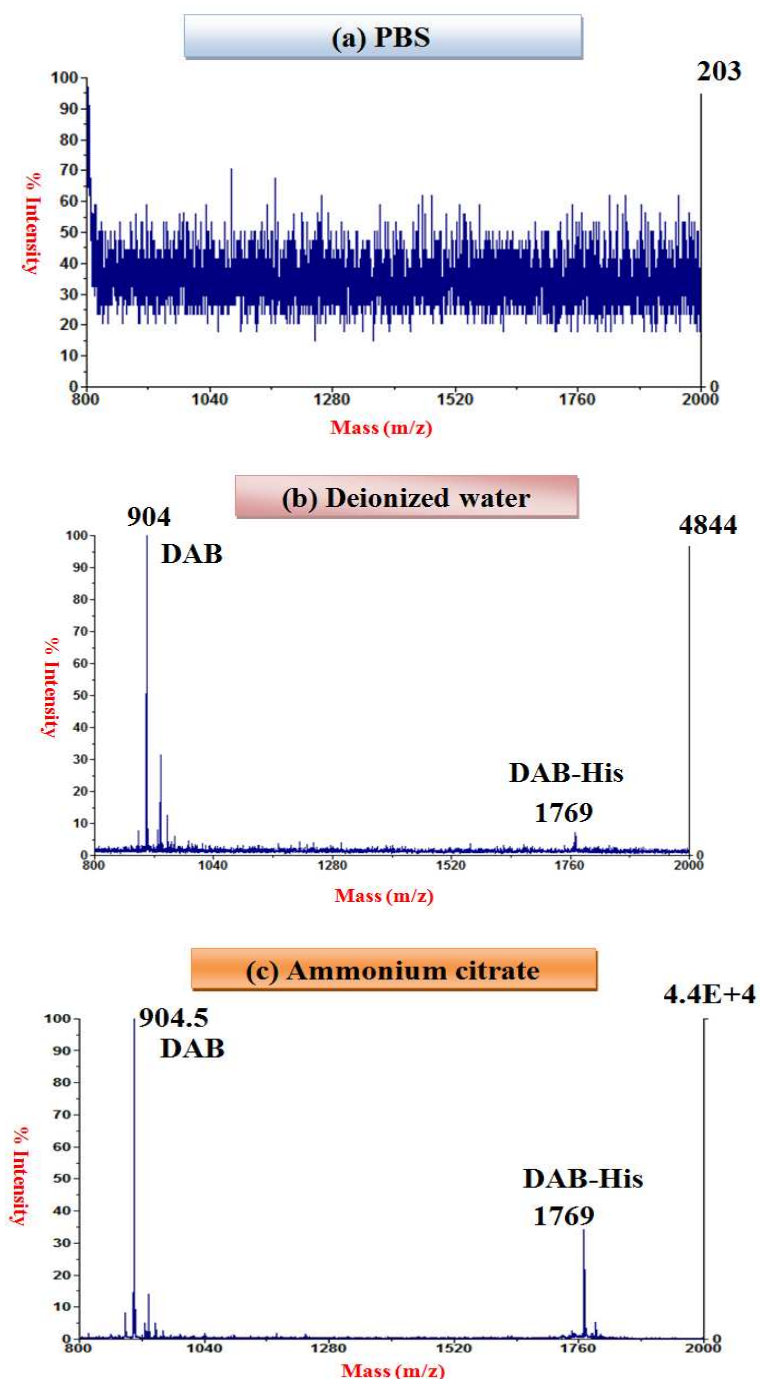
Figure 4.13: Mass spectra obtained from DIOS-MS analysis of a peptide mixture (DAB-His and DAB (1/1)) in different buffers: (a) PBS, (b) deionized water, (c) ammonium citrate.

Buffer	S/N of DAB (SD%)	S/N of DAB-His (SD%)	Intensity (SD%)
PBS	nd	nd	nd
Deionized water	286 (13%)	7 (no reproducible)	4229 (20%)
Ammonium citrate	1582 (26%)	793 (27%)	49000 (19%)

Table 4.4: Values of S/N ratios and signal intensities with their standard deviation (SD) (%) for each tested buffer corresponding to Figure 4.13. (nd: not detected)

4.5.4. Affinity-DIOS-MS analysis and peptide enrichment

The peptides were diluted in a 1 mM adjusted ammonium citrate buffer (1 mM, pH 7.5) solution at 100 fmol/µL. We prepared three peptide solutions: a solution of DAB, a solution of DAB-His and an equimolar solution of DAB/DAB-His (1/1). The NTA-Ni^{2+}-terminated NanoSi surfaces were incubated in the three peptide solutions for 1h and 5h in 500 µL polypropylene tube at room temperature. After incubation, the surfaces were washed thoroughly several times with ammonium citrate (1 mM) buffer solution before DIOS-MS analysis. The mass spectra and the average S/N ratios values are displayed in Figure 4.14 and Table 4.5. From Figure 4.14 and Table 4.5, one can deduce that:

1. For pure solution (DAB-His or DAB) on NanoSi-NTA-Ni^{2+} surface:

✓ DAB-His and DAB peptides were detected by DIOS-MS analysis from their pure solution and for different incubation times of 1h or 5h.

✓ For 1h incubation, the average S/N value (S/N=141) and signal intensity (I*=2127) of DAB is higher than DAB-His (S/N=30, I*=553). In contrary for 5 h incubation, DAB gave (S/N= 233, I*=3354) and DAB-**His** led to (S/N=406, I*=9873).

✓ When the incubation time was 5-fold longer, the quality of MS of DAB (S/N and I* value) is 1.5 times higher. While for DAB-**His**, the S/N and I* values increased 13 and 17 times, respectively. It means that a specific interaction between DAB-His peptide and NanoSi-NTA-Ni^{2+} surface took place, although non-specific interaction occurred on this surface.

2. For peptide mixture solution (DAB-His and DAB) on NanoSi-NTA-Ni^{2+} surface

✓ Only DAB-His was detected (S/N ≈ 32, I*≈ 550) and no peak corresponding to DAB peptide was identified. The result clearly demonstrates DAB-His peptide enrichment thanks to its specific interaction with NanoSi-NTA-Ni^{2+} surface.

✓ In comparison between the incubation times of 1 and 5h, the S/N (about 32) and I* (about 550) values were identical for both cases. Thus, with increasing incubation time, the quality of MS of DAB-His peptide was not enhanced, suggesting that the interaction between DAB-His with the NTA-Ni^{2+} terminal group may be saturated.
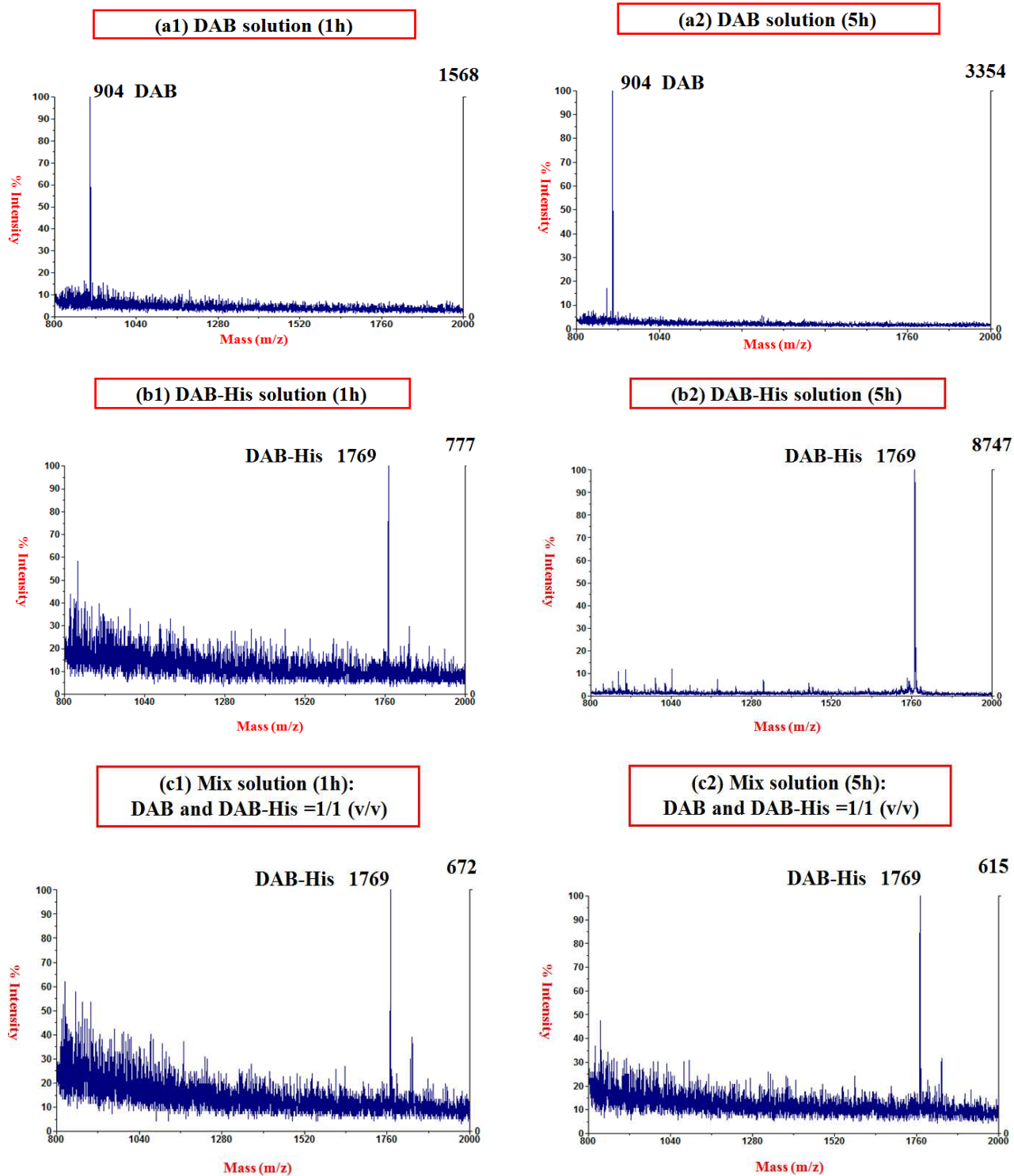
Figure 4.14: DIOS-MS spectra of DAB-His and DAB and their equimolar mixture for different incubation times with NTA-Ni^{2+}-terminated NanoSi interfaces.

186

| | Pure peptide solution | | | | | |
| | 1h | | | 5h | | |
	S/N	Base peak	Signal intensity (I*)	S/N	Base peak	Signal intensity (I*)
DAB	141 (29%)	904	2127 (28%)	233[#]	904	3354[#]
DAB-His	30 (20%)	1769	553 (24%)	406 (34%)	1769	9873 (13%)
	Peptide mixture solution					
	1h			5h		
	S/N	Base peak	Signal intensity	S/N	Base peak	Signal intensity (I*)
DAB	nd	nd	nd	Nd	nd	nd
DAB-His	32 (9%)	1769	578 (17%)	34 (14%)	1769	541 (13%)

Table 4.5: The average S/N values of DAB and DAB-His peptides for pure peptide solution and peptide mixture solution (DAB and DAB-His) corresponding to Figure 4.14. (nd: not detected; #: tested one time)

In a control experiment, the peptide mixture was incubated on NanoSi-NTA surface for 1h (in this case, the NTA was not complexed with Ni^{2+} ions). No peptide was detected in the MS spectrum, as shown in Figure 4.15. It confirms again the absence of non specific interaction between DAB-His and the NTA terminal group.
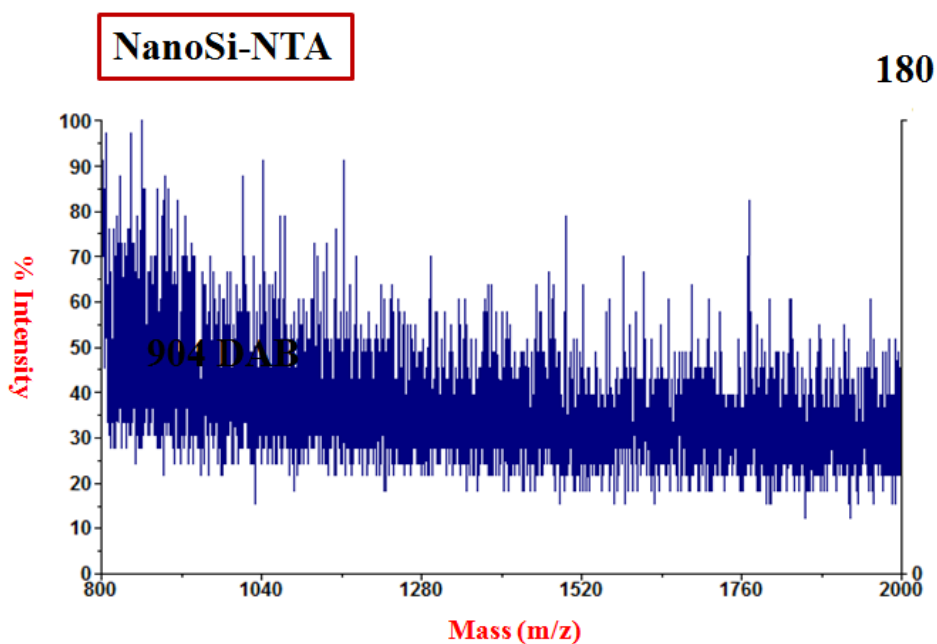
Figure 4.15: Mass spectrum of the peptide mixture solution (DAB and DAB-His) incubated for 1h on NanoSi-NTA surface (without complexation with Ni^{2+}).

Summary

We have demonstrated that depending on the experimental conditions, NanoSi-OTS interfaces permit the detection of both DAB and DAB-His peptides. On the other hand, no peptides were detected on NanoSi-NTA substrates (in the absence of Ni^{2+} ions).

The results indicate the absence of a specific interaction between His-DAB and these surfaces. However, upon complexation of the terminal NTA groups with Ni^{2+} ions (NTA-Ni^{2+}-terminated-NanoSi surface), His-DAB peptide is detected specifically from a mixture of His-tagged and untagged peptides.

4.6. Conclusion

In this chapter, we developed affinity DIOS-MS interfaces based on silicon nanostructures carrying NTA-Ni^{2+} complex. This complex allowed a specific capture of a His-tagged peptide and its subsequent DIOS-MS analysis. It has to be noted that only few examples of such affinity SALDI interfaces are described in the literature.

We have shown that:

1. The chemical modification of hydrogen-terminated NanoSi surfaces led to the successful introduction of NTA-Ni^{2+} complex. All the different chemical steps were characterized using CA measurements, FT-IR and XPS analysis proving unambiguously the immobilization of the complex.

2. The NTA-Ni^{2+}-terminated NanoSi interface allowed specific binding of DAB-His peptide from a mixture of His-tagged and un-tagged peptides. Then, the captured DAB-His peptide was desorbed and ionized *via* a pulsed laser and analyzed by mass spectrometry.

In this study, we presented preliminary results and some problems that have to be overcome to improve the sensitivity of our interfaces such as:

1. Addition of small quantities of imidazole in the incubation buffer for limiting the non-specific adsorption.
2. The optimization of the rinsing protocol after the incubation step to decrease the background in the mass spectrometry (addition of surfactant, for example).
3. We can also functionalize the NanoSi surfaces with multi-branched NTA molecules to increase the maximum capture capacity of Histidine-tagged peptide than on NTA monolayer, as already shown by Lui *et al.* (2010) on flat silicon [170].

The interfaces developed in this work are very promising in the field of affinity- DIOS-MS analysis. For example, with the successful introduction of NTA terminal group onto NanoSi surface, we assume that the NanoSi-NTA interfaces can be complexed with other metal ions such as: Fe^{3+}, Ga^{3+} for the enrichment of phosphopeptides. Furthermore, our NanoSi interfaces can be coupled with other small ligands for specific capture of various molecules of interest such as sugars, lipids, nucleotides, other peptides and proteins and their subsequent MS analysis.

General Conclusion and Perspectives

This work deals with the fabrication of nano or multiscaled (micro/nano) silicon surfaces and their application as liquid repellent surfaces and analytical tools for biomolecules analysis by mass spectrometry. Different structured surface morphologies were obtained by two different techniques: metal-assisted electroless etching and nanowires growth by CVD *via* VLS mechanism. The resulting substrates are either simple structured such as silicon nanostructures (NanoSi) and silicon nanowires (SiNWs), or double structured such as micro-nanoscale (combination of silicon micropillars with either NanoSi or SiNWs) or nano-nanoscale (double layer of nanowires).

In the first part of my work, the obtained interfaces were used to develop superhydrophobic and superomniphobic surfaces. In a second part, the interfaces were used as inorganic matrices for the realization of laser desorption/ionization of small biomolecules for their mass spectrometry analysis. Finally, functionalized nanostructured surfaces with a specific ligand (NTA-Ni^{2+}) were used to perform Histidine-tagged peptide enrichment and its subsequent mass spectrometry analysis.

This work was organized in four chapters: Chapters 1 and 2 are dedicated to the NanoSi and SiNWs fabrication techniques and characterization of their wetting properties. Chapters 3 and 4 focus on the use of these NanoSi and SiNWs substrates for mass spectrometry analysis of molecules.

In chapter 1, two methods for the preparation of nanostructured silicon surfaces were used. The first one consists on metal-assisted electroless etching of crystalline silicon and the second one concerns the growth of silicon nanowires (SiNWs) by CVD *via* the VLS mechanism (Vapor-Solid-Liquid). These methods could be applied on both flat and micropillars silicon substrates leading to the formation of simple or double structured surfaces.

➢ **Metal-assisted electroless etching technique (Top-down approach):** two types of solutions were used for the silicon etching: HF/AgNO$_3$ or NaBF$_4$/AgNO$_3$ aqueous solutions.

- Among them, NaBF$_4$/AgNO$_3$ aqueous solutions have been used for the first time for the fabrication of nanostructured silicon substrates. Two types of NanoSi surface morphologies were obtained by changing the etching parameters i. e. concentration of

reagents, etching time, temperature and type of wafer. These NanoSi structures have isosceles triangles or nozzle-like shapes. The height, apex and base length varying from 0.5 to 3 µm, 0.06 to 0.27 µm, and 0.1 to 0.5 µm, respectively.

- NanoSi synthesized using chemical etching of crystalline silicon in HF/AgNO$_3$ aqueous solutions consist of vertically aligned and packed nanofilament-like structures. The height of NanoSi varies from 0.5 to 20 µm, and the diameter from 10 to 100 nm. Furthermore, their morphology is independent of the etching parameters.

➤ **VLS technique (Bottom-up approach):** Silicon nanowires (SiNWs) were grown on both flat and micropillar silicon surfaces, resulting in simple or double scaled structuration. Their morphology depends on the growth parameters such as: time, temperature, pressure. In our case, we have prepared three types of SiNWs with their length varying between 7 and 45 µm and their diameters ranging from 80 to 150 nm:

- VLS1 consists of one layer of NWs of 7 µm in length. Most of the nanowires are straight and have an orientation ranging from 30 to 80° with respect to the horizontal plane.

- VLS2 comprises a dense lower layer of tangled NWs of 25 µm in length and a top layer of straight wires of 20 µm in length with an orientation about 80° with respect to the horizontal plane.

- VLS3 comprises a 2 µm-thick dense layer made of short entangled SiNWs with few straight SiNWs of 7 µm in length. In this case, the orientation is more irregular and the average angle with the horizontal is smaller compared to VLS1.

In chapter 2, NanoSi and SiNWs surfaces with simple or double scaled structuration were used for the preparation of superhydrophobic (-SH) and superomniphobic (-SO) surfaces. Their wetting properties were characterized by contact angle (static, advancing, receding, and hysteresis) measurements and pressure threshold with various liquids (water and organic liquids). Thereby, we focused on determining the threshold surface tension of liquid γ_{CA} and γ_H for each surface with CA>140° and θ_H<10°.

- Microstructured surfaces: $32.0 < \gamma_{CA} \leq 42.0$ mN/m, $64.0 \leq \gamma_H \leq 72.2$ mN/m.
- Nanostructured surfaces: $27.4 < \gamma_{CA} \leq 32.0$ mN/m, $50.0 \leq \gamma_H \leq 64.0$ mN/m.
- Nanowires surfaces: $27.47 < \gamma_{CA} \leq 32$ mN/m, 32 mN/m $\leq \gamma_H$.

- Double structured surfaces (micro and nanostructures): $21.3 < \gamma_{CA} \leq 23.8$ mN/m, $50.0 \leq \gamma_H \leq 64.0$ mN/m.

- Double structured surfaces (micro and nanowires): $23.8 \leq \gamma_{CA} \leq 27.4$ mN/m, 32.0 mN/m $\leq \gamma_H$.

- Double structured surfaces (double layers of nanowires): $23.8 \leq \gamma_{CA} \leq 27.4$ mN/m, $23.8 \leq \gamma_H \leq 27.4$ mN/m.

We found that the repellent properties increased from micro to nanostructured and from simple to double structured surfaces. Especially, the surface based on silicon nanowires presented the highest non-wetting behavior i. e. it showed high static contact angle, low hysteresis and high robustness. Moreover, we demonstrated that even though the surface did not possess "re-rentrant" features, it displayed a superomniphobic character.

In chapter 3, NanoSi and SiNWs substrates were used and optimized for the detection of peptides. Herein, we showed that our NanoSi and Nanowires interfaces can be successfully used as good platforms of DIOS-MS analysis. Our interfaces allow a detection of a peptide mixture with a high sensitivity (0.2 fmol/µL) with a signal-to-noise ratio of 6, and a standard deviation of 16%. Furthermore, we also investigated the influence of several parameters on the DIOS-MS efficiency such as: type and level of dopants, SiO_x deposition, and chemical derivatization of the DIOS surfaces. This study has demonstrated that:

- NanoSi, fabricated by chemical etching of crystalline silicon in $HF/AgNO_3$ aqueous solutions, showed the best performance in DIOS-MS analysis and there was no influence of the doping type and level of the silicon substrate on the LDI-MS efficiency. However, in the case of NanoSi prepared by chemical etching in $NaBF_4/AgNO_3$ aqueous solutions, it was hard to draw a final conclusion on the influence of the doping type or level of the silicon on DIOS-MS efficiency. Indeed, the different silicon types led to various NanoSi surface morphologies, making difficult to assess any comparison. While DIOS-MS analysis performed on SiNWs surfaces have shown that undoped SiNWs presented a better performance of LDI-MS than the doped SiNWs. Moreover, p-doped SiNWs gave better results than the n-doped SiNWs.

- SiO_x deposition (thermal insulator) on the NanoSi surface led to a decrease of its DIOS-MS efficiency due to the diminution of thermal conductivity of the surface. The level of influence depends on the SiO_x layer thickness.

- Among the various terminal groups tested on our DIOS surfaces such as: $-CH_3$ UV/O_3 treated, $-CH_3$, $-CF_3$, $-C_6F_5$ and $-COOH$, we found that all of them can be used in DIOS-MS analysis. However, the $-COOH$ terminal group exhibited a lower LDI-MS efficiency than the other surface terminations.

In chapter 4, we prepared a NanoSi surface functionalized with nickel (II)-nitrilotriacetic acid complex (NTA-Ni^{2+}) and evaluated its performance as an affinity DIOS interface. This interface allows histidine-tagged peptide enrichment. The NTA-Ni^{2+} terminal groups were immobilized on the NanoSi surface *via* Si-C covalent bonds. The NTA-Ni^{2+} modified NanoSi interface was characterized using Fourier transform infrared spectroscopy (FT-IR), X-ray photoelectron spectroscopy (XPS) and contact angle measurements. The interface showed a good selectivity towards histidine-tagged peptides. Indeed, the NTA-Ni^{2+}-terminated NanoSi interface was able to specifically capture a histidine-tagged peptide from a mixture solution (histidine-tagged and untagged peptides) and to perform its mass spectrometry analysis.

However, non-specific binding occurred on the surface when the NTA-Ni^{2+}-terminated NanoSi substrate was incubated in a pure solution of untagged peptide, probably due to the lack of efficiency of the rinsing protocol. To overcome this problem, we optimized the process by adding, for example, small quantities of imidazole in the incubation buffer.

Based on the results obtained in this thesis, we can further suggest as perspectives:

1. Using our DIOS interfaces for LDI-MS analysis of other small molecules.
2. Application of the -SO surfaces for DIOS-MS analysis of non-polar biomolecules such as lipids.
3. Development of functionalized NanoSi or SiNWs in the field of affinity DIOS-MS analysis. For example, with the successful introduction of NTA terminal group onto NanoSi surface, it is possible to form complexes with other metal ions such as: Fe^{3+} or Ga^{3+} for the enrichment of phosphopeptides. Furthermore, functionalized NanoSi interfaces can be coupled to small ligands for capturing other molecules of interest such as peptides, sugars, lipids...and their subsequent identification by MS analysis.
4. The next step is the development of a digital microsystem based on EWOD for simultaneous separation, enrichment, purification, and identification of histidine-tagged peptides, as shown in Figure CP.1. For that, the same microsystem that is already used in our group and described by Lapierre *et al.* will be applied. [13] Indeed, Lapierre *et al.* have demonstrated, for the first time, the combination of a microfluidic system with

DIOS interfaces for detecting small peptides. The analytes were distributed in superhydrophilic areas *via* EWOD actuation prior to their DIOS-MS analysis. Here, we propose to improve this microsystem by:

- Introducing NTA-Ni^{+2} terminal groups onto the superhydrophilic areas. So, when a droplet of a peptide mixture consisting of histidine-tagged and untagged peptides will be displaced over these affinity areas, the histidine-tagged peptide will be captured by NTA-Ni^{+2} complex and subsequently analyzed by mass spectrometry.

- Changing the superhydrophobic by a superomniphobic coating using perfluoroalkyl modified surfaces. This will allow the system to be used with liquids of low surface tensions (organic solvents) or aqueous solutions containing small amounts of surfactants to limit the non-specific interaction and enhance the efficiency of detection.
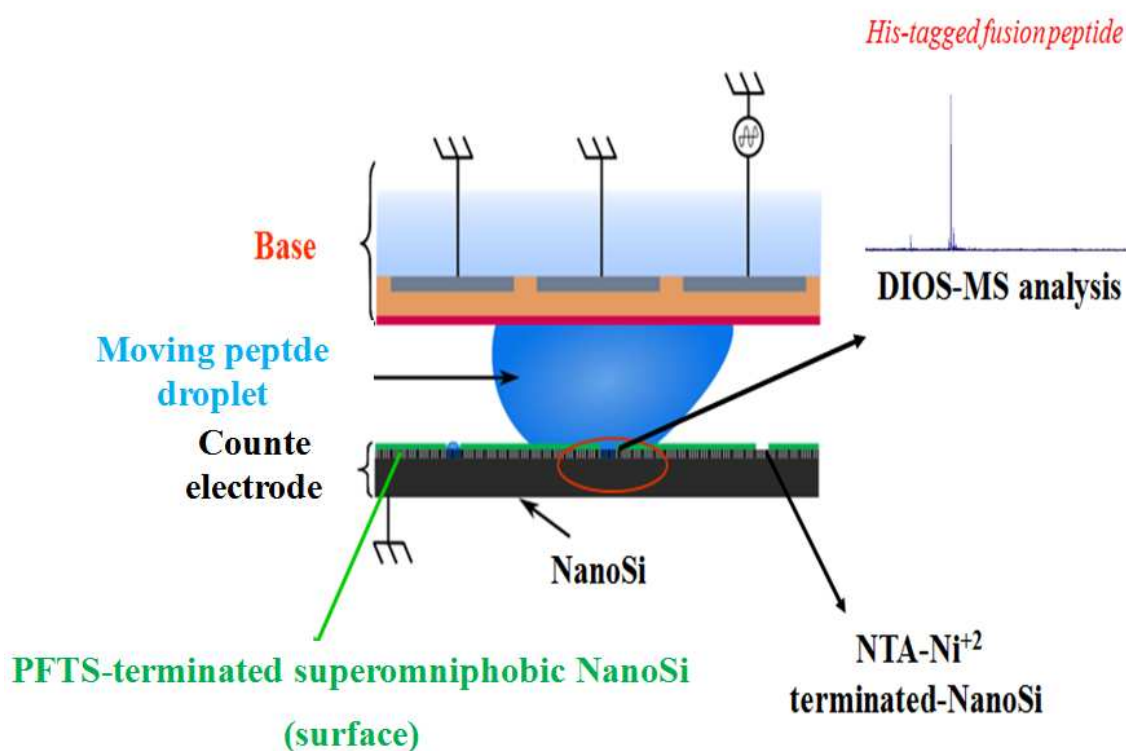
Figure CP.1: Scheme of lab-on-chip using digital microfluidic, in which the capot (counter electrode) consists of a patterned superomniphobic/superhydrophilic (PFTS/NTA-Ni^{+2}) NanoSi substrate.

Appendix

Appendix 1: Silicon wafer cleaning

Objective: To remove all contaminants (dust, organic or metallic ones) on the silicon substrate, the following protocol was used:

i. The substrate is first degreased in solvent in order to remove all organic contaminants and dust
   - ✓ Acetone (ultrasonic bath) : 5 min
   - ✓ Isopropanol (ultrasonic bath) : 5 min
   - ✓ Milli-Q water (ultrasonic bath) : 5 min
   - ✓ Drying under N_2 stream

ii. Then the surface is cleaned in piranha solution in order to remove all metallic contaminants and the last organic traces:
   - ✓ Piranha solution (98% H_2SO_4/30% H_2O_2=1/1): 20 minutes.
   - ✓ Milli-Q water (ultrasonic bath): 10 minuntes.
   - ✓ Drying under N_2 stream.

Here, a native oxide layer is formed.

iii. Eventually the native oxide layer can be removed by dipping in 50% HF during 1 minute.

Appendix 2: Material safety

1/Sodium Fluroborate-NaBF$_4$[i]

Emergency overview: NaBF$_4$ is a white powder with bitter and sour smell. Harmful or may be fatal if swallowed. May cause skin and eye irritation. Not flammable.

Potential Health Hazards:

Skin: Contact with powder or solution may cause irritation.

Eyes: Direct eye contact with powder or mist may produce severe irritation.

Delayed effects:

There is no chronic toxicity data on this material; however, NIOSH links inorganic fluoborates with inorganic fluorides. Chronic exposure to fluorides is associated with osseous fluorosis-increased radiographic density of bones, mottling of teeth, etc. These conditions will no develop if permissible exposure levels are not exceeded. Kidney damage, asthma and symptoms resembling rheumatism may occur.

2/HF[ii]

Emergency overview: Clear, colorless, corrosive fuming liquid with an extremely acrid odor. May produce white fumes if spilled. Both liquid and vapor can cause severe burns to all parts of the body. Specialized medical treatment is required for all exposures.

Potential Health Hazards:

Skin: Both liquid and vapor can cause severe burns, which may not be immediately painful or visible. HF will penetrate skin and attack underlying tissues. Large or multiple burns totaling over 25 square inches of body surface area may also cause (depletion of calcium in the body), and other toxic affects which may be fatal. Prolonged contact with very dilute HF solutions will cause burns.

Eyes: Both liquid and vapor can causes irritation or corneal burns.

Delayed effects:

The effect of contact with dilute solutions of HF acid or its vapor may be delayed. The potential delay in clinical signs or symptom for dilute solutions is given in Table 1.A.

HF Concentration	Delay in symptoms
>50%	Immediately Apparent
20%-50%	1-8 hours
0%-20%	Up to 24 hours

Table A. 1: The potential delay in clinical signs or symptom for dilute solutions.

3. Piraha solutions (H_2SO_4/H_2O_2)

The H_2SO_4/H_2O_2 (Piranha) solution is a strong oxidant. It reacts violently with organic materials and can cause severe skin burns. It must be handled with extreme care in a well-ventilated fume hood while wearing appropriate chemical safety protections.

Appendix 3: Thermal oxidation

The thermal oxidation of Si consists of exposing the silicon substrate to an oxidizing environment of O_2 or H_2O at elevated temperatures (usually between 700-1300°). Thermal oxidation is accomplished using a low pressure chemical vapor deposition (LPCVD) furnace, which provides the heat needed to raise the temperature. Depending on which oxidant species used (O_2 or H_2O), the thermal oxidation of Si will be called ***dry oxidation*** if the oxidant is pure O_2 or called ***wet oxidation*** if the oxidant is H_2O. The reactions for dry and wet oxidations are governed by the following equations:

     1) For dry oxidation: Si (solid) + O_2 (gaz) --> SiO_x (solid).

     2) For wet oxidation: Si (solid) + $2H_2O$ (vapor) --> SiO_x (solid) + $2H_2$ (gaz).
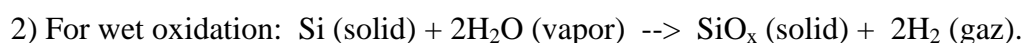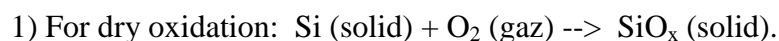
In our case, the SiO_x layer is formed on the wafer *via* dry thermal oxidation using the parameters displayed in Table A.2.

Gas	Pressure	Temperature
O$_2$/2.5 slm	Ambient	1100°C

Table A.2 : Silicon oxidation parameters.

Appendix 4: Steps of micropillars fabrication

The silicon micropillars are fabricated using the following steps:

1. Si substrate is cleaned following the protocol in Appendix 1.
2. Then, 6 µm thick of a negative resist AZnLOF 2035 is spin-coated (Clariant, France). The spin-coating typically runs at 2700 rpm with an acceleration of 1000 rpm/s during 20 seconds.
3. A soft bake at 110°C for 1 minute.
4. Exposure 80 mW/cm^2 for 10 seconds.
5. A post-bake at 110°C for 1 minute.
6. Developing in AZ326 MIF for 1 minute and 30 seconds.
7. Dry etching by RIE using the parameters in Table A.3.
8. Removal of the resist by acetone bath with Ultra-wave Milli-Q water (ultrasonic bath) and oxygen plasma (O$_2$: 30 sccm, power: 150 W, Pressure: 100 mTorr, time: 1 minute).
9.

Material	Power of etching	Gas1: SF$_6$	Etching time	Power of passivation	Gas2: C$_4$F$_8$	Time of passivation
Silicon	2500 W	450 sccm	3 seconds	1000W	100 sccm	2.8 seconds

Table A.3: Etching parameters used for DRIE process .

Appendix 5: Fluoropolymer-C$_4$F$_8$ deposition

The surface is placed onto a holder and then directly transferred in the plasma chamber (STS-Silicon Technology System) leading to a C$_4$F$_8$ layers deposition. The parameters are presented in Table A.4 and the calibration of C$_4$F$_8$ deposition is shown in Figure A.1.

Gas C$_4$F$_8$	Power of passivation	Pressure
220 sccm	1000 W	949 mTorr

Table A.4: Parameter of C$_4$F$_8$ deposition.
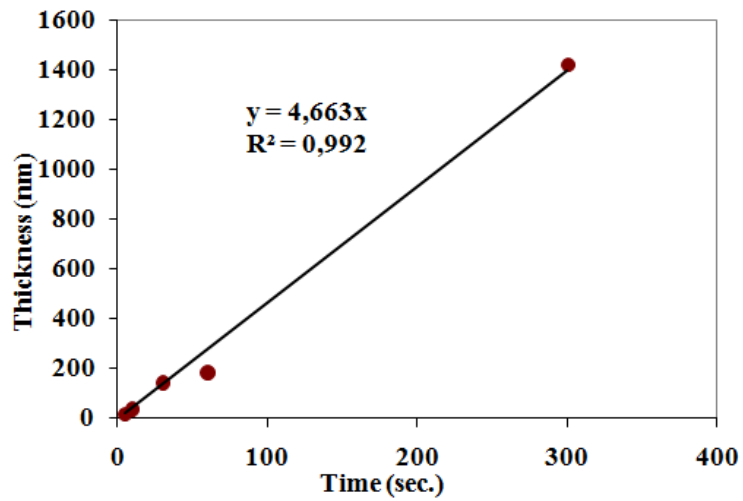
Figure A.

Figure A.1: Calibration curve for C$_4$F$_8$ deposition.

Appendix 6: Silanization

Silanization is the surface coating through self-assembly of organofunctional alkoxysilane molecules. The surface presents terminal hydroxyl groups, which react with the alkoxysilane forming a covalent Si-O-Si- bond. By silanization, the surface can be modified with different terminations.

In our case, we used silanization to coat the surface with hydrophobic layers (OTS and PFTS). The silanization protocols are:

✓ The silicon surface is cleaned using UV/O$_3$ irradiation for 30 minutes (*UV* O cleaner, Jelight Company, Inc., 4 mW/cm^2 at 220 nm). The goal is to remove any organic contaminant and to generate surface silanol groups (-Si-OH).

✓ The activated surface is directly dipped into a freshly prepared silane solution (2.87×10^{-3}M) in hexane for 4 h at room temperature in a dry nitrogen purged glove box. Herein, the silane is either Octadecyltriclorosilane (OTS) or *1H,1H,2H,2H-* perfluorodecyltrichlorosilane (PFTS).

✓ The resulting surface was rinsed first in hexane and then twice in dichloromethane, twice in ethanol and then dried under a gentle nitrogen flow. Each rinsing step is performed for 5 minutes with agitation.

Appendix 7: Contact angle measurements

The wetting properties were determined by contact angle measurements (static, advancing, receding and hysteresis) using a Drop Shape Analysis System (DSA100, Krüss GmbH Germany). It consists of an automated tilting table which incorporates a light source, a CDD camera (52frames/sec) and an automatic dosing system. A liquid drop is deposited onto the surface then the table rotates from 0° to 60° (by step of 0.3 every 0.3 sec) while drop deformation and contact angle variations are recorded every 20 ms. This configuration corresponds to 16 measurements for a unique angle up to the sliding angle. Before the sliding, we assume that we are in a quasi static state. Static contact angles are measured just after the liquid droplet deposition, while advancing and receding angles are measured just before contact line depining during tilting. An error of ± 2° is assumed on contact angle computation and each measurement is operated 3 times. Furthermore, in some cases, when setting the tilting angle at

60°, no sliding droplet has been observed, the contact angle hysteresis-θ_H is noted higher than 60°. It is to be noted that the rotation axis of the tilting table and the optical axis (corresponding to CDD camera) are the same. Thus on the images and video taken, the surface appears horizontal while the droplet shape is deformed. Among the different existing methods to calculate the contact angle, we chose the one dealing with the polynomial triple line approximated fitting.

Appendix 8: Plasma-enhanced chemical vapor deposition (PECVD)

PECVD is a process used to deposit thin films from a gas state (vapor) to a solid state on a substrate. Chemical reactions are involved in the process, which occur after creation of a plasma of the reacting gases. The plasma is generally created by RF (AC) frequency or DC discharge between two electrodes, the space between which is filled with the reacting gases. [iii]

At IEMN, we use PECVD OXPORD Plasmalab 80Plus (cold process) as shown in Figure A.2. [iv]

- ✓ Top electrode RF driven (13.56 MHz and 50-400 KHz).
- ✓ Film stress can be controlled by high/low frequency mixing techniques.
- ✓ Silicon nitride, oxide deposition.
- ✓ Gases used: SiH_4 in N_2, NH_3, N_2O, N_2 and He.
- ✓ Deposition temperature: 100 to 340°C.
- ✓ Deposition rate: 100 to 650 Å/min.
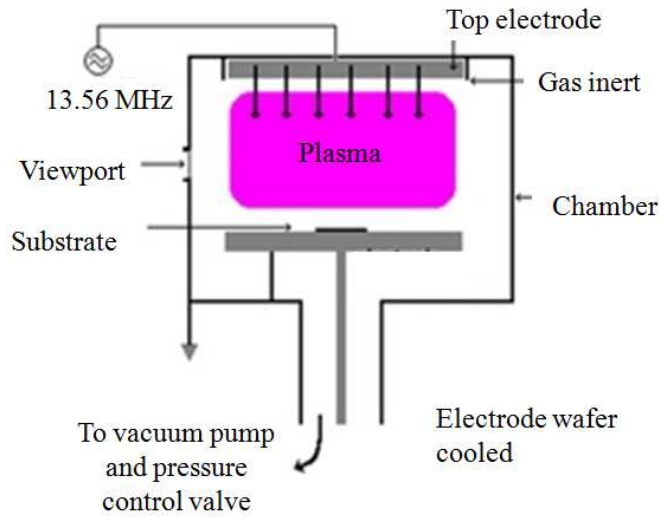
Figure A.2: Schematic illustration of PECVD deposition principal.

In our case, SiO_x layers were deposited using the parameters in Table A.5.

Gas1 SiH₄ (5% in N₂)	Gas2 N₂O	Pressure	Temperature	Power
150 sccm	800 sccm	10 Torr	300°C	10 W

Table A.5: Parameters of SiO_x deposition by PECVD.

Appendix 9: Fourier Transform Infrared Spectrometry (FT-IR)[v]

FTIR is the preferred method of infrared spectrometry, in which, IR radiation is passed through a sample. Some of the infrared radiation is absorbed by the sample and some of it is passed through (transmitted). The resulting spectrum displays the molecular absorption and transmission, creating a molecular fingerprint of the sample as shown in Figure A.3. Thus, an infrared spectrum represents a fingerprint of a sample with absorption peaks which correspond to the frequencies of vibrations between the bonds of the atoms making up the material.
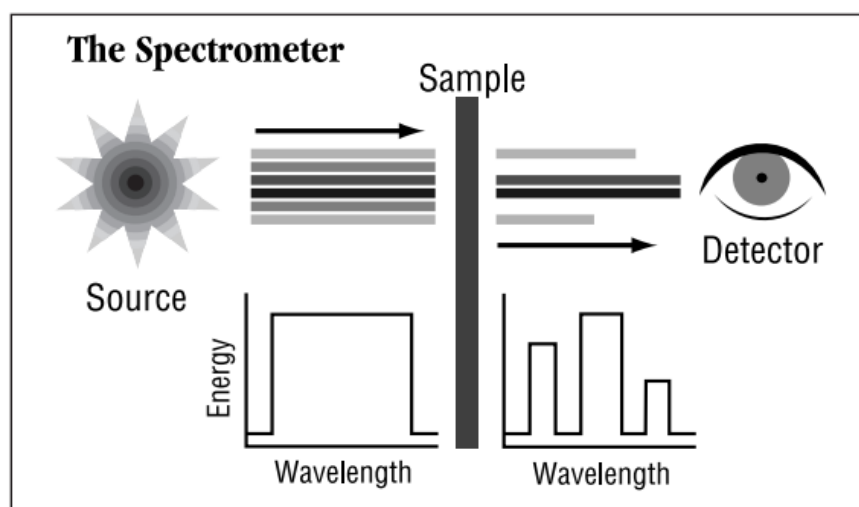
Figure A.3: Schematic representation of FTIR.

In our case:

Transmission FT-IR spectra were recorded using a Perkin-Elmer Spectrum 2000 single-beam spectrophotometer equipped with a tungsten-halogen lamp and a liquid nitrogen cooled MCT detector. All measurements were made after purging the sample chamber for 30 min with dry N_2. Spectra were recorded at 4 cm^{-1} resolution and averaged over 200 scans. Background spectra were obtained using a flat H -terminated Si (100) surface.

Appendix 10: X-ray Photoelectron Spectroscopy- XPS[vi]

XPS is a surface analysis technique that is unique in providing chemical state bonding information. It is widely used to determine localized bonding chemistry of carbon and to differentiate oxidation states of inorganic compounds. This technique can detect all elements except H and He with detection limits of approximately 0.1 % atomic. Furthermore, XPS is an ultra-high vacuum surface analysis technique with a sampling volume that extends from the surface to a depth of 5-10 nm. The minimum area of analysis for XPS is approximately 30 µm.

The principal of XPS is shown in Figure A.4: Irradiated by X photons, atoms of a surface emit electrons (called photoelectrons) due to the photoelectric effect. XPS principle consists in analyzing kinetic energy of the photo-emitted electrons at the time of irradiation by a monoenergetic beam of X photons. An electron of a given electronic level is characterized by its binding energy, E_b which is specific to an atom and can be directly calculated using the energy conservation law:

$$E_b = h\nu - E_{kin}$$

Where $h\nu$ is the incident energy of an X photon and E_{kin} is the measured kinetic energy of the photoelectron.
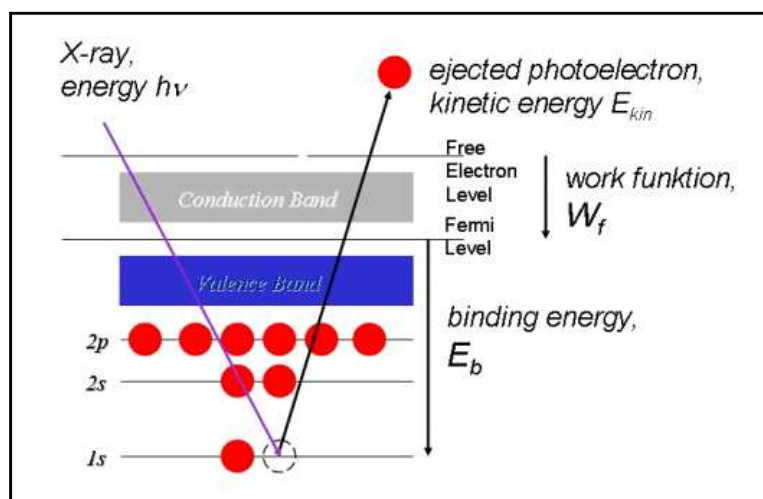
Figure A.4: Principe of XPS.

In our case:

XPS measurements were performed with an ESCALAB 220 XL spectrometer from vacuum Generators. A monochromatic Al Kα X-ray source (1486.6 eV) was operated in the constant analyzer energy (CAE) mode (CAE= 100 eV for survey spectra and CAE = 40 eV for high resolution spectra), using the electromagnetic lens mode. The angle between the incident X-rays and the analyzer is 58°. The detection angle of the photoelectrons is 90°, as referenced to the sample surface.

Appendix11: Porous silicon fabrication[vii]

Silicon wafer (Double-Side polised Si (100)-oriented, boron-doped, 5-10 Ω/cm) was first cleaned using the protocol in Appendix 1. The hydrogen-terminated surface was electrochemically etched in a 1/1 (v/v) solution of pure ethanol and 50% HF for 5 min at a current density of 10 mA/cm^2. After etching, the porous silicon substrate was rinsed with ethanol and dried under a stream of dry nitrogen. The obtained porous silicon displays pores with an average diameter <10 nm.

Appendix12: Reflectance measurements by spectrophotometry

Spectrophotometry is used for measurement of the amount of reflection or transmission properties of a material as a function of wavelength. In our case, the reflectance of the nanostructured surfaces was measured using a UV-*vis* spectrophotometer (Hitachi model U-3010) equipped with an integrating sphere attachment (Hitachi, 60 mm DIA). This measurement is realized by Bernard Gelloz, University of Agriculture and Technology, Tokyo, Japan.

Résumé:

Mes travaux de thèse concernent la fabrication de micro et de nanostructures en silicium dans le but de développer des surfaces non-mouillantes et des outils analytiques pour applications en biochimie et en microfluidique. Pour ce faire, nous avons utilisé d'une part la gravure chimique humide qu'est la « metal-assisted electroless etching » (approche descendante) et d'autre part la croissance de nanofils par « Chemical Vapor Deposition » *via* le mécanisme « Vapor-Liquid-Solid » (approche ascendante). Des surfaces structurées possédant des morphologies différentes ont été obtenues. Grâce à ces méthodes de fabrication nous avons préparé des structurations simples et doubles, à savoir des structurations nanométriques et micrométriques et des doubles structurations micro-nanométriques.

Dans une première partie, les surfaces structurées ont permis de développer des surfaces superomniphobes, capables de repousser des liquides présentant des tensions de surface comprise : 20 <γ< 72 mN/m. Les surfaces présentant une double structuration donnent les meilleures propriétés de non-mouillage

Dans une deuxième partie, ces surfaces nanostructurées ont été utilisées comme matrices inorganiques pour la désorption/ionisation assistée par laser permettant l'analyse en spectrométrie de masse de petites molécules sans utilisation de matrice organique. Nous avons étudié l'influence de la morphologie, du type de dopage et de la terminaison chimique sur l'analyse en spectrométrie de masse d'un mélange de peptide standard.

Finalement, nous avons réalisé l'enrichissement d'un peptide et son analyse en spectrométrie de masse à partir d'un mélange donné, grâce à l'introduction d'un ligand spécifique.

Mots-clés : *Nanostructures de silicium, Nanofils de silicium, Superomniphobe, Spectrométrie de masse, Analyse DIOS-MS, Tag-Histidine*

Abstract

This work concerns the fabrication of micro/nanostructured silicon substrates and their application as non-wetting surfaces, and analytical tools for biomolecules' analysis and in microfluidic devices. Two different techniques were investigated for the formation of nanostructured silicon substrates: chemical wet etching *via* metal-assisted electroless etching (Top-down approach) and nanowire growth by « Chemical Vapor Deposition » *via* Vapor-Liquid-Solid mechanism (Bottom-up approach). Different structured surface morphologies were then obtained. These were either simple structured such as: Micro or Nanoscale, or double structured such as: Micro-Nano or Nano-Nanoscale.

The first part of the thesis deals with the preparation of superominiphobic surfaces capable of repelling almost any liquid (20 <γ< 72 mN/m). The surfaces consisting of double structured substrates gave the best non-wetting properties.

Secondly, nanostructured silicon substrates were used as inorganic matrices for the detection of small molecules without using an organic matrix in laser desorption/ionization mass spectrometry. Herein, we investigated the influence of surface morphology, doping type and chemical termination on mass spectrometry analysis of a standard peptide mixture.

Finally, functionalized silicon nanowires surfaces with a specific ligand were used to perform peptide enrichment and its subsequent analysis by mass spectrometry from a mixture solution

Keys words: *Silicon nanostructure, Silicon nanowires, Superomniphobe, Mass spectrometry, DIOS-MS analysis, Tag-Histidine*

Bibliography

1. **L.Canham.** Will a chip every day keep the doctor away? Physics Word, 2001, pp. 27-32.

2. **D.S.Kumar, D.Banji, B.Madhavi.B, V.Bodanapu, S.Dondapati, A.P.Sri.** Nanostructured Porous Silicon-Anovel Biomaterial for Drugdelivery. International Journal of Pharmacy and Pharmaceutical Sciences, 2009, pp. 8-16.

3. **Y.He, C.Fan, S.T.Lee.** Silicon Nanostructures for Bioapplications. 282-295 : Nano Today, 2010.

4. **V.T.Costa, R.J.M.Palma.** Application of Nanostructured Porous Silicon in the Field of Optics. J Mater Sci, 2010, pp. 2823–2838.

5. **A.C.R.Grayson, R.S.Shawgo, A.M.Johnson, N.T.Flynn, Y.Li, M.J.Cima, R.Langer.** A BioMEMS Review: MEMS Technology for Physiologically Integrated Devices. Proceeding of the IEEE, 2004, pp. 6-21.

6. **Y.Chen, A.Pépin.** Nanofabrication: Convention and Nonconventional Methods. Electrophoresis , 2001, pp. 187-207.

7. **K.Peng, H.Fang, J.Hu, Y.Hu, J.Zhu, Y.Yan, S.Lee.** Metal-Particle-Induced, Highly Localized Site-Specific Etching of Si and Formation of Single-Crystalline Si Nanowires in Aqueous Fluoride Solution. Chem.Eur.J, 2006 , pp. 7942-7947.

8. **K.W.Kolasinski.** Silicon Nanostructures from Electroless Electrochemical. Current opinion in solid state and Materials Science, 2005, pp. 73-83.

9. **D.S.Peterson.** Matrix-Free Methods for Laser Desorption/ionization mass spectrometry. Mass spectrometry Reviews, 2007, pp. 19-34.

10. **E.Galopin, J.Barbrillat, Y.Coffinier, S.Szunerits, G.Patriarche, R.Boukherroub.** Silicon Nanowire Coated with Silver Nanostructres as Ultrasensitive Interfaces for Surface-Enhanced Raman Spectroscopy. applied materials and interfaces, 2009, pp. 1396–1403.

11. **D.Mijatovic, J.C.T.Eijkel, A.V.D.Berg.** Technologies for Nanofluidic Systems: Top-Down as. Bottom-up a Review. Lab chip, 2005, pp. 492-500.

12. **P.Menna, G.D.Francia, V.L.Ferrara.** Porous Silicon in Solar Cells: A Review and a Description of Its Application as an AR Coating. Solar Energy Materials and Solar Cells, 1995, pp. 13-14.

13. **F.Lapierre, G.Piret, H.Grobecq, Y.Coffinier, V.Thomy, R.Boukherroub.** High Sensitive Mass Spectrometry Analysis of Peptides Using EWOD/Matrix-Free LDI-MS Device. Lab-on-Chip, 2011, pp. 1620-1628.

14. **F.Lapierre, M.Jonsson-Niedziolka, Y.Coffinier, S.J.Parry, F.Zoueshtiagh, T.Foat, V.Thomy, R.Boukherroub.** EWOD Driven Clearning of Bioparticles on Hydrophobic and Superhydrophobic Surfaces. Lab-on-Chip, 2011, pp. 490-496.

15. **E.Galopin, G.Piret, S.Szunerits, Y.Lequette, C.Faille, R.Boukherroub.** Selective Adhesion of Bacillus cereus Spores on Heterogeneously Wetted Silicon Wanowires. Langmuir, 2010, pp. 3479–3484.

16. **R.Blossey.** Self-Clearning Surfaces-Virtual Realites. Nature Material, 2003, pp. 301-306.

17. **X.Hu, G.Li, J.C.Yu.** Design, Fabrication, and Modification of Nanostructured Semiconductor Materials for Environmental and Energy Applications. Langmuir, 2010, pp. 3031-3039.

18. **X.L.Li, D.Reinhoudt, M.C.Calama.** What Do We Need for a Superhydrophobic Surface? A review on the Recent Progress in The Preparation of Superhydrophobic Surface. Chem.Soc.Rev, 2007, pp. 1350-1368.

19. **X.Li, H.S.Seo, H.D.Um, S.W. Jee, Y.W. Cho, B.Yoo, J.H. Lee.** A Periodic Array of Silicon Pillars Fabricated by Photoelectrochemical Etching. Electrochimica Acta, 2009, pp. 6978–6982.

20. **K.A.Dick.** A Review of Nanowire Growth Promoted by Alloys and Non-Alloys Element With Emphasis on Au-assisted III-IV Nanowire. Progress in crystal growth and characterization of materials, 2008, pp. 138-173.

21. **C.H.Choi, C.J.Kim.** Fabrication of a Dense Array of Tall Nanostructures over a Large Sample Area With Sidewall Profile and Tip Sharpness Control. Nanotechnology, 2006, pp. 5326-5333.

22. **M.E.Dudley, K.W.Kolasinski.** Wet Etching of Pillar-Covered Silicon Surfaces: Formation of Crystallographically Defined Macropores. Electrochemical Society, 2008, pp. 164-171.

23. **J.S.Lee, N.H.Cho.** Nanostructural and Photoluminescence Feature of Nanoporous Silicon Prepared by Anodic Etching. Applied surface science, 2002, pp. 171-175.

24. **A. El-Bahar, Y. Nemirovsky.** Porous Silicon Multiplexers and Demultiplexers. phys. stat. sol., 2003, pp. 293–297.

25. **L. Koker, KW. Kolasinski.** Laser-assisted Formation of Porous Silicon in Diverse Fluoride Solution: Reactions Kinetics and Mechanistic Implication. J.Phys.Chem B, 2001, pp. 3864-3871.

26. **V.Schmidt, J.V.Wittemann, S.Senz, U.Gosele.** Silicon nanowire: A review on aspects of their growth and their electrical properties. Adv.Mater, 2009, pp. 2681-2702.

27. **B.D.Gates, Q.Xu, M.Stewart, D.Ryan, C. G.Willson, G.M. Whitesides.** New Approaches to Nanofabrication: Molding, Printing, and Other Techniques. Chem. Rev, 2005, pp. 1171-1196.

28. **L.Yang, I.Akhatov, M.Mahinfalah, B.Z. Jang.** Nano-Fabrication: A Review. Journal of the Chinese Institute of Engineers, 2007, pp. 441-446 .

29. **B.Bilenberg, S.Jacobsen, C.Pastore, T.Nielsen, S.R.Enghoff, C.Jeppesen, A.V.Larsen, A.Kristensen.** Technology for Fabrication of Nanostructures by Standard Cleanroom Processing and Nanoimprint Lithography. Japanese Journal of Applied Physics, 2005, pp. 5606-5608.

30. **I.A. Shah, B.M.A. van der Wolf, W. J.P. van Enckevort, E.Vlieg.** Wet chemical etching of silicon {111}: Etch pit analysis by the Lichtfigur method. Journal of Crystal Growth, 2009, pp. 1371–1377.

31. **K.R.Williams, S.Member, K.Gupta, S.Member, M.Wasilik.** Etch Rates for Micromachining Processing—Part II. Microelectromechanical, 2003, pp. 761-777.

32. **I.Zubel.** Silicon Anisotropic Etching in Alkaline Solution III: On The Possibility of Spatial Structures Forming in The Course of Si (100) Anisotropic Etching in KOH and KOH +IPA Solutions. Sensors and Actuators,, 2000, pp. 116-125.

33. —. Silicon Anisotropic Etching in Alkaline Solution II: On The Possibility of Spatial Structures Forming in The Course of Si (100) Anisotropic Etching in KOH and KOH +IPA. Sensors and Actuators, 1998, pp. 116-125.

34. **H.Robbins, B.Schwartz.** Chemical Etching of Silicon .I. The System HF, HNO3, and H2O. J.chemical Soc, 1959, pp. 505-508.

35. —. Chemical Etching of Silicon .II. The System HF, HNO3, H2O and HC2H3O2. J.chemical Soc, 1959, pp. 505-508.

36. —. Chemical Etching of Silicon .III. The System HF, HNO3, and H2O. J.chemical Soc, 1959, pp. 505-508.

37. **N.Verplanck.** Développement de Microsystèmes EWOD sur Surfaces Hydrophobes and Superhydrophobes Application à la Spectrométrie de Mass. Thèse de Doctorat de l'Université des Sciences et Technologies de Lille, 2007, p. 189.

38. **M.C.Reyssat.** Splendeur et Misère de l'Effet Lotus . Thèse de doctorat de l'Université Paris VI, 2007, p. 38.

39. **N.Megouda, R.Douani, T.Hadjersi, R.Boukherroub.** Formation of aligned silicon nanowire on silicon by electroless etching HF solution. Journal of Luminescence, 2009, pp. 1750-1753.

40. **N.Megouda, T.Hadjersi, G.Piret, R.Boukherroub, O.Elkechai.** Au-assisted Electrode Etching of Silicon in Aqueous HF/H2O2. Applied Surface Science, 2009, pp. 18271-18277.

41. **K.W.Kolasinski.** Etching of Silicon in Fluoride Solutions. Surface science, 2009 , pp. 1904-1911.

42. **D.H.V.Dorp, J.J.H.B.Sattler, J.H.den Otter, J.J.Kelly.** Electrochemistry of Anodic Etching of 4H and 6H-SiC in Fluoride Solution of pH3. elecrochimica Acta, 2009, pp. 6269-6275.

43. **H.Gerischer, P.Allongue, V.K.Costa.** The Mechanisme of Anodic Oxydation of Silicon in Acidic Solutions Revisited. Phys Chem, 1993, pp. 753-757.

44. **A. Loni, L.T. Canham, M.G. Berger , R. Arens-Fischer , H. Munder , H. Luth ,F. Arrand, T.M. Benson.** Porous silicon multilayer optical waveguides. Thin Solid Films, 1996, pp. 143-146.

45. **A.Nordström, G.Suizdak.** Desorption/ionization on Silicon (DIOS). Elsevier, 2007, pp. 676-683.

46. **P.Menna, G.D.Francia, V.L.Ferrara.** Porous Silicon in Solar Cells: A Review and a Description of Its Application as an AR Coating. Solar Energy Materials and Solar Cells, 1995, pp. 13-14.

47. **R.V.J.Viard.** Porous Silicon Platform for Device Fabrication. Ecole central de Lille, 2006, p. 6.

48. **D.Mills, M.Nahidi, K.W.Kolasinski.** Stain Etching of Silicon Pillars and Macropores. phys. stat. sol, 2005, pp. 1422–1426.

49. **A.Huang, N.Geyer, P.Werner, J.D.Boor, U.Gösele.** Metal-Assisted Chemical Etching of Silicon: A Review. Adv.Mater, 2011, pp. 285-308.

50. **C.Chartier, S.Bastide, C.L.Clément.** Metal-assisted Chemical Etching of Silicon in HF-H2O2. Electrochimica, 2008, pp. 5509-5516.

51. **Y.Xiu, S.Zhang, V.Yelundur, A.Rohatgi, D.W.Hess, C.P.Wong.** Superhydrophobic and Low Light Reflectivity Silicon Surfaces Fabricated by Hierarchical Etching. Langmuir, 2008, pp. 10421-10426.

52. **K.W.Kolasinski.** Silicon Nanostructures from Electroless Electrochemica lEtching. Current opinion in solid state and Materials Science, 2005, pp. 73-83.

53. **K.Peng, Y.Wu, H.Fang, X.Zhong, Y.Xu, J.Zhu.** Uniform, Axial-Orientation Alignment of One-Dimentional Single-Crystal Silicon Nanostructure Array. Angrew.Chem.Int.Ed, 2005, pp. 2737-2742.

54. **Y.H.Ogata, K.Kobayashi, M.Motoyama.** "Electrochemical Metal Deposition on Silicon. Current Opinion in Solid State and Material Science, 2006, pp. 163-172.

55. **G.Piret, H.Drobeq, Y.Coffinier, O.Melnyk, R.Boukherroub.** Matrix-Free Laser Desorption/Ionization Mass Spectrometry on Silicon Nanowire Arrays Prepared by Chemical Etching of Crystalline Silicon. Langmuir, 2010, pp. 1354-1361.

56. **G.Piret, R.Desmet, E.Diesis, H.Drobecq, J.Segers, C.Rouanet, A.S.Debrie, R.Boukherroub, C.Locht, O.Melnyk.** Chips from Chips: Application to the Study of Antibody Responses to Methylated Proteins. Journal of Proteome Research, 2010, pp. 6467–6478.

57. **G.Piret.** Nanofils de Silicium Pour une Analyse Sensible de Biomolécules par Spectrométrie de Masse et pour l'adressage Fluidique de Cellules en vue des Applications Laboratoire sur Puce et Biopuces . Thèse de Doctorat de l'Université des Sciences et Technologies, 2010.

58. **M.Anbar, S.Guttmann.** The Isotopic Exchange of Fluoroboric Acid with Hydrofluoric Acid. J.Phys.Chem, 1960, pp. 1896-1899.

59. **R.E.Mesmer, A.C.Rutenberg.** Fluorine-19 Nuclear Magnetic Resonance Studies on Fluoroborate Species in Aqueous Solution. Inorg. Chem, 1973, pp. 699-702.

60. **M.L.Zhang, K.Q.Peng, X.Fan, J.S.Jie, R.Q.Zhang, S.T.Lee, N.B.Wong.** Preparation of Large-Area Uniform Silicon NanoWires Arrays though Metal-Assisted Chemical Etching. J.Phys.Chem.C, 2008, pp. 4444-4450.

61. **K.W.Kolasinski.** Catalytic growth of nanowires: Vapor–Liquid–Solid, Vapor–Solid–Solid, Solution–Liquid–Solid and Solid–Liquid–Solid Growth. Current Opinion in Solid State and Materials Science, 2006, pp. 182–191.

62. **V.Schmidt, J.V.Wittemann, U.Gösele.** Growth, thermodynamics, and electrical properties of silicon nanowires. Chemical reviews, 2010, pp. 361-388.

63. **A.K.Chu, J.S.Wang, Z.Y.STai, C.K.Lee.** A Simple and Cost-effective Approach for Fabrication Pyramids on Crystalline Silicon Wafers. Solar Energy Material and Solar Cells, 2009, pp. 1276-1280.

64. **T.P.N.Nguyen, P.Brunet, Y.Coffinier, R.Boukherroub.** Quantitative Testing of Robustness on Super-omniphobic surfaces by drop impact. Langmuir, 2010, pp. 8908-8913.

65. **H.J.Fan, P.Werner, M.Zacharias.** Semiconductor Nanowires: From Self-Organization to Patterned Growth. Small, 2006, pp. 700-717.

66. **F.Lapierre, V.Thomy, Y.Coffinier, R.Boukherroub.** Reversible Electrowetting on Superhydrophobic Double-NanotexturedSurfaces. Langmuir, 2009, pp. 6551-6558.

67. **P.Brunet, F.Lapierre, V.Thomy, Y.Coffinier, R.Boukheroub.** Extreme Resistance of Superhydrophobic surfaces to implalement: Reversible Electrowetting Related to the Impacting/Bouncing Drop Test. Langmuir, 2008, pp. 11203-11208.

68. **W.Choi, A.Tuteja, J.Mabry, R.E.Cohen, G.H.Mckinly.** A modified Cassie-Baxter Relationship to Explain Contact Angle Hysteresis and Anisotropy on Non-wetting Textured Surfaces. Journal of Colloid and Interface Science, 2009, pp. 208-21.

69. **R.N.Wenzel.** Resistance of Solid Surfaces to Wetting by Water. Ind. Eng. Chem., 1936, pp. 988–994.

70. **B.Cassie.** Wettability of Porous Surfaces. Trans. Faraday Soc, 1944, pp. 546–551.

71. **A.Tuteja, W.Choi, J.M.Mabry, G.H.McKinley, R.E.Cohen.** Engineering Superhyrophobic and Superoleophobic Surfaces. Nanotech, 2008, pp. 439-442.

72. —. Robust omniphobic surfaces. PNAS, 2008, pp. 18200-182005.

73. **W.Wu, X.Wang, D.Wang, M.Chen, F.Zhou, W.Liu, Q.Xue.** Alumina Nanowire Forests via nconventional Anodization and Super-repellency plus Low Adhesion to Diverse Liquids. Chem.commun, 2009, pp. 1043-1045.

74. **J.Bico, C.Tordeux, D.Quéré.** Rough Wetting. Europhys.Lett, 2001, pp. 214-220.

75. **D. Richard, D. Quéré´.** Bouncing water drops. Europhys. Lett., 2002, pp. 769–775.

76. **P.G.Gennes.** Wetting: statics and dynamics. Rev.Mod.Phys, 1985, p. 827.

77. **J. Bico, C. Marzolin, D. Quéré.** Pearl drops. Europhys. Lett, 1999, pp. 220-226.

78. **S.K.Cho, H.Moon.** Electrowetting on Dielectric (EWOD): New Tool for Bio/Micro Fluids Handling. biochip journal, 2008, pp. 79-96.

79. **H.Y.Erbil, C.E.Cansoy.** Range of Applicability of the Wenzel and Cassie-Baxter Equation for Superhydrophobic Surfaces. Langmuir, 2009, pp. 14135-14145.

80. **A.Marmur.** Wetting on Hydrophobic Rough Surfaces: To Be Heterogeneous or Not To Be. Langmur, 2003, pp. 8343-8348.

81. **M.Ma, R.M. Hill.** Superhydrophobic Surfaces. Current Opinion in Colloid & Interface Science, 2006, pp. 193–202.

82. **M.Nosonovsky.** Multiscale roughness and stability of superhydrophobic biomimetic interfaces. Langmuir, 2007, pp. 3157-3161.

83. **J. Bico, C. Marzolin, and D. Quéré.** Pearl drops. Europhys. Lett, 1999, pp. 220-226.

84. **R.Dufour, M.Harnois, Y.Coffinier, V.Thomy, R.Boukherroub, V.Senez.** Engineering Sticky Superomniphobic Surfaces on Transparent and Flexible PDMS Substrate. Langmuir, 2010, pp. 17242-17247.

85. **M.Im, H.Im, J.H Lee, J.B.Yoon,Y.K.Choi.** A Robust Superhydrophobic and Superoleophobic Surface with Inversetrapezoidal Microstructures on a Large Transparent Flexible Substrate. Soft Matter, 2010, pp. 1401–1404.

86. **D.Bartolo, F.Bouamrirene, E.Verneuil, A.Buguin, P.Silberzan, S.Moulinet.** Bouncing or Sticky Droplets: Impalement Transition Superhydrophobic Micropatterned Surfaces. 299-305 : Europhys.Lett, 2006 .

87. **Y.C.Jung, B.Bhushan.** Dynamic Effects of Bouncing Water Droplets on SuperhydrophobicSurfaces. Langmuir, 2008, pp. 6262-6269.

88. **D. Richard, D. Quéré´.** Bouncing water drops. Europhys. Lett., 2002, pp. 769–775.

89. **S.Moulinet, D.Bartolo.** Life and Death of a Fakir Droplet: Impalement Transitions on Superhydrophobic Surfaces. Eur.Phys.J.E, 2007, pp. 1-9.

90. **A.Lafuma, D.Quéré.** Superhydrophobic States. Nature materials, 2003, pp. 457-460.

91. **D.Bartolo, F.Bouamrirene, E.Verneuil, A.Buguin, P.Silberzan, S.Moulinet.** Bouncing or Sticky Droplets: Impalement Transition Superhydrophobic Micropatterned Surfaces. Europhys.Lett,, 2006, pp. 299-305.

92. **T.G.Cha, J.W.Yi, M.W.Moon, K.R.Lee, H.Y.Kim.** Nanoscale Patterning of Microtextured Surfaces to Control Superhydrophobic Robustness. Langmuir, 2010, pp. 8319–8326.

93. **Z.Guo, W.Liu, B.L.Su.** Superhydrophobic surfaces: From Natural to Biomimetic to Functional. 335-355 : Journal of Colloid and Interface Science, 2011 .

94. **W.Wu, X.Wang, D.Wang, M.Chen, F.Zhou, W.Liu, Q.Xue.** Alumina Nanowire Forests via nconventional Anodization and Super-repellency plus Low Adhesion to Diverse Liquids. Chem.commun, 2009, pp. 1043-1045.

95. **S. Shibuichi, T. Yamamoto, T. Onda, K. Tsujii.** Super Water- and Oil-Repellent Surfaces Resulting from Fractal Structure. Journal of colloid and interface science, 1998, pp. 287–294.

96. **W.A.Zisman.** Relation of The Equilibrium Contact Angle to Liquid and Solid Construction. American Chemical Society, 1964, pp. 1-51.

97. **C.Aulin, S.H.Yun, L.Wagberg, T.Lindstrom.** Design of Highly Oleophobic Cellulose Surfaces From Structured Silicon Templates. Applied Materials & Interfaces, 2009, pp. 2443-1452.

98. **A.Tuteja, W.Choi, M.Ma, J.M Mabry, S.Mazzella, G.C.Rutledge, G.H.McKinley, R.E.Cohen.** Designing superoleophobic surfaces. Science, 2007, pp. 1618-1622.

99. **S.A. Kulinich, M. Farzaneh.** Hydrophobic Properties of Surfaces Coated with Fluoroalkylsiloxane and Alkylsiloxane Monolayers. Surface Science, 2004, pp. 379-390.

100. **A.W.Adamson, A.P Gast.** Physical chemistry of Surface. Wiley, New York,, 1997, p. 368 .

101. **J.Vojtechovska, L.Kvitek.** Surface Energy-effect of Physical and Chemical Surface Properties. Acta universitaits palackianae olomoucesis facultas rerum natruralium, 2005, pp. 25-48.

102. **A. Thünemann, A.Lieske, B.R.Paulke.** Low Surface Energy Coatings From Waterborn NanoDispersions of Polymer Complexes. Adv.Mater, 1999, pp. 321-324.

103. **Y.Coffinier, Z.Galopin, S.Szunerits, R. Boukherroub.** Preparation of Superhydrophobic and Oleophobic Diamond Nanograss Array. J. Mater. Chem, 2010, pp. 10671-1067 .

104. **G.Kwak, M.Seol, Y.Tak, K.Yong.** Superhydrophobic ZnO Nanowire Surface: Chemical Modification and Effects of UV Irradiation. J.Phys.Chem.C, 2009, pp. 12085-12089.

105. **M.T.Khorasani, H.Mirzadeh, Z.Kermani.** Wettability of Porous Polydimethylsiloxane Surface Morphology Study. Applied Surface Science, 2005, pp. 339–345.

106. **L.Cao, H.H.Hu, D.Gao.** Design and Fabrication of Micro-textures for Induction a Superhydrophobic Behavior on Hydrophilic Materials. Langmuir, 2007, pp. 4310-4314.

107. **J.L.Liu, X.Q.Feng, G.Wang, S.W.Yu.** Machanisms of Superhydrophobicity on Hydrophilic Substrates. J.Phys.:Condens, Matter, 2007, pp. 356002-356014.

108. **A.Ahuja, J.A.Taylor, A.A.Sidorenko, T.R.Salamon, E.J. Lobaton, P.Kolodner, T.N.Krupenkin.** Nanonails: A Simple Geoometrical Approach to Electrically Tunable Superlyophobic Surfaces. Langmuir, 2007, pp. 9-14.

109. **R.Zenobi, R.Knochenmuss.** Ion Formation in MALDI Mass Spectrometry. Mass Spectrometry Reviews, 1998, pp. 337–366.

110. **G.Siuzdak.** The Expanding Role of Mass Spectrometry In Biotechnology. book : MCC Press, 2003.

111. **Y.Xu, M.L.Bruening, J.T.Watson.** Non-Specific, on-Probe Cleanup Methods for MALDI-MS Samples. Mass Spectrom. Rev., 2003 , pp. 429-440.

112. **X. Wen, S.Dagan, V.H.Wysocki.** Small-Molecule Analysis with Silicon-Nanoparticle-Assisted Laser Desorption/Ionization Mass Spectrometry. Anal. Chem, 2007, pp. 434-444.

113. **K.L.Bush.** Desorption Ionization Mass Spectrometry. Journal of mass spectrometry, 1995, pp. 233-240.

114. **Y.Chen, A.Pépin.** Nanofabrication: Convention and Nonconventional Methods. Electrophoresis, 2001, pp. 187-207.

115. **Y.Chen, Y.Verte.** Adjustable Fragmentation in Laser Desorption/Ionization from Laser induced Silicon Micorcolumn Arrays. Analytical Chemistry, 2006, pp. 5835-5844.

116. **Y.Chen, H.Chen, A.Aleksandrov, T.M.Orlando.** Roles of Water, Acidity, and Surface Morphology in Surface-Assisted Laser Desorption/Ionization of Amino Acids. J.Phys.Chem.C, 2008, pp. 6953-6960.

117. **R.D.Lowe, G.E.Guild, P.Harpas, P.Kirkbride, P.Hoffmann, N.H.Voelcker, H.Kobus.** Rapid drug detection in oral samples by porous silicon assisted laser desorption/ionization mass spectrometry. Rapid Communications in Mass Spectrometry, 2009, pp. 3543-3548.

118. **R.D.Lowe, E.J.Szili, P.Kirkbride, H.Thissen, G.Suizdak, N.H.Voelker.** Combined Immunocapture and Laser Desorption/Ionization Mass Spectrometry on Porous Silicon. Anal. Chem, 2010, pp. 4201–4208.

119. **K.Dreiwerd.** The Desorption Process in MALDI. Chem.Rev, 2003, pp. 395-425.

120. **G.Luo, Y.Chen, G.Siuzdak, A.Vertes.** Surface Modification and Laser Pulse Length Effects on Internal Energy Transfer in DIOS. J. Phys. Chem. B, 2005, pp. 24450-24456.

121. **S.R.Weinberger, E.Boschetti, P.Santambien, V.Brenac.** Surface-Enhanced Laser Desorption/Ionization Retente Chromatography Mass Spectrometry (SELDI-RC-MS): a New Method for Rapid Development of Process Chomatography Conditions. J.Chromatogr. B Anal. Technol, 2002, pp. 307-316.

122. **J.Wei, J.M.Buriak, G.Suizdak.** Desorption/ionization Mass Spectrometry on Porous Silicon. Nature, 1999, pp. 243-246.

123. **Y.Xiao, S.T.Retterer, D.K.Thomas, J.Y.Tao, L.He.** Impacts of Surface Morphology on Ion Desorption and Ionization On Porous Silicon (DIOS) Mass spectrometry. J.Phys.Chem C, 2009, pp. 3076-3083.

124. **E.P.Go, J.V.Apon, G.Luo, E. P. Go, G.Luo, A. Saghatelian, R. H. Daniels, V. Sahi, R. Dubrow, B. F. Cravatt, A. Vertes, G. Siuzdak.** Desorption/Ionization on Silicon Nanowires. Anal. Chem, 2005, p. 1641 1646.

125. **C.W.Tsao, P.Kumar, J.Liu, D.L. Devote.** Dynamic Electro Wetting on Monofilament Silicon for Matrix-Free Laser Desorption/Ionization Mass Spectrometry. Anal. Chem, 2008, pp. 2973-2981.

126. **J.K.Lewis, J.Wei, G.Suizdak.** Matrix-assisted Laser Desorption/Ionization Mass-Spectrometry in Peptide and Protein Analysis. Encylopedia of Analytical Chemistry, 2000, pp. 5580-5894.

127. **S.H.Bhattacharya, T.J.Raiford, K.K.Murray.** Infrared Laser Desorption/Ionization on Silicon. Anal.Chem, 2002 , pp. 2228-2231.

128. **S.Alimpiev, S.Nikiforov, V.Karavanskii.** On The Mechanism of Laser-Induced Desorption–Ionization of Organic Compounds from Etched Silicon and Carbon Surfaces. J. Chem. Phys, 2001, pp. 1891-1901.

129. **E.Nordhoff, A. Ingendoh, R.Cramer, A.Overberg, B.Stahl, M. Karas, F.Hillenkamp.** Matrix-assisted Laser Desorption/Ionization Mass Spectrometry of Nucleic Acids with Wavelengths in the Ultraviolet and Infrared", Rapid commucations in mass spectrometry. Rapid Commucations in Mass Spectrometry, 1992, pp. 771-776.

130. **W.Y.Chen, J.T.Huang, Y.C.Cheng, C.C.Chien, C.W.Tsao.** Fabrication of Nanostructured Silicon by Metal-Assisted Etching and its Effects on Matrix-Free Laser Desorption/Ionization Mass Spectrometry. Anal.Chem, 2010, pp. 97-104.

131. **R.Arakawa, H.Kawasaki.** Funtionalized Nanoparticles and Nanostructured Surfaces for Surface-Assisted Laser Desorption/Ionization Mass Spectrometry. Analytical Sciences, 2010, pp. 1229-1240.

132. **M.Najam-ul-Haq, M.Rainer, C.W.H.P.Hausberger, H.Kraushaar, G.K.Bonn.** Nanostructured Diamond-Like Carbon on Digital Versatile Disc as a Matrix-Free Target for Laser Desorption/Ionization Mass Spectrometry. Anal. Chem, 2008, pp. 7467-7472.

133. **Q.Li, A.Ricardo, S.A.Benner, J.D.Winefordner, D.H.Powell.** Desorption/Ionization on Porous Silicon Mass Spectrometry Studies on Pentose-Borate Complexes. Anal.Chem, 2005, pp. 4503-4508.

134. **J.Shen, T.Ahmed, A.Vogt, J.Wang, J.Severin, R.Smith, S.Dorwin, R.Johnson, J.Harlan, T. Holzman.** Preparation and Characterization of Nitrolotriacetic-Acid-Terminated Self-Assembled Monolayer on Gold Surfaces for Matrix-Assisted Laser Desorption/Ionization. Anal. Biochem., 2005, pp. 258-269.

135. **E.P.Go, Z.Shen, K.Harris, G.Siuzdak.** Quantative Analysis with Desorption/Ionization on Silicon Mass Spectrometry Using Electrospray Deposition. Anal.Chem, 2003, pp. 5475-5479.

136. **R.A.Kruse, X.Li, P.W.Bohn, J.V.Sweedler.** Experimental Factors Controlling Analyte Ion Generation in Laser Desorption/Ionization Mass Spectrometry on Porous Silicon. Anal.Chem, 2001, pp. 3639-3645.

137. **S.A.Trauger, E.P.Go, Z.Shen, J.V.Apon, B.J.Compton, E.S.P. Bouvier, M. G. Finn, and G.Siuzdak.** High Sensitivity and Analyte Capture with Desorption/Ionization Mass Spectrometry on Silylated Porous Silicon. Anal. Chem, 2004, pp. 4484-4489.

138. **W.J.Shin, J.H.Shin, J.Y.Song, S.Y.Han.** Effects of ZnO Nanowire Length on Surface-Assisted Laser Desorption/Ionization of Small Molecules. J Am Soc Mass Spectrom, 2010, pp. 989–992.

139. **C.Y.Lo, J.Y.Lin, W.Y.Chen, C.T.Chen, Y.C.Chen.** Surface-assisted Laser Desorption/Ionization Mass Spectrometry on Titania Nanotube Arrays. Am Soc Mass Spectrom, 2008, pp. 1014-1020.

140. **C.L.Su, W.L.Tseng.** Gold Nanoparticles as Assisted Matrix for Determining Neutral Small Carbohydrates through Laser Desorption/Ionization Time-of-Flight Mass Spectrometry. Anal. Chem., 2007, pp. 1626-1633.

141. **H.Kawasaki, T.Yonezawa, T.Watanabe, R.Arakawa.** Platinum Nanoflowers for Surface-Assisted Laser Desorption/Ionization Mass Spectrometry of Biomolecules. J.Phys.Chem. C, 2007, pp. 16278-16283.

142. **J.Sunner, E.Dratz, Y.C.Chen.** Graphite Surface-Assisted Laser Desorption/Ionization Time-of-Flight Mass Spectrometry of Peptides and Proteins from Liquids Solution. Anal.Chem, 1995, pp. 4335-4342.

143. **N.M.Suni, M.Haapala, E.Färm, E.Härkönen, M.Ritala, L.Sainiemi, S.Franssila, T.Kotaho, R.Kostiainen.** Fabrication of Nanocluster Silicon Surface with Electric Discharge and The Application in Desorption/Ionization on Silicon-Mass Spectrometry. Lab Chip, 2010, pp. 1689-1695.

144. **B.Gulbakan, D.Park, M.Kang, K.Kececi, C.R.Martin, D.H.Powell, W.Tan.** Laser Desorption Ionization Mass Spectrometry on Silicon Nanowell Arrays. Anal.Chem, 2010, pp. 7566-7575.

145. **S.Okuno, R.Arakawa, K.Okamoto,Y.Matsui, S.Seki, T.Kozawa, S.Tagawa, Y.Wada.** Requirements for Laser-Induced Desorption/Ionization on Submicrometer Structures. Anal. Chem, 2005, pp. 5364-5369.

146. **D.J.Rousell, S.M.Dutta, M.W.Little, K.K.Murray.** Matrix-Free Infrared Soft Laser Desorption/Ionization. J.Mass Spectrom, 2004, pp. 1182-1189.

147. **A.Muck, T.Stelzner, U.Hübner, S.Christiansen, A.Svatos.** Lithographically patterned silicon nanowire arrays for matrix free LDI-TOF/MS analysis of liquids. Lap-on-Chip, 2010, pp. 320-325.

148. **C.C.Chiang, W.T.Chen, H.T.Chang.** Nanoparticle-Based Mass Spectrometry for the Analysis of Biomolecules. Chemical Society Reviews, 2010, p. view online.

149. **A.G.Nassiopoulou, G.Kaltsas.** Porous Silicon as an Effective Material for Thermal Isolation on Bulk Crystalline Silicon. Phys.stat.sol, 2000, pp. 307-311.

150. **E.P.Go, W.Uritboonthai, J.V.N.Apon, S.A.Trauger, A.Nordstrom, G.O'Maille, S.M.Brittain, E.C.Peters, G.J.Siuzdak.** Selective Metabolite and Peptide Capture/Mass Detection Using Fluorous Affinity Tags. Proteome Res, 2007, pp. 1492-1499.

151. **A. Ressine, G.M.Varga, T.Laurell.** Porous Silicon Protein Microarray Technology and Ultra-/Superhydrophobic States for Improved Bioanalytical Readout. Biotechnology annual review, 2007, pp. 149-200.

152. **C.M.Ho, T-S.Wong, X.Shen.** Coffee rings for microscale biomolecular processing. Biomedical Optics & Medical Imaging, 2010, pp. 1-2.

153. **A.Ressine, D.Finnskog, G.M.Varge, T.Laurell.** Superhydrophobic Properties of Nanostructured-Microstructured Porous Silicon for Improved Surface-Based Bioanalysis. Nanobiotechnol, 2008 , pp. 17-28.

154. **P.Brunet, N.T.P.Nguyen, Y.Coffinier, R.Boukherroub.** Drying of Particle-Laden on Superhydrophobic surface. poster, 2010.

155. **N.A.Guzman, T.Blanc, T.M.Phillips.** Immunoaffinity Capillary Electrophoresis as a Powerful Strategy for the Quantification of Low-Abundance Biomarkers, Drugs, and Metabolites in Biological Matrices. Electrophoresis, 2008, pp. 3259-3278.

156. **P.C.Lin, M.C.Tseng, A.K.Su, Y.J.Chen, C.C.Lin.** Functionalized Magnetic Nanoparticles for Small-Molecules Isolation, Identification, and Quantification. Anal.Chem, 2007, pp. 3401-3408.

157. **J.D.Dunn, E.A.Igrisan, A.M.Palumbo, G. E.Reid, M.L.Bruening.** Detection of Phosphopeptide Using Fe(III)-Nitrilotriacetate Complexes Immobilized on a MALDI Plate. Anal. Chem., 2008, pp. 5727-5735.

158. **M.Najam-ul-Haq, M.Rainer, T.Schwarzenauer, C.W.Huck, G.K.Bonn.** Chemically modified carbon nanotubes as material enhanced laser desorption ionisation (MELDI) material in protein profiling. Aalytitca Chemica Acta, 2006, pp. 32-39.

159. **A.Eriksson, J.Bergquist, K.Edwards, A.Hagfeldt, D.Malmström, V.Hermandez,.** Mesoporous TiO2-Based Experimental Layout for On-Target Enrichment and Separation of Multi- and Monophosphorylated Peptides Prior to Analysis with Matrix-Assisted Laser Desorption-Ionization Mass Spectrometry. anal.Chem, 2011, pp. 761-766.

160. **H. .Zou, Q.C.Zhang, Z.Guo, B.C.Guo, Q.Zhang, X M.Chen.** A Mass Spectrometry Based Direct-Binding Assay for Screening Binding Partners of Proteins. Angew. Chem. Int. Ed., 2002, pp. 646-648.

161. **L.G.Hu, S.Y.Xu, C.S Pan, H.Zou, G. B. Jiang.** Preparation of a Biochip on Porous Silicon and Application for Label-Free Dectection of Small Molecule-Protein interactions. " Rapid Commun. Mass Spectrom, 2007, pp. 1277-1281.

162. **J.C.Meng, G.Siuzdak, M.G.Finn.** Affinity Mass Spectrometry from a Tailored Porous Silicon Surface. Chem. Commun, 2004, pp. 2108-2109.

163. **H.Bi, L.Qiao, J.M.Busnel, V.Devaud, B.Liu, H. H. Girault.** TiO2 Printed Aluminum Foil: Singnal-Use Film for a Laser Desorption/Ionization Target Plate. Anal. Chem, 2009, pp. 1177-1183.

164. **N.Haddour, S.Cosnier, C.Gondran.** Electrogeneration of Poly(pyrrole)-NTA Cheletor Film for a Reversible Oriented Immobilization of Histidine-Tagged Proteins. J.Am.Chem.Soc, 2005, pp. 5752-5753.

165. **B.Nastasijevic, N.A.Becker, S.E.Wurster, L.J.Maher.** Sequence-specific binding of DNA and RNA to Immobilized Nickel ions. BioChemical and Biophysical, 2008, pp. 420-425.

166. **R.Blankespoor, B.Limoges, B.Schöllhorn, J.L.S.Magalé, D.Yazidi.** Dense Monolayer of Metal-Chelating Ligands Covalently Attached to Carbon Electrodes Electrochemically and Their Useful Application in Affinity Binding of Histidine-Tagged Proteins. Langmuir.

167. **L.Nieba, S.E.N.Axamann, A.Petsson, M.Hämäläniem, F.Edebratt, A.Hanson, J.Lidholm, K.Magnusson.** BIACORE Analysis of Histidine-Tagged Proteins Using a Chalating NTA Sensor Chip. Anal.Biochem, 1995, pp. 217-228.

168. **P.Rigler, W.P.Ulrich, P.Hoffmann, M.Mayer, H.Voge.** Reversible Immobilization of Peptide: Surface Modification and In Situ Detection by Attenuated Total Reflection FTIR Spectroscopy. ChemPhyChem, 2003, pp. 268-275.

169. **J.Kim, H.Y.Park, J.Kim, J.Ryu, D.Y.Kwon, R.Grailhe, R.Song.** Ni-Nitrilotriacetic Acid-modified Quantum Dots as a Site-specific Labelling Agent of Histidine-tagged Proteins in Live Cells. Chem.Commun, 2008, pp. 1910-1912.

170. **X.Liu, H.M.Han, H.B.Liu, S.J.Xiao.** Enhanced protein loading on a planar Si (111)-H surface with second generation NTA. Surface Science, 2010, pp. 1315-1319.

171.   **R.Boukherroub, J.T.C.Wojtyk, D.D.M.Wayner, D.J.Lockwood.** Thermal Hydrosilylation of Undecylenic Acid with Porous Silicon. J.Am.Chem.Soc, 2002, pp. H59-H63.

172. **R.Voicu, R.Boukherroub, V.Bartzoka, T.Ward, J.J.C.Wojtyk, D.D.M.Wayner.** Formation, Characterization, and Chemistry of Undecanoic Acid-Teminated Silicon Surfaces: Patterning and Immobilization of DNA. Langmuir, 2004, pp. 11713-11720.

173. **R.Boukherroub.** Chemical Reactivity of Hydrogen-terminated Crystalline Silicon Surface. Current Opinion in Solid State and Materials Science , 2005, pp. 66-72.

174. **YJ.Li, R.Tero, T.Nagasawa, T.Nagata, T.Urisu.** Deposition of 10-Undecenoic Acid Self-Assembled Layers on H–Si (111) Surfaces Studied With AFM and FTIR. Japanese Journal of Applied Physics, 2004, pp. 4591–4594.

175. **J.M.Buriak.** Chemical Reviews: Organometallic Chemistry on Silicon and Germanium Surfaces. J.Am.Chem.Soc, 2002, pp. 1272-1308.

176. **N.L.Rowell, L.Tay, R.Boukherroub, D.J.Lockwood.** Infrared Spectroscopy of Self-assembled Monolayer Films on Silicon. Surface Science, 2007, pp. 2566-2570 .

177. **P.O.Andersson, M.Lundquist, L.Tegler, S.Börjegren, L.Baltzer, L.Österlund.** A Novel ATR-FTIR Approach for Characterisation and Identification of Ex Situ Immobilised Species. ChemPhysChem, 2007, pp. 712-722.

178. **R.Valiokas, G.Klenkar, A.Tinazli, A.Reichel, R.Tampé, J.Pieher, B.Liedberg.** Self-Assembled Monolayers Containing Terminal Mono-, Bis-, and Tris-nitrilotriacetic Acid Groups: Characterization and Application. Langmuir, 2008, pp. 4959-4967.

---

i   *http://www.royalepigments-chem.com/index_files/SodiumFluoroborateHazMSDS.pdf*

ii   *http://www.chem.purdue.edu/chemsafety/Equip/hfmsds.pdf*

iii   *http://en.wikipedia.org/wiki/Chemical_vapor_deposition*

iv   *http://www.iemn.univ-lille1.fr/en/facilities/clean-room/facilities/growth-and-deposition-of-thin-   layer/pe-cvd-cold-process.html*

v   *http://www.eaglabs.com/files/techniquenote/TN100.pdf*

vi   *http://www.eaglabs.com/files/techniquenote/TN100.pdf*

vii   *N.Chiboub, R.Boukherroub, S.Szunerits, N.Gabouze, S.Moulay, S.Sam « Chemcial and electrochemical   graftin of plyaniline on aniline-terminated porous silicon" , interface analysis, (2010), 42, 1342-1346*

Résumé:

Mes travaux de thèse concernent la fabrication de micro et de nanostructures en silicium dans le but de développer des surfaces non-mouillantes et des outils analytiques pour applications en biochimie et en microfluidique. Pour ce faire, nous avons utilisé d'une part la gravure chimique humide qu'est la « metal-assisted electroless etching » (approche descendante) et d'autre part la croissance de nanofils par « Chemical Vapor Deposition » *via* le mécanisme « Vapor-Liquid-Solid » (approche ascendante). Des surfaces structurées possédant des morphologies différentes ont été obtenues. Grâce à ces méthodes de fabrication nous avons préparé des structurations simples et doubles, à savoir des structurations nanométriques et micrométriques et des doubles structurations micro-nanométriques.

Dans une première partie, les surfaces structurées ont permis de développer des surfaces superomniphobes, capables de repousser des liquides présentant des tensions de surface comprise : 20 <γ< 72 mN/m. Les surfaces présentant une double structuration donnent les meilleures propriétés de non-mouillage

Dans une deuxième partie, ces surfaces nanostructurées ont été utilisées comme matrices inorganiques pour la désorption/ionisation assistée par laser permettant l'analyse en spectrométrie de masse de petites molécules sans utilisation de matrice organique. Nous avons étudié l'influence de la morphologie, du type de dopage et de la terminaison chimique sur l'analyse en spectrométrie de masse d'un mélange de peptide standard.

Finalement, nous avons réalisé l'enrichissement d'un peptide et son analyse en spectrométrie de masse à partir d'un mélange donné, grâce à l'introduction d'un ligand spécifique.

Mots-clés *: Nanostructures de silicium, Nanofils de silicium, Superomniphobe, Spectrométrie de masse, Analyse DIOS-MS, Tag-Histidine*

Abstract

This work concerns the fabrication of micro/nanostructured silicon substrates and their application as non-wetting surfaces, and analytical tools for biomolecules' analysis and in microfluidic devices. Two different techniques were investigated for the formation of nanostructured silicon substrates: chemical wet etching *via* metal-assisted electroless etching (Top-down approach) and nanowire growth by « Chemical Vapor Deposition » *via* Vapor-Liquid-Solid mechanism (Bottom-up approach). Different structured surface morphologies were then obtained. These were either simple structured such as: Micro or Nanoscale, or double structured such as: Micro-Nano or Nano-Nanoscale.

The first part of the thesis deals with the preparation of superominiphobic surfaces capable of repelling almost any liquid (20 <γ< 72 mN/m). The surfaces consisting of double structured substrates gave the best non-wetting properties.

Secondly, nanostructured silicon substrates were used as inorganic matrices for the detection of small molecules without using an organic matrix in laser desorption/ionization mass spectrometry. Herein, we investigated the influence of surface morphology, doping type and chemical termination on mass spectrometry analysis of a standard peptide mixture.

Finally, functionalized silicon nanowires surfaces with a specific ligand were used to perform peptide enrichment and its subsequent analysis by mass spectrometry from a mixture solution

Keys words: *Silicon nanostructure, Silicon nanowires, Superomniphobe, Mass spectrometry, DIOS-MS analysis, Tag-Histidine*